Physical processes in small temperate lakes

By

Jordan S. Read

A dissertation submitted in partial fulfillment
of the requirements for the degree of

Doctor of Philosophy

(Civil and Environmental Engineering)

at the

University of Wisconsin – Madison

2012

Date of final oral examination: May 24, 2012

This dissertation is approved by the following members of the Final Oral Committee:
Chin W. Wu, Civil and Environmental Engineering
Katherine McMahon, Civil and Environmental Engineering
Steven P. Loheide, Associate Professor, Civil and Environmental Engineering
Ankur R. Desai, Associate Professor, Atmospheric and Oceanic Sciences
Paul C. Hanson, Associate Research Professor, Limnology
John Lenters, Associate Professor, Climate Science

ABSTRACT

Small temperate lakes are numerically dominant and globally relevant to nutrient and carbon cycles, but physical processes in these lakes have been historically understudied. The primary objective of this research is to examine physical processes in small temperate lakes and explore differences between relevant physical drivers across different size classes of lakes. This research consisted of the instrumented physical monitoring of many lakes in addition to the creation of a hydrodynamic model that was designed and calibrated for small (< 10 ha) lakes. Instrumented buoy data was collected from 40 temperate lakes and used to compare the relative importance of wind versus convectively driven mixing for lakes of different sizes. This information was then used to parameterize a turbulence-based gas exchange model (the surface renewal model) from these physical observations. Convection was found to be dominant on small lakes (all 11 lakes < 10 ha in the analysis) and convection was also of increased importance on smaller lakes as a driver of the gas transfer velocity.

The numerical model (CLM) was designed for small convectively dominated lakes and was calibrated and validated on 8 small lakes. CLM simulations suggested that water column transparency is a very important driver of water temperatures and surface mixed layer depths. Darker lakes were colder with shallower mixed layers compared to more transparent simulations. Clearer lakes were found to be more sensitive to climate variability, as indicated by interseasonal variability in average water temperatures. CLM was also used to estimate the vertical diffusivity of heat in these small lakes, and the model indicated that heat transfer was at or near the rate of the molecular diffusion of heat. This finding is relevant to the vertical flux of dissolved gases in small lakes, where vertical diffusion below the mixed layer is likely to be near the molecular rate of diffusion for the gas of interest. A new method (the paired thermistor method) was devised to

estimate water column transparency from time series of temperature measurements. This method can be used to follow patterns in water transparency as well as to estimate water column transparency for the purposes of numerical modeling.

An artificial destratification device, the Gradual Entrainment Lake Inverter (GELI), was designed to eliminate thermal stratification in small lakes. GELIs were used to destratify a normally strongly stratified bog lake (North Sparkling Bog, Wisconsin, USA) over the course of eight days, reducing the surface to bottom temperature difference from 19.2 to 0.2°C. The GELI method employs alternating stages of positive and negative buoyancy to move a large (8 m diameter) steel frame and geomembrane through the water column. GELIs introduce turbulence by generating internal waves, creating a large trailing wake, and via shear flows and circulation. GELIs are a more efficient artificial destratification method than bubbler aeration, and provide a potentially useful alternative management option.

Data analysis and data sharing platforms were created to aid in the analysis of environmental data from sensor networks. A simple file sharing standard, gFile, was developed for use in products of this research such as the hydrodynamic model CLM. The software package "Lake Analyzer" was designed for the analysis of instrumented buoy data using the gFile data standard. Lake Analyzer is a numerical program suite coupled with supporting visualization tools for determining indices of mixing and stratification that are critical to the biogeochemical cycles of lakes and reservoirs. Lake Analyzer provides an adaptable program structure and best practices for the comparison of mixing and stratification indices for instrumented lakes.

ACKNOWLEDGEMENTS

A large portion of the credit for the completion of this dissertation belongs to my incredible family, graduate committee members, friends, scientific peers, and field helpers that I have been surrounded with during the course of my graduate work. The various sources of travel and research funding I have received were also invaluable towards the cultivation of many of these research questions and gave me the ability to share my work with others. I appreciate the many people that made my successes seem bigger and my failures seem smaller during the PhD journey, as well as those who pushed me to improve upon my weaknesses.

I have received travel and research monies from NSF, the Gordon and Betty Moore Foundation, the Juday Family, Becker Family, Frasier Family, Anna Grant Birge Memorial Award, and the Wisconsin Department of Natural Resources (specific grant numbers are cited in text). The Frasier Fellowship award, given to me on my first year of graduate school, was especially valuable. The Family's generous gift allowed me to discover my own research direction that was independent of specific project goals. This funding flexibility was integral to the discovery of my ultimate research path. Support from GLEON (in the form of NSF and Gordon and Betty Moore grants) for meeting and workshop attendance inspired new research paths and gave me access to countless new friends and collaborators to exchange ideas with. I also appreciated teaching assistant opportunities for Fluid Mechanics and the Limnology Lab course.

My graduate committee has been integral to the exploration and completion of these research avenues. Special thanks to Chin Wu, Ankur Desai, Paul Hanson, John Lenters, Steve Loheide, and Trina McMahon for their continuous support. Thanks to Chin for pulling me into limnology, pushing me towards my goals, and supporting me along the way. Thanks to all for

believing in my work, offering great career and research advice, and encouraging me to share my research with others. Thanks to Tim Kratz and Emily Stanley, for encouraging my involvement with GLEON and LTER, and for always having an open door. The support and friendship I gained from Trout Lake Station staff and researchers was something I will never forget. Getting to know Ken, Tim, Carl, Noah, Pam, Mike and others was one of the highlights of my graduate career. Zach Lawson and Eric Brown deserve medals for their tireless field work, appreciation for collaborative problem solving, and patience. My GLEON family of collaborators is one of the defining relationships of my young career. Thanks to Paul, David, Evelyn, Jim, Kathie, Justin, Eleanor, Liz, Kohji, Alo, Peter, Robyn, and others for providing perspective, sharing ideas, giving students a voice, and capturing the essence of collaboration. Two of my best friends, Kevin and Luke, have always been available for discussion about science and life. I appreciate the countless hours the two of you dedicated to helping me improve drafts and research questions. Trina and Ashley have been great friends and mentors during my PhD journey. Trina, thanks for your friendship and your continued emotional and financial support. Ashley, thank you for raising the scientific bar and for believing that we could mix that bog. My officemates in room 1261 have been great friends and scientific peers. Special thanks to Eric, Josh, Adam, Nathan, Dave, Henry and Yvonne. Henry provided incredible sage advice during the early stages of my PhD and Eric and my good friend Jamon from the geography department still continue to help me along the way. Steve, Lucas, Jereme, Jamin, Gretchen, and Ryan were excellent resources and peers.

My parents, Bill and Barbara Read, have been incredible role models. My parents have instilled in me a love for science, an undying appreciation for education, and the drive that both keeps me working and keeps me balanced. My sister (the social Read) has helped me shape

myself into a collaborative scientist and has given me valuable perspectives from the policy and social realms. My dog, Tsavo, must be given at least partial credit for my ability to maintain my sanity during my PhD journey. I am convinced that the countless mind-clearing walks and jogs were part of an important recipe for balance during the difficult times. To Jon and Ryan – we grew up playing music together when we were 12 – I think that is the first time I really put my all into something, and the work ethic has stayed with me ever since. My friend Tony gave me a new perspective on adversity and life this year. My childhood public school teachers were the best in the business and one of the many reasons that Wisconsin is great. Finally, my fiancée Emily has been an incredible inspiration in all aspects of my life and my science. She has kept me motivated, kept me positive, inspired me with her patience, and encouraged me to do my best work. These days in Merril cabin, writing side-by-side, have been as enjoyable as they have been productive.

TABLE OF CONTENTS

CHAPTER 1 Introduction **1**

1.1 Physical processes in small lakes **1**
1.2 Research objectives **2**
1.3 Introduction to the dissertation **3**
1.4 References **4**

CHAPTER 2 Derivation of lake mixing and stratification indices from high-resolution lake buoy data using "Lake Analyzer" **7**

2.1 Abstract **7**
2.2 Introduction **8**
2.3 Comparative indices **11**
2.3.1 Thermocline/pycnocline depth 11
2.3.2 Mixed layer depth 13
2.3.3 Schmidt Stability 15
2.3.4 Wedderburn Number 15
2.3.5 Lake Number 16
2.4 Materials and methods **17**
2.4.1 Program structure 17
2.4.2 Program flow 17
2.4.3 Data sources 18
2.5 Results **18**
2.5.1 Lake Annie, Florida (USA) 18
2.5.2 Lake Rotorua, Bay of Plenty (NZ) 20
2.5.3 Lake Mendota, Wisconsin (USA) 21
2.6 Discussion **21**
2.6.1 Program availability 22
2.6.2 Program performance 23
2.6.3 Program limitations 23
2.7 Conclusions **25**
2.8 Acknowledgements **25**
2.9 References **26**

CHAPTER 3 Lake-size dependency of wind shear and convection as controls on gas exchange **36**

3.1 Abstract **36**
3.2 Introduction **36**
3.3 Methods **38**
3.3.1 Measurements 38
3.3.2 Calculating the convective velocity scale (w_*) 39
3.3.3 Calculating the wind shear velocity scale (u_*) 42
3.3.4 Comparing the contributions of u_* and w_* to mixed layer turbulence 43

3.3.5 Calculating the gas transfer velocity (*k*) 44
3.4 Results **45**
3.5 Discussion **46**
3.6 Acknowledgements **49**
3.7 References **50**

CHAPTER 4 Physical responses of small temperate lakes to variation in dissolved organic carbon concentrations **63**

4.1 Abstract **63**
4.2 Introduction **64**
4.3 Methods **66**
4.3.1 Site description 66
4.3.2 Physical measurements 67
4.3.3 Lab methods 68
4.3.4 Water temperature model 69
4.3.5 Modeling scenarios 72
4.3.6 Statistical methods 72
4.4 Results **74**
4.5 Discussion **76**
4.6 Acknowledgements **81**
4.7 References **82**

CHAPTER 5 "Gradual Entrainment Lake Inverter" (GELI): A novel device for experimental lake mixing **96**

5.1 Abstract **96**
5.2 Introduction **97**
5.3 Materials and procedures **99**
5.3.1 Experimental description 99
5.3.2 GELI design 100
5.3.3 Operation 101
5.3.4 Measurements 102
5.3.5 GELI efficiency 103
5.3.6 Water temperature model 105
5.4 Assessment and discussion **107**
5.4.1 Lake response to treatment 107
5.4.2 GELI mixing mechanisms 108
5.4.3 Efficiency/power use 111
5.5 Comments and recommendations **112**
5.6 Acknowledgements **114**
5.7 References **114**

CHAPTER 6 A method for estimating the diffuse attenuation coefficient (K_d) from paired thermistors **130**

6.1 Abstract **130**
6.2 Introduction **130**
6.3 Methods and procedures **132**
6.3.1 Site description 132
6.3.2 Physical measurements 132
6.3.3 Modeling attenuated temperature gains 133
6.3.4 Procedure 135
6.4 Assessment and discussion **137**
6.4.1 Model assumptions 137
6.4.2 Model validation 138
6.4.3 Optimal thermistor placement 139
6.5 Comments and recommendations **141**
6.6 References **142**

CHAPTER 7 Conclusions **150**

7.1 Summary **150**
7.2 Conclusions **152**
7.3 Recommendations for future research **154**
7.4 References **157**

Appendix A Appendix for the software package "Lake Analyzer" **160**

A.1 Additional calculations **160**
A.1.1 Density of water (ρ_i) 160
A.1.2 Seasonal thermocline (*SthermD*) 160
A.1.3 u-star (u_*) 161
A.1.4 Buoyancy frequency (N^2) 162
A.1.5 Mode 1 vertical seiche period (T_1) 162
A.1.6 Error-checking of input data 162
A.1.7 Down-sampling of input data 163
A.2 Program variables **163**
A.2.1 Outputs 163
A.2.2 Inputs 165
A.3 References **168**

Appendix B A file sharing standard for GLEON data: gFile **171**

B.1 Background **171**
B.2 gFile format **171**
B.3 File compression **173**
B.4 References **173**

Appendix C Estimating sensible and latent heat fluxes **175**

C.1 Background **175**

C.2 Methods **177**
C.2.1 Bowen Ratio Energy Budget (BREB) 177
C.2.2 Evaporation estimates using a free and forced convection model 182
C.3 References **184**

Appendix D An open-source one-dimensional water temperature model (CLM): Model description **190**

D.1 Introduction **190**
D.2 Model details **190**
D.2.1 Surface energy fluxes 190
D.2.2 Attenuation of penetrative shortwave energy 193
D.2.3 Wind-driven mixing 194
D.2.4 Mixing driven by density instability 196
D.2.5 Vertical gradient changes driven by thermal diffusivity 196
D.3 Model procedure **198**
D.3.1 Input values 198
D.3.2 Parameter functions 199
D.3.3 CLM initialization 201
D.3.4 CLM temporal loop 202
D.4 References **203**

Appendix E Calculating the diffuse attenuation coefficient (K_d) from radiometer profiles **205**

E.1 Introduction **205**
E.2 Radiometer measurements using the PUV **205**
E.3 Calculating K_d from PUV profiles **206**
E.4 Acknowledgements **208**
E.5 References **209**

LIST OF FIGURES

Figure 2.1 Algorithm for estimating the thermocline/pycnocline depth from example data. **a**) Continuous thermal profile (CTD cast, 10 cm resolution; thin black line) sampled at 0.5 m intervals (1 to 5 m) and 1 m intervals (5 to 14 m) to simulate discrete buoy thermistor measurements (○). **b**) Discrete temperature measurements from **a** converted into water density. **c**) Changes in density with respect to changes in depth ($\partial\rho/\partial z$) for discrete measurements. Maximum change is shown as ∗. Lake Analyzer's thermocline uses weighting from adjacent calculations (slopes shown as $\Delta\rho_{-1}$ and $\Delta\rho_{+1}$) to improve upon the discrete maximum (∗). **d**) Original temperature profile from **a** with thermocline depth estimate (♦; z_T), calculation boundaries (○; z_ζ and $z_{\zeta+1}$), and discrete maximum (∗; $z_{\zeta\Delta}$).....30

Figure 2.2 Thermocline algorithm for 24 days of CTD casts from Crystal Lake, WI, USA, converted to water density (thin black lines, smoothed using a 0.5 m running average from 10 cm measurements). Casts are offset by 0.2 kg m^{-3} on the x-axis for each day. **a**) CTD measurements are discretely sampled at 1 m intervals (●), and ∗ represents the maximum discrete change in density, while ♦ is the Lake Analyzer estimate (see Figure 1; 2.1.2). Actual maximum change in density (+) is calculated with knowledge of the continuous profile, and error between estimates and actual is taken as the absolute vertical distance between the two. Average error for ∗ was 22.9 cm over all 24 days, with a maximum single day error of 75 cm. Average error for ♦ was 13.9 cm, with a maximum single day error of 44.4 cm. **b**) Same as **a**, but with 2 m resolution on discrete sampling (●). Average error for ∗ was 32.5 cm, with a maximum single day error of 125 cm. Average error for ♦ was 26.7 cm over all 24 days, with a maximum single day error of 68.2 cm.....31

Figure 2.3 Algorithm for estimating the extent of the metalimnion (top and bottom) from example data. **a**) Same as **Figure 2.1a. b**) Same as **Figure 2.1b**. Casts started on 20 July 2009, and were completed within 1 hour from 17:00 on each day. **c**) Moving away from the maximum discrete change in density (from ∗: upward for z_e, downward for z_h), metalimnion top and bottom are estimated by linear interpolation between discrete density changes (○) to a user-specified threshold ($\delta_{\min}$). **c**) Original temperature profile from **a** with metalimnion top estimate (−; z_e), metalimnion bottom (−; z_h), and discrete maximum (∗; $z_{\zeta\Delta}$).....32

Figure 2.4 An example workflow of the Lake Analyzer program (only partial outputs are used here to highlight flexibility of the program structure). The ***configuration file*** specifies the structure of the program flow, based on user input for desired program outputs (see A.2.2.1). The ***configuration file*** has the specific extension .lke, with the file name common to source files (such as clearLake.lke, clearLake.wtr, etc.). The ***program constructor*** assembles the Lake Analyzer program structure through a series of logical statements based on output requirements and function needs. ***Primary functions*** are direct functions relative to the user specified outputs. ***Data files*** are the data sources required for the program run (.wtr, .wnd, and .bth; see A.2.2.2-A.2.2.4). ***Data file*** .sal is not shown here because it is an optional input file which is not required for the program to run. ***Secondary functions*** are functions called by primary functions if

required as part of the ***primary function*** output. ***Unused functions*** are shown here (gray overlay) as functions that are not called during this example workflow. 32

Figure 2.5 Program output for Lake Annie, Florida (USA) beginning in 2008. **a**) Temperature plot ('wTemp': colors) with color divisions every 0.5°C (buoy thermistors are shown on left edge:●). Seasonal thermocline and maximum gradient thermocline are overlaid ('SthermD', ○ and 'thermD', ◊). **b**) Seasonal Wedderburn number ('SW', light blue dashed line) and seasonal Lake Number ('SLN', dark red line) for the same period. **c**) Schmidt stability ('St'). 33

Figure 2.6 Thermal profiles taken every 12 hours from 1 April 2008 to 1 May 2008 on Lake Annie (see **Figure 2.5a**: ▽ to ▼) offset 1.5°C on the x-axis (thin black lines, taken from 'wTemp' discrete buoy measurements). Seasonal thermocline ('SthermD', ○), maximum gradient thermocline ('thermD', ◊), seasonal metalimnion top and bottom ('SmetaT', **–**; 'SmetaB', **–**), and maximum gradient metalimnion top and bottom ('metaT', –; 'metaB', –) are shown for each profile. 34

Figure 2.7 Same as **Figure 2.5**, but for Lake Rotorua (NZ) starting in 2008. 34

Figure 2.8 Metalimnion dynamics for Lake Mendota, Wisconsin (USA) during 2009. **a**) Temperature plot ('wTemp', colors) with color divisions every 0.5°C. Locations of buoy thermistors are shown on right edge (●). Metalimnion bounds for the parent thermocline ('SmetaT' and 'SmetaB', black dots) are overlaid after transforming with a 6 hour running average. **b**) Thickness of the seasonal metalimnion, taken as the difference between 'SmetaB' and 'Smeta' in meters. 35

Figure 3.1 Error analysis for water temperature smoothing for three of the 20 thermistors in Sparkling Lake, WI (USA). Panel **a** shows the surface thermistor raw data (grey line) and residuals (black bars) of the wavelet de-noised signal (black line), while panel **b** shows the resulting bootstrapped 95% confidence intervals for the surface temperature after 1000 iterations. **c** and **d** are the same as **a** and **b**, but for the 1-m thermistor. **e** and **f** are for the 5-m thermistor. anel **g** shows the final estimate of Q_s calculated by the thermistor method (dotconnected red line) and 95% confidence intervals for this estimate (grey shading). The meteorological method for Q_s is shown for comparison (thick black line). 54

Figure 3.2 Calculation of ε and k during a relatively windy period (August 2-3) where hourly averaged winds exceeded 6 m s^{-1} during the daytime, and a relatively calm period (August 4) for Sparkling Lake, WI-USA (top panel). Turbulence from buoyancy flux (ε_w) and wind shear (ε_u) are used to estimate $\varepsilon_{u,w}$. k is scaled from $\varepsilon_{u,w}{}^{1/4}$ (black line) and k(w_*) from $\varepsilon_w{}^{1/4}$ (blue circles) according to the surface renewal model (bottom panel). 55

Figure 3.3 Ratio between the temporally-averaged velocity scales for wind shear (u_*) and convection (w_*), where averages were applied over the entire time series of observations for each lake. Lake shapes were used for plot symbols, and were shifted when overlapping (see tip of arrows). 56

Figure 3.4 Average, normalized values of u^* and w^* across 40 lakes, plotted on 3-week intervals. u^* and w^* were offset by 4 days to improve figure clarity. Seasonal periods were based on day-of-year 81-173, 173-265, and 265-356 for Northern Hemisphere lakes, while Southern Hemisphere lakes were shifted by 182 days. Error bars represent the interquartile range (across lakes) of individually normalized values in each interval. The number of lakes used for each interval is displayed inside each marker. 57

Figure 3.5 Temporally-averaged convective fraction (%) of total gas transfer velocity calculated using the surface renewal model for 40 lakes. Seasonal differences in $k(w^*)$% were tested for lakes with at least 21 days of observations for spring and summer periods (day-of-year 81-173; 173-265, respectively) using a Mann-Whitney U-test. Lakes without sufficient data are shown as black dots, lakes with no significant seasonal difference ($p > 0.01$) are shown as open black circles, and lakes where summer $k(w^*)$% was significantly higher than spring $k(w^*)$% are shown as red, upward-pointing triangles. 58

Figure 4.1 Relationship between the diffuse attenuation coefficient (K_d) and DOC for 7 NTL-LTER lakes and North Sparkling Bog from a 2009 survey. Line is DOC·0.22, the relationship used in this study. 88

Figure 4.2 **a**) Temperature profiles on Trout Bog separated by 40 days. **b**) Temperature gains are shown as averages for 10 cm intervals (red line). Modeled temperature gains for depths below the remnant mixed layer depth are shown as 10 cm bins, which combine the additive effects of temperature gains and losses from the vertical diffusion of heat (dashed black line) and the attenuation of penetrating radiation (thick black line). 89

Figure 4.3 Observed **a**) and modeled **b**) temperatures for Trout Bog during 2009. Contour intervals represent one °C. 90

Figure 4.4 Volumetric average water temperatures for 22 simulation years and 3 DOC scenarios for Trout Bog. 1000 iterations were used where DOC concentrations were randomly chosen (with replacement) from the 22 years on record, and the simulation years were also chosen the same manner (see **Table 4.3**). Medians are represented by open circles, and error bars represent the interquartile range for all iterations. 91

Figure 4.5 Effects of transparency on mixed layer depth. Trout Bog simulated water temperature for 1 July 2008 13:00 using normal DOC concentrations (18.7 mg L-1; black line) and a 50% DOC reduction scenario (dashed black line). Heat loss during the subsequent 15 hours in each simulation eliminated near-surface microstratification, resulting in isothermal nocturnal mixed layer depths of 1.01 m and 1.45 m, respectively (black line; dashed black line). Meteorological drivers and starting conditions for the two simulations were identical. 92

Figure 4.6 **a**) A model system with the morphometry of Trout Bog was simulated for a range of DOC concentrations (2 to 30 mg L-1) to assess the sensitivity of water temperature to natural climate variability (1989-2010). Temperature range was calculated as the difference between

maximum and maximum volumetric average temperatures for all 22 seasons (open circles). **b**) We calculated the DOC-induced temperature variability for Trout Bog, where we simulated water temperatures for a given year over the full range of DOC 1989-2010 concentrations measured in Trout Bog (**Table 4.3**). Each of 22 simulation years had a range between the maximum and minimum average temperatures, and the median of this range is plotted as a black diamond, and error bars represent the minimum and maximum range of all years (which were 2009 and 2003, respectively). 93

Figure 5.1 North Sparkling Bog (NSB, maximum depth 4.3m) is a strongly stratified, dimictic (spring and fall turnover), wind sheltered lake. NSB is located in the northern highlands lake district of Wisconsin. Multiple near real-time environmental sensors were deployed throughout the duration of the manipulation. T1-T4 represent local HOBO temperature profiles. B represents an instrumented buoy that measures meteorological variables as well as water temperature and dissolved oxygen. G1 and G2 represent the GELI mixing devices used to artificially mix NSB. V is an Acoustic Doppler Current Profiler (ADCP) which measured far-field velocity profiles during treatment. Camera shows perspective view of picture. 120

Figure 5.2 GELI components and secondary test deployment on Crystal Lake. **a**) GELI on 10 August 2009 on Crystal Lake, soon after surfacing. Lateral spreading is evident in the northwestern direction (towards the right in the image). An instrumented buoy, similar to "B" in **Figure 5.1**, is anchored behind the GELI. One of the major improvements to the 2008 design – a 1 inch airline – is visible in the foreground. **b**) Components and materials of the GELI mixing device. The flexible polyvinyl chloride (PVC) hose comprises the outer shell of the buoyancy controlled ring (BCR) and collapses when air is removed, but inflates to a fixed volume when air is pressurized (does not stretch). The metal frame provides structural support for the outer ring, and is internally threaded through the BCR. The ethylene propylene diene M-class (EPDM) rubber membrane is attached to the BCR via lash straps which are looped through grommet supported holes in the membrane. The flexible membrane deforms with the drag and differential density of water when moving through the water column and takes on a bowl or parachute shape when in motion. 121

Figure 5.3 Oscillatory vertical motion of the GELI is controlled by alternating buoyancy stages of the BCR (buoyancy controlled ring) with the use of solenoid valves. During the evacuation stage (represented with red arrows), a normally closed solenoid valve is energized (**right**), allowing a pump to remove air from the BCR. After air is removed from the BCR, the GELI becomes negatively buoyant and sinks. During the inflation stage (represented by blue arrows), energizing a second solenoid valve (**left**) allows compressed air to enter the BCR from a nearby pressurized buffer tank. After the inflation stage, the buoyant GELI rises through the water column and the evacuation stage begins. 122

Figure 5.4 A histogram of wind speed measured at the buoy location ("B" in **Figure 5.1**) during the month of July 2008. Histogram bins are 0.25 m s^{-1} wide and the two time periods (night and day) are shifted by 0.05 m s^{-1} to avoid direct overlap. The upper right panel represents a typical nighttime drop in wind speed (this "night" period corresponds to the low-wind period of

"a" in **Figure 5.8**). Propeller anemometers are inaccurate at low speeds, but we expect this basic distribution to represent day/night variability of wind speed on NSB during the study period. 123

Figure 5.5 Thermal transects which show relative spatial homogeneity of NSB during mixing treatment. Transects were aggregates of high-frequency buoy data ("B" in **Figure 5.1**) and multiple HOBO logger chains ("T1-T4" in **Figure 5.1**). The lower waters were gradually mixed with surface waters by two GELI mixing devices ("G1-G2" in **Figure 5.1**), resulting in a warming trend at depth. Surface waters were cooled by mixing, augmenting the surface heat flux. 124

Figure 5.6 Simulated and measured temperatures during the ice-free season of 2008. **a**) Measured water temperature on North Sparkling Bog from buoy thermistors ("B" in **Figure 5.1**). **b**) Modeled water temperature during the same period, in the absence of an artificial mixing event (mixing experiment was 2 July to 10 July 2008). 125

Figure 5.7 Volumetrically averaged measurements of changes in temperature and dissolved oxygen. **a**) Volumetric average temperature during the 2008 experiment, where cooler surface temperatures reduced heat loss and increase gains due to colder surface waters. **b**) Volumetric average dissolved oxygen concentration during the experiment, where changes in water column metabolism were evident as pre-manipulation oxygen levels were not conserved. 125

Figure 5.8 ADCP measurements taken during the 2008 experiment (30 m north of the GELIs, positive values to the north) and spectral analysis. **a**) Water column velocity measured during the length of ADCP deployment (8 July 3:00 to 10 July 9:00, 2008). High-frequency internal waves are notable throughout most of the water column, seen here as thin vertical stripes. Higher velocities were found at depths of stronger stratification (0.5 to 1.5 m), which supported the oscillations of wave motion. **b**) Spectral analysis of the 80 cm depth velocity cell. A Fast-Fourier Transform (FFT) was applied to the northern velocity data with a moving window of 30 minutes. Waveforms show spectral peaks with a strong diel signal. The buoyancy frequency (N) had a strong relationship with observed wave forms. $N/8$ is displayed as a dashed line, which shows good agreement with high-frequency internal wave peaks....126

Figure 5.9 ADCP measurements for two periods in Figure 5.8a, in addition to secondary measurements taken at Crystal Lake in 2009 (35 m east of the GELI), with FFT of each time period during GELI operation. **a**) Northern velocities soon after midnight on 10 July 2008 (0:30-1:00). Waveforms were evident in the 0.5 to 1.5 m range as oscillations in the velocity signal. **b**) Northern velocities 2 hours after panel **a**, where lower frequency waveforms are present. **c**) A 12 minute period of 1 Hz eastern velocity ADCP data from the Crystal Lake test, where waveforms are located between 8 and 10 m depths. Waveforms are higher frequency and stronger than panels **a** and **b**, likely due to stronger stratification. **d**) FFT analysis of panel **a**, with spectral peak pointed out (3.28 minutes) and $N/8$ (N is 0.0401 s^{-1}) plotted as a dashed line. **e**) Same as **d** and **e**, with spectral peak of 7.1 minutes and N as 0.0224 s^{-1}. **f**) Same as **e**, with spectral peak of 1.8 minutes and N as 0.0702 s^{-1}. 127

Figure 5.10 Lateral flow patterns on 8 July 2008 as observed by measurements of temperature and velocity (northern direction ADCP). **a**) Pooled mean velocities from 2.2 to 2.7 m depth, where small open circles are 20 second ensemble velocities, with the gray-black dashed line is a 3rd order Savitzky-Golay filter applied to 30 minute moving windows of the 20 second measurements. Oscillations are clear in velocity signals, where periods range from 30 to 50 minutes. During this measurement period, there was a net flow in the southern direction, potentially the result of return flows from circulation cells. **b**) Temperature measurements logged as 20 second ensemble averages from the body of the ADCP. These temperature fluctuations appeared in tandem with lagged velocity fluctuations (in **a**), potentially representing lateral exchange flows. The observed wave periods were variable and did not follow patterns related to ambient stratification. 128

Figure 5.11 Observed and modeled changes in energy resulting from the 2008 mixing manipulation. **a**) Potential energy of the water column for both observed (black line) and modeled (gray dash-dot line). Modeled temperature (which was used to calculate changes in potential energy) is expected to represent the effects of positive and negative buoyancy fluxes in the absence of the mixing manipulation. **b**) Mechanical efficiency of the GELI method as calculated from isentropic work and changes in potential energy (except during a 12 hour break in operation 6 July to 7 July 2008). Efficiency is well above 1% for most of the experiment, but drops below 0 during nighttime convection towards the end of the experiment. We believe this trend results from modeled water column losing stability faster at night because heat is partitioned closer to the surface, so the rate of change of potential energy is greater in the unaltered case during several intervals of low stratification.....129

Figure 6.1 Relative temperature gains for North Sparkling Bog from 20 April to 20 June for 2009 (black triangles) and 2010 (open circles).....145

Figure 6.2 Scaled fits of daily cumulative shortwave radiation (thick grey line) to 0.5 m depth temperature measurements for Timber Bog (black dots).....145

Figure 6.3 Workflow for estimating Kd from paired thermistor measurements. 146

Figure 6.4 Estimates of K_d from paired thermistors on Timber Bog. **a**) Measurements of daily water temperatures were truncated (**Figure 6.3**) for Kd estimates, where dots are measurements outside the truncated range for the datasets. Temperatures from 0.25 m (grey line), 0.5 m (black dotted line), 0.75 m (grey dash-dot line), 1 m (black line) and 1.25 m (grey dotted line). **b**) α and K_d estimates from 0.25 m and 0.5 m thermistors, where black line is α, and dashed line is a 1:1 line. **c**) same as b, but for 0.25 m and 0.75 m thermistors. **d**) same as b, but for 0.25 m and 1 m thermistors. **e**) same as b, but for 0.25 m and 1.25 m thermistors. 147

Figure 6.5 Estimated K_d (model K_d) compared to log-linear fits to the decay rate of PAR measured using Biospherical profilers (K_d observed). Error bars were calculated as 95% confidence intervals to the log-linear fit to PAR versus depth (K_d observed) and calculating model K_d using 95% confidence intervals for α. 148

Figure 6.6 Estimates of K_d from the paired thermistor method for **a**) an unusually dry year (2009) and **b**) an unusually wet year (2010; precipitation comparisons made to the 1981-2010 record). 2009 had a decreasing trend in K_d, while 2010 increased in K_d during the summer period. Error bars were created by calculating K_d with the 95% confidence intervals to the linear fit of α.....148

Figure C.1 The ratio of the stability sensitive latent heat transfer coefficient (C_E) to the neutral latent heat transfer coefficient (C_{EN}) for 39 temperate lakes (see Chapter 3 for details for specific lakes). Transfer coefficients were calculated according to the methods of Verburg and Antenucci (2010). 187

Figure C.2 Energy budget components for BREB analysis. a) The lake system with thermistors (black dots) representing horizontal slices (dashed lines). The hypsography of the lake defines the area-depth relationship. b) Flux components for the BREB analysis, including surface heat fluxes, advected energy, and sediment heat flux. 187

Figure C.3 An example of the dominant terms for the BREB for Trout Bog during 2009. Changes in internal energy (dSdt) reflect the balance of radiation (Rnet) and sensible (H) and latent (E) heat fluxes. 188

Figure C.4 Calibration of the free and forced evaporation model of Adams et al. (1990; see Section C.2.2) coefficients. Best-fits to the data (minimizing the sum of squared errors) was found with $a = 2.1$ and $b = 5.1$ (see equation C.13). Circles are the median of the estimates, and error bars represent the inter-quartile range of the data for each interval.....189

Figure E.1 An example PUV profile from North Sparkling Bog. PAR irradiance values have been normalized according to the irradiance at the water surface. 209

LIST OF TABLES

Table 3.1 Properties for the 40 temperate lakes included in this analysis. 59

Table 3.2 Components of the iterative error analysis and assumed error for each variable when using the thermistor method to estimate Q_s. 60

Table 3.3 Temporally-averaged values for wind shear velocity (u_*), convective velocity (w_*), SML depth (z_{mix}), gas transfer velocity (k), and convective fraction of k. 61

Table 3.4 Spearman rank correlation coefficients (across lakes) between temporally-averaged turbulence parameters and lake properties. 62

Table 4.1 Properties for the 8 lakes used in this analysis. 93

Table 4.2 Simulation results for 8 sheltered lakes. Model K_d is the best fit to the observed data if K_d is treated as an unknown, observed K_d is a single-point estimate of PAR K_d taken during the observation year, 95% confidence intervals are from non-linear least squared fits to the exponential decay of light, and SE is the standard error between all observed and modeled water temperatures with the exception of surface thermistors.....94

Table 4.3 DOC measurements and modeling details for 1989-2010. Ice-on and Ice-off values are the daynumbers for the first and last observed open water on Trout Bog for the observation year. DOC (mg L^{-1}) values are the median of all measurements made between and including 0 and 3 meters, and K_d (m^{-1}) was estimated from DOC measurements using the DOC-specific attenuation coefficient. 95

Table 6.1 Properties for the 6 lakes used in this analysis. 149

Table 6.2 Depth (cm) placement for thermistors based on the desired temperature gain (ΔT, in °C) relative to a priori knowledge of K_d, for an average incoming solar radiation flux of 800 W m^{-2} during a six hour period.....149

Table A.1 Definitions of key physical parameters used in this text. 168

Table A.2 Output options and definitions.....169

Table B.1 Example water temperature gFile (.wtr) for measurements at 0, 0.5, 1.0, 1.5, and 2.0 m. 173

Table B.2 Extensions for commonly used gFiles and corresponding unit standards. 174

Table E.1 K_d fits and 95% confidence interval range for 131 PUV profiles from 10 lakes. z_1 and z_2 are the top and bottom depths (respectively) for K_d fits, and represent approximately 50%

and 1% of E_0. In cases where the bottom depth measurement was 1% of E_0, the maximum depth of the profile was used for z_2.....210

Chapter 1 – Introduction

1.1 Physical processes in small lakes

Small lakes have been historically underrepresented in estimates of inland waters (Downing et al. 2006; Downing 2010) due to the difficulty of accurate identification of small features from spatial surveys with limited mapping resolution (Carroll et al. 2009). Recent work has refined the global estimates of the number of lakes (potentially in excess of 300 million) and the areal contribution of these lakes (> 3% of land area) using a combination of remote sensing and modeling (Downing et al. 2006). While areal estimates of small lakes (< 10 ha) likely require refinement (Seekell and Pace 2011; Mcdonald et al. 2012), these lakes undoubtedly dominate the global distribution of lake abundance and perimeter (Downing et al. 2006; Winslow et al. in review).

The inclusion of lakes into global processes such as the carbon cycle has lead to a renewed view of the important role of inland waters (Cole et al. 2007; Tranvik et al. 2009). Small lakes are often disproportionately active in biogeochemical cycles, and are no longer considered negligible to these processes on global and regional scales (Downing 2009; Downing 2010; Lewis 2011). Small lakes have large perimeters (relative to their volumetric processing capacity), and consequently are often heavily subsidized with allochthonous inputs (Cole et al. 2011). These lakes frequently differ from larger lakes in physical (Read et al. 2012) and biogeochemical (Downing 2010) characteristics.

Many efforts to up-scale the role of lakes into global biogeochemical cycles consider lakes to behave as reactors, where function is determined by basic measureable parameters like morphology, residence time, regional conditions, and the relevant processing rates (Downing 2009; Hanson et al. 2011; Lewis 2011). These studies rely on an assumed basic knowledge of the

drivers of lake water temperature, vertical mixing, and air-water exchanges; all of which directly influence processing rates of carbon (Hanson et al. 2011). As such, a physical understanding of the many different lake types that make up the global distribution of lakes is an important component to proper formulization of the role of lakes in global processes.

Earlier work used poorly resolved maps to estimate a global inventory of lentic waters, which ultimately minimized the role of small lakes in the global cycling of water, nutrients, and carbon (Thienemann 1925). As a consequence, physical limnological work on lakes has historically focused efforts towards large lakes that are important to regional water supply (Fischer et al. 1979; Imberger 1985), represent a large share of biodiversity (Verburg et al. 2003; Verburg and Antenucci 2010), or have a large influence local climate (Austin and Colman 2007; Desai et al. 2009). Much of our limnological knowledge has also been derived from physical oceanography (Wanninkhof 1992; Csanady 2001; Mcgillis et al. 2004) – and while applicable to larger lakes – likely fails to adequately describe physical processes in small lakes.

1.2 Research objectives

Spigel and Imberger (1980) classically defined dominant mechanisms controlling mixing and stratification dynamics in medium and large lakes (in text defined as small to medium sized lakes). This earlier work was integral to the proper scaling of physical processes across different lake types. This dissertation shares similar motivation with the work of Spigel and Imberger (1980), namely to define size-dependent physical processes that are relevant to up-scaling the role of lakes into global and continental analyses. The goals of this dissertation are to improve the understanding of physical processes in small lakes and to increase the availability and standardization of comparative physical limnological methods for future investigators. Specifically, the objectives of this body of research are as follows:

1.2.1 Create a data management and analysis platform for instrumented buoy data which is modular, adaptable, and designed for high volumes of environmental sensor data

1.2.2 Identify patterns in the dominant drivers of mixed layer processes for a diverse global dataset of instrumented lakes

1.2.3 Parameterize air-water gas exchange from lakes using high-frequency physical measurements

1.2.4 Design and parameterize a numerical model for the simulation of vertical mixing and temperature dynamics in small lakes

1.2.5 Identify the controls on mixed layer depths and hypolimnetic temperatures in small lakes

1.2.6 Design and implement an artificial destratification device for small lakes

1.3 Introduction to the dissertation

Compared to much of the seminal work in physical limnology (e.g., Imberger 1985), the contents of this dissertation focus on much smaller (and numerically dominant) size classes, and this research has resulted in the creation of several new resources for the examination and comparison of lake physics; including a software package designed for instrumented lakes (Chapter 2; Appendix A), a file type standard for environmental sensor data (Appendix B), an analysis of the drivers of surface mixed layer dynamics across a range of lake sizes (Chapter 3), a hydrodynamic model created for small lakes (Chapter 4; Chapter 5; Appendix D), a detailed examination of the role of transparency as a control on the mixed layer depths and water temperatures of small lakes (Chapter 4; Chapter 6), a method designed to eliminate stratification in small lakes (Chapter 5), and the development of an analytical approach for estimating water clarity from physical measurements (Chapter 6). Research objectives 1.2.1-1.2.5 are addressed in

the following five chapters (2-6), five appendices (A-E), and conclusions and recommendations for future work are summarized in chapter 7.

1.4 References

Austin, J. A., and S. M. Colman. 2007. Lake Superior summer water temperatures are increasing more rapidly than regional air temperatures: A positive ice-albedo feedback. Geophysical Research Letters **34:** -, doi: Doi 10.1029/2006gl029021.

Carroll, M. L., J. R. Townshend, C. M. Dimiceli, P. Noojipady, and R. A. Sohlberg. 2009. A new global raster water mask at 250 m resolution. International Journal of Digital Earth **2:** 291-308, doi: 10.1080/17538940902951401.

Cole, J. J., S. R. Carpenter, J. Kitchell, M. L. Pace, C. T. Solomon, and B. Weidel. 2011. Strong evidence for terrestrial support of zooplankton in small lakes based on stable isotopes of carbon, nitrogen, and hydrogen. Proceedings of the National Academy of Sciences of the United States of America **108:** 1975-1980, doi: 10.1073/pnas.1012807108.

Cole, J. J., Y. T. Prairie, N. F. Caraco, W. H. Mcdowell, L. J. Tranvik, R. G. Striegl, C. M. Duarte, P. Kortelainen, J. A. Downing, J. J. Middelburg, and J. Melack. 2007. Plumbing the global carbon cycle: Integrating inland waters into the terrestrial carbon budget. Ecosystems **10:** 171-184, doi: 10.1007/S10021-006-9013-8.

Csanady, G. T. 2001. Air-sea interaction: Laws and mechanisms, first ed. Cambridge University Press.

Desai, A. R., J. A. Austin, V. Bennington, and G. A. Mckinley. 2009. Stronger winds over a large lake in response to weakening air-to-lake temperature gradient. Nature Geoscience **2:** 855-858, doi: 10.1038/ngeo693.

Downing, J. A. 2009. Global limnology: Up-scaling aquatic services and processes to planet Earth. Verh. Internat. Verein. Limnol. **30:** 1149-1166.

Downing, J. A. 2010. Emerging global role of small lakes and ponds: little things mean a lot. Limnetica **29:** 9-23.

Downing, J. A., Y. T. Prairie, J. J. Cole, C. M. Duarte, L. J. Tranvik, R. G. Striegl, W. H. Mcdowell, P. Kortelainen, N. F. Caraco, J. M. Melack, and J. J. Middelburg. 2006. The

global abundance and size distribution of lakes, ponds, and impoundments. Limnology and Oceanography **51:** 2388-2397, doi: 10.4319/LO.2006.51.5.2388.

Fischer, H. B., J. E. List, C. R. Koh, J. Imberger, and N. H. Brooks. 1979. Mixing in inland and coastal waters. Academic Press.

Hanson, P. C., D. P. Hamilton, E. H. Stanley, N. Preston, O. C. Langman, and E. L. Kara. 2011. Fate of Allochthonous Dissolved Organic Carbon in Lakes: A Quantitative Approach. Plos One **6**, doi: 10.1371/journal.pone.0021884.

Imberger, J. 1985. The diurnal mixed layer. Limnology and Oceanography **30:** 737-770.

Lewis, W. M. 2011. Global primary production of lakes: 19th Baldi Memorial Lecture. Inland Waters **1:** 1-28, doi: 10.5268/IW-1.1.384.

Mcdonald, C. P., J. A. Rover, E. G. Stets, and R. G. Striegl. 2012. The regional abundance and size distribution of lakes and reservoirs in the United States and implications for estimates of global lake extent. Limnology and Oceanography **57:** 597-606, doi: 10.4319/lo.2012.57.2.0597.

Mcgillis, W. R., J. B. Edson, C. J. Zappa, J. D. Ware, S. P. Mckenna, E. A. Terray, J. E. Hare, C. W. Fairall, W. Drennan, M. Donelan, M. D. Degrandpre, R. Wanninkhof, and R. A. Feely. 2004. Air-sea CO2 exchange in the equatorial Pacific. Journal of Geophysical Research-Oceans **109:** C08s02, doi: 10.1029/2003JC002256.

Read, J. S., D. P. Hamilton, A. R. Desai, K. C. Rose, S. Macintyre, J. D. Lenters, R. L. Smyth, P. C. Hanson, J. J. Cole, P. A. Staehr, J. A. Rusak, D. C. Pierson, J. D. Brookes, A. Laas, and C. H. Wu. 2012. Lake-size dependency of wind shear and convection as controls on gas exchange. Geophysical Research Letters, doi: 10.1029/2012GL051886.

Seekell, D. A., and M. L. Pace. 2011. Does the Pareto distribution adequately describe the size-distribution of lakes? Limnology and Oceanography **56:** 350-356, doi: 10.4319/lo.2011.56.1.0350.

Spigel, R. H., and J. Imberger. 1980. The classification of mixed-layer dynamics in lakes of small to medium size. Journal of Physical Oceanography **10:** 1104-1121, doi: 10.1175/1520-0485(1980)010<1104:tcomld>2.0.co;2.

Thienemann, A. [ed.]. 1925. Die Binnengewasser Mitteleuropas (The inland water of Central Europe). E. Schweitzerbart'sche Verlagsbuchhandlung.

Tranvik, L. J., J. A. Downing, J. B. Cotner, S. A. Loiselle, R. G. Striegl, T. J. Ballatore, P. Dillon, K. Finlay, K. Fortino, L. B. Knoll, P. L. Kortelainen, T. Kutser, S. Larsen, I. Laurion, D. M. Leech, S. L. Mccallister, D. M. Mcknight, J. M. Melack, E. Overholt, J. A. Porter, Y. Prairie, W. H. Renwick, F. Roland, B. S. Sherman, D. W. Schindler, S. Sobek, A. Tremblay, M. J. Vanni, A. M. Verschoor, E. Von Wachenfeldt, and G. A. Weyhenmeyer. 2009. Lakes and reservoirs as regulators of carbon cycling and climate. Limnology and Oceanography **54:** 2298-2314.

Verburg, P., and J. P. Antenucci. 2010. Persistent unstable atmospheric boundary layer enhances sensible and latent heat loss in a tropical great lake: Lake Tanganyika. Journal of Geophysical Research-Atmospheres **115:** D11109, doi: 10.1029/2009JD012839.

Verburg, P., R. E. Hecky, and H. Kling. 2003. Ecological consequences of a century of warming in Lake Tanganyika. Science **301:** 505-507, doi: 10.1126/science.1084846.

Wanninkhof, R. 1992. Relationship between wind-speed and gas-exchange over the ocean. Journal of Geophysical Research-Oceans **97:** 7373-7382.

Chapter 2 - Derivation of lake mixing and stratification indices from high-resolution lake buoy data using "Lake Analyzer"

The following is reproduced with permission from a publication that is catalogued according to doi:10.1016/j.envsoft.2011.05.006

Read JS, DP Hamilton, ID Jones, K Muraoka, LA Winslow, R Kroiss, CH Wu, E Gaiser. 2011. Derivation of lake mixing and stratification indices from high-resolution lake buoy data. Environmental Modelling & Software. 26: 1325-1336.

2.1 Abstract

Lake Analyzer is a numerical code coupled with supporting visualization tools for determining indices of mixing and stratification that are critical to the biogeochemical cycles of lakes and reservoirs. Stability indices, including Lake Number, Wedderburn Number, Schmidt Stability, and thermocline depth are calculated according to established literature definitions and returned to the user in a time series format. The program was created for the analysis of high-frequency data collected from instrumented lake buoys, in support of the emerging field of aquatic sensor network science. Available outputs for the Lake Analyzer program are: water temperature (error-checked and/or down-sampled), wind speed (error-checked and/or down-sampled), metalimnion extent (top and bottom), thermocline depth, friction velocity, Lake Number, Wedderburn Number, Schmidt Stability, mode-1 vertical seiche period, and Brunt-Väisälä buoyancy frequency. Secondary outputs for several of these indices delineate the parent thermocline depth (seasonal thermocline) from the shallower secondary or diurnal thermocline. Lake Analyzer provides a program suite and best practices for the comparison of mixing and stratification indices in lakes across gradients of climate, hydro-physiography, and time, and enables a more detailed understanding of the resulting biogeochemical transformations at different spatial and temporal scales.

2.2 Introduction

Thermal stratification in lake ecosystems exerts an important control on the in-lake vertical fluxes of dissolved and particulate material (Robertson and Imberger 1994; Aeschbach-Hertig et al. 2007). Stratification is facilitated by the thermal expansion properties of water, which create a stable vertical density gradient owing to heating (or cooling if below 3.98°C) of surface waters. These density gradients are often observed as a region of sharp change in water temperature (metalimnion) that delineates an upper well-mixed region (epilimnion) from a relatively quiescent deep zone (hypolimnion) (Monismith and Macintyre 2009). This vertical partitioning of the water column has important implications for the availability of nutrients, light and microbial substrates, as well as vertical distribution, migration, and feeding of higher trophic levels like zooplankton and fish. Density stratification suppresses vertical transfer between bottom and surface waters, often resulting in a nutrient rich but light-limited hypolimnion in stark contrast to an epilimnion rich in light but poor in nutrients (Macintyre et al. 1999). Connectivity between the hypolimnion and the atmosphere is also limited by stratification, which creates a barrier to the replenishment of oxygen (Wetzel 1983) and the efflux of hypolimnetic carbon (Cole et al. 2007).

Stratification can be transient or persistent, varying at time scales of hours (Rueda and Schladow 2009) to decades (Jellison et al. 1998; Verburg et al. 2003), finally decaying to near vertical homogeneity as mixing mechanisms such as wind and convection outweigh the stabilizing inputs of surface heating. Lakes range in stratification strength (as measured by the Brunt-Väisälä buoyancy frequency: N^2) by as much as nine orders of magnitude (Wuest and Lorke 2003), resulting in substantial

variations in the energy required to break down stratification. Stratification can therefore vary on global and regional scales as destratifying drivers such as wind follow synoptic patterns but are also affected by local topography (Mcgowan and Sturman 1996).

With expanding global coverage of sensor networks (Porter et al. 2009) a large volume of data is rapidly being accumulated for lakes across the world. Lake monitoring networks show promise for addressing science questions that span broad geographic regions and ecosystem gradients, but adequate tools are required to rapidly process this information to contribute towards comparative studies. These studies will benefit from the available gradients of climate, land-use, hydro-physiography and time that are provided by a global network (Hanson 2007).

Comparative studies in limnological research that span broad spatial or temporal extents are often limited by the large effort and investment in infrastructure required to conduct large-scale research (Magnuson et al. 1997). The few large comparative surveys that do exist (e.g., Fee et al. 1996) have improved our understanding of physical drivers of ecosystem processes, while highlighting the large amount of variability in space and time. A common, but non-exclusive theme to these large-scale studies is the synthesis of several spatially disparate – often global – data sources, driven by cross-site collaborative efforts (e.g., Magnuson et al. 2000). Barriers to these collaborations have historically been the physical separation of researchers, but recent advancements in cyber-tools have helped to simplify global collaborations and reinforce trust (Hanson 2007). A synchronous increase in deployments of instrumented buoys has led to the unprecedented ability to increase the temporal resolution and spatial extent of comparative lake research

(Porter et al. 2009) as these buoys can be used as sentinels for the dynamics of entire eco-regions (Williamson et al. 2009).

Physical indices derived from instrumented buoys can be used to effectively parse out the contributions of drivers like wind (Lake Number; Wedderburn Number), convective cooling (decrease in Schmidt Stability), and destratifying forces that weaken vertical density gradients (decrease in buoyancy frequency) on measured biological signals (e.g., Robertson and Imberger 1994); but we currently lack standards and best practices for these calculations. These indices of lake behaviour have been well established in the literature, but several nuances persist over the exact definition of ubiquitous concepts such as the extent of the mixed layer or the thermocline depth, hampering our ability for cross-site comparison. For example, depth of the mixed layer has been calculated as a threshold of turbulence (Macintyre et al. 2009), a temperature gradient (Coloso et al. 2008), a density gradient (Lamont et al. 2004), or chemical gradient (Cole et al. 2000). The current state of aquatic sensor network science stands to benefit from the unification of various methods used in the calculation of physical indices of biogeochemical processes, allowing more robust conclusions and future synthesis. We therefore require a consistent methodology which is robust over many types of lakes and is easily applied to data from lake monitoring buoys. We present here a numerical scheme and accompanying program suite, specifically designed for data-rich aquatic sensor networks. Our software package is founded on robust and unified methods, establishing a physical basis for future biogeochemical studies in a simplified framework. This assemblage of open-source tools is unprecedented in the field of sensor network

science, and provides a basis for scientific advancement in lake dynamics through transparency and information sharing.

2.3 Comparative indices

The following methods for calculating lake-specific indices offer an approach which is consistent with the existing literature and has been specifically designed to accommodate the sensor arrays of instrumented lake buoys. As instruments are most commonly referenced from a floating surface-mounted buoy, we employ a coordinate system frequently used by the limnological community, but which differs from established physical literature (e.g., Imberger 1985; Wuest and Lorke 2003), as we treat the air/water interface as depth 0 with positive z in the downward direction. Lake Analyzer can be used for calculation of the extent of the metalimnion (top and bottom), the depth of the thermocline, Schmidt Stability, Wedderburn Number, Lake Number and the Brunt-Väisälä buoyancy frequency, as well as other related parameters (as detailed in 2.3.1-2.3.5 and Apendix A.1).

2.3.1 *Thermocline/pycnocline depth*

The depth to the thermocline has been used as a climate change indicator, or to show lake response to coupled changes in heat budget and mixing dynamics. Hambright et al. (1994) for example, calculated changes in thermocline depth for Lake Kinneret (Israel) over a period of 23 years (1969-1990), using a scheme based on the maximum change in temperature with respect to change in depth. Because temperature measurements are taken at discrete intervals, the vertical resolution of thermocline estimates has typically been limited by the resolution of the measurements. This methodology presents an issue of "steps" in a time series of thermocline estimates, often

incorrectly representing a gradual lowering of the thermocline depth with a series of sharp drops. To minimize this issue, we present a scheme designed to improve this discretized method by adding weighting to adjacent measurements:

Water density (ρ) is calculated according to the contributions of temperature and solutes (if applicable) (Figure 2.1a, 2.1b; see Appendix A.1.1). For *k* number of measurements referenced from the surface, for $i = 1$ to $i = k - 1$:

$$\frac{\partial \rho}{\partial z_{i\Delta}} = \frac{\rho_{i+1} - \rho_i}{z_{i+1} - z_i}, \tag{2.1}$$

which applies to the depth characterized by $z_{i\Delta} = (z_{i+1} + z_i)/2$, where $z_{i\Delta}$ represents a midpoint depth between measurements *i* and *i*+1. If the maximum $\partial\rho/\partial z_{i\Delta}$ is found when $i = \zeta$ for discrete measurements (Figure 2.1c), the true depth of the maximum change in density (z_T) likely occurs within the bounds defined by the two depths at which the discrete measurements were taken ($z_\zeta < z_T < z_{\zeta+1}$). An improvement on the initial guess of $z_T \approx z_{\zeta\Delta}$ can be made by weighting the magnitudes of the difference between the maximum calculated density change and the adjacent calculations (Figure 2.1c; 2.1d);

$$z_T \approx z_{\zeta+1}\left(\frac{\Delta\rho_{+1}}{\Delta\rho_{-1} + \Delta\rho_{+1}}\right) + z_\zeta\left(\frac{\Delta\rho_{-1}}{\Delta\rho_{-1} + \Delta\rho_{+1}}\right) \tag{2.2}$$

where $(z_{\zeta\Delta+1} - z_{\zeta\Delta})/(\partial\rho/\partial z_{\zeta\Delta} - \partial\rho/\partial z_{\zeta\Delta+1})$ has been simplified to $\Delta\rho_{+1}$ and $(z_{\zeta\Delta} - z_{\zeta\Delta-1})/(\partial\rho/\partial z_{\zeta\Delta} - \partial\rho/\partial z_{\zeta\Delta-1})$ to $\Delta\rho_{-1}$. This scheme shows a potential improvement

in accuracy over existing methods when compared to known density profiles (for Crystal Lake CTD casts, 39% reduction in average error for 1m intervals and 18% reduction in average error for 2 m intervals: Figure 2.2). The same relationship can be used to estimate the maximum change in temperature with respect to depth (a decreasing gradient when T>3.98°C), but we focus here on the density gradient because it holds more physical relevance to the suppression of vertical mixing. Because of the significance of both the parent and secondary thermocline (e.g., Kling 1988), we include a scheme that allows the output of either (or both) of these estimates (see Appendix A.1.2).

2.3.2 *Mixed layer depth*

Imberger (1985) defined the surface mixed layer as the vertical portion of the water column which is directly influenced by the surface drivers of wind and convective cooling. The upper boundary of this layer is the air/water interface, while the bottom is defined as a threshold between active and transient turbulence. Because most instrumented lakes lack direct measurements of turbulence, it is usually assumed that the mixed layer will be relatively vertically homogeneous in both temperature and density, owing to active mixing. This assumption leads to a partitioning of the mixed layer based on the lack of vertical gradients in temperature and density. Lamont et al. (2004), for example, defined the mixed layer as the region above the thermocline where the density gradient was less than 0.5 kg m^{-3} per meter, while Fee et al. (1996) defined the layer as the region where the temperature gradient is less than 1 °C m^{-1}. Similar to Lamont et al. (2004), the scheme we have chosen relies on a density gradient threshold ($\delta_{\min}$) to define the depth of the mixed layer. Calculations of the density gradient ($\partial\rho/\partial z$) are based on discrete thermistor locations, and the depth of the lower boundary of the mixed layer can

be estimated by linear interpolation of the slopes derived from Equation 2.1 (Figure 2.3). This numerical scheme can be described (following the notation in section 2.3.1): from $i = \zeta$ to $i = 1$, find *i* where $\partial\rho/\partial z_{i\Delta} \le \delta_{\min}$, interpolate between *i* and *i*+1 to yield the approximate depth of the base of the mixed layer, z_e (also referred to as the top of the metalimnion)

$$z_e = z_{i\Delta} + \left(\delta_{\min} - \frac{\partial\rho}{\partial z_{i\Delta}} \right) \frac{z_{i\Delta} - z_{i\Delta+1}}{\frac{\partial\rho}{\partial z_{i\Delta}} - \frac{\partial\rho}{\partial z_{i\Delta+1}}} \tag{2.3}$$

Likewise, for the base of the metalimnion, z_h (the theoretical division between the metalimnion and the hypolimnion), from $i = \zeta$ to $i = k - 1$, find *i* where $\partial\rho/\partial z_{i\Delta} \le \delta_{\min}$, interpolate between *i*-1 and *i*:

$$z_h = z_{i\Delta-1} + \left(\delta_{\min} - \frac{\partial\rho}{\partial z_{i\Delta-1}} \right) \frac{z_{i\Delta} - z_{i\Delta-1}}{\frac{\partial\rho}{\partial z_{i\Delta}} - \frac{\partial\rho}{\partial z_{i\Delta-1}}} \tag{2.4}$$

The searching algorithm used to perform these calculations (Equations 2.3 and 2.4) requires knowledge of the pycnocline index (ζ from section 2.3.1), and searches upward towards the water surface from ζ to find the depth of the top of the metalimnion, and downward towards the lake bottom from ζ to find the depth of the base of the metalimnion (Figure 2.3). As in 2.3.1, the Lake Analyzer program allows the calculation of metalimnion bounds relative to the parent or secondary thermoclines (see A.1.2).

2.3.3 *Schmidt Stability*

The resistance to mechanical mixing due to the potential energy inherent in the stratification of the water column was first defined by Schmidt (1928) and later modified by Hutchinson (1957). This stability index was formalized by Idso (1973) to reduce the effects of lake volume on the calculation (resulting in a mixing energy requirement per unit area). Various authors have adopted Idso's (1973) methodology; Kling (1988) for example, found a range of stability of 0 to 5,784 J m^{-2} across 39 West African lakes, while Ferris and Burton (1988) used Schmidt Stability to compare seasonal dynamics in Deep Lake, a hypersaline lake in Antartica. We present Idso's (1973) version of Schmidt Stability here as

$$S_T = \frac{g}{A_s}\int_0^{z_D}(z - z_v)\rho_z A_z \partial z \qquad (2.5)$$

where g is the acceleration due to gravity, A_s is the surface area of the lake, A_z is the area of the lake at depth z, z_D is the maximum depth of the lake, and z_v is the depth to the centre of volume of the lake, written as $z_v = \int_0^{z_D} zA_z\partial z \Big/ \int_0^{z_D} A_z \partial z$.

2.3.4 *Wedderburn Number*

The Wedderburn Number (*W*), was introduced by Thompson and Imberger (1980) to describe the likelihood of upwelling events under stratified conditions. For $W \leq 1$ there is a high probability that the thermocline will tilt to the surface at the upwind end of the lake and metalimnetic water will be entrained into the surface mixing layer, causing an

increase in mixed layer depth; otherwise (W >1) the mixed layer will deepen slowly (Imberger and Patterson 1990). W has frequently been used as a parameter to describe potential upwelling events in lakes (e.g., Stevens and Lawrence 1997; Macintyre et al. 2002; Lamont et al. 2004; Shintani et al. 2010). The Wedderburn Number can be written as

$$W = \frac{g' z_e^2}{u_*^2 L_s} \tag{2.6}$$

where $g' = g \cdot \Delta\rho / \rho_h$ is the reduced gravity due to the change in density ($\Delta\rho$) between the hypolimnion (ρ_h) and epilimnion (ρ_e), z_e is the depth to the base of the mixed layer (Equation 2.3), L_s is the lake fetch length and u_* is the water friction velocity due to wind stress (A.1.3, Equation A.9).

2.3.5 *Lake Number*

The Lake Number (L_N), defined by Imberger and Patterson (1990), has been used to describe processes relevant to the internal mixing of lakes induced by wind forcings. As with W, lower values of L_N represent a higher potential for increased diapycnal mixing, which increases the vertical flux of mass and energy across the metalimnion through the action of non-linear internal waves (Macintyre and Melack 2009). It has been used, for example, to estimate the flux of oxygen across the thermocline in a small lake (Robertson and Imberger 1994), and to explain the magnitude of the vertical flux of ammonium in a lake (Romero et al. 1998). Lake Number is given by

$$L_N = \frac{S_T\left(z_e + z_h\right)}{2\rho_h u_*^2 A_s^{1/2} z_v} \qquad (2.7)$$

where z_e and z_h are the depths to the top and bottom of the metalimnion, respectively (Equations 2.3 and 2.4).

2.4 Materials and methods

Lake Analyzer is a numerical program suite and supporting visualization tools for the calculation of indices of mixing and stratification in lakes and reservoirs. These physical indices are calculated according to established literature with a time series output format. The Lake Analyzer program was created for the rapid analysis of large volumes of high-frequency data collected from instrumented lake buoys.

2.4.1 *Program structure*

The Lake Analyzer program suite allows a user to specify desired outputs (such as Lake Number or the depth to the bottom of the mixed layer), and structures the program flow based on these outputs (Figure 2.4). This allows the program to be flexible to different data sources, instead of rigidly requiring all potential data files or functions for each program run. This flexible structure increases program speed when only a subset of outputs are selected, and also allows users with data limitations to use the program (as Schmidt Stability, for example, can be calculated without wind speed measurements). The structure of the program is defined by the user output requirements in the .lke *configuration file* (Appendix A.2.1), and is adapted to avoid the overhead of redundant calculations or files.

2.4.2 *Program flow*

After the program workflow is established by the *program constructor* from the .lke *configuration file*, *primary functions* are called, which then call *secondary functions* and/or trigger the opening of *data files* (.wtr, .wnd, .sal, or .bth), if necessary (Figure 2.4). The results from *primary functions* are then organized into a text output file and/or visualized using plotting defaults (see A.2.1.9 and A.2.1.10 for details). Details for each function can be found in section 2.3, while additional supporting calculations are explained in A.1.

2.4.3 *Data sources*

Data requirements for Lake Analyzer vary based on the user defined output selections (see 2.4.1), but every Lake Analyzer program run requires either the creation of, or the use of an existing .lke file, which is used to create the program structure. Additional files (.wtr, .wnd) hold time series data of water and wind speed measurements, while a .bth file holds observations of bathymetric areas with respect to depth. An optional input file which holds salinity measurements (.sal) can also be used to improve the density calculations of water, although these effects are ignored if this file is not present. All data source files are simple tab-delimited ASCII text files, with file extensions altered (e.g., .txt changed to .wnd) to facilitate pointer functions in the Lake Analyzer program. See lakeanalyzer.gleonrcn.org for a more detailed user manual for Lake Analyzer.

2.5 Results

Data are shown for three example lakes, covering a range of size, geographic location and typical stability to illustrate the robustness of the LakeAnalyzer Program.

2.5.1 *Lake Annie, Florida (USA)*

An example program output for Lake Annie, a subtropical, warm monomictic sinkhole lake (27.21°N, 81.35°W, 19 m maximum depth, 37 ha surface area; see Gaiser et al., 2009 for additional details) is shown in Figure 2.5. Measurements of wind speeds and water temperatures were sampled from sensors on 15 minute intervals, and were used in raw format (no error checking or down-sampling) to create .wnd and .wtr *data files* (Figure 2.4). Figure 2.5a is the water temperature ('wTemp') output with thermocline depth outputs ('thermD' and 'SthermD') overlaid. The output resolution for this example Lake Analyzer run was 6 hours (.lke {2}=21600). The effects of a tropical storm (Tropical Storm Fay, see Landsea et al., 2010) were notable in mid-August, as surface water temperatures decreased by approximately 3°C within hours of the storm, and thermocline depth increased by more than 2 m. Transient stratification patterns of heating and cooling are also evident during winter mixing in late December into March 2009. Figure 2.5b shows the Wedderburn Number and Lake Number, based on the seasonal thermocline (outputs defined by 'SW' and 'SLn', respectively). Both of these dimensionless indices are used to explain the potential for diapycnal mixing events, but the Wedderburn Number displays a higher amount of variability when compared to Lake Number. While W is dependent on the highly variable mixed layer depth (equation 2.6), L_N relies on the depth to midpoint of the metalimnion (equation 2.7), which tends to reduce variability through averaging with the more stable base of the metalimnion. Schmidt Stability is shown in Figure 2.5c, where diel patterns in stability are evident as day-night oscillations driven by alternating periods of heating and cooling. The cooling events that increase the depth of the thermocline in mid-April as well as the effects of the mid-August tropical storm are shown clearly as sudden reductions in Schmidt Stability.

Lake Annie has periods of transient stratification, where surface heating with limited mixing inputs leads to the formation of a secondary near-surface thermocline. Figure 2.6 highlights the difference between outputs based on the parent thermocline ('SthermD') and the maximum gradient thermocline ('thermD') for the period of 1 April to 1 May 2008 on Lake Annie. Water temperature profiles show the merging of the shallower thermocline with the parent thermocline (33rd profile; 17 May), and the establishment of an additional near-surface thermocline (46th profile; 24 May). Depending on the application required by the Lake Analyzer user, parent thermocline (denoted by an 'S' in front of applicable output selections, see A.2.1.11) or maximum gradient thermocline (A.2.1.1- A.2.1.10) can be used.

2.5.2 *Lake Rotorua, Bay of Plenty (NZ)*

An example program output for Lake Rotorua, a volcanic crater (38.1°S, 176.3°E 22 m maximum depth (central lake), 79 km^2 surface area, see Burger et al. (2008) for additional details) is shown in Figure 2.7. Input data for Lake Rotorua were generated with an instrumented buoy sampled at 30 minute intervals from 20 May 2008 to 6 April 2009. Selected outputs and output resolution are the same as for Figure 2.5. Lake Rotorua is typically well-mixed, with short periods of defined stratification lasting seldom longer than a week before convective and wind-driven destratification events restore near-isothermal conditions (Figure 2.7a). Lake Rotorua's lack of stratification leads to Wedderburn Number and Lake Number values typically below 1 (Figure 2.7b), representing a high likelihood of substantial diapycnal fluxes . Schmidt Stability reflects near-isothermal conditions with values close to 0, but (southern hemisphere) summer-time periods of stratification are evident as larger positive values in December 2008 to

March 2009 (Figure 2.7c). Compared to Lake Annie, Lake Rotorua is much larger (7900 vs. 37 ha), and because of increased wind mixing due to a larger fetch and differences in both climate and latitude (Macintyre and Melack 2009), Wedderburn Number and Lake Number are much lower in the Lake Rotorua dataset.

2.5.3 *Lake Mendota, Wisconsin (USA)*

Metalimnion dynamics for Lake Mendota (43.0°N, 89.42°W; 24 m maximum depth; 3940 ha surface area; see Robertson and Ragotzkie, 1990 for additional details) are shown for the stratified period of 2009 in Figure 2.8 (outputs 'wTemp', 'SmetaT', and 'SmetaB'). These results were obtained using the Lake Analyzer program with a specified output resolution of 1 hour (.lke {2} = 3600, see A.2.2.1) from buoy thermistor data sampled at 1 minute intervals. The presence of internal waves is visible on this higher frequency analysis, as internal seiches can be seen as the coupled oscillations of the metalimnion top and bottom (Figure 2.8a). Using the outputs for seasonal metalimnion ('SmetaT', and 'SmetaB' as opposed to 'metaT' and 'metaB') allowed the parent metalimnion to be accurately resolved even during periods of strong surface heating (e.g., mid September 2009). The thickness of the metalimnion, calculated as the difference between the outputs of 'SmetaB' and 'SmetaT', also shows seasonal dynamics related to surface forcings, as the peak thickness is found during late summer (mid-August) when stratification is greatest (Figure 2.8b). Conversely, periods of cooling resulted in thinning of the metalimnion (late September-October 2009), while deepening the surface mixed layer.

2.6 Discussion

The methods outlined above have been used to create a set of standards and best practices for the calculation of physical indices of stratification – such as Wedderburn Number, Lake Number, and Schmidt Stability – and have been collated into a complete open-source program suite called "Lake Analyzer." This program establishes a framework for the analysis of high-frequency instrumented buoy data, specifically designed for the rapid analysis of large datasets. The Lake Analyzer program provides a much needed analytical tool for the expanding global network of instrumented lakes, where available data is currently increasing at a rate that exceeds scientific output (see GLEON: Hanson 2007). Data-rich research can benefit from powerful tools like wavelet and time series analyses (Kara et al. 2012), which require researchers to combine high-resolution indicators of state with driver and response variables on the same time scales (Moberg et al. 2005; Hanson et al. 2006). Use of these cutting-edge analytical tools is facilitated by the creation of Lake Analyzer, which outputs standardized physical state variables in a time series format.

2.6.1 *Program availability*

The program Lake Analyzer was developed for the GLEON (Global Lake Ecological Observatory Network: www.gleon.org) community, a grassroots organization centred around scientific collaboration and data sharing to further the understanding and management of lakes. The Lake Analyzer program is free to download (http://code.google.com/p/lakeanalyzer-2/) under the GNU General Public Licence. Running Lake Analyzer on MATLAB requires a minimum version number of MATLAB 7.4 (additional details for computational requirements for versions of MATLAB can be found at http://mathworks.com/). Alternatively, users without access to MATLAB can

use GLEON's web interface for Lake Analyzer (lakeanalyzer.gleon.org/), which runs Lake Analyzer on a remote server based on user input files and allows users to download results after completion.

2.6.2 *Program performance*

Instrumented buoys can output high-resolution measurements that quickly become overwhelmingly data-rich, as one year of data easily surpasses a million data points when multiple sensors are polled every minute. Simple operations like file opening and routine calculations on this type of data can be cumbersome. The Lake Analyzer program was designed to avoid excessive computational expense in comparative science, as the program can digest large datasets on a common personal computer in seconds instead of hours. We tested the program on an Intel i5 2.4 GHz processor with 4 GB of RAM, using one minute measurements from Lake Mendota taken over a 200 day period from 23 unique depths and 1 wind sensor (6,896,496 measurements in 49,052 KB of data files). We simply calculated a time series of Lake Number for each day that was written to a text file and had the program plot the time series. All operations in the program took a total of 33 seconds, with 60% of this time spent finding and removing sensor errors and 20.6% loading the files. All other time was broken down into much more minor fractions of this total, including the Lake Number calculations.

2.6.3 *Program limitations*

The Lake Analyzer program was designed to be robust in the handling of different resolutions of instrumented data, including irregular time intervals. This flexibility adds a layer of user responsibility to the quality of input data, as the program provides limited quality control of the data (limited to error-checking and down-sampling) and assumes

that instrument calibration has been performed before creation of input data (or is not needed). Because instrumented buoys vary in vertical and temporal resolution, the user of the Lake Analyzer program should undertake a rigorous quality analysis/quality control program, including error analysis based on the accuracy of sensors and the resolution of the input data. For example, if thermal data is only available at 5 m depth intervals in a highly stratified lake, the accuracy of the thermocline depth and related outputs from the program will suffer compared with measurements made at 1 m intervals (see Figure 2.2a versus Figure 2.2b).

The .lke configuration file gives the user control over error checking parameters, in addition to effective smoothing ranges (e.g., temporal averaging of layers: .lke {6}; see A.2.2.5). These parameters are designed to increase the utility of the program for both high-resolution applications (Figure 2.6a; temporal averaging of layers) and lower-resolution outputs (e.g., Lake Number; see Figure 2.5c where epilimnion and hypolimnion layers are averaged over 6 hours to reduce the variability due to internal seiches). Lake Analyzer does not provide recommendations for these parameter values, as they are instrument and lake specific. When using Lake Number or Wedderburn Numbers ('Ln', 'SLn', 'W', or 'SW'), we suggest that the user follow the recommendations of MacIntyre et al. (2009) and use temporal averaging of wind and layers of sufficient duration to exceed one quarter of the first vertical mode internal seiche period (output selection 'T1' or 'ST1').

While Lake Analyzer is limited by a one-dimensional representation of a lake body (as the contributions of horizontal heterogeneity in the wind field, stratification, and basin shape are ignored), future improvements of the program will be a product of the

needs and ideas of a diverse body of users, potentially expanding the bounds of some of these restrictions. In the development of Lake Analyzer, we have attempted to maintain a transparent coding structure in an effort to encourage development and further expansion of this useful tool.

2.7 Conclusions

We have presented a numerical scheme for extracting lake-specific comparative indices of lake stratification and mixing from high-resolution instrumented buoy data, and described some of the potential applications for several of the program outputs. The Lake Analyzer program provides a powerful and easily accessible tool for comparative analyses of lake indices in both time and space, while also including a systematic error-checking algorithm designed for buoy-specific data streams. Any of these tools can be used together for a multiple variable program output, or in any combination to perform specific analyses (such as simply down-sampling and error-checking temperature data). The availability of the program lends it to a high level of transparency for users, as source codes are free to download online. Users without access to the MATLAB scripting language can also use the program on the GLEON online interface (http://lakeanalyzer.gleon.org/), which requires only the proper input files for the analysis. In conclusion, the Lake Analyzer program has been designed to increase the accessibility of physical lake parameters, extending the overlap between ecological and hydrodynamic research, with the intent to facilitate continued collaboration and enable improved data processing.

2.8 Acknowledgements

We thank the Global Lake Ecological Observatory Network (GLEON) and the Archbold Biological Station for working with GLEON to establish the buoy on Lake Annie. We also thank Dale Robertson, Sally MacIntyre, Chris McBride and the GLEON Physics/Climate working group for assisting in the program development, and Paul Hanson and three anonymous reviewers for proving guidance on an earlier version of this manuscript. This work was funded by the National Science Foundation via grants DBI-0446017 and DBI 0639229, in addition to funding provided by the Gordon and Betty Moore Foundation.

2.9 References

Aeschbach-Hertig, W., C. P. Holzner, M. Hofer, M. Simona, A. Barbieri, and R. Kipfer. 2007. A time series of environmental tracer data from deep, meromictic Lake Lugano, Switzerland. Limnology and Oceanography **52:** 257-273.

Burger, D. F., D. P. Hamilton, and C. A. Pilditch. 2008. Modelling the relative importance of internal and external nutrient loads on water column nutrient concentrations and phytoplankton biomass in a shallow polymictic lake. Ecological Modelling **211:** 411-423, doi: 10.1016/j.ecolmodel.2007.09.028.

Cole, J. J., M. L. Pace, S. R. Carpenter, and J. F. Kitchell. 2000. Persistence of net heterotrophy in lakes during nutrient addition and food web manipulations. Limnology and Oceanography **45:** 1718-1730.

Cole, J. J., Y. T. Prairie, N. F. Caraco, W. H. Mcdowell, L. J. Tranvik, R. G. Striegl, C. M. Duarte, P. Kortelainen, J. A. Downing, J. J. Middelburg, and J. Melack. 2007. Plumbing the global carbon cycle: Integrating inland waters into the terrestrial carbon budget. Ecosystems **10:** 171-184, doi: 10.1007/S10021-006-9013-8.

Coloso, J. J., J. J. Cole, P. C. Hanson, and M. L. Pace. 2008. Depth-integrated, continuous estimates of metabolism in a clear-water lake. Canadian Journal of Fisheries and Aquatic Sciences **65:** 712-722, doi: 10.1139/f08-006.

Fee, E. J., R. E. Hecky, S. E. M. Kasian, and D. R. Cruikshank. 1996. Effects of lake size, water clarity, and climatic variability on mixing depths in Canadian Shield lakes. Limnology and Oceanography **41:** 912-920.

Ferris, J. M., and H. R. Burton. 1988. The annual cycle of heat-content and mechanical stability of hypersaline Deep Lake, Vestfold Hills, Antartica. Hydrobiologia **165:** 115-128.

Gaiser, E. E., N. D. Deyrup, R. W. Bachmann, L. E. Battoe, and H. M. Swain. 2009. Effects of climate variability on transparency and thermal structure in subtropical, monomictic Lake Annie, Florida. Fundamental and Applied Limnology **175:** 217-230, doi: 10.1127/1863-9135/2009/0175-0217.

Hambright, K. D., M. Gophen, and S. Serruya. 1994. Influence of long-term climatic changes on the stratification of a subtropical, warm monomictic lake. Limnology and Oceanography **39:** 1233-1242.

Hanson, P. C. 2007. A grassroots approach to sensor and science networks. Frontiers in Ecology and the Environment **5:** 343-343.

Hanson, P. C., S. R. Carpenter, D. E. Armstrong, E. H. Stanley, and T. K. Kratz. 2006. Lake dissolved inorganic carbon and dissolved oxygen: Changing drivers from days to decades. Ecological Monographs **76:** 343-363, doi: 10.1890/0012-9615(2006)076[0343:ldicad]2.0.co;2.

Hutchinson, G. E. 1957. A Treatise on Limnology, Volume 1. John Wiley & Sons, Inc.

Idso, S. B. 1973. Concept of lake stability. Limnology and Oceanography **18:** 681-683.

Imberger, J. 1985. The diurnal mixed layer. Limnology and Oceanography **30:** 737-770.

Imberger, J., and J. C. Patterson. 1990. Physical limnology. Advances in Applied Mechanics **27:** 303-475.

Jellison, R., J. Romero, and J. M. Melack. 1998. The onset of meromixis during restoration of Mono Lake, California: Unintended consequences of reducing water diversions. Limnology and Oceanography **43:** 706-711.

Kara, E. L., P. C. Hanson, D. P. Hamilton, M. Hipsey, K. D. Mcmahon, J. S. Read, L. A. Winslow, J. Dedrick, K. C. Rose, C. C. Carey, S. Bertilsson, D. Motta-Marques, L. Beversdorf, T. Miller, C. H. Wu, Y. F. Hsieh, E. Gaiser, and T. K. Kratz. 2012. Time-scale dependence in numerical simulations: Assessment of physical, chemical, and biological predictions in a stratified lake from scales of hours to

months. Environmental Modelling & Software**:** in press, doi: 10.1016/j.envsoft.2012.02.014.

Kling, G. W. 1988. Comparative transparency, depth of mixing, and stability of stratification in lakes of Cameroon, West-Africa. Limnology and Oceanography **33:** 27-40.

Lamont, G., B. Laval, R. Pawlowicz, R. Pieters, and G. A. Lawrence. 2004. Physical mechanisms leading to upwelling of anoxic bottom water in Nitinat Lake, p. 8. 17th ASCE Engineering Mechanisms Conference.

Landsea, C. W., G. A. Vecchi, L. Bengtsson, and T. R. Knutson. 2010. Impact of Duration Thresholds on Atlantic Tropical Cyclone Counts. Journal of Climate **23:** 2508-2519, doi: 10.1175/2009jcli3034.1.

Macintyre, S., K. M. Flynn, R. Jellison, and J. R. Romero. 1999. Boundary mixing and nutrient fluxes in Mono Lake, California. Limnology and Oceanography **44:** 512-529, doi: 10.4319/LO.1999.44.3.0512.

Macintyre, S., J. P. Fram, P. J. Kushner, N. D. Bettez, W. J. O'brien, J. E. Hobbie, and G. W. Kling. 2009. Climate-related variations in mixing dynamics in an Alaskan arctic lake. Limnology and Oceanography **54:** 2401-2417.

Macintyre, S., and M. Melack. 2009. Mixing dynamics in lakes across climatic zones, p. 603-612. *In* G. E. Likens [ed.], Encyclopedia of Inland Waters. Elsevier.

Macintyre, S., J. R. Romero, and G. W. Kling. 2002. Spatial-temporal variability in surface layer deepening and lateral advection in an embayment of Lake Victoria, East Africa. Limnology and Oceanography **47:** 656-671, doi: 10.4319/LO.2002.47.3.0656.

Magnuson, J. J., T. K. Kratz, T. F. Allen, D. E. Armstrong, B. J. Benson, C. J. Bowser, D. W. Bolgrien, S. R. Carpenter, T. M. Frost, S. T. Gower, T. M. Lillesand, J. A. Pike, and M. G. Turner. 1997. Regionalization of long-term ecological research (LTER) on north temperate lakes. Internationale Vereinigung fuer Theoretische und Angewandte Limnologie Verhandlungen **26:** 522-528.

Magnuson, J. J., D. M. Robertson, B. J. Benson, R. H. Wynne, D. M. Livingstone, T. Arai, R. A. Assel, R. G. Barry, V. Card, E. Kuusisto, N. G. Granin, T. D. Prowse,

K. M. Stewart, and V. S. Vuglinski. 2000. Historical trends in lake and river ice cover in the Northern Hemisphere. Science **289:** 1743-1746.

Mcgowan, H. A., and A. P. Sturman. 1996. Regional and local scale characteristics of foehn wind events over the south island of New Zealand. Meteorology and Atmospheric Physics **58:** 151-164.

Moberg, A., D. M. Sonechkin, K. Holmgren, N. M. Datsenko, and W. Karlen. 2005. Highly variable Northern Hemisphere temperatures reconstructed from low- and high-resolution proxy data. Nature **433:** 613-617, doi: 10.1038/nature03265.

Monismith, S., and S. Macintyre. 2009. The surface mixed layer in lakes and reservoirs, p. 15. *In* G. E. Likens [ed.], Encyclopedia of inland waters. Elsevier.

Porter, J. H., E. Nagy, T. K. Kratz, P. Hanson, S. L. Collins, and P. Arzberger. 2009. New Eyes on the World: Advanced Sensors for Ecology. Bioscience **59:** 385-397, doi: 10.1025/bio.2009.59.5.6.

Robertson, D. M., and J. Imberger. 1994. Lake Number, a quantitative indicator of mixing used to estimate changes in dissolved-oxygen. Int. Rev. Gesamten Hydrobiol. **79:** 159-176.

Robertson, D. M., and R. A. Ragotzkie. 1990. Changes in the thermal structure of moderate to large sized lakes in response to changes in air-temperature. Aquatic Sciences **52:** 360-380.

Romero, J. R., R. Jellison, and J. M. Melack. 1998. Stratification, vertical mixing, and upward ammonium flux in hypersaline Mono Lake, California. Archiv Fur Hydrobiologie **142:** 283-315.

Rueda, F., and G. Schladow. 2009. Mixing and stratification in lakes of varying horizontal length scales: Scaling arguments and energy partitioning. Limnology and Oceanography **54:** 2003-2017.

Schmidt, W. 1928. Über Temperatur and Stabilitätsverhaltnisse von Seen. Geographiska Annaler **10:** 145-177.

Shintani, T., A. De La Fuente, Y. Nino, and J. Imberger. 2010. Generalizations of the Wedderburn number: Parameterizing upwelling in stratified lakes. Limnology and Oceanography **55:** 1377-1389, doi: 10.4319/lo.2010.55.3.1377.

Stevens, C. L., and G. A. Lawrence. 1997. Estimation of wind-forced internal seiche amplitudes in lakes and reservoirs, with data from British Columbia, Canada. Aquatic Sciences **59:** 115-134.

Thompson, R. O. R. Y., and J. Imberger. 1980. Response of a numerical model of a stratified lake to wind stress, p. 562-570. Proceedings from the 2nd International Symposium of Stratified Flows.

Verburg, P., R. E. Hecky, and H. Kling. 2003. Ecological consequences of a century of warming in Lake Tanganyika. Science **301:** 505-507, doi: 10.1126/science.1084846.

Wetzel, R. G. 1983. Limnology, first ed. Saunders College Publishing, Fort Worth.

Williamson, C. E., J. E. Saros, W. F. Vincent, and J. P. Smol. 2009. Lakes and reservoirs as sentinels, integrators, and regulators of climate change. Limnology and Oceanography **54:** 2273-2282.

Wuest, A., and A. Lorke. 2003. Small-scale hydrodynamics in lakes. Annual Review of Fluid Mechanics **35:** 373-412, doi: 10.1146/annurev.fluid.35.101101.161220.

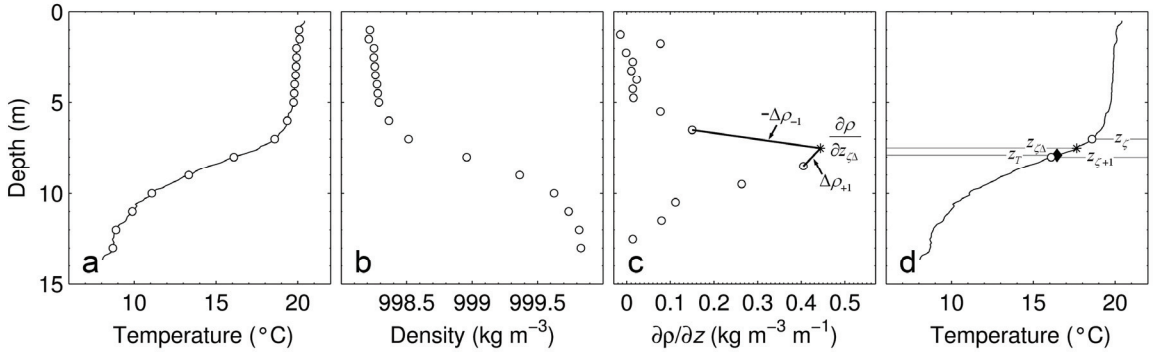

Figure 2.1: Algorithm for estimating the thermocline/pycnocline depth from example data. **a**) Continuous thermal profile (CTD cast, 10 cm resolution; thin black line) sampled at 0.5 m intervals (1 to 5 m) and 1 m intervals (5 to 14 m) to simulate discrete buoy thermistor measurements (○). **b**) Discrete temperature measurements from **a** converted into water density. **c**) Changes in density with respect to changes in depth ($\partial\rho/\partial z$) for discrete measurements. Maximum change is shown as ✳. Lake Analyzer's thermocline uses weighting from adjacent

calculations (slopes shown as $\Delta\rho_{-1}$ and $\Delta\rho_{+1}$) to improve upon the discrete maximum (✳). **d**) Original temperature profile from **a** with thermocline depth estimate (♦; z_T), calculation boundaries (○; z_ζ and $z_{\zeta+1}$), and discrete maximum (✳; $z_{\zeta\Delta}$).

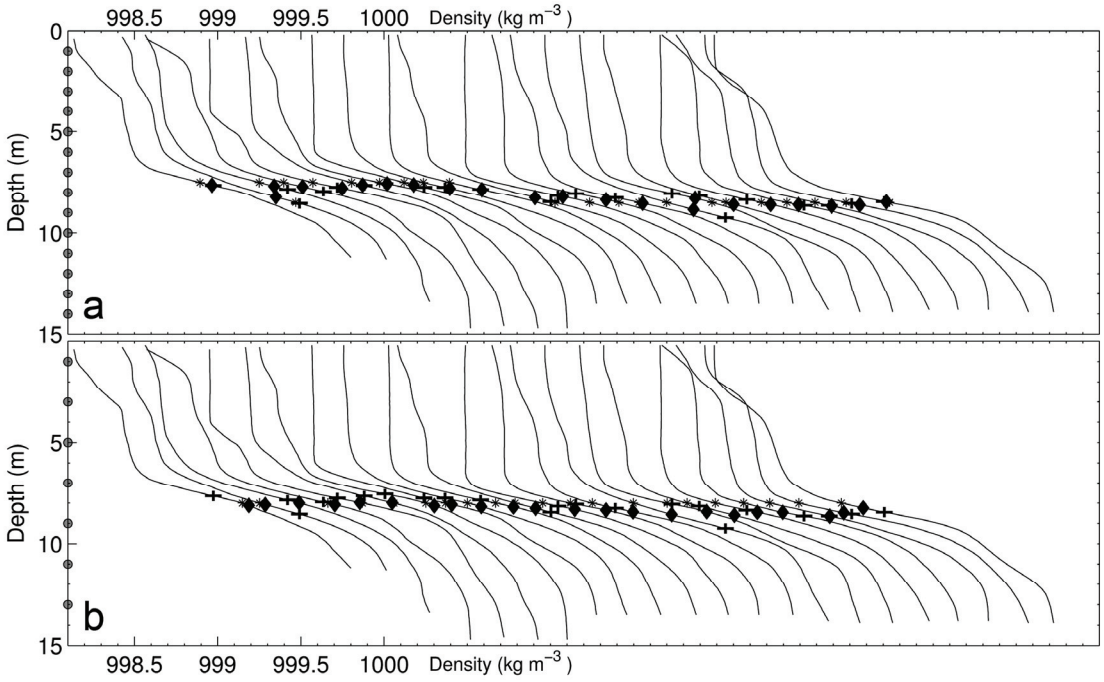

Figure 2.2: Thermocline algorithm for 24 days of CTD casts from Crystal Lake, WI, USA, converted to water density (thin black lines, smoothed using a 0.5 m running average from 10 cm measurements). Casts are offset by 0.2 kg m^{-3} on the x-axis for each day. **a**) CTD measurements are discretely sampled at 1 m intervals (◎), and ✳ represents the maximum discrete change in density, while ♦ is the Lake Analyzer estimate (see Figure 1; 2.1.2). Actual maximum change in density (✚) is calculated with knowledge of the continuous profile, and error between estimates and actual is taken as the absolute vertical distance between the two. Average error for ✳ was 22.9 cm over all 24 days, with a maximum single day error of 75 cm. Average error for ♦ was 13.9 cm, with a maximum single day error of 44.4 cm. **b**) Same as **a**, but with 2 m resolution on discrete sampling (◎). Average error for ✳ was 32.5 cm, with a maximum single day error of 125 cm. Average error for ♦ was 26.7 cm over all 24 days, with a maximum single day error of 68.2 cm.

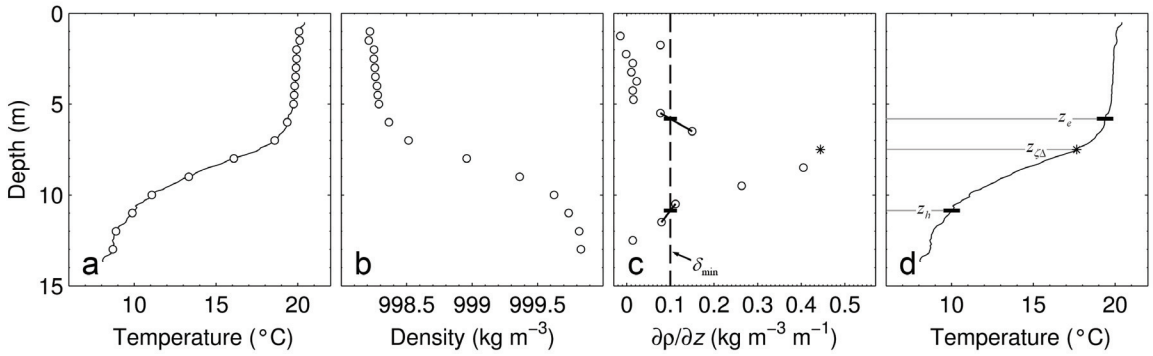

Figure 2.3: Algorithm for estimating the extent of the metalimnion (top and bottom) from example data. **a**) Same as **Figure 2.1a. b**) Same as **Figure 2.1b**. Casts started on 20 July 2009, and were completed within 1 hour from 17:00 on each day. **c**) Moving away from the maximum discrete change in density (from ∗: upward for z_e, downward for z_h), metalimnion top and bottom are estimated by linear interpolation between discrete density changes (○) to a user-specified threshold ($\delta_{\min}$). **c**) Original temperature profile from **a** with metalimnion top estimate (**–**; z_e), metalimnion bottom (**–**; z_h), and discrete maximum (∗; $z_{\zeta\Delta}$).

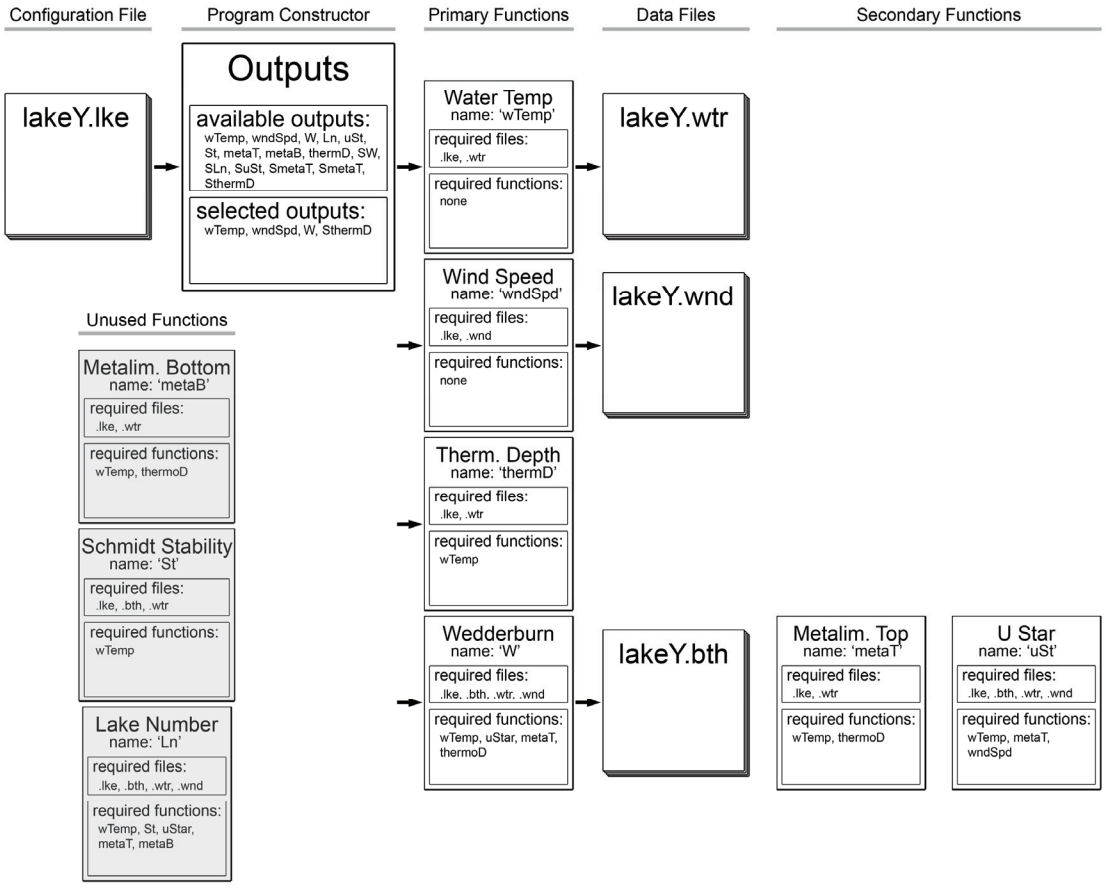

Figure 2.4: An example workflow of the Lake Analyzer program (only partial outputs are used here to highlight flexibility of the program structure). The ***configuration file*** specifies the structure of the program flow, based on user input for desired program outputs (see A.2.2.1). The ***configuration file*** has the specific extension .lke, with the file name common to source files (such as clearLake.lke, clearLake.wtr, etc.). The ***program constructor*** assembles the Lake Analyzer program structure through a series of logical statements based on output requirements and function needs. ***Primary functions*** are direct functions relative to the user specified outputs. ***Data files*** are the data sources required for the program run (.wtr, .wnd, and .bth; see A.2.2.2-A.2.2.4). ***Data file*** .sal is not shown here because it is an optional input file which is not required for the program to run. ***Secondary functions*** are functions called by primary functions if required as part of the ***primary function*** output. ***Unused functions*** are shown here (gray overlay) as functions that are not called during this example workflow.

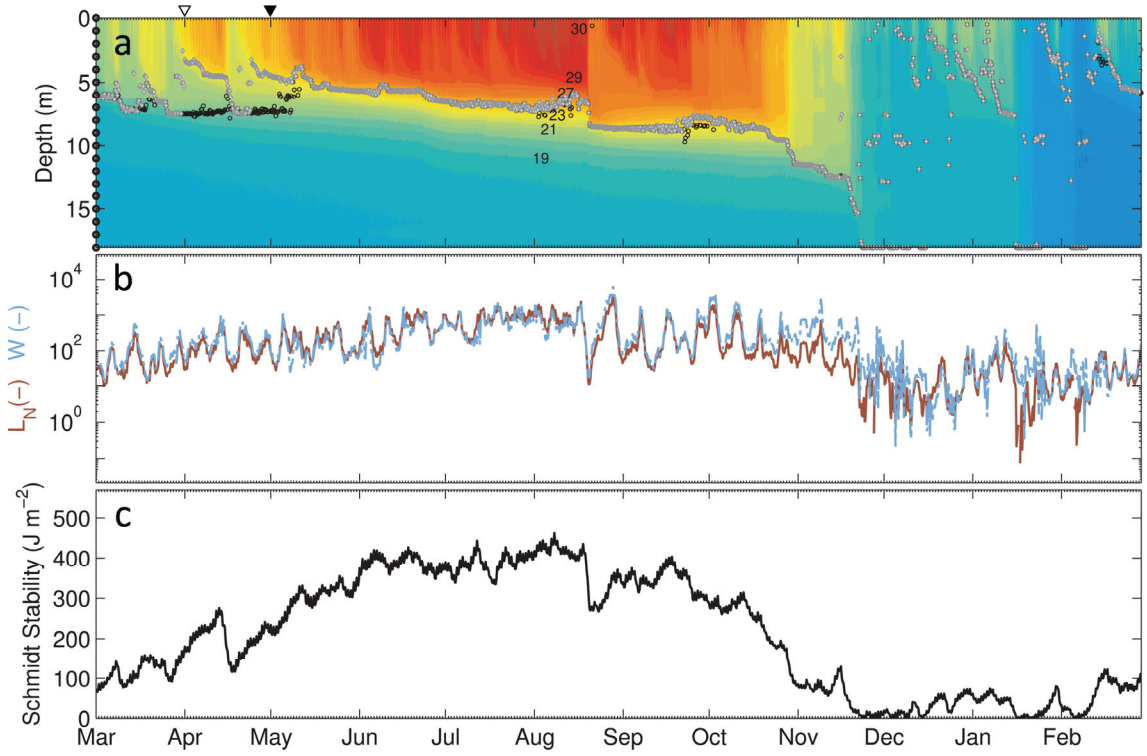

Figure 2.5: Program output for Lake Annie, Florida (USA) beginning in 2008. **a**) Temperature plot ('wTemp': colors) with color divisions every 0.5°C (buoy thermistors are shown on left edge:⊙). Seasonal thermocline and maximum gradient thermocline are overlaid ('SthermD', ○ and 'thermD', ◈). **b**) Seasonal Wedderburn number ('SW', light blue dashed line) and seasonal Lake Number ('SLN', dark red line) for the same period. **c**) Schmidt stability ('St').

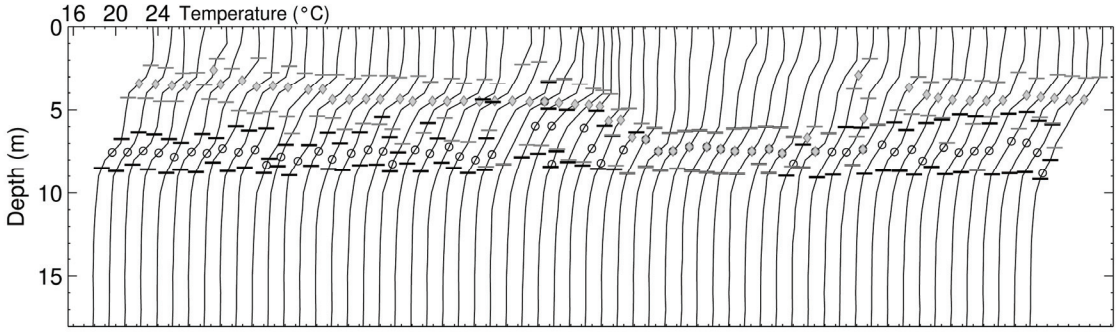

Figure 2.6: Thermal profiles taken every 12 hours from 1 April 2008 to 1 May 2008 on Lake Annie (see **Figure 2.5a**: ▽ to ▼) offset 1.5°C on the x-axis (thin black lines, taken from 'wTemp' discrete buoy measurements). Seasonal thermocline ('SthermD', ○), maximum gradient thermocline ('thermD', ◈), seasonal metalimnion top and bottom ('SmetaT', **–**; 'SmetaB', **–**), and maximum gradient metalimnion top and bottom ('metaT', –; 'metaB', –) are shown for each profile.

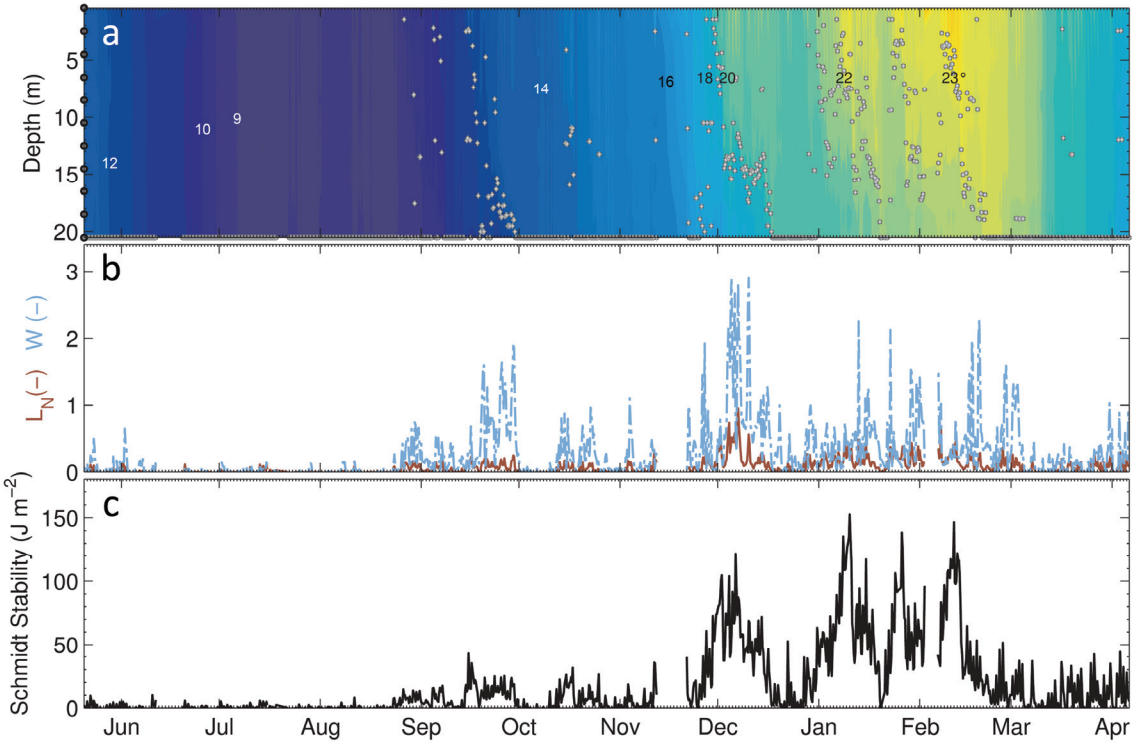

Figure 2.7: Same as **Figure 2.5**, but for Lake Rotorua (NZ) starting in 2008.

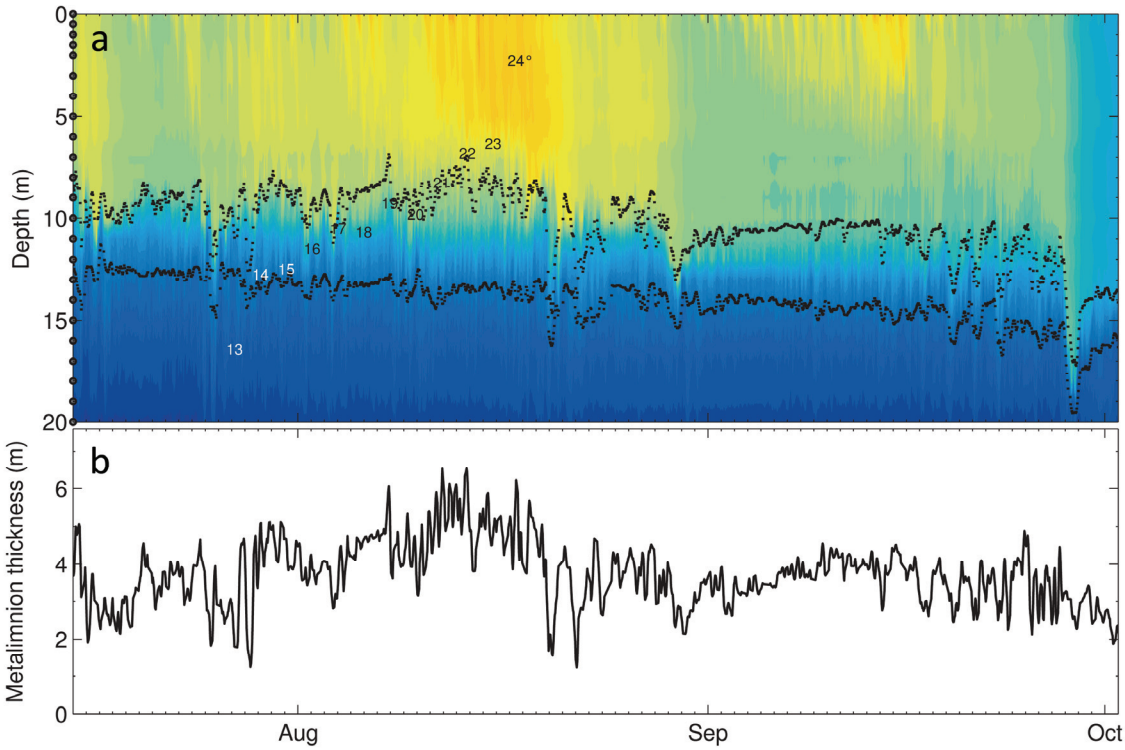

Figure 8: Metalimnion dynamics for Lake Mendota, Wisconsin (USA) during 2009. **a**) Temperature plot ('wTemp', colors) with color divisions every 0.5°C. Locations of buoy thermistors are shown on right edge (●). Metalimnion bounds for the parent thermocline ('SmetaT' and 'SmetaB', black dots) are overlaid after transforming with a 6 hour running average. **b**) Thickness of the seasonal metalimnion, taken as the difference between 'SmetaB' and 'Smeta' in meters.

Chapter 3 – Lake-size dependency of wind shear and convection as controls on gas exchange

The following is reproduced with permission from a publication that is catalogued according to doi:10.1029/2012GL051886

Read JS, DP Hamilton, AR Desai, KC Rose, S MacIntyre, JD Lenters, RL Smyth, PC Hanson, JJ Cole, PA Staehr, JA Rusak, DC Pierson, JD Brookes, A Laas, CH Wu. 2012. Lake-size dependency of wind shear and convection as controls on gas exchange

3.1 Abstract

High-frequency physical observations from 40 temperate lakes were used to examine the relative contributions of wind shear (u_*) and convection (w_*) to turbulence in the surface mixed layer. Seasonal patterns of u_* and w_* were dissimilar; u_* was often highest in the spring, while w_* increased throughout the summer to a maximum in early fall. Convection was a larger mixed-layer turbulence source than wind shear ($u_*/w_* < 0.75$) for 18 of the 40 lakes, including all 11 lakes < 10 ha. As a consequence, the relative contribution of convection to the gas transfer velocity (k, estimated by the surface renewal model) was greater for small lakes. The average k was 0.54 m day^{-1} for lakes < 10 ha. Because u_* and w_* differ in temporal pattern and magnitude across lakes, both convection and wind shear should be considered in future formulations of lake-air gas exchange, especially for small lakes.

3.2 Introduction

Lakes are important components of regional carbon budgets, where terrestrial and atmospheric sources of carbon can be sequestered via sedimentation, effluxed to the atmosphere in the form of greenhouse gases like CO_2 and CH_4, or lost to outflows (Cole et al. 2007; Bastviken et al. 2011). The turbulent surface mixed layer (SML) plays an important role in regulating these processes, for example, vertically distributing resources and regulating the physical environment experienced by phytoplankton, as well as controlling diffusive fluxes of

partially soluble gases across the air-water interface. Two of the most important properties of the SML are its depth (z_{mix}) and the intensity of turbulence within it (quantified by the turbulent kinetic energy dissipation rate, ε). These SML properties are dynamic through time and space within lakes and vary widely among lakes, being largely regulated by the balance between solar radiation (acting to enhance stratification) and wind and heat loss (acting to destabilize and deepen the layer). Efforts to quantify the generation of turbulence from these mixing sources have led to water-side velocity scales for convection (w_*) and wind shear (u_*), allowing SML turbulence to be parameterized according to the additive effects of w_* and u_* (Imberger 1985).

In addition to homogenizing the SML, the intensity of near-surface turbulence controls the exchange rate of gases across the air-water interface (Mcgillis et al. 2004; Zappa et al. 2007; Macintyre et al. 2010). Therefore, an understanding of SML dynamics is integral to accurately estimating the efflux of gases like CO_2 and CH_4 from lakes. Gas flux can be calculated as the product of the gas transfer velocity (k) and the difference between the equilibrium and ambient gas concentration in the surface water (Cole and Caraco 1998). k has a strong dependence on ε (Zappa et al. 2007), and thus can increase in response to wind, waves, convection, and rain events (Zappa et al. 2004; Soloviev et al. 2007). Despite a basic understanding of the influence of these drivers on ε, the most commonly used models for k predict transfer velocity based only on wind speed measurements (e.g., Cole and Caraco 1998), resulting in other drivers of k being implicitly integrated into the empirical model. Convection is also an important source of near-surface turbulence in lakes that has been shown to enhance gas exchange (Eugster et al. 2003; Macintyre et al. 2010; Rutgersson et al. 2011). Despite this recognition, the relative roles of w_* and u_* in SML processes (such as gas exchange) have been quantified in only a small number of lakes (e.g., Macintyre and Melack 2009).

Progress in quantifying the role of lakes in globally important processes such as the carbon cycle requires identifying common and predictable patterns in the controls of mixing within lakes (Cole et al. 2007). Differences in mixed layer depths and water temperatures are related to water color (Persson and Jones 2008; Tanentzap et al. 2008), wind sheltering (Markfort et al. 2010), morphometry, and other properties of lakes (Fee et al. 1996). Analyses from a small number of tropical, temperate, and Arctic lakes indicate that both lake size and latitude are related to predictable variability in w_* and u_* (Macintyre and Melack 2009). To develop robust generalizations that will allow scaling within regional and global models, we test the hypothesis that lake surface area and latitude influence the relative role of convection versus wind shear for mixing within the SML and inducing gas exchange in 40 temperate lakes. Additionally, we illustrate seasonal patterns of the magnitude and relative importance of u_* and w_* and quantify the contribution of wind shear and convection to k using a surface renewal model (Lamont and Scott 1970).

3.3 Methods

3.3.1 *Measurements*

We collected high-frequency observations of water temperature and meteorological drivers from 40 temperate lakes (absolute latitude range: 24.6° to 60°) ranging in surface area from 0.06 ha to over 64,000 ha and totaling more than 24 million measurements (Table 3.1). Instrumented buoys measured water temperature at multiple depths, as well as wind speed above the surface of the water. Incoming shortwave and longwave radiation, relative humidity, and air temperature were either measured on the buoys (or a nearby location) or modeled as functions of other measured variables. Hypsographic curves for each lake were extracted from bathymetric maps or from concurrent GPS/depth-sounder data. For locations where neither of these datasets

existed, the lakes were assumed to have a conical shape constrained by surface area and maximum depth.

3.3.2 *Calculating the convective velocity scale* (w_*)

The velocity scale for convective heat loss (w_*) was calculated from $w_* = (-\beta z_{mix})^{1/3}$, where z_{mix} is the SML depth, and buoyancy flux (β) was estimated using the mean of two separate approaches for calculating surface heat fluxes to reduce uncertainty, including measured changes in internal energy and the sum of surface fluxes (Jonas et al. 2003; Verburg and Antenucci 2010). We set $w_* = 0$ when buoyancy flux was positive (i.e. gaining stratification). Buoyancy flux (β) is the rate of change of potential energy in the water column, driven by the net surface energy flux, Q_s (described later), and the attenuation of visible light as quantified by the diffuse attenuation coefficient (K_d). Accurate measurements of shortwave radiation and the penetration of its visible component, photosynthetically active radiation (PAR), into the water column are crucial for estimating daytime values of β. We estimated PAR (the 400-700 nm spectrum) as 46% of total shortwave radiation and calculated K_d using one of the following, listed in order of preferential data sources: 1) exponential fits of *in situ* measurements of downwelling irradiance in the 400-700 nm range (see Appendix E), 2) a model which includes the attenuating properties of water, dissolved organic carbon concentration, and chlorophyll *a* (Morris et al. 1995), or 3) a function of Secchi depth (Kirk 1994).

The effective surface heat flux (H^*) and β were calculated according to the methods of *Kim* (1976) as $H^* = Qs\text{-}R_0[(2\text{-}2\exp(\text{-}z_{mix}K_d))/(z_{mix}K_d\text{-}\exp(\text{-}z_{mix}K_d)]$ and $\beta = g\alpha H^*/(C_p \rho_w)$, where R_0 is PAR (in W m^{-2}), g is the acceleration due to gravity, α is the coefficient of thermal expansion, and C_p is the specific heat of water. z_{mix} was calculated as the depth where the difference between the local water temperature and the surface temperature exceeded the

accuracy of the thermistors. We did not have accuracy specifications for all thermistors, and assumed all lake temperature measurements to be accurate within 0.2 °C for this calculation.

Similar to *Jonas et al.* (2003), we calculated Q_s based on the change in heat content of the water column, as measured by our thermistor arrays. This approach assumes advected components, sediment heating, and changes in lake levels are negligible. We also computed Q_s from the surface energy budget (Imberger 1985) using meteorological observations from the 39 lakes where air temperature, relative humidity, longwave and shortwave radiation, and wind speed data were available. Following Verburg and Antenucci (2010), we corrected for atmospheric stability in our calculations of latent and sensible heat fluxes (see Appendix C). When longwave radiation observations were not available, net longwave was estimated based on the emissivity and temperatures of the atmosphere and the lake surface (Crawford and Duchon 1999).

To reduce the impacts of temperature fluctuations that can confound estimates of short-term changes in heat storage (such as the influence of internal wave activity), we used a wavelet de-noising routine (daubechies 4 wavelet, single rescaling, min/max thresholds used on MATLAB's wden.m function; see www.mathworks.com). This technique results in smoother temporal variations in water temperature, while preserving patterns of diurnal heat gain and loss. Temperature measurements taken between the surface and the depth where 50% of light penetrates ($-\log(0.5)/K_d$) used 2 levels of wavelet filtering, depths between the 50% threshold and the depth of 1% light ($-\log(0.01)/K_d$) had 3 levels of filtering, and depths below 1% were not used, as heat gains below this depth were considered negligible. After de-noising, the temperature profiles were combined with lake hypsography to calculate the change in internal energy (at a timestep of one hour), which was then assumed to be equal to Q_s. Each lake in this

analysis had a unique combination of meteorological instrumentation and thermistor arrays. Therefore, to limit the potential for bias and create a "best estimate" of Q_s (used for w_*, ε and k), we averaged the results of the two methods (when available) and also calculated approximate error bounds for the thermistor method, as described below.

The accuracy of the thermistor method is sensitive to the vertical coverage of thermistors, sources of physical noise (such as internal waves), and the accuracy of the temperature measurements. Thermistor arrays varied among lakes, but the total number of thermistors used was 520 (an average of 13 per lake), and the average vertical spacing was 1 m (0.5 m for lakes < 10 ha; 1.2 for lakes > 10 km^2). We performed an uncertainty analysis by propagating potential errors in Q_s (and w_*) due to uncertainties in temperature, hypsography, and other variables (Table 3.2). We then used only meteorological flux estimates of Q_s for lakes that had large uncertainties in the thermistor-based estimate of Q_s (instead of averaging the two methods). For each time series, we assigned random errors to our measured values and constants and applied a bootstrapping technique to establish uncertainty in both Q_s and w_*. Similar to *Lenters et al.* (2005), the random errors were introduced through Monte Carlo sampling of a normal distribution which had a mean of zero and a standard deviation of half the assumed uncertainty. These errors were then added to the measured values or constants. In addition to applying random measurement errors, we also bootstrapped the residuals of our wavelet de-noising algorithm. This technique allowed us to assess the quality of each smoothed signal's representation of the raw observations. For the bootstrapping routine, we followed a four-step process: 1) each thermistor was smoothed using the wavelet de-noising function, 2) the residuals were calculated between the raw measurements and the de-noised signal, 3) the residuals were shuffled at random and added back to the smoothed signal, 4) the de-noising function was then

re-applied to the resulting time series. We repeated these steps (bootstrapping and Monte Carlo sampling) for 1000 iterations and established 95% confidence intervals for the mean values of Q_s and w_*. If the range between the 95% confidence intervals (the 2.5 and 97.5 percentiles) was > 10% of the median of all iterations of w_*, the thermistor method was considered to be an inadequate estimate of surface heat fluxes for the lake (18 of the 40 lakes; Figure 3.1). For result calculations that included the thermistor method, median values of the 1000 iterations were used to represent the respective result variables. The difference between each of the methods used to calculate w_* and the representative mean of the two methods was generally small (an average of 6 %, with a maximum of 26% for the 22 lakes).

3.3.3 *Calculating the wind shear velocity scale* (u_*)

The turbulent velocity scale for wind shear (u_*) was calculated as $u_* = (\tau_0/\rho_w)^{1/2}$ where $\tau_0 = C_D U_{10}^2 \rho_a$ is the wind-shear, ρ_w and ρ_a are the densities of water and air, respectively, C_D is the drag coefficient (as a function of wind speed and atmospheric stability) (Verburg and Antenucci 2010), and U_{10} is the measured wind speed transformed to a 10 m height (Amorocho and Devries 1980).

When calculating u_*, we accounted for overestimates that would occur when wind measurements were made within the transitional shadow between terrestrial to lacustrine boundary layers (Markfort et al. 2010). This method involved calculating theoretical estimates of wind shear in the absence of terrestrial sheltering, followed by a process which scaled these values onto the lake surface relative to the distance from the edge of sheltering. To do this, we first assumed that the wind measurements were made in the center of a circle equal in area to the lake. If the radius (R) of this circle was less than 50 times the terrestrial canopy height (hc; which we assumed to be 5 m for all lakes), our on-lake wind measurements (U) were considered to be

affected by terrestrial sheltering, as *Markfort et al.* (2010) found sheltering was negligible beyond this distance. These measurements were then up-scaled to be more representative of the free-stream velocity (U_{fs}) using a log-linear fit to observations from *Markfort et al.* (2010) that were made at various distances and heights relative to the edge of sheltering. Our model for scaling U to U_{fs} was $U_{fs} = U/(\log10(R/hc)*0.323+0.016)$ based on a measurement height that was 40% of hc (see Markfort et al. 2010). This choice corresponds to the 2 m measurement height that was used on most of these sheltered lakes, and this model was only valid for the range $R < 50hc$. We then calculated u_* as the area-weighted average of $u_*(x) = (\tau(x)/\rho_w)^{1/2}$, where $u_*(x)$ was the u_* value calculated at a distance x meters from the canopy edge. We used additional observations from *Markfort et al.* (2010) to define a log-linear relationship between $\tau(x)$ and τ_0 of $\tau(x) = \tau_0*x/(50hc)$, where $\tau_0 = C_D U_{fs}^2 \rho_a$. A circle was used as a simplified representation of the lake for area-weighted averages of u_*.We did not use area-weighted estimates of u_* for lakes where $R > 50hc$ and only applied these methods to the 14 smallest lakes.

3.3.4 *Comparing contributions of* u_* and w_* *to mixed layer turbulence*

We used the velocity scales for wind shear and convection (u_* and w_*, respectively) as proxies for the magnitude of turbulence driven by wind and heat loss. The ratio of u_* to w_* is a dimensionless index which can be used to compare the relative importance of wind shear to convection as components in the SML turbulent kinetic energy budget (Imberger 1985; Rutgersson et al. 2011). u_* and w_* have different efficiencies of integration into SML turbulence, and we used the ratio proposed by *Imberger* (1985), which considers $u_*/w_* = 0.75$ to be the threshold for equal input from the two components. Thus, ratios < 0.75 would represent conditions where convection is a larger source of turbulent mechanical energy to the SML. u_*, w_*, β, and z_{mix} were calculated on an hourly timestep using filtering routines from *Read et al.*

(2011) and the atmospheric stability functions from *Verburg and Antenucci* (2010). Indices hereafter reported as *temporally-averaged* were averages of hourly variables over the entire time series for each lake.

To compare patterns in the seasonality of u_* and w_*, we aggregated normalized 3-week averages for both parameters across all 40 lakes (i.e. subtracting the long-term mean and dividing by the standard deviation of the 3-week averages). 3-week averages were the mean of all values of u_* or w_* that fell within each interval. This process was used to remove lake-specific variations in the seasonal amplitude of w_* and u_* that might arise from differences in geographic location, while still preserving seasonal patterns. For each interval, we calculated the mean and inter-quartile ranges of u_* and w_* across all lakes.

3.3.5 *Calculating the gas transfer velocity* (k)

We estimated an hourly time series of near-surface ε for each lake following the approach of *Soloviev et al.* (2007), with ε being the sum of inputs from wind shear (ε_u) and convection (ε_w) (Figure 3.2). Our approach differed slightly from *Soloviev et al.* (2007) in that we ignored the breaking-wave component of ε. Turbulence from wind shear was calculated as $\varepsilon_u = (\tau_t/\rho_w)^{1.5}/(\kappa\delta_v)$, where τ_t is the tangential shear stress, κ is the Von Karman constant, and δ_v is the stirring-dependent thickness of the viscous sublayer (see Soloviev et al. 2007). For ε_w, we used $\varepsilon_w = -\beta$, but we caution that this scaling relationship deviates from unity at depths below the near-surface layer (Jonas et al. 2003). The surface renewal model was used to predict k from ε as $k = \eta(\varepsilon\nu)^{1/4}Sc^{-n}$, where η is the constant of proportionality, ν is the kinematic viscosity of water, Sc is the Schmidt number of the gas, and n is a coefficient representing surface conditions. k was calculated using this equation and with $\eta = 0.29$, $n = 0.5$, and $Sc = 600$. We also calculated k as a

function of ε_w alone, namely $k(w_*) = \eta(\varepsilon_w \nu)^{1/4} Sc^{-n}$, and this relationship was used to parameterize the percentage of total k driven by convection as $k(w_*)\% = (k(w_*)/k)100\%$.

3.4 Results

The relative importance of wind and convection for SML turbulence varied greatly among the 40 lakes, but several basic patterns emerged that were related to lake size, latitude, and SML depth (Table 3.3). We used a non-parametric test (Spearman rank correlation) to evaluate the statistical dependence between paired variables. The ratio of u_* to w_* had a significant relationship with lake size ($p<0.01$; Figure 3.3), with wind shear dominating large lakes and convection dominating small lakes, although both u_* to w_* were positively related to lake surface area ($p < 0.01$; Table 3.4). w_*, but not u_*, had a significant negative relationship with latitude ($p < 0.05$; Table 3.4). The average of $u_*^3 + w_*^3$, which is often used to parameterize turbulent flux into the mixed layer (Imberger 1985), was significantly related to SML depth ($p < 0.01$).

Seasonal patterns in u_* and w_* were dissimilar when aggregated across all 40 lakes (Figure 3.4). w_* was typically lowest during the early spring, and increased to a maximum during late summer and early fall before declining again near the end of fall. In contrast, u_* was more often at a maximum during late spring, with a common minimum during the middle of summer (Figure 3.4).

As expected, k was of greater magnitude on larger lakes ($p < 0.01$; Table 3.4). The percentage of this transfer velocity that was driven by convection alone ($k(w_*)\%$) was significantly related to lake size and season ($p < 0.01$; Table 3.4; Figure 3.5). Similar to the seasonal patterns in u_* and w_* (Figure 3.4), the average convective influence on gas transfer was

significantly higher (Mann-Whitney U-test; $p < 0.01$) during summer than spring for 23 of the 29 lakes with representative data for both periods (at least 21 days).

3.5 Discussion

Our analysis leveraged physical measurements from 40 temperate lakes to examine the relative roles of wind shear and convection in driving turbulence-dependent SML processes (such as gas exchange). Convection was of increasing importance for the smaller lakes in our analysis. This result is important for scaling biogeochemical measurements, as small lakes are numerically dominant across the global landscape (Downing et al. 2006) and often represent disproportionately large areal fluxes of greenhouse gases, even when k is estimated conservatively (Cole et al. 2007). Many investigators have shown evidence of gas transfer enhancement during convective conditions (Eugster et al. 2003; Jeffery et al. 2007; Macintyre et al. 2010; Rutgersson et al. 2011), but our analysis is the first to highlight – across a broad range of lakes – the importance of convectively derived turbulence in small lakes. In particular, we found a strong size dependence for u_*/w_* (Figure 3.3), as well as a pattern of increased convective contribution to gas transfer velocities in smaller lakes (Figure 3.5). w_* was of greater magnitude on larger lakes (likely due to greater mixed layer depths and more rapid wind-driven heat losses), and generally increased at lower latitudes for the lakes in our analysis (Table 3.4). Both of these patterns were consistent with *MacIntyre and Melack* (2009). While our results revealed a likely dependence of w_* on surface area and latitude, convection was the dominant temporally-averaged source of SML turbulence in small lakes (< 10 ha), regardless of latitude.

Wind shear followed the expected temporal pattern for most of the lakes included in this analysis, with maximum values occurring during the spring and fall (Figure 3.4), periods that often represents the windiest time of the year in temperate regions. Conversely, w_* lagged u_* by

several months, generally reaching a maximum during late summer and early fall. This lag is a result of the thermal inertia of these lakes, which causes maximum cooling to lag maximum summer water temperatures (as a function of lake depth and vertical mixing). Because of the contrasting seasonal patterns in u_* and w_*, as well as their differing contributions according to lake size, we would expect processes driven by SML turbulence (such as k) to exhibit patterns that are closely related to the relative contribution of these two drivers to ε.

Convection made a large contribution to k for smaller lakes, where temporally-averaged $k(w_*)$% was greater than 60% for the six smallest lakes, and as much as 79% of total k for the smallest lake (Figure 3.5). Larger lakes (> 10 km^2) had a range in $k(w_*)$% between 12-21%, indicating that while convection was a much smaller driver of k than wind shear, it was still important. The convective component of k was often greater in summer compared to spring. For example, of the 29 lakes that had sufficient data for the spring and summer periods, 23 of these lakes had significantly higher $k(w_*)$% during the summer ($p < 0.01$; Figure 3.5). Most models for gas transfer are parameterized by wind speed and, therefore, have temporal patterns that are closely aligned with the dynamics of u_* (Wanninkhof 1992; Cole and Caraco 1998). Wind-based models may be appropriate for larger lakes with higher u_*/w_*, but for smaller lakes where convection is increasingly important, they likely fail to adequately reproduce the temporal dynamics of k.

While our results highlight a potential lack of coherence between wind-modeled k and k that is modeled from both ε_u and ε_w (particularly for small lakes; Figure 3.4; Figure 3.5), our methods are based purely on physical principles. Therefore, further improvements to gas exchange estimates should couple the analysis used here with continuous turbulent flux observations (e.g., Macintyre et al. 2010; Huotari et al. 2011) across a wide distribution of lakes.

However, the mechanistic physical model employed here is likely more transferable across a variety of diverse water bodies compared to site-specific empirical models for gas exchange.

The lakes included in this analysis span large gradients in size, latitude, shape, and color (Table 3.1), and these factors drive unique SML dynamics in each lake. The temporal coverage of the measurement campaigns also varied among lakes. We applied consistent and sometimes redundant methods for most lakes for the calculation of ε, u_*, and w_*, with an understanding that our methods may not represent ideal approaches for individual lakes. Despite these limitations, we have highlighted several important and robust physical patterns for a diverse set of lakes.

At present, the constant of proportionality relating $\varepsilon^{1/4}$ to k is poorly constrained, with recent investigators disagreeing by almost 3-fold on the magnitude of η (e.g., Zappa et al. 2007; Macintyre et al. 2010; Vachon et al. 2010). We used a modified version of the estimate of η from *Zappa et al.* (2007), a study where ε and k were measured during various forcings. Because the depths of our near-surface estimates of ε were shallower than field measurements in *Zappa et al.* (2007), we used their lower boundary of $\eta = 0.29$. We assumed that disagreement in η is related to the corresponding depth of ε (as surface-generated turbulence decreases with depth) and parameterized our model of k accordingly, but this topic warrants further examination.

Using a conservative value for η, our average k for the 11 smallest lakes (< 10 ha) was 0.54 m day^{-1} (standard deviation of 0.12 m day^{-1}; Table 3.3). This range is in good agreement with transfer velocity estimates for small temperate lakes from a variety of different methods (Cole et al. 2010) and slightly higher than *Cole et al.*'s (1994) 0.5 m day^{-1}, which was used as an estimate of the global average k. Our results suggest that $k = 0.54$ m day^{-1} is a conservative mean value for extremely common small (< 10 ha) temperate lakes, and that larger lakes likely have stronger winds and higher k (Table 3.3).

Our results build on earlier work that highlights the role of convection in enhancing the gas transfer velocity for lakes (sensu Eugster et al. 2003; Macintyre et al. 2010). Given that convection is a significant component of k, then the seasonal, diurnal, and latitudinal dependence of w_* has likely been missing from most efflux estimates to date. These potential errors include the sub-daily parameterization of k in free-water metabolism models (Staehr et al. 2010), as well as gas exchange in cases where seasonal variation in both k and gas concentration would combine to significantly influence total flux magnitudes. Because the majority of lakes are small and often wind-sheltered, the convective component of near-surface turbulence must be considered in future formulations of k and in calculations of lake gas exchange.

3.6 Acknowledgements

This work is a product of the Physics and Climate working group from GLEON meetings G11, G12, and G13 (www.gleon.org). Funding for this research was provided by the U.S. National Science Foundation (NSF) grants DEB-0822700, MCB-0702395, DBI-0446017, DBI-0639229, and the Gordon and Betty Moore Foundation, award 1182. Funding for sensor platforms: NSF grant number DGE-0903560 and DEB-0743192 (AC, ET, WT); University of Nebraska Water Resources Research Initiative (AK); Archbold Biological Station (AN); Trophic Cascade Project, UW-Madison, U Virginia, Cary Institute of Ecosystem Studies (CP, PT, WD); U.S. NSF DEB-0822700 (CR, CB, JB, ME, MB, NSB, SP, TM, TB, TR, WD, WG); University of Michigan Ocean Engineering Laboratory (DG); field staff at the Erken Laboratory, particularly Björn Mattsson (EK); Marine Institute, Co. Mayo, Ireland (FE); Ontario Ministry of the Environment and Christopher McConnell (HP); German Ministry of Science and Education, in collaboration with the Israeli Ministry of Science and Technology (KN); NSF DEB-9306978, Lacawac Sanctuary Foundation (LC); NSF OCE 0235238 and DEB 0640953 (LW, WN); U.S.

Geological Survey (MA); Leibniz-Institut für Gewässerökologie und Binnenfischerei (MU); N.Z. Ministry for Science and Innovation Contract UOWX0505, and Bay of Plenty Regional Council (RT, WA); Lake Sunapee Protective Association (SN); Darren Bade, Kent State University (SY); Estonian Science Foundation grant 8729 (VJ); Academia Sinica (YYL). PAS was financed by the Danish Council for Independent Research, Natural Sciences grant 10-085238 (CA, GS, HS, VS) and the Danish Centre for Lake Restoration (CLEAR). We would also like to thank Luke Winslow, Chris McBride, John Ong, Vitaly Zlotnik, and Dominic Skinner for assisting in data collection and analysis, and two anonymous reviewers for suggestions and feedback that helped to improve this manuscript.

3.7 References

Amorocho, J., and J. J. Devries. 1980. A new evaluation of the wind stress coefficient over water surfaces. Journal of Geophysical Research-Oceans and Atmospheres **85:** 433-442, doi: 10.1029/JC085iC01p00433.

Bastviken, D., L. J. Tranvik, J. A. Downing, P. M. Crill, and A. Enrich-Prast. 2011. Freshwater Methane Emissions Offset the Continental Carbon Sink. Science **331:** 50, doi: 10.1126/science.1196808.

Cole, J. J., D. L. Bade, D. Bastviken, M. L. Pace, and M. Van De Bogert. 2010. Multiple approaches to estimating air-water gas exchange in small lakes. Limnol. Oceanogr. Meth. **8:** 285-293, doi: 10.4319/LOM.2010.8.285.

Cole, J. J., and N. F. Caraco. 1998. Atmospheric exchange of carbon dioxide in a low-wind oligotrophic lake measured by the addition of SF6. Limnology and Oceanography **43:** 647-656, doi: 10.4319/LO.1998.43.4.0647.

Cole, J. J., N. F. Caraco, G. W. Kling, and T. K. Kratz. 1994. Carbon-dioxide supersaturation in the surface waters of lakes. Science **265:** 1568-1570, doi: 10.1126/SCIENCE.265.5178.1568.

Cole, J. J., Y. T. Prairie, N. F. Caraco, W. H. Mcdowell, L. J. Tranvik, R. G. Striegl, C. M. Duarte, P. Kortelainen, J. A. Downing, J. J. Middelburg, and J. Melack. 2007. Plumbing

the global carbon cycle: Integrating inland waters into the terrestrial carbon budget. Ecosystems **10:** 171-184, doi: 10.1007/S10021-006-9013-8.

Crawford, T. M., and C. E. Duchon. 1999. An improved parameterization for estimating effective atmospheric emissivity for use in calculating daytime downwelling longwave radiation. J. Appl. Meteorol. **38:** 474-480.

Downing, J. A., Y. T. Prairie, J. J. Cole, C. M. Duarte, L. J. Tranvik, R. G. Striegl, W. H. Mcdowell, P. Kortelainen, N. F. Caraco, J. M. Melack, and J. J. Middelburg. 2006. The global abundance and size distribution of lakes, ponds, and impoundments. Limnology and Oceanography **51:** 2388-2397, doi: 10.4319/LO.2006.51.5.2388.

Eugster, W., G. Kling, T. Jonas, J. P. Mcfadden, A. Wuest, S. Macintyre, and F. S. Chapin. 2003. CO2 exchange between air and water in an Arctic Alaskan and midlatitude Swiss lake: Importance of convective mixing. Journal of Geophysical Research-Atmospheres **108**, doi: 10.1029/2002JD002653.

Fee, E. J., R. E. Hecky, S. E. M. Kasian, and D. R. Cruikshank. 1996. Effects of lake size, water clarity, and climatic variability on mixing depths in Canadian Shield lakes. Limnology and Oceanography **41:** 912-920.

Huotari, J., A. Ojala, E. Peltomaa, A. Nordbo, S. Launiainen, J. Pumpanen, T. Rasilo, P. Hari, and T. Vesala. 2011. Long-term direct CO_2 flux measurements over a boreal lake: Five years of eddy covariance data. Geophysical Research Letters **38:** L18401, doi: 10.1029/2011GL048753.

Imberger, J. 1985. The diurnal mixed layer. Limnology and Oceanography **30:** 737-770.

Jeffery, C. D., D. K. Woolf, I. S. Robinson, and C. J. Donlon. 2007. One-dimensional modelling of convective CO2 exchange in the Tropical Atlantic. Ocean Model. **19:** 161-182, doi: 10.1016/j.ocemod.2007.07.003.

Jonas, T., A. Stips, W. Eugster, and A. Wuest. 2003. Observations of a quasi shear-free lacustrine convective boundary layer: Stratification and its implications on turbulence. Journal of Geophysical Research-Oceans **108:** 3328, doi: 10.1029/2002JC001440.

Kim, J. W. 1976. Generalized bulk model of oceanic mixed layer. Journal of Physical Oceanography **6:** 686-695.

Kirk, J. T. O. 1994. Light and Photosynthesis in Aquatic Ecosystems, 2 ed. Cambridge University Press.

Lamont, J. C., and D. S. Scott. 1970. An eddy cell model of mass transfer into a surface of a turbulence liquid. Aiche Journal **16:** 513-519.

Lenters, J. D., T. K. Kratz, and C. J. Bowser. 2005. Effects of climate variability on lake evaporation: Results from a long-term energy budget study of Sparkling Lake, northern Wisconsin (USA). Journal of Hydrology **308:** 168-195, doi: 10.1016/j.jhydrol.2004.10.028.

Macintyre, S., A. Jonsson, M. Jansson, J. Aberg, D. E. Turney, and S. D. Miller. 2010. Buoyancy flux, turbulence, and the gas transfer coefficient in a stratified lake. Geophysical Research Letters **37:** L24604, doi: 10.1029/2010GL044164.

Macintyre, S., and M. Melack. 2009. Mixing dynamics in lakes across climatic zones, p. 603-612. *In* G. E. Likens [ed.], Encyclopedia of Inland Waters. Elsevier.

Markfort, C. D., A. L. S. Perez, J. W. Thill, D. A. Jaster, F. Porte-Agel, and H. G. Stefan. 2010. Wind sheltering of a lake by a tree canopy or bluff topography. Water Resources Research **46:** W03530, doi: 10.1029/2009WR007759.

Mcgillis, W. R., J. B. Edson, C. J. Zappa, J. D. Ware, S. P. Mckenna, E. A. Terray, J. E. Hare, C. W. Fairall, W. Drennan, M. Donelan, M. D. Degrandpre, R. Wanninkhof, and R. A. Feely. 2004. Air-sea CO2 exchange in the equatorial Pacific. Journal of Geophysical Research-Oceans **109:** C08s02, doi: 10.1029/2003JC002256.

Morris, D. P., H. Zagarese, C. E. Williamson, E. G. Balseiro, B. R. Hargreaves, B. Modenutti, R. Moeller, and C. Queimalinos. 1995. The attentuation of solar UV radiation in lakes and the role of dissolved organic carbon. Limnology and Oceanography **40:** 1381-1391.

Persson, I., and I. D. Jones. 2008. The effect of water colour on lake hydrodynamics: a modelling study. Freshwater Biology **53:** 2345-2355, doi: 10.1111/J.1365-2427.2008.02049.x.

Read, J. S., D. P. Hamilton, I. D. Jones, K. Muraoka, L. A. Winslow, R. Kroiss, C. H. Wu, and E. Gaiser. 2011. Derivation of lake mixing and stratification indices from high-resolution lake buoy data. Environmental Modelling & Software **26:** 1325-1336, doi: 10.1016/j.envsoft.2011.05.006.

Rutgersson, A., A. Smedman, and E. Sahlee. 2011. Oceanic convective mixing and the impact on air-sea gas transfer velocity. Geophysical Research Letters **38:** L02602, doi: 10.1029/2010GL045581.

Soloviev, A., M. Donelan, H. Graber, B. Haus, and P. Schlussel. 2007. An approach to estimation of near-surface turbulence and CO2 transfer velocity from remote sensing data. J Marine Syst **66:** 182-194, doi: 10.1016/j.jmarsys.2006.03.2007.

Staehr, P. A., D. Bade, M. C. Van De Bogert, G. R. Koch, C. Williamson, P. Hanson, J. J. Cole, and T. Kratz. 2010. Lake metabolism and the diel oxygen technique: State of the science. Limnol. Oceanogr. Meth. **8:** 628-644, doi: 10.4319/LOM.2010.8.628.

Tanentzap, A. J., N. D. Yan, B. Keller, R. Girard, J. Heneberry, J. M. Gunn, D. P. Hamilton, and P. A. Taylor. 2008. Cooling lakes while the world warms: Effects of forest regrowth and increased dissolved organic matter on the thermal regime of a temperate, urban lake. Limnology and Oceanography **53:** 404-410, doi: 10.4319/LO.2008.53.1.0404.

Vachon, D., Y. T. Prairie, and J. J. Cole. 2010. The relationship between near-surface turbulence and gas transfer velocity in freshwater systems and its implications for floating chamber measurements of gas exchange. Limnology and Oceanography **55:** 1723-1732, doi: DOI 10.4319/lo.2010.55.4.1723.

Verburg, P., and J. P. Antenucci. 2010. Persistent unstable atmospheric boundary layer enhances sensible and latent heat loss in a tropical great lake: Lake Tanganyika. Journal of Geophysical Research-Atmospheres **115:** D11109, doi: 10.1029/2009JD012839.

Wanninkhof, R. 1992. Relationship between wind-speed and gas-exchange over the ocean. Journal of Geophysical Research-Oceans **97:** 7373-7382.

Zappa, C. J., W. E. Asher, A. T. Jessup, J. Klinke, and S. R. Long. 2004. Microbreaking and the enhancement of air-water transfer velocity. Journal of Geophysical Research-Oceans **109:** C08S16, doi: 10.1029/2003JC001897.

Zappa, C. J., W. R. Mcgillis, P. A. Raymond, J. B. Edson, E. J. Hintsa, H. J. Zemmelink, J. W. H. Dacey, and D. T. Ho. 2007. Environmental turbulent mixing controls on air-water gas exchange in marine and aquatic systems. Geophysical Research Letters **34:** L10601, doi: 10.1029/2006GL028790.

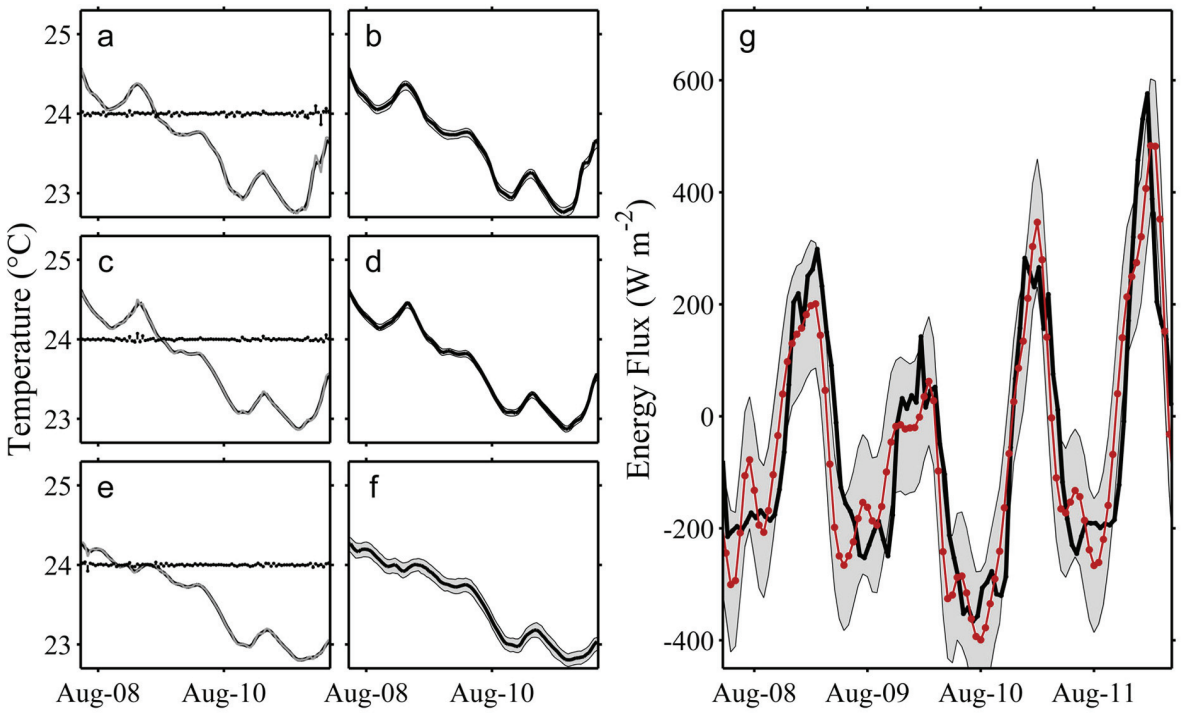

Figure 3.1: Error analysis for water temperature smoothing for three of the 20 thermistors in Sparkling Lake, WI (USA). Panel **a** shows the surface thermistor raw data (grey line) and residuals (black bars) of the wavelet de-noised signal (black line), while panel **b** shows the resulting bootstrapped 95% confidence intervals for the surface temperature after 1000 iterations. **c** and **d** are the same as **a** and **b**, but for the 1-m thermistor. **e** and **f** are for the 5-m thermistor. anel **g** shows the final estimate of Q_s calculated by the thermistor method (dotconnected red line) and 95% confidence intervals for this estimate (grey shading). The meteorological method for Q_s is shown for comparison (thick black line).

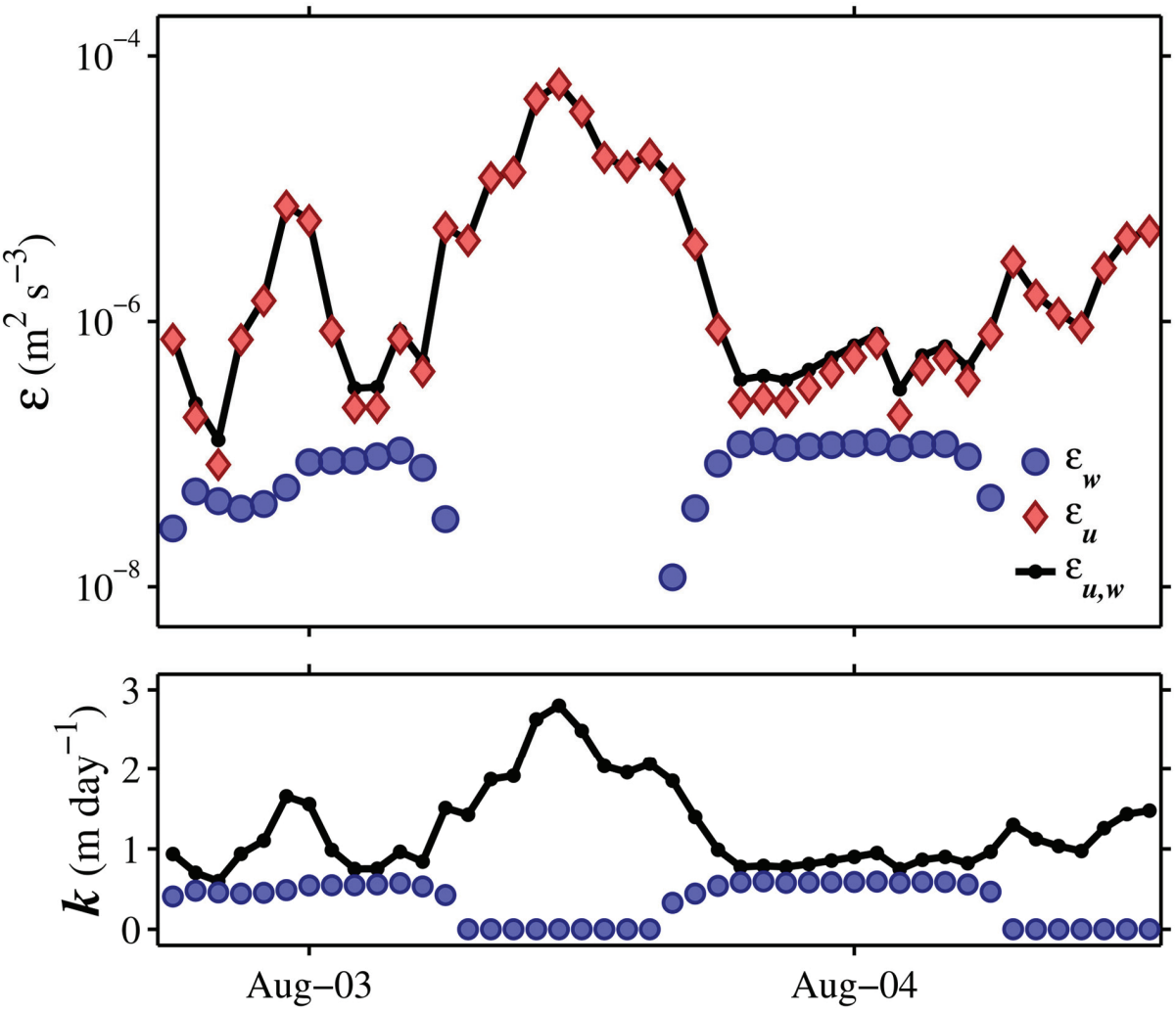

Figure 3.2: Calculation of ε and k during a relatively windy period (August 2-3) where hourly averaged winds exceeded 6 m s^{-1} during the daytime, and a relatively calm period (August 4) for Sparkling Lake, WI-USA (top panel). Turbulence from buoyancy flux (ε_w) and wind shear (ε_u) are used to estimate $\varepsilon_{u,w}$. k is scaled from $\varepsilon_{u,w}^{1/4}$ (black line) and k(w_*) from $\varepsilon_w^{1/4}$ (blue circles) according to the surface renewal model (bottom panel).

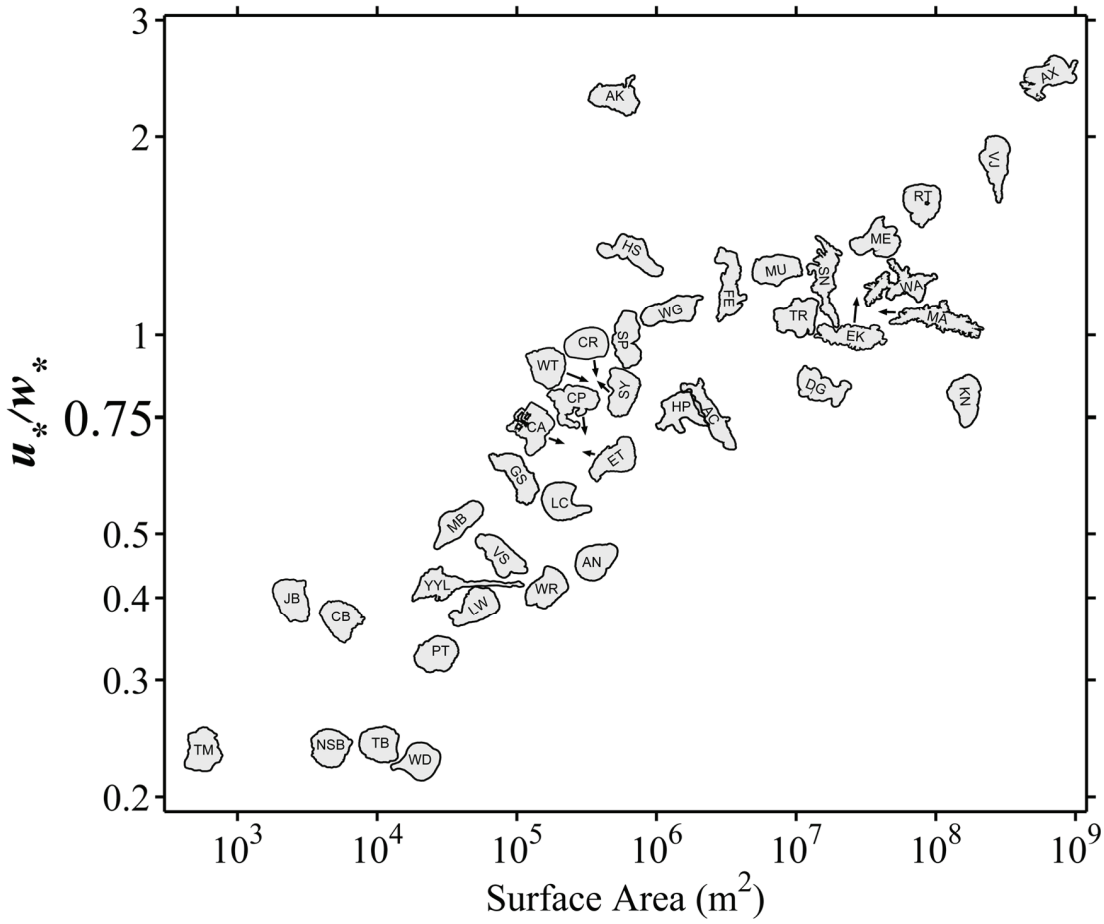

Figure 3.3: Ratio between the temporally-averaged velocity scales for wind shear (u_*) and convection (w_*), where averages were applied over the entire time series of observations for each lake. Lake shapes were used for plot symbols, and were shifted when overlapping (see tip of arrows).

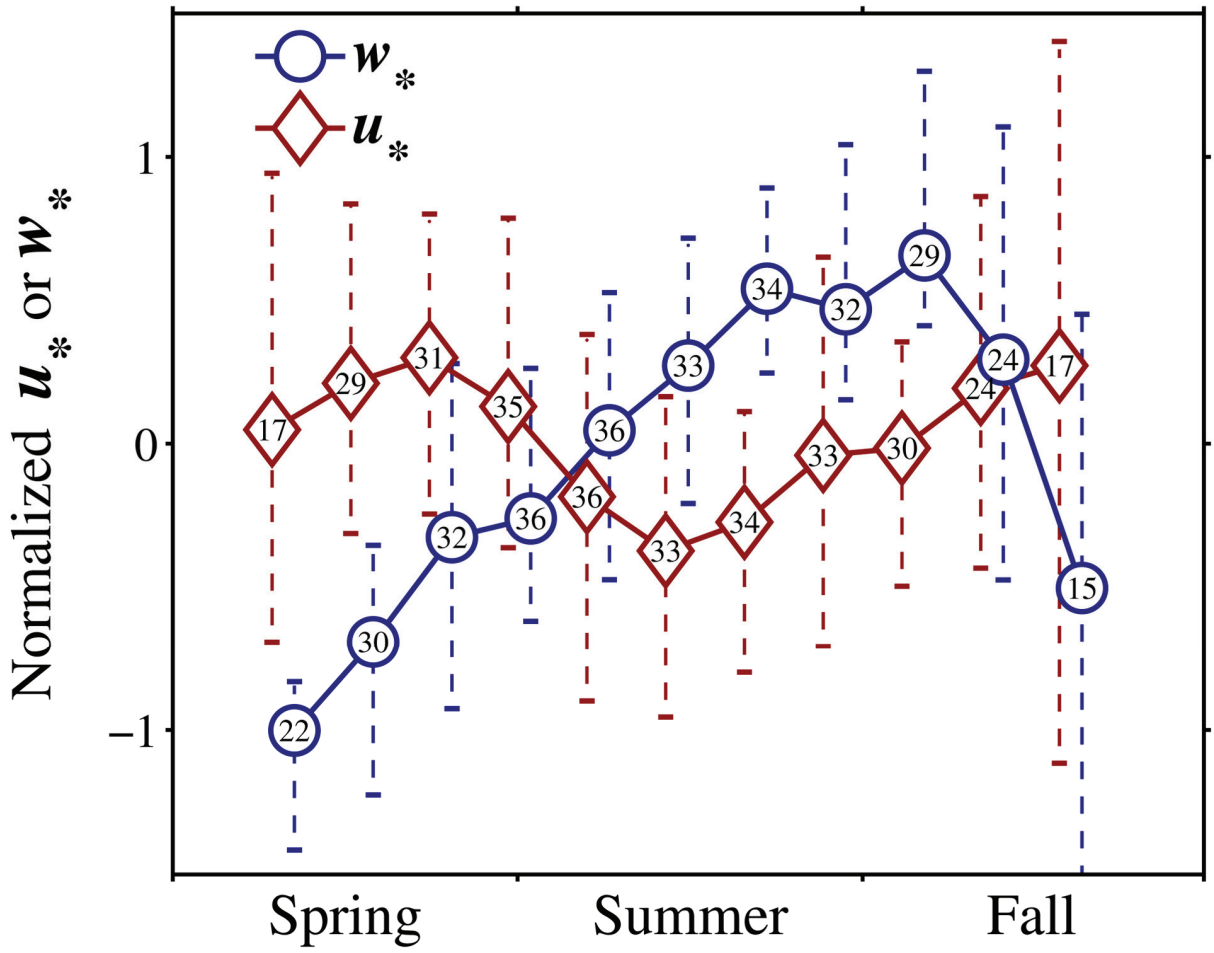

Figure 3.4: Average, normalized values of u_* and w_* across 40 lakes, plotted on 3-week intervals. u_* and w_* were offset by 4 days to improve figure clarity. Seasonal periods were based on day-of-year 81-173, 173-265, and 265-356 for Northern Hemisphere lakes, while Southern Hemisphere lakes were shifted by 182 days. Error bars represent the interquartile range (across lakes) of individually normalized values in each interval. The number of lakes used for each interval is displayed inside each marker.

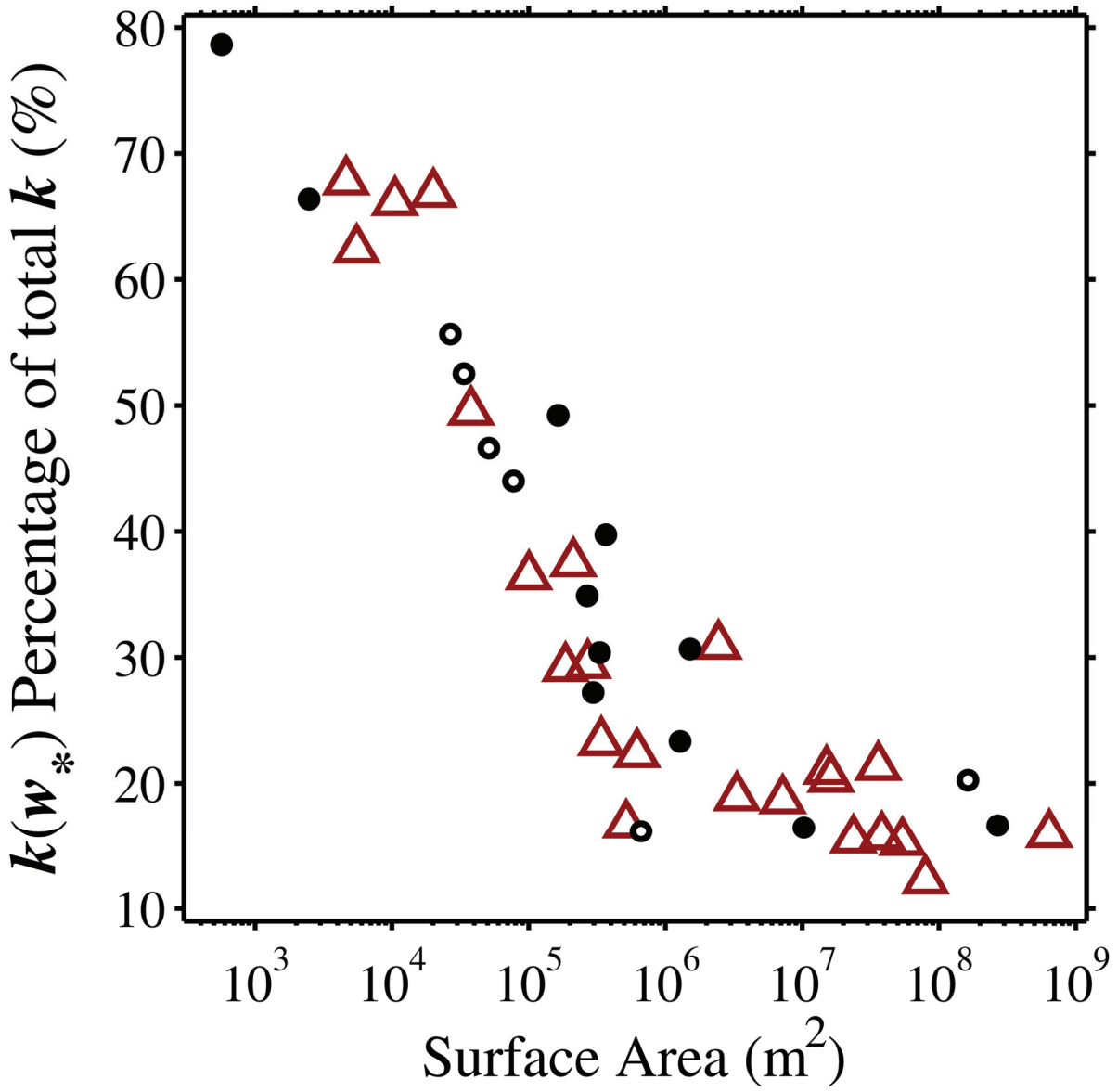

Figure 3.5: Temporally-averaged convective fraction (%) of total gas transfer velocity calculated using the surface renewal model for 40 lakes. Seasonal differences in $k(w_*)$% were tested for lakes with at least 21 days of observations for spring and summer periods (day-of-year 81-173; 173-265, respectively) using a Mann-Whitney U-test. Lakes without sufficient data are shown as black dots, lakes with no significant seasonal difference ($p > 0.01$) are shown as open black circles, and lakes where summer $k(w_*)$% was significantly higher than spring $k(w_*)$% are shown as red, upward-pointing triangles.

Table 3.1: Properties for the 40 temperate lakes included in this analysis.

Lake Name	K_d (m^{-1})	Latitude (°)	Longitude (°)	Surface area (m^2)	Max depth (m)	Days (day)	Symbol (-)
Acton	2.58	39.571	-84.747	2439366	9.1	166	AC
Alexandrina	6.05	-35.434	139.121	640339300	4.2	218	AX
Alkali	15	41.819	-102.602	515390	0.9	155	AK
Annie	0.84	27.208	-81.351	366048	19	86	AN
Castle	2.1	55.934	12.303	185466	9	226	CA
Crampton	0.87	46.21	-89.475	270675	18.7	86	CP
Crystal	0.38	46.002	-89.612	340000	20	142	CR
Crystal Bog	3.45	46.008	-89.606	5524	2.25	186	CB
Douglas	0.65	45.579	-84.699	15078900	24.4	68	DG
East Twin	1.53	41.195	-81.334	268207	12	110	ET
Erken	0.4	59.846	18.587	23674200	20.7	182	EK
Feeagh	0.74	53.943	-9.575	3327559	45	335	FE
Grib Sø	2.3	55.985	12.303	100285	12	226	GS
Hampen Sø	0.9	56.02	9.391	664549	13.1	229	HS
Harp	0.64	45.3796	-79.1356	1513724	19	128	HP
Jekl Bog	1.9	45.995	-89.678	2468	2.5	42	JB
Kinneret	0.5	32.817	35.588	163268000	46	263	KN
Lacawac	0.82	41.382	-75.293	211810	12	252	LC
Lawrence	0.53	42.441	-85.349	51000	12.3	206	LW
Maumelle	0.37	34.884	-92.575	35620000	13.5	107	MA
Mendota	0.82	43.105	-89.424	38282400	25	213	ME
Mouser Bog	2.44	45.998	-89.722	37833	4.3	58	MB
Muggelsee	4.06	52.438	13.649	7198749	8	272	MU
N Sparkling Bog	2.54	46.005	-89.705	4624	4.3	231	NSB
Peter	0.95	46.253	-89.504	26778	18	112	PT
Rotorua	0.63	-38.082	176.267	79855500	22	352	RT
Sandy	1.1	41.12	-81.297	329717	10	108	SY
S Trout	0.39	46.029	-89.672	14918400	34	171	TR
Sparkling	0.39	46.008	-89.7	618453	20	57	SP
Sunapee	0.39	43.391	-72.059	16248900	33	177	SN
Timber Bog	1.9	46.003	-89.431	566	2	46	TM
Trout Bog	2.75	46.041	-89.686	10478	8	199	TB
Vedsted Sø	0.8	55.192	9.363	77275	12	202	VS
Vortsjarv	2.52	58.306	26.035	270000000	6	56	VJ
Waikaremoana	0.13	-38.768	177.088	54000000	256	235	WA
Ward	1.54	46.255	-89.517	20107	8.3	122	WD

West Twin	1.99	41.198	-81.341	296099	12	110	WT
Wingra	3.2	43.053	-89.42	1281242	4.3	71	WG
Wintergreen	1.3	42.398	-85.383	164000	7.9	105	WN
Yuan Yang	2	24.577	121.402	33615	4.5	349	YYL

Table 3.2: Components of the iterative error analysis and assumed error for each variable when using the thermistor method to estimate Q_s.

Variable	Definition	Units	Value	Error (%)
K_d	Diffuse attenuation coefficient	m^{-1}	-	50
Area(z)	Hypsographic area at depth z	m^2	-	20
α_{sw}	Shortwave albedo	-	0.07	10
S_{rat}	Ratio of PAR to total shortwave	-	0.46	10
R_{sw}	Downwelling shortwave radiation	W m^{-2}	-	2
T(z)	Temperature at depth z	°C	-	bootstrap; 0.2 (°C)

Table 3.3: Temporally-averaged values for wind shear velocity (u_*), convective velocity (w_*), SML depth (z_{mix}), gas transfer velocity (k), and convective fraction of k.

Lake Name	u_* (mm s^{-1})	w_* (mm s^{-1})	z_{mix} (m)	k (m day^{-1})	$k(w_*)$ (%)
Acton	2.78	3.64[c]	2.79	1.09	30.9
Alexandrina	6.89	2.82	2.01	2.29	15.9
Alkali	6.52	2.81	0.83	2.02	16.7
Annie	2.03	4.49[c]	5.29	0.85	39.7
Castle	2.27[a]	3.33[c]	4.72	0.95	29.2
Crampton	2.75	4.07[c]	3.99	1.09	29.4
Crystal	3.52	4.07[c]	4.86	1.34	23.3
Crystal Bog	0.84[a]	2.3	0.97	0.52	62.4
Douglas	3.87	4.61[c]	8.89	1.43	21.0
East Twin	2.83	4.26	3.72	0.99	34.9
Erken	4.13	3.61[c]	10.02	1.51	15.5
Feeagh	3.81	3.19	14.16	1.31	18.9
Grib Sø	1.65[a]	2.75[c]	3.43	0.74	36.5
Hampen Sø	5.07	3.84	7.94	1.6	16.2
Harp	3.3	4.26	4.51	1.14	30.7
Jekl Bog	1.01[a]	2.56	0.9	0.54	66.4
Kinneret	5.93	7.53	15.95	1.7	20.3
Lacawac	1.83	3.25[c]	4.18	0.77	37.5
Lawrence	1.57[a]	4.03[c]	3.14	0.77	46.6
Maumelle	5.02	4.65	5.36	1.65	21.3
Mendota	7.36	5.15	9.85	2.24	15.8
Mouser Bog	1.39[a]	2.7	1.02	0.66	49.5
Muggelsee	4.22[b]	3.36[d]	4.36	1.52	18.7
N Sparkling Bog	0.55[a]	2.32	1.61	0.39	67.8
Peter	1.05[a]	3.19[c]	1.92	0.58	55.7
Rotorua	8.96	5.74	16.14	2.58	12.3
Sandy	3.15	3.73[c]	2.18	1.21	30.4
S Trout	6.17	5.80[c]	12.03	2.08	16.5
Sparkling	4.28	4.34	6.53	1.48	22.4
Sunapee	4.98	4.17	5.74	1.67	20.4
Timber Bog	0.61[a]	2.57	0.9	0.45	78.6
Trout Bog	0.64[a]	2.66	1.53	0.43	66.2
Vedsted Sø	1.43[a]	3.08[c]	3.56	0.69	44.0
Vortsjarv	4.09	2.34[c]	2.4	1.44	16.6
Waikaremoana	8.17	6.75	19.49	2.32	15.3
Ward	0.59[a]	2.6	1	0.45	66.8

West Twin	3.48	4.15[c]	3.07	1.31	27.2
Wingra	4.18	3.82[c]	2.3	1.54	23.4
Wintergreen	1.61[a]	3.84[c]	2.53	0.74	49.2
Yuan Yang	0.85[a]	2.01	1.42	0.46	52.5

[a]Sheltered scaling of u_* was used
[b]Neutral C_D used for u_*
[c]Q_s calculated using only meteorological methods
[d]Q_s calculated using only thermistor methods

Table 3.4: Spearman rank correlation coefficients (across lakes) between temporally-averaged turbulence parameters and lake properties.[a]

	w_*	u_*	$u_*^3+w_*^3$	u_*/w_*	$k(w_*)$%	$k(w_*,u_*)$
Surface Area	0.626^{++}	0.914^{++}	0.873^{++}	0.877^{++}	-0.917^{++}	0.918^{++}
Latitude	-0.382^{+}	-0.228	-0.307	0.071	0.047	-0.238

[a] ($p < 0.05$: $^{+}$; $p < 0.01$: $^{++}$)

Chapter 4 - Physical responses of small temperate lakes to variation in dissolved organic carbon concentrations

The following is currently in review at Limnology & Oceanography

Read JS, KC Rose. Physical responses of small temperate lakes to variation in dissolved organic carbon concentrations

4.1 Abstract

We used a mechanistic physical model to examine the impact of variability in dissolved organic carbon (DOC) concentrations on the physical properties of small temperate lakes. The model was validated on eight small (0.06-3.8 ha) lakes in Wisconsin and Michigan. Attenuation of photosynthetically active radiation (400-700 nm) in the water column was regulated by DOC concentrations, and was important in the vertical structuring of water temperatures. Epilimnetic depths were a function of attenuation, and the vertical partitioning of heat and nocturnal convection were the primary controls on the epilimnion depth. Heat exchange below the surface mixed layer was near the molecular rate, increasing the importance of water clarity as a control on the heat content of deeper waters. We applied scenarios of a 50% increase and 50% decrease to historical measurements of DOC concentrations for one lake (Trout Bog, Wisconsin), and found average seasonal water temperatures to vary in response, with the increased DOC scenario being > 2 °C colder than the reduced scenario. We modeled a range of DOC concentrations (2 mg L^{-1} to 30 mg L^{-1}), and found clearer (lower DOC) simulations to be more sensitive to climate variability, as the model showed that the range of inter-seasonal water temperatures was greater in decreased DOC simulations during the same simulation periods (1989-2010). Small lakes are globally important regulators of biogeochemical cycles and are structurally different from larger lakes. Important feedbacks to physical processes must be accounted for when understanding the effects of changing DOC and climate on small lakes.

4.2 Introduction

Small lakes (< 10 ha) are globally numerically dominant, especially in temperate latitudes (Downing et al. 2006). These lakes often possess physical (Read et al. 2012) and biogeochemical (Downing 2010) characteristics that differ from larger, more well-studied lakes. Small lakes have large perimeters (relative to their volumetric processing capacity), and consequently, are often more heavily subsidized with allochthonous inputs (Cole et al. 2011). Although these lakes make up a small fraction of surface waters (both in area and volume), they are hotspots for biogeochemical cycling (Cole et al. 2007; Downing 2010), and likely play a disproportionately large role in the global carbon cycle.

Physical and biogeochemical characteristics of lakes are changing in response to shifts in regional air temperatures (Destasio et al. 1996; Fang and Stefan 1999), hydrologic fluxes (Schindler et al. 1996), and anthropomorphically induced change at the watershed-scale (Carpenter et al. 2007; Tanentzap et al. 2008). Lakes can respond to these multiple forcings in complex ways (Tanentzap et al. 2008; Adrian et al. 2009). Lake size can influence physical responses to various drivers, for example, changes in air temperatures and wind speeds may be important for larger lakes (Robertson and Ragotzkie 1990; Desai et al. 2009), while small lakes might be more sensitive to variations in the hydrologic cycle (due to a smaller volumetric buffering capacity). Lake transparency may regulate the magnitude of these climate responses, as Snucins and Gunn (2000) hypothesized that clear lakes would be more sensitive to climate variability compared to less transparent lakes. Decreased precipitation often reduces terrestrial carbon loading to lakes, and many small lakes have exhibited enhanced drought responses through reductions in dissolved organic carbon (DOC) concentrations (e.g., Schindler et al. 1996; Dillon and Molot 1997).

DOC concentration is related to many important physical properties of small lakes (Fee et al. 1996; Houser 2006), and many investigators have highlighted long-term changes in lacustrine DOC loading (Zhang et al. 2010; Couture et al. 2012) and catchment export (Schindler et al. 1996; Striegl et al. 2005; Tanentzap et al. 2008). Climate and recovery from anthropogenic acidification are implicated as the two primary mechanisms driving these long-term changes (Monteith et al. 2007; Jennings et al. 2010). High DOC concentrations reduce transparency, which can alter the vertical structure of water temperature and lead to shallower surface mixed layers (Kling 1988; Fee et al. 1996; Persson and Jones 2008). In turn, water temperature and the depth of the mixed layer can significantly influence ecosystem-scale characteristics, such as the processing rates of carbon (Stets et al. 2010; Hanson et al. 2011).

Despite a wealth of studies that highlight the relationship between water transparency and the physical properties of lakes (such as epilimnetic depth and water temperature), a large majority of these studies are based solely on empirical observations, and few mechanistic studies have been performed (e.g., Caplanne and Laurion 2008; Persson and Jones 2008). Understanding the mechanisms behind physical change is critical to assessing climate impacts, feedbacks, and effects on lake ecosystems. With both increasing (e.g., Monteith et al. 2007) and decreasing (e.g., Striegl et al. 2005) DOC concentrations observed in regions around the world, it is important to determine the magnitude and direction of physical responses to changes in water transparency, and the modulation of these responses due to climate variability.

We focus here on modeling several physical responses of small temperate lakes to changing DOC concentrations because these lakes are numerically dominant and globally important (Downing et al. 2006; Downing 2010). Small lakes play a disproportionately large role in the global carbon budget (Cole et al. 2007; Tranvik et al. 2009), and physical processes are

often not well represented when knowledge from larger lakes is scaled down (Read et al. 2012). In this study, we mechanistically model the processes that regulate the vertical structure of water temperatures and identify controls on epilimnetic depth and the inter-annual variability of water temperatures in small lakes. We hypothesize that because small lakes are often convectively dominated (Read et al. 2012), mixed layer deepening is driven by heat loss, and vertical water temperatures are primarily a function of molecular diffusion of heat and the attenuation of light. Using a one-dimensional hydrodynamic model, we examine the influence of DOC on physical processes in small temperate lakes, and simulate two DOC concentration scenarios in the context of broadly observed long-term changes in DOC.

4.3 Methods

4.3.1 *Site description*

We included eight instrumented humic lakes in this analysis that were located in northern Wisconsin or in the Upper Peninsula of Michigan in the United States of America. Lakes ranged in size from 0.06 ha to 3.8 ha, with maximum depths varying from 2 m to 18 m (Table 4.1). These lakes were surrounded with a mixture of low-lying forest cover and catchments with minimal relief. All lakes had low wind speeds, with the highest median wind speed for any of the lakes < 1.3 m s^{-1} (Mouser Bog). While detailed hydrologic measurements exist only for a few lakes in this analysis, none of the lakes have measureable surface inflows or outflows. The hydrologic budgets for these lakes are dominated by precipitation, evaporation, and net groundwater losses. Crystal Bog and Trout Bog are long-term study lakes under the North Temperate Lakes Long-Term Ecological Research program (lter.limnology.wisc.edu), Peter Lake and Ward Lake have been extensively studied (e.g., Pace and Cole 2002) and are part of the University of Notre Dame Environmental Research Centre (UNDERC), and North Sparkling

Bog has been monitored since 2003 as part of the University of Wisconsin-Madison Microbial Observatory (Read et al. 2011). This effort, to the best of our knowledge, is the first detailed study of Jekl, Timber, and Mouser Bogs. Six of the eight study lakes (all non-UNDERC lakes) are site members of the Global Lake Ecological Observatory Network (GLEON; gleon.org), where these sensor data are openly accessible.

4.3.2 *Physical measurements*

Lakes were fitted with instrumented buoys for parts of multiple open-water seasons, but we focused on ice-free periods in 2009 and 2011 because these years had supporting optical and chemical surveys. Buoys were of two types: type 1 buoys had meteorological sensors for measuring wind speed, relative humidity, and air temperature, as well as thermistor strings in the water column; type 2 buoys had observations of only wind speed and water temperatures. Type 2 sites assumed air temperature and relative humidity was equal to measurements made on nearby lakes of similar type (for example, Peter Lake data was used on Ward Lake, which is approximately 1 km west of Peter). We used a single station (the Noble F. Lee Airport) for measurements of incoming solar and terrestrial radiation (Eppley PSP pyranometer; Eppley PIR radiometer) that was located at 45.93° N, -89.73° W. Estimates of the diffuse attenuation coefficient (K_d) of photosynthetically active radiation (PAR, 400-700 nm) were made with observations of the depth-decay of PAR using a profiling radiometer (Biospherical Instruments Inc. BIC). K_d was estimated according to the relationship

$$E_z = E_0 \exp(-K_d \cdot z) \qquad (4.1)$$

where E_z is PAR irradiance at a given depth (z), and E_0 is PAR irradiance at the surface. Diffuse attenuation coefficient estimates were made using PAR measurements taken between depths of 50% to 1% of E_0, or the depth of 50% of E_0 to the maximum measurement depth (in cases where the depth of 1% E_0 was greater than the depth of the lake). Occasionally, this depth range incorporated non-log-linearity in attenuation, which increased uncertainty in these estimates. Integrating over this depth range provided a more representative average whole water column K_d as opposed to augmented our fitting range to only include the log-linear portion of measurements.

During the summer of 2010, a self-contained automated microstructure profiler (SCAMP; Precision Measurement Engineering) was used to measure the fine-scale distribution of water temperatures in Trout Bog. We used the SCAMP in upward profiling mode (see MacIntyre et al. 1999), which sampled at 100 Hz and ascended at approximately 10 cm s^{-1}, yielding a vertical resolution near 1 mm.

4.3.3 *Lab methods*

Samples for DOC concentration and chlorophyll *a* were collected from eight lakes (including 3 of the instrumented lakes) in northern Wisconsin in October 2009 to understand what regulated variability in PAR K_d among lakes in this region, and to characterize the DOC:K_d ratio of small temperate bog lakes. DOC was measured with three replicate samples collected from within the surface mixed layer (1-3 m). We report the mean of the three replicates. Samples were collected, immediately filtered through 0.7 μm Watman GF/F filters, and stored in the cold and dark until analysis. DOC concentration was measured using a Shimadzu TOC-VCPH Total Organic Carbon Analyzer. DOC was measured in standard sensitivity mode, and we subtracted

Milli-Q deionized water blanks (c. 0.2 mg C L^{-1}) from standards and samples, and calibrated to dilutions of a certified DOC standard (Aqua Solutions, 50 mg L^{-1} potassium biphthalate).

Chlorophyll *a* concentrations were collected with two replicate samples from within the surface mixed layer (1-3 m). Water was filtered through pre-ashed 0.7 μm Watman GF/F filters and filters were folded, wrapped in foil, and frozen until analysis immediately upon returning from the field. Chlorophyll was extracted using an acetone-methanol mixture and the extract was clarified by centrifugation following the methods of Pechar (1987). Chlorophyll *a* concentrations were determined fluorometrically after correcting for the presence of phaeopgiments.

LTER measurements of DOC (lter.limnology.wisc.edu) were pooled over the depth range of 0-3 m measured during the ice-free period of Trout Bog for each year from 1989 to 2010. This depth range bounded the range used to estimate PAR K_ds in optical measurements in Trout Bog. Measurements of DOC were typically made monthly during the ice-free period, with varying depths and numbers of replicates for each depth. We used the total measurements for each ice-free season (that were in the specified depth range) to calculate the median annual DOC concentration.

We modeled the physical response of lakes to several DOC scenarios, including baseline (the measured DOC concentration), a 50% increase, and a 50% decrease in DOC concentration in Trout Bog. We assumed these changes in DOC altered water column transparency relative to our derived DOC specific attenuation coefficients.

4.3.4 *Water temperature model*

We used a one-dimensional physical water temperature model to simulate water temperatures and mixing dynamics in small sheltered lakes, where convective mixing is typically greater in magnitude than wind-driven mixing (Read et al. 2012). The model, referred to as the

convective lake model (CLM), uses a vertical distribution of mixed layers and iteratively calculates the changes in energy (and corresponding changes in temperature) of the layers for each time step. Surface energy fluxes, the attenuation of shortwave energy in the water column, as well as surface mixing dynamics like wind shear and convection are included in the model, but surface water flows, groundwater fluxes, and changes in lake levels are not. An earlier version of the model is described elsewhere (Read et al. 2011a), and differs from many common water temperature models (e.g., Honzo and Stefan 1993; Patterson and Imberger 1984) in that CLM was designed and calibrated for small (< 10 ha) temperate lakes. In brief, the model calculates the net surface energy flux (Q_0) as

$$Q_0 = R_{net} - E - H, \tag{4.2}$$

where R_{net} is the sum of surface radiation, E is the latent heat flux, and H is the sensible heat flux. R_{net} includes the sum of incoming longwave radiation (minus 3% that is reflected by the water surface), outgoing longwave radiation (parameterized according to the Stefan-Boltzman relationship for the water surface temperature radiating at 97.2% emissivity), and the portion of shortwave radiation that is not either reflected (7%) or allowed to penetrate into the water column (45% of the remaining shortwave energy). E and H were calculated according to the additive air-side renewal processes of both buoyancy flux and wind (Rasmussen et al. 1995), instead of parameterizing these fluxes based on bulk aerodynamic transfer coefficients. These surface energy fluxes are then summed and applied to the temperature of the near-surface layer. The remaining radiation is attenuated according to the simulation value of K_d, where the depth-loss of radiation in equation 4.1 (applying incremental steps to z for each vertical layer of the

model) is converted to thermal energy (i.e., a temperature increase) for each vertical layer. We parameterized K_d with a single bulk coefficient, approximated by PAR K_d, because previous studies have shown the wavelengths shorter than PAR (400-700 nm) contribute only a few percent to the thermal energy gain below the near-surface layer (Kirk 1994; Caplanne and Laurion 2008), and our radiometer measurements showed that in all modeled lakes over 99% of UV was attenuation within the upper 80 cm (data not shown). Water molecules strongly absorb wavelengths longer than 700 nm, rapidly attenuating these wavelengths in the near-surface layer (Kirk 1994). Next, the surface mixed layer (z_{mix}) is propagated downward relative to the strength of wind shear and convective heat loss versus the ambient stratification (Imberger 1985). This process mixes the available thermal energy between all layers above z_{mix}. Next, the model applies an eddy diffusion flux (K_z) of thermal energy at the division between all layers, incrementing or decrementing layer temperatures relative to the thermal gradient between neighbors (Fang and Stefan 1999). These processes are applied iteratively at each time step (in this order) for the duration of each simulation.

We used CLM to examine the roles of both K_z and K_d in the vertical structuring of water temperatures in the study lakes using two methods. First, we used two SCAMP temperature profiles from Trout Bog that were separated by 40 days in the summer of 2010 to partition heat gains (or losses) attributed to K_z compared to the temperature increases from the vertical attenuation of penetrating radiation (the role of K_d). We used an hourly time step of CLM, and iterated through values for K_z and K_d to minimize the sum of squared errors between modeled and observed heat gains in 10 cm intervals. Only measurements below the maximum nocturnal mixed layer depth were used for this optimization (a maximum of 1.6 m during the 40 days). Second, we used the entire buoy observation period for each of the eight lakes, and iterated

through realistic potential ranges of K_z and K_d to minimize the sum of squared errors between thermistor measurements and CLM hourly modeled temperatures at the same depths (excluding surface thermistors). For both of these methods, the CLM starting water temperatures were initialized with the first observed water column profile (SCAMP or buoy thermistor string) and linear interpolation was used when necessary for the initialization (when temperature observations were coarser than model layers).

4.3.5 *Modeling scenarios*

Trout Bog has a long-term record of physical, chemical, and biological observations which began in 1981. Meteorological measurements at the Noble F. Lee Airport were added to the NTL-LTER program in 1989 (see Lenters et al. 2005), providing a period of more than 20 years where routine measurements can be coupled with a physical model of Trout Bog. For all years from 1989 to 2010, we used NTL-LTER observations ice-on and ice-off dates, DOC concentrations, and meteorological driver data to simulate open-water temperatures for Trout Bog. After simulating and adjusting the model for size-specific parameters like the wind sheltering coefficient (Markfort et al. 2010), we randomized yearly DOC concentrations (holding the derived relationship between DOC and K_d constant), and randomly iterated through simulation years. This process was repeated for 1000 simulations, and we calculated the volumetric average water temperature for each simulation. We also used two DOC change scenarios, a 50% increase and 50% decrease in yearly DOC concentrations. These scenarios were applied to the randomized DOC choice of the "baseline" case, resulting in 3000 total simulations and corresponding estimates of average water temperatures.

4.3.6 *Statistical methods*

K_d was estimated by fitting depth-dependent measurements of PAR to an exponential decay curve (see equation 4.1). We used raw data for K_d fitting (instead of log-transforming irradiance observations and using a linear regression) because we wanted an accurate representation of uncertainty in K_d. For these exponential fits, we applied an algorithm that minimized nonlinear least squares for irradiance and depth data (MATLAB's fit.m function, mathworks.com). Both K_d and E_0 were treated as unknowns for this optimization routine. We also calculated 95% confidence intervals for the fit of K_d.

A stepwise linear regression analysis was used to test if DOC concentration and chlorophyll *a* concentration were significant predictors of PAR K_d in the eight lakes where these measurements were made. Based on the results from this analysis, we estimated DOC specific PAR attenuation coefficients by dividing PAR K_ds by DOC concentrations in the three bog lakes (Trout Bog, Crystal Bog, and North Sparkling Bog). DOC specific PAR attenuation coefficients assume that DOC is the only significant regulator of PAR K_d in these systems. This assumption allowed us to estimate the total PAR attenuation contribution of DOC independent of wavelength specific absorption coefficients or other potential attenuating substances.

Estimates for modeled K_z and K_d for each of the simulated lakes were obtained using a minimization routine to determine the "best fit" between simulations and observations. For simulations, CLM was initialized using the first observation of water temperatures, and simulations included the total duration between the first and last thermistor measurements for the calendar year. For some lakes, intermittent instrument errors caused a short-term loss of observations. To avoid artificially changing the error structure, we did not interpolate these missing periods. Instead, we only compared actual buoy observations to our model output when both existed. CLM simulated water temperatures at a finer resolution than thermistors, so we

extracted the model depths that matched the depths of in situ observations and calculated the total sum of squared errors for all matched depths (except the near-surface thermistor). Our minimization routine minimized this total error quantity across values for K_z and K_d. We calculated standard errors for each of these simulations following the same procedures as Rasmussen et al. (1995).

4.4 Results

Across the eight lakes sampled, variation in PAR *Kd* was a first order function of variation of DOC concentrations (Figure 4.1, $p < 0.01$, $R^2 = 0.95$). Holding the y-intercept at zero, the slope of the linear model predicting PAR *Kd* from DOC concentrations was 0.217 (± 0.04). Adding variation in chlorophyll *a* concentration to this model did not significantly improve model fit. Among the three bog lakes that were sampled, the average DOC specific PAR K_d was 0.232 m^{-1} mg^{-1} L (± 0.04). We used the relationship between attenuation and DOC concentration proposed by Morris et al. (1997) (0.22 m^{-1} mg^{-1} L; which is also the approximate mean of these two estimates) to estimate K_d per unit (mg L^{-1}) of DOC for scenario (+50% and -50%) and baseline concentrations of DOC.

We found heat transfer below the mixed layer to occur at a molecular, or near-molecular, rate (Figure 4.2). Changes in hypolimnetic temperatures were explained by including the effects of vertical diffusion of heat (best fit for K_z was 1.5e-7 m^2 s^{-1}) and the attenuation of penetrating radiation (best fit for K_d was 2.2 m^{-1}). CLM was fit to the buoy-based observation data by simulating water temperatures across a range of K_d and K_z values, and the best model performance for all eight lakes was achieved by limiting K_z to the molecular level of 1.4e-7 m^2 s^{-1} (Figure 4.2; Table 4.2). Minimizing the difference between modeled and observed data resulted in best-fit estimates of K_d that were within 10% of field estimates for 5 of the 8 lakes (Table 4.2).

Two notable exceptions were Crystal Bog and Ward Lake, where differences between modeled and observed K_d were approximately 50%. The other exception was North Sparkling Bog. Excluding Crystal Bog and Ward Lake, all modeled estimates K_d were slight underestimates of field K_d.

CLM performed well in the simulations of water temperature for the 8 lakes. 7 of the 8 lakes had a standard error (SE) between simulations and observations of less than 1 °C, and the worst fit was obtained on the largest, windiest lake (SE: 1.28 °C; Mouser Bog). Trout Bog had the lowest model error (0.37 °C), and the best agreement between field and model estimates of K_d (Figure 4.3; Table 4.2).

Because attenuation was strongly regulated by DOC in these systems (Figure 4.1), modeled increases and decreases in DOC concentrations had a substantial effect on the vertical distribution of water temperatures. Increased transparency (decrease in K_d) occurred in our scenario where DOC concentrations were reduced (as we assumed K_d to be a function of DOC), which resulted in a warmer hypolimnion compared to baseline and DOC increase scenarios. Volume-weighted average water temperatures were warmer for lower DOC scenarios (Figure 4.4), although near-surface temperatures generally increased with higher DOC concentrations (data not shown).

Darker lakes were generally colder (when compared to the clearer simulations) even though the simulations were driven by the same meteorological observations. Volumetrically colder lakes have less internal energy storage compared to a morphometrically-equal warmer lake (thermal energy is proportional to temperature). We used identical incoming radiative inputs for both increased and decreased DOC scenarios. As a result, the colder (darker) simulations had larger outward fluxes of energy in order to satisfy the conservation of energy between scenarios.

Our simulations revealed that the largest energy flux variant across the range of DOC concentrations was the outward flux of radiation from the water surface (data not shown). Colder, darker simulations, in general, had warmer surface temperatures compared to more transparent simulations. This higher surface temperature in high DOC scenarios increased the rate of outward radiation from the water surface, and these fluxes were more important to balancing the aforementioned water temperature energy deficit than variations in the sum of sensible and latent heat fluxes (data not shown).

4.5 Discussion

We found that the vertical exchange of heat below the mixed layer occurred at (or near) the rate of molecular diffusion in these lakes (Figure 4.1; Table 4.2), and that DOC concentrations (as the primary driver of K_d) strongly influenced water temperatures, outward heat fluxes, and mixed layer depths. Because diffusive heat transfer at the molecular rate is slow, water temperatures were highly sensitive to variability in attenuation. Many authors have found relationships between water color and the physical properties in lakes (such as stratification and thermocline depth) that weakened with increasing lake size (Gorham and Boyce 1989; Mazumder and Taylor 1994; Fee et al. 1996). We hypothesize that this finding is due to increased K_z on larger lakes (e.g., Macintyre et al. 1999), which could effectively mute the influence of variations in K_d. In contrast with large lakes, vertical water temperature profiles in the small lakes studied here resembled the exponential curves of decaying light (Figure 4.1), a pattern that was also observed by Fee et al. (1996) in many small Canadian Shield lakes. This finding highlights the importance of color in driving the thermal structure of small, sheltered lakes and suggests that the shape of the temperature versus depth relationship characterizes the relative importance of K_d versus K_z as regulators of thermal structure.

Actual and modeled K_d differed by less that 10% in most lakes, which highlights the success of this relatively simple hydrodynamic model. Variation between modeled K_d and actual K_d was expected, because our mechanistic model did not include all components that have influence on the thermal structure of lakes (e.g., groundwater fluxes). Modeled K_ds in Crystal Bog were greater than expected, perhaps because heat flux from the shallow water column into sediments that was not part of the model formulation, requiring an artificial amplification of K_d to improve the fit between modeled temperature and observations. This was not an issue in the other shallow bog (Timber Bog) likely due to a shorter simulation period that was biased towards the beginning of the season, when water and sediment temperatures would be similar (Table 4.1). The large difference between modeled and measured K_d in Ward Lake may be due to large seasonality in K_d that was not measured in situ. Ward Lake increased in DOC from 7 to 15 mg L^{-1} in 2010 during a period similar to the length of our deployment (R. Batt pers. comm.), and our only in situ measurement of K_d was taken several days before the buoy was deployed.

We modeled K_d purely as a function of DOC and used a DOC specific K_d of 0.22 m^{-1}. The colored or chromophoric portion of DOC is responsible for regulating attenuation in most systems (Morris et al. 1995; Rose et al. 2009b). Our use of 0.22 m^{-1} to characterize the unit specific DOC contribution to attenuation is similar to other estimates, but DOC specific attenuation may be region specific (Williamson et al. 1996). For example, Morris et al. (1995) identified a DOC specific contribution to PAR K_d of 0.22 m^{-1}, while another investigator used a coefficient of 0.24 m^{-1} (Perez-Fuentetaja et al. 1999). In the systems we studied here, we assumed that chlorophyll did not contribute to attenuation because our stepwise regression analysis showed that chlorophyll was not a significant predictor of PAR K_d. However, researchers have found that chlorophyll has an influence on PAR attenuation, and Morris et al.

(1995) found a chlorophyll *a* specific contribution of 0.07 m^{-1}. Reductions in DOC may stimulate greater primary production and chlorophyll, while increasing DOC may reduce chlorophyll through shading (Carpenter et al. 1998). If we had included a contribution from chlorophyll *a* for PAR K_d, our modeled changes in DOC would contribute slightly less to changes in K_d.

The depth of the mixed layer is important in structuring aquatic ecosystems, and lake transparency (and DOC concentration) has been linked to mixed layer depths for a variety of lakes (Kling 1988; Fee et al. 1996; Perez-Fuentetaja et al. 1999). Many investigators have proposed a simple mechanism for this finding, assuming that increased attenuation in darker waters creates a stronger density gradient which reduces wind-driven mixed layer deepening (e.g., Kling 1988). However, wind is not as important as convection in regulating mixed layer dynamics of very small lakes (Read et al. 2012). This distinction is important for small lakes, as scenarios of decreasing diel variability in air temperatures (which would likely result in less nocturnal heat loss) (Michaels and Stooksbury 1992) may lead to reduced mixed layer depths even during periods of increasing wind speeds (Mcinnes et al. 2011). Instead, the vertical partitioning of heat, and not the differential resistance to wind-driven mixing, is more likely to be responsible for the observed relationship between mixed layer depth and transparency. The effect of the vertical partitioning of heat on mixed layer depth can be observed in Trout Bog simulations (Figure 4.5). In the normal (18.7 mg L^{-1}) DOC scenario for 2008, heat loss created a (night time) convectively mixed layer that was 1.01 m deep. In contrast, the 50% DOC reduction scenario mixed down to 1.45 m during the same period while losing 7% less heat (compared to the normal case). Thus, despite losing 7% less energy from the lake, the mixing depth of the 50% DOC reduction simulation was 44% deeper compared to the normal case for this example. This difference is evident throughout the stratified period, as the temporally averaged 15 June to 15

August 2008 mixed layer depths (calculated at sunrise for comparison) were 0.85 m and 1.4 m for the normal (18.7 mg L^{-1}) DOC and 50% reduction scenarios, respectively. This mechanism is likely the mechanism responsible for the empirical relationship between transparency and epilimnetic depths for small, sheltered lakes (e.g., Fee et al. 1996).

We found that small sheltered lakes are sensitive to changes in DOC loading, and that water transparency influences water temperatures and mixed layer depths. It has been hypothesized that transparent lakes (e.g., alpine lakes) may be more sensitive indicators of climate than stained lakes because even small changes in energy, water chemistry, or precipitation may results in large changes in transparency, physical structure, and ecosystem linkages (Snucins and Gunn 2000; Rose et al. 2009a). We mechanistically tested this hypothesis by comparing the temperature variability of 22 open-water seasons in model lakes that were mophometrically identical to Trout Bog. By iterating through 15 DOC concentrations (2 to 30 mg L^{-1}) and simulating each model system for 22 seasons (1989-2010), our model results support the hypothesis that clearer lakes are more sensitive to climate variability (Figure 4.6a). Clearer simulations (i.e., 2 mg L^{-1}) had nearly a 3 °C temperature range between the warmest (volumetric and temporally averaged) and coldest simulation years. For greater concentrations of DOC, this temperature range was reduced by almost 50%. Climate variability in higher DOC (i.e., the 15 to 25 mg L^{-1} range, which would characterize Trout Bog) simulations during 1989-2010 lead to a similar magnitude in temperature variability compared to the transparency/temperature effect from the range of DOC concentrations observed in Trout Bog during the same time period (Figure 4.6b; Table 4.3). Darker lakes partition incoming solar radiation closer to the surface, leading to larger outward energy fluxes and colder waters compared to clearer lakes. Alternatively, clearer lakes integrate more of the climate signal into deeper waters, both through

less resistance to vertical mixing and via greater penetration of incoming solar radiation. These lakes are therefore likely to be more sensitive to variations in climate.

While the magnitude of DOC change modeled here was large (a 50% increase and a 50% decrease), it is within the range observed in many regions. For example, Striegl et al. (2005) observed a 40% reduction in DOC export in the Yukon between growing seasons 1978-1980 and 2001-2003, and Schindler et al. (1996) found decreases in catchment DOC export during periods of drought and decreased precipitation. Elsewhere, increases in DOC concentration have been reported. For example, Eimers et al.(2008) reported a 52-72% increase in DOC concentrations in small Canadian streams and Evans et al. (2006) documented a 91% average increase in DOC concentrations across the United Kingdom. Thus, the change in transparency, mixed layer depths, and volumetric temperatures modeled here are within the range that may be currently occurring in many regions.

Changes in DOC due to, for example, climatically induced reductions in catchment export of DOC may precipitate positive biological and photochemical feedbacks regulating DOC mineralization rates to rapidly alter DOC concentrations in small lakes. DOC mineralization rates increase with increasing temperatures, mixed layer depths, and residence times (Stets et al. 2010; Hanson et al. 2011). Thus, as DOC concentrations are increased, lakes decrease in volumetrically averaged temperature and stratify more shallowly, and this can depress biological mineralization rates to further increase DOC concentrations. The opposite feedback could be occurring in regions experiencing decreased DOC loading, where longer water residence times and more transparent water facilitates greater biological and photochemical mineralization, further reducing DOC concentrations.

Small lakes play a disproportionately large role in the global carbon budget (Cole et al. 2007; Tranvik et al. 2009), and these lakes may be more sensitive to changes in hydrologic fluxes compared to larger lakes. For small temperate lakes, we have shown that water temperatures and mixed layer depths are controlled by transparency, and clear lakes are more thermally sensitive to climate variability. Because small lakes are expected to respond faster to climate variability, future investigators should consider feedbacks between climate and DOC loading when predicting future lacustrine function in the global carbon budget.

4.6 Acknowledgements

JSR was supported by National Science Foundation grants DEB-0822700 and MCB-0702395. KCR was supported by the EARS (Environmental Aquatic Resource Sensing) IGERT (Integrative Graduate Education and Research Traineeship) program, NSF DGE-0903560, and a Smithsonian Institution postdoctoral fellowship. This research could not have been completed without the intellectual and logistical support of the C. Williamson lab of Miami, Ohio, and the support, discussion, and/or field work from K. McMahon, E. Stanley, L.Winslow, E. Kara, A. Shade, T. Meinke, K. Morrison, S. Yeo, and C. Watras. This manuscript was improved by incorporating valuable feedback received at the Global Lakes Ecological Observatory (GLEON; gleon.org) G11 meeting, where travel costs for the meeting were covered by the Gordon and Betty Moore Foundation (award 1182). Buoys on Crystal Bog, North Sparkling Bog, and Trout Bog were funded by NSF grant DEB-0822700. The buoy on Mouser Bog was funded by NSF grant MCB-0702395. Buoys on Timber and Jekl bogs were supplied by the EARS IGERT program. We thank PIs J. Cole and S. Carpenter from the Tropic Cascade Project for providing buoy data from Peter and Ward lakes, and PI M. Pace and student R. Batt for thoughtful

discussion on this topic. C. Williamson helped improve an earlier version of this manuscript with thoughtful comments.

4.7 References

Adrian, R., C. M. O'reilly, H. Zagarese, S. B. Baines, D. O. Hessen, W. Keller, D. M. Livingstone, R. Sommaruga, D. Straile, E. Van Donk, G. A. Weyhenmeyer, and M. Winder. 2009. Lakes as sentinels of climate change. Limnology and Oceanography **54:** 2283-2297.

Caplanne, S., and I. Laurion. 2008. Effect of chromophoric dissolved organic matter on epilimnetic stratification in lakes. Aquatic Sciences **70:** 123-133, doi: 10.1007/s00027-007-7006-0.

Carpenter, S. R., B. J. Benson, R. Biggs, J. W. Chipman, J. A. Foley, S. A. Golding, R. B. Hammer, P. C. Hanson, P. T. J. Johnson, A. M. Kamarainen, T. K. Kratz, R. C. Lathrop, K. D. Mcmahon, B. Provencher, J. A. Rusak, C. T. Solomon, E. H. Stanley, M. G. Turner, M. J. Vander Zanden, C. H. Wu, and H. L. Yuan. 2007. Understanding regional change: A comparison of two lake districts. Bioscience **57:** 323-335, doi: 10.1641/b570407.

Carpenter, S. R., J. J. Cole, J. F. Kitchell, and M. L. Pace. 1998. Impact of dissolved organic carbon, phosphorus, and grazing on phytoplankton biomass and production in experimental lakes. Limnology and Oceanography **43:** 73-80.

Cole, J. J., S. R. Carpenter, J. Kitchell, M. L. Pace, C. T. Solomon, and B. Weidel. 2011. Strong evidence for terrestrial support of zooplankton in small lakes based on stable isotopes of carbon, nitrogen, and hydrogen. Proc. Natl. Acad. Sci. U. S. A. **108:** 1975-1980, doi: 10.1073/pnas.1012807108.

Cole, J. J., Y. T. Prairie, N. F. Caraco, W. H. Mcdowell, L. J. Tranvik, R. G. Striegl, C. M. Duarte, P. Kortelainen, J. A. Downing, J. J. Middelburg, and J. Melack. 2007. Plumbing the global carbon cycle: Integrating inland waters into the terrestrial carbon budget. Ecosystems **10:** 171-184, doi: 10.1007/S10021-006-9013-8.

Couture, S., D. Houle, and C. Gagnon. 2012. Increases of dissolved organic carbon in temperate and boreal lakes in Quebec, Canada. Environ. Sci. Pollut. Res. **19:** 361-371, doi: 10.1007/s11356-011-0565-6.

Desai, A. R., J. A. Austin, V. Bennington, and G. A. Mckinley. 2009. Stronger winds over a large lake in response to weakening air-to-lake temperature gradient. Nature Geoscience **2:** 855-858, doi: 10.1038/ngeo693.

Destasio, B. T., D. K. Hill, J. M. Kleinhans, N. P. Nibbelink, and J. J. Magnuson. 1996. Potential effects of global climate change on small north-temperate lakes: Physics, fish, and plankton. Limnology and Oceanography **41:** 1136-1149.

Dillon, P. J., and L. A. Molot. 1997. Effect of landscape form on export of dissolved organic carbon, iron, and phosphorus from forested stream catchments. Water Resources Research **33:** 2591-2600, doi: 10.1029/97wr01921.

Downing, J. A. 2010. Emerging global role of small lakes and ponds: little things mean a lot. Limnetica **29:** 9-23.

Downing, J. A., Y. T. Prairie, J. J. Cole, C. M. Duarte, L. J. Tranvik, R. G. Striegl, W. H. Mcdowell, P. Kortelainen, N. F. Caraco, J. M. Melack, and J. J. Middelburg. 2006. The global abundance and size distribution of lakes, ponds, and impoundments. Limnology and Oceanography **51:** 2388-2397, doi: 10.4319/LO.2006.51.5.2388.

Eimers, M. C., S. A. Watmough, and J. M. Buttle. 2008. Long-term trends in dissolved organic carbon concentration: a cautionary note. Biogeochemistry **87:** 71-81, doi: 10.1007/s10533-007-9168-1.

Evans, C. D., P. J. Chapman, J. M. Clark, D. T. Monteith, and M. S. Cresser. 2006. Alternative explanations for rising dissolved organic carbon export from organic soils. Global Change Biology **12:** 2044-2053, doi: 10.1111/j.1365-2486.2006.01241.x.

Fang, X., and H. G. Stefan. 1999. Projections of climate change effects on water temperature characteristics of small lakes in the contiguous US. Climatic Change **42:** 377-412, doi: 10.1023/a:1005431523281.

Fee, E. J., R. E. Hecky, S. E. M. Kasian, and D. R. Cruikshank. 1996. Effects of lake size, water clarity, and climatic variability on mixing depths in Canadian Shield lakes. Limnology and Oceanography **41:** 912-920.

Gorham, E., and F. M. Boyce. 1989. Influence of lake surface-area and depth upon thermal stratification and the depth of the summer thermocline. Journal of Great Lakes Research **15:** 233-245.

Hanson, P. C., D. P. Hamilton, E. H. Stanley, N. Preston, O. C. Langman, and E. L. Kara. 2011. Fate of Allochthonous Dissolved Organic Carbon in Lakes: A Quantitative Approach. Plos One **6**, doi: e21884
10.1371/journal.pone.0021884.

Houser, J. N. 2006. Water color affects the stratification, surface temperature, heat content, and mean epilimnetic irradiance of small lakes. Canadian Journal of Fisheries and Aquatic Sciences **63:** 2447-2455, doi: 10.1139/f06-131.

Imberger, J. 1985. The diurnal mixed layer. Limnology and Oceanography **30:** 737-770.

Jennings, E., M. Jarvinen, N. Allott, L. Arvola, K. Moore, P. Naden, C. Nic Aongusa, T. Noges, and G. A. Weyhenmeyer. 2010. Impacts of climate on the flux of dissolved organic carbon from catchments, p. 199-220. *In* D. G. George [ed.], The Impact of Climate Change on European Lakes. Springer.

Kirk, J. T. O. 1994. Light and Photosynthesis in Aquatic Ecosystems, 2 ed. Cambridge University Press.

Kling, G. W. 1988. Comparative transparency, depth of mixing, and stability of stratification in lakes of Cameroon, West-Africa. Limnology and Oceanography **33:** 27-40.

Lenters, J. D., T. K. Kratz, and C. J. Bowser. 2005. Effects of climate variability on lake evaporation: Results from a long-term energy budget study of Sparkling Lake, northern Wisconsin (USA). Journal of Hydrology **308:** 168-195, doi: 10.1016/j.jhydrol.2004.10.028.

Macintyre, S., K. M. Flynn, R. Jellison, and J. R. Romero. 1999. Boundary mixing and nutrient fluxes in Mono Lake, California. Limnology and Oceanography **44:** 512-529, doi: 10.4319/LO.1999.44.3.0512.

Markfort, C. D., A. L. S. Perez, J. W. Thill, D. A. Jaster, F. Porte-Agel, and H. G. Stefan. 2010. Wind sheltering of a lake by a tree canopy or bluff topography. Water Resources Research **46:** W03530, doi: 10.1029/2009WR007759.

Mazumder, A., and W. D. Taylor. 1994. Thermal structure of lakes varying in size and water clarity. Limnology and Oceanography **39:** 968-976.

Mcinnes, K. L., T. A. Erwin, and J. M. Bathols. 2011. Global Climate Model projected changes in 10 m wind speed and direction due to anthropogenic climate change. Atmos. Sci. Lett. **12:** 325-333, doi: 10.1002/asl.341.

Michaels, P. J., and D. E. Stooksbury. 1992. GLOBAL WARMING - A REDUCED THREAT. Bull. Amer. Meteorol. Soc. **73:** 1563-1577, doi: 10.1175/1520-0477(1992)073<1563:gwart>2.0.co;2.

Monteith, D. T., J. L. Stoddard, C. D. Evans, H. A. De Wit, M. Forsius, T. Hogasen, A. Wilander, B. L. Skjelkvale, D. S. Jeffries, J. Vuorenmaa, B. Keller, J. Kopacek, and J. Vesely. 2007. Dissolved organic carbon trends resulting from changes in atmospheric deposition chemistry. Nature **450:** 537-U539, doi: 10.1038/nature06316.

Morris, D. P., and B. R. Hargreaves. 1997. The role of photochemical degradation of dissolved organic carbon in regulating the UV transparency of three lakes on the Pocono Plateau. Limnology and Oceanography **42:** 239-249.

Morris, D. P., H. Zagarese, C. E. Williamson, E. G. Balseiro, B. R. Hargreaves, B. Modenutti, R. Moeller, and C. Queimalinos. 1995. The attentuation of solar UV radiation in lakes and the role of dissolved organic carbon. Limnology and Oceanography **40:** 1381-1391.

Perez-Fuentetaja, A., P. J. Dillon, N. D. Yan, and D. J. Mcqueen. 1999. Significance of dissolved organic carbon in the prediction of thermocline depth in small Canadian shield lakes. Aquatic Ecology **33:** 127-133.

Persson, I., and I. D. Jones. 2008. The effect of water colour on lake hydrodynamics: a modelling study. Freshwater Biology **53:** 2345-2355, doi: 10.1111/J.1365-2427.2008.02049.x.

Rasmussen, A. H., M. Hondzo, and H. G. Stefan. 1995. A test of several evaporation equations for water temperature simulations in lakes. Water Resources Bulletin **31:** 1023-1028.

Read, J. S., D. P. Hamilton, A. R. Desai, K. C. Rose, S. Macintyre, J. D. Lenters, R. L. Smyth, P. C. Hanson, J. J. Cole, P. A. Staehr, J. A. Rusak, D. C. Pierson, J. D. Brookes, A. Laas, and C. H. Wu. 2012. Lake-size dependency of wind shear and convection as controls on gas exchange. Geophysical Research Letters, doi: 10.1029/2012GL051886.

Read, J. S., A. Shade, C. H. Wu, A. Gorzalski, and K. D. Mcmahon. 2011. "Gradual Entrainment Lake Inverter" (GELI): A novel device for experimental lake mixing. Limnol. Oceanogr. Meth. **9:** 14-28, doi: 10.4319/lom.2011.9.14.

Robertson, D. M., and R. A. Ragotzkie. 1990. Changes in the thermal structure of moderate to large sized lakes in response to changes in air-temperature. Aquatic Sciences **52:** 360-380.

Rose, K. C., C. E. Williamson, J. E. Saros, R. Sommaruga, and J. M. Fischer. 2009a. Differences in UV transparency and thermal structure between alpine and subalpine lakes: implications for organisms. Photochemical & Photobiological Sciences **8:** 1244-1256, doi: 10.1039/b905616e.

Rose, K. C., C. E. Williamson, S. G. Schladow, M. Winder, and J. T. Oris. 2009b. Patterns of spatial and temporal variability of UV transparency in Lake Tahoe, California-Nevada. J. Geophys. Res.-Biogeosci. **114:** 9, doi: G00d03
10.1029/2008jg000816.

Schindler, D. W., S. E. Bayley, B. R. Parker, K. G. Beaty, D. R. Cruikshank, E. J. Fee, E. U. Schindler, and M. P. Stainton. 1996. The effects of climatic warming on the properties of boreal lakes and streams at the Experimental Lakes Area, northwestern Ontario. Limnology and Oceanography **41:** 1004-1017.

Snucins, E., and J. Gunn. 2000. Interannual variation in the thermal structure of clear and colored lakes. Limnology and Oceanography **45:** 1639-1646.

Stets, E. G., R. G. Striegl, and G. R. Aiken. 2010. Dissolved organic carbon export and internal cycling in small, headwater lakes. Glob. Biogeochem. Cycle **24**, doi: Gb4008
10.1029/2010gb003815.

Striegl, R. G., G. R. Aiken, M. M. Dornblaser, P. A. Raymond, and K. P. Wickland. 2005. A decrease in discharge-normalized DOC export by the Yukon River during summer through autumn. Geophysical Research Letters **32**, doi: L21413
10.1029/2005gl024413.

Tanentzap, A. J., N. D. Yan, B. Keller, R. Girard, J. Heneberry, J. M. Gunn, D. P. Hamilton, and P. A. Taylor. 2008. Cooling lakes while the world warms: Effects of forest regrowth and increased dissolved organic matter on the thermal regime of a temperate, urban lake. Limnology and Oceanography **53:** 404-410, doi: 10.4319/LO.2008.53.1.0404.

Tranvik, L. J., J. A. Downing, J. B. Cotner, S. A. Loiselle, R. G. Striegl, T. J. Ballatore, P. Dillon, K. Finlay, K. Fortino, L. B. Knoll, P. L. Kortelainen, T. Kutser, S. Larsen, I. Laurion, D. M. Leech, S. L. Mccallister, D. M. Mcknight, J. M. Melack, E. Overholt, J. A. Porter, Y. Prairie, W. H. Renwick, F. Roland, B. S. Sherman, D. W. Schindler, S. Sobek, A. Tremblay, M. J. Vanni, A. M. Verschoor, E. Von Wachenfeldt, and G. A.

Weyhenmeyer. 2009. Lakes and reservoirs as regulators of carbon cycling and climate. Limnology and Oceanography **54:** 2298-2314.

Williamson, C. E., R. S. Stemberger, D. P. Morris, T. M. Frost, and S. G. Paulsen. 1996. Ultraviolet radiation in North American lakes: Attenuation estimates from DOC measurements and implications for plankton communities. Limnology and Oceanography **41:** 1024-1034.

Zhang, J., J. Hudson, R. Neal, J. Sereda, T. Clair, M. Turner, D. Jeffries, P. Dillon, L. Molot, K. Somers, and R. Hesslein. 2010. Long-term patterns of dissolved organic carbon in lakes across eastern Canada: Evidence of a pronounced climate effect. Limnology and Oceanography **55:** 30-42, doi: 10.4319/lo.2010.55.1.0030.

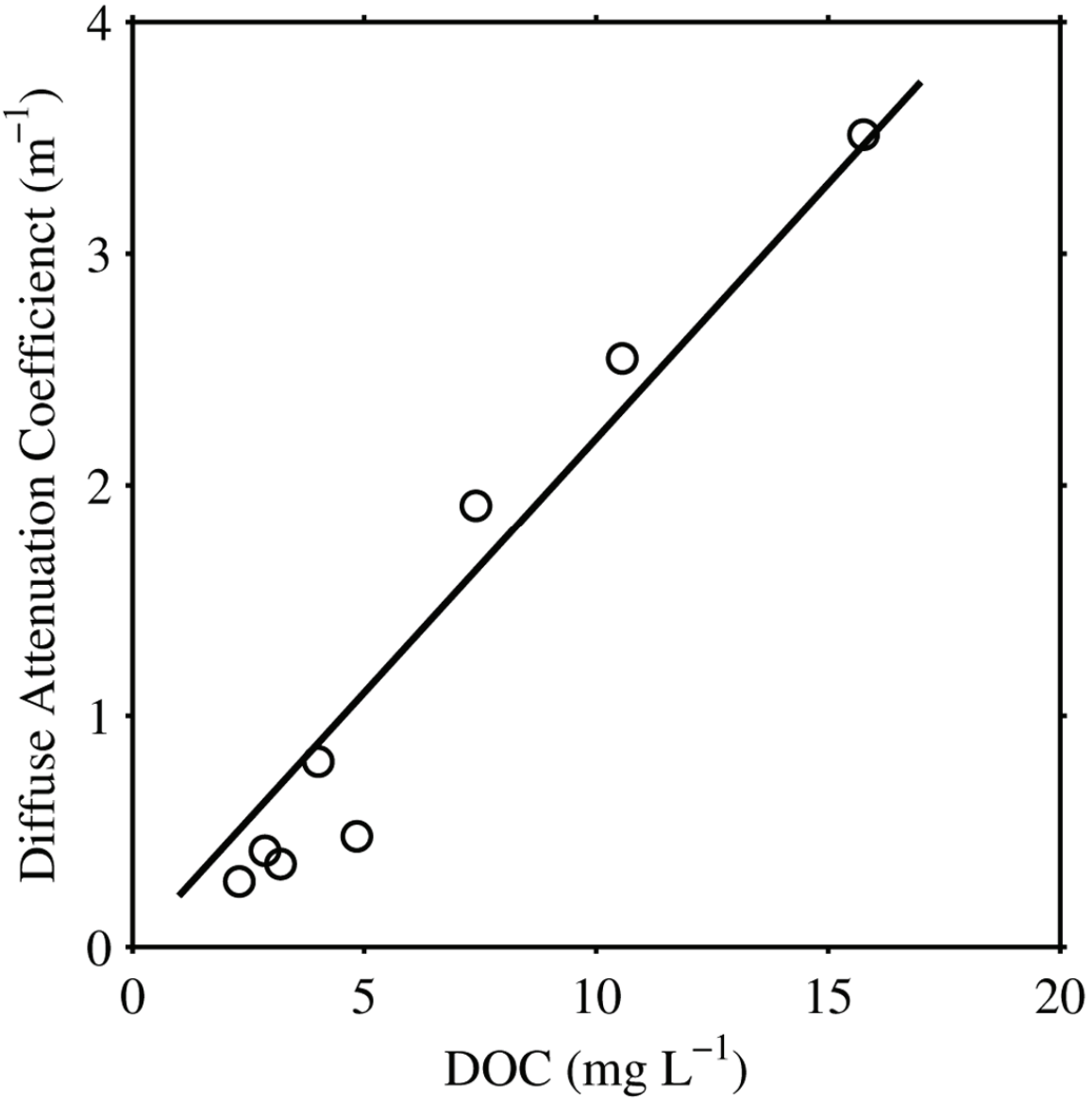

Figure 4.1: Relationship between the diffuse attenuation coefficient (K_d) and DOC for 7 NTL-LTER lakes and North Sparkling Bog from a 2009 survey. Line is DOC·0.22, the relationship used in this study.

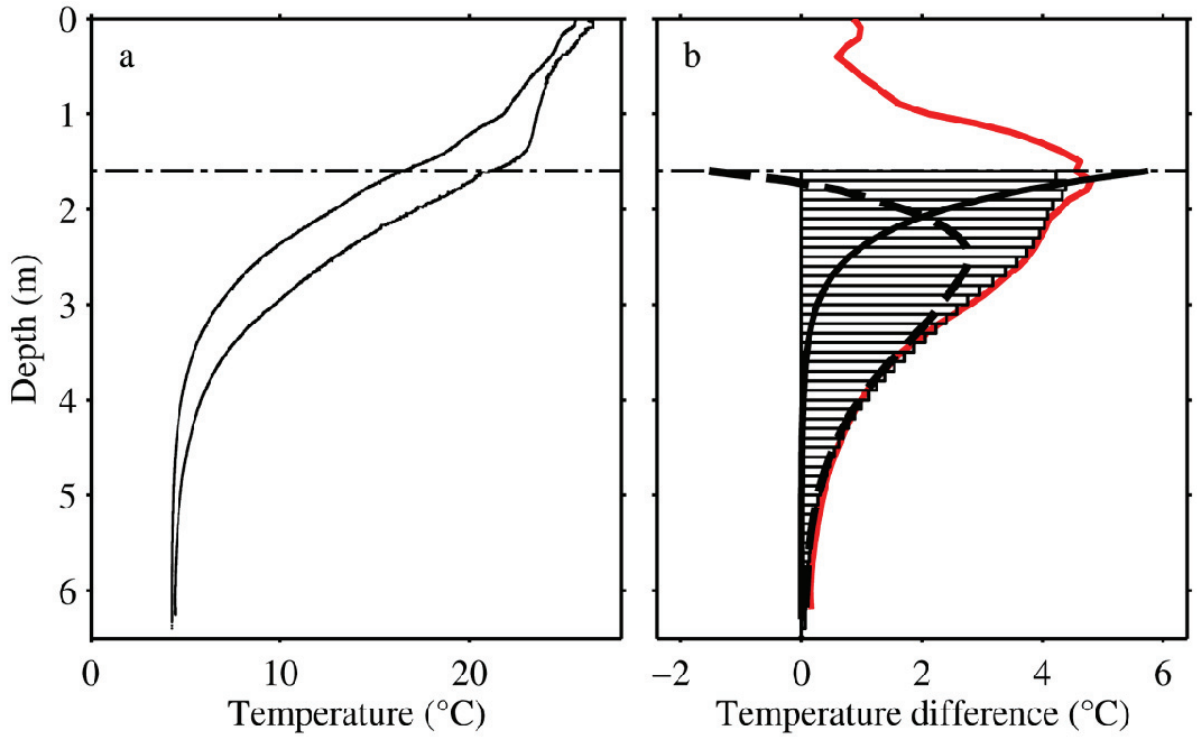

Figure 4.2: a) Temperature profiles on Trout Bog separated by 40 days. **b**) Temperature gains are shown as averages for 10 cm intervals (red line). Modeled temperature gains for depths below the remnant mixed layer depth are shown as 10 cm bins, which combine the additive effects of temperature gains and losses from the vertical diffusion of heat (dashed black line) and the attenuation of penetrating radiation (thick black line).

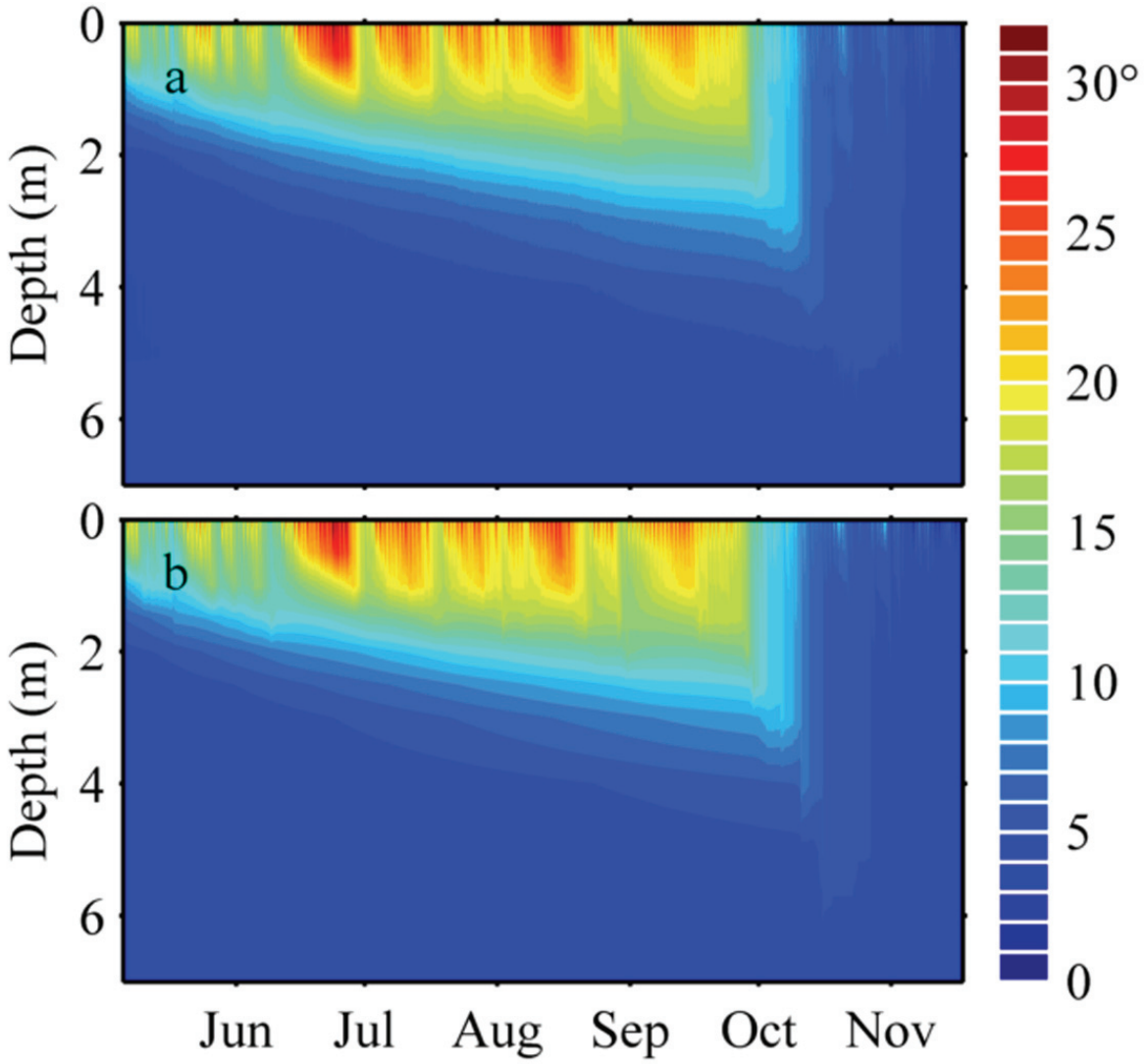

Figure 4.3: Observed **a**) and modeled **b**) temperatures for Trout Bog during 2009. Contour intervals represent one °C.

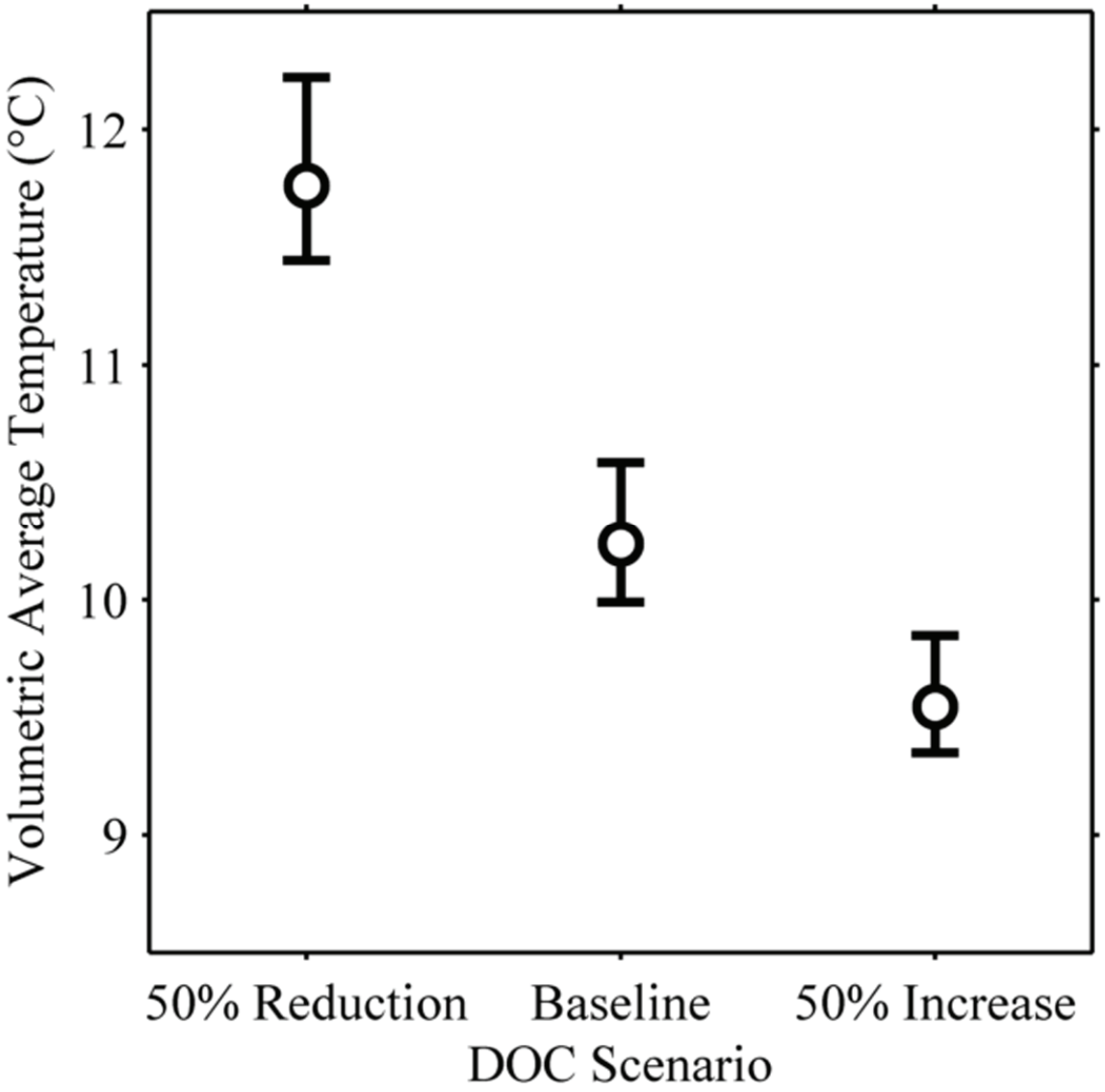

Figure 4.4: Volumetric average water temperatures for 22 simulation years and 3 DOC scenarios for Trout Bog. 1000 iterations were used where DOC concentrations were randomly chosen (with replacement) from the 22 years on record, and the simulation years were also chosen the same manner (see Table 4.3). Medians are represented by open circles, and error bars represent the interquartile range for all iterations.

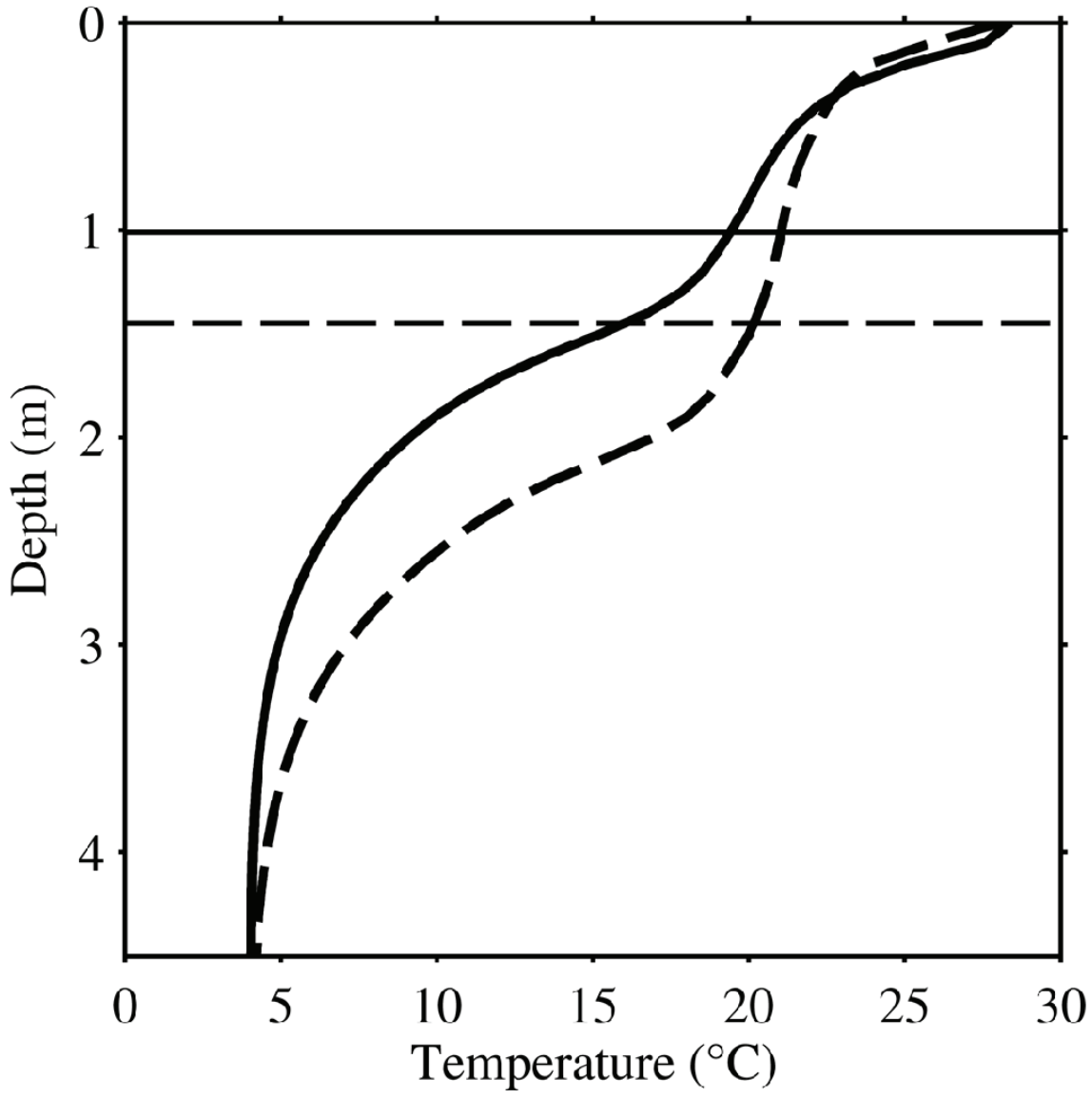

Figure 4.5: Effects of transparency on mixed layer depth. Trout Bog simulated water temperature for 1 July 2008 13:00 using normal DOC concentrations (18.7 mg L^{-1}; black line) and a 50% DOC reduction scenario (dashed black line). Heat loss during the subsequent 15 hours in each simulation eliminated near-surface microstratification, resulting in isothermal nocturnal mixed layer depths of 1.01 m and 1.45 m, respectively (black line; dashed black line). Meteorological drivers and starting conditions for the two simulations were identical.

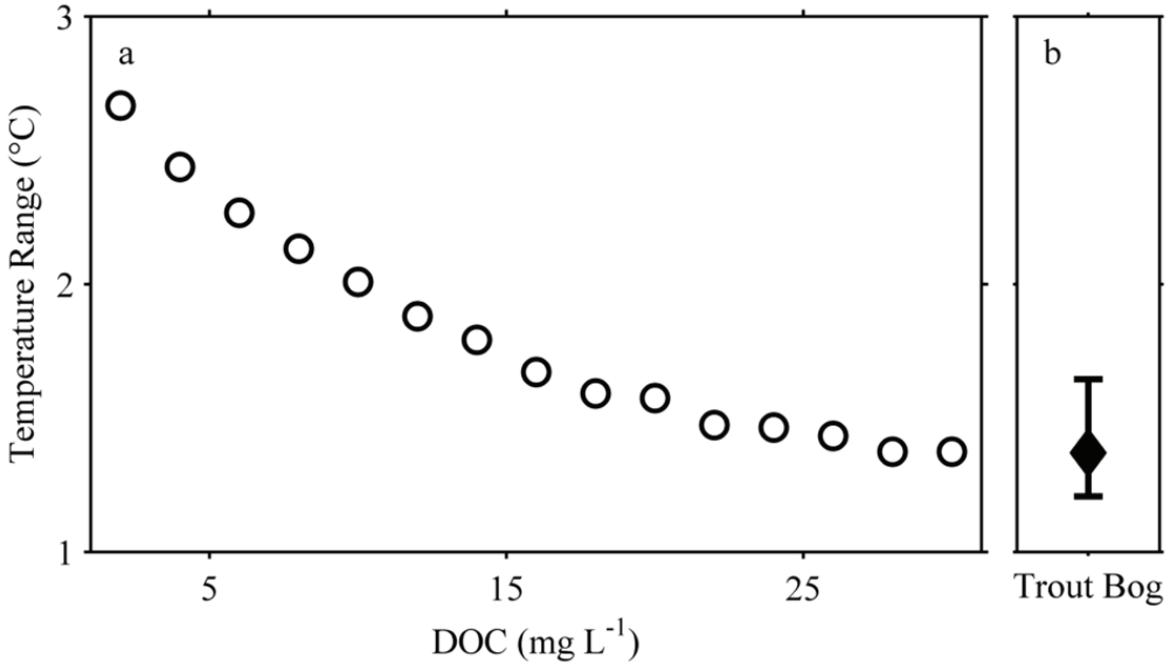

Figure 4.6: a) A model system with the morphometry of Trout Bog was simulated for a range of DOC concentrations (2 to 30 mg L^{-1}) to assess the sensitivity of water temperature to natural climate variability (1989-2010). Temperature range was calculated as the difference between maximum and maximum volumetric average temperatures for all 22 seasons (open circles). **b**) We calculated the DOC-induced temperature variability for Trout Bog, where we simulated water temperatures for a given year over the full range of DOC 1989-2010 concentrations measured in Trout Bog (Table 4.3). Each of 22 simulation years had a range between the maximum and minimum average temperatures, and the median of this range is plotted as a black diamond, and error bars represent the minimum and maximum range of all years (which were 2009 and 2003, respectively).

Table 4.1: Properties for the 8 lakes used in this analysis.

Lake Name	Latitude	Longitude	Surface area (ha)	Max depth (m)	Buoy type	DOY range	Year
Crystal Bog	46.0076	-89.606	0.55	2.5	1	133-201	2009
Jekl Bog	45.9946	-89.678	0.25	3.1	1	132-173	2011
Mouser Bog	45.9977	-89.722	3.78	4	2	138-195	2011
N Sparkling Bog	46.0048	-89.705	0.46	4.3	1	107-338	2009
Peter	46.2529	-89.504	2.68	18	1	132-246	2011
Timber Bog	46.0034	-89.431	0.06	2	1	132-177	2011
Trout Bog	46.0411	-89.686	1.05	7.9	1	125-321	2009
Ward	46.2548	-89.517	2.01	8.3	2	142-264	2011

Table 4.2: Simulation results for 8 sheltered lakes. Model K_d is the best fit to the observed data if K_d is treated as an unknown, observed K_d is a single-point estimate of PAR K_d taken during the observation year, 95% confidence intervals are from non-linear least squared fits to the exponential decay of light, and SE is the standard error between all observed and modeled water temperatures with the exception of surface thermistors.

Lake Name	Model K_d (m^{-1})	Observed K_d (m^{-1})	K_d 95% CI (m^{-1})	SE (ºC)
Crystal Bog	3.62	2.55	2.51-2.58	0.73
Jekl Bog	1.85	1.93	1.91-1.94	0.75
Mouser Bog	2.46	2.54	2.48-2.60	1.28
N Sparkling Bog	1.6	1.91	1.88-1.94	0.84
Peter	0.84	0.93	0.89-0.97	0.70
Timber Bog	1.72	1.83	1.8-1.86	0.96
Trout Bog	3.5	3.51	3.41-3.62	0.37
Ward	2.58	1.66	159-1.75	0.66

Table 4.3: DOC measurements and modeling details for 1989-2010. Ice-on and Ice-off values are the daynumbers for the first and last observed open water on Trout Bog for the observation year. DOC (mg L^{-1}) values are the median of all measurements made between and including 0 and 3 meters, and K_d (m^{-1}) was estimated from DOC measurements using the DOC-specific attenuation coefficient.

	1989	**1990**	**1991**	**1992**	**1993**	**1994**	**1995**	**1996**	**1997**	**1998**	**1999**	**2000**	**2001**	**2002**	**2003**	**2004**	**2005**	**2006**	**2007**	**2008**	**2009**	**2010**
Ice-Off	116	113	109	120	118	110	117	130	119	101	105	95	113	114	113	112	105	103	108	121	112	90
Ice-On	317	327	305	316	309	327	311	314	316	341	328	322	340	317	311	328	325	333	319	322	334	327
DOC	13.5	14.8	20.2	20.5	19	18.7	21.2	21.3	20.9	21.8	21	22.6	23.3	23.9	27.5	23.5	24.8	21.8	19.6	18.7	17.4	16
K_d	2.97	3.25	4.45	4.5	4.18	4.12	4.67	4.69	4.59	4.8	4.62	4.98	5.13	5.25	6.04	5.16	5.45	4.8	4.3	4.11	3.82	3.53

Chapter 5 – "Gradual Entrainment Lake Inverter" (GELI): A novel device for experimental lake mixing

The following is reproduced with permission from a publication that is catalogued according to doi: 10:4319/lom.2011.9.14

Read JS, A Shade, CH Wu, A Gorzalski, KD McMahon. 2011. "Gradual Entrainment Lake Inverter" (GELI): A novel device for experimental lake mixing. Limnology and Oceanography: Methods. 9: 14-28.

5.1 Abstract

A Gradual Entrainment Lake Inverter (GELI) designed to destroy thermal stratification was constructed and used to destratify a darkly stained humic lake. The GELI was developed to gain insight to the effects of altered lake mixing regimes, but has utility in other mixing applications. The GELI is comprised of an 8.25m diameter rubber membrane with a tubular inflatable ring around its circumference that can be raised and lowered repeatedly through the water column using compressed air to control the buoyancy of the ring. Three mixing mechanisms for the GELIs were observed: (i) the increase of high-frequency internal waves (ii), shear and circulation resulting from lateral exchange flows, and (iii) generation of turbulence via both surface spreading and a trailing wake. Field experiments of the GELI reset vertically stratified variables to a near-homogeneous state. As the surface to bottom water column temperature differential changed from 19.2 to 0.2°C, dissolved oxygen concentrations increased transiently from below detection to 2.8 mg L^{-1} in the hypolimnion, and decreased from 7.0 to 3.2 mg L^{-1} in the epilimnion. Results demonstrate that the GELI is an efficient lake mixing device that can minimize gas exchange associated with traditional mixing methods, and the GELI is particularly useful when circumstances require non-disruption of this parameter. The GELI can also be useful in hydrodynamic studies as an internal wave generation device.

5.2 Introduction

Mixing events in temperate lakes are thought to represent an important ecological reset for vertically stratified variables such as nutrients and dissolved oxygen (Alvarez-Cobelas et al. 2005), while also potentially increasing surface fluxes of mass and energy (e.g., Eugster et al. 2003; Wuest and Lorke 2003). Lake mixing is also important for the ecology of temperate lakes, and influences available thermal habitat for aquatic species (Meyer et al. 1999), ice cover duration (Robertson et al. 1992; Jensen et al. 2007), and carbon sequestration (e.g., Eugster et al. 2003; Cole et al. 2007).

Mixing events can vary in frequency and magnitude; such as, the controls of diurnal heating and cooling on surface layer dynamics (Imberger 1985), deepening of the seasonal thermocline resulting from short-term variations in atmospheric forcing (Gaiser et al. 2009; Macintyre et al. 2009), and seasonal overturns caused by complete thermal destratification (Malm and Zilitinkevich 1994). For temperate regions, climate change scenarios have predicted general increases in air temperatures (e.g., Meehl et al. 2006), and deviation of storm frequencies and intensities from the historical norm (Trenberth 1999; Trapp et al. 2009). As an example specific to small lakes, MacIntyre et al. (2009) showed that local climate patterns heavily influenced stratification and internal mixing through a detailed study of intra- and inter-seasonal variations in mixing dynamics of a small artic lake over four ice-free seasons. Furthermore, climate changes, as well as anticipated land use changes (e.g., Carpenter et al. 2007), could alter the mixing regimes of temperate lakes (Gerten and Adrian 2001), with unknown ecological consequences.

Non-seasonal mixing events that result in complete overturn frequently correspond with changes in extrinsic variables that indirectly alter within-lake processes.

For example, increased terrestrial runoff and rainwater volume (variables associated with severe storms) could affect within-lake dissolved oxygen concentrations, carbon dioxide flux, and sediment re-suspension (e.g., Tsai et al. 2008; Jones et al. 2009). Therefore, direct and indirect effects of mixing, as well as inter-strata exchange during mixing events, are difficult to measure and isolate. Automated sensing technologies, such as instrumented buoys, can enable real-time observation of mixing events (Jones et al. 2008). Thus, a remaining challenge is to isolate within-lake mixing mechanisms by observing mixing events in the absence of the influence of extrinsic variables.

Destratification has been often employed as a method of ameliorating water quality issues in stratified lakes and reservoirs; both to control algal blooms (Visser et al. 1996; Scharf 1999; Chipofya and Matapa 2003) and oxygenate deeper waters (e.g., Lawson and Anderson 2007). The most common destratification method is the use of bubble plumes (see Baines and Leitch 1992; Lemckert and Imberger 1993; Schladow 1993), which can alter in-lake gas concentrations via the aeration mechanisms described by Sahoo and Luketina (2003) and Wuest et al. (1992). Other destratification options include mechanical mixers (e.g., Stephens and Imberger 1993; Kirke and Elgezawy 1997), which are more costly and sometimes less efficient than bubble plumes (Szyper 1996; Lawson and Anderson 2007). Lydersen et al. (2008) used a fixed propeller mixer, similar to the design proposed by Stephens and Imberger (1993), to deepen the seasonal thermocline of a small lake as part of a climate change scenario. The design used by Lydersen et al. (2008) was horizontally mounted, but a vertical orientation of impellers (Stephens and Imberger 1993) also concentrates turbulence closer to the impellers and results in a non-uniform distribution of vertical mixing. While this design has the

potential to simulate wind-driven deepening of the thermocline, the effects on deeper waters remain unknown.

Several studies have highlighted the importance of turbulence on biotic interactions like nutrients intake and metabolism (e.g., Regel et al. 2004), but few have extended this work into controlled ecosystem-scale manipulations. Commonly, turbulence generated at laboratory-scales is often used to mimic natural scales to simulate the enhanced diffusivity of natural environments. This type of mixing is often achieved through the oscillation of a grid-like mesh, which is used to simulate natural water motions by inducing turbulence (see Hondzo and Warnaars 2008) while minimizing gas exchange. To the best of our knowledge, no such device exists to experimentally elevate mixing on a controlled whole-lake scale. A controlled manipulation to cause non-seasonal lake mixing would provide valuable insight on mechanisms driving response to thermal structure changes, and also minimize distortion from other extrinsic variables.

The purpose of this paper is to introduce a new lake-mixing device, the Gradual Entrainment Lake Inverter (GELI), and to assess GELI performance and illustrate the utility of this device for future limnological studies. The GELIs were named after the mechanisms of gradual erosion of thermal stratification in a lake system. The GELIs were employed to induce the whole-lake thermal mixing of a small dystrophic lake in 2008. We evaluated the physical response of the lake using both high-frequency measurements and a one-dimensional water temperature model, allowing comparisons with existing methods and the characterization of hydrodynamic influence of the GELI.

5.3 Materials and procedures

5.3.1 *Experimental description*

During early July 2008, we artificially mixed North Sparkling Bog Lake (NSB), located in northern Wisconsin (46°0.2'N, 89°42.3'W), as part of a whole-lake mixing manipulation designed to study the ecosystem response to a non-seasonal mixing event. NSB is 0.47 ha, has a maximum depth of 4.3 m, and is darkly stained (9.5 mg L^{-1} dissolved organic carbon) (see Figure 5.1). It is a wind-sheltered dimictic lake that stratifies strongly during the ice-free season. First we manipulated the lake using two GELI mixing devices over a period of eight days from 02 July to 10 July 2008. To further improve our understanding of the hydrodynamic effects of the method, we also deployed a single GELI for a period of three days on nearby Crystal Lake from 7 August to 10 August 2009 (Crystal Lake is a larger, deeper lake; 34 ha and 21 m maximum depth; 46°0.3'N, 89°36.7'W; see Beisner et al. 2003 or http://lter.limnology.wisc.edu for additional details about Crystal Lake). The 2009 deployment was further used to validate observations made during the primary 2008 experiment.

5.3.2 *GELI design*

The GELIs were comprised of a centered parachute-like membrane surrounded by a buoyancy controlled ring (BCR) (Figure 5.2a; Figure 5.2b). The exterior of the BCR was constructed from 101.6mm (4 inch) diameter flexible polyvinyl chloride (PVC) discharge hose (Goodyear Spiraflex, Akron, Ohio). A rigid skeleton made of 12 sections of 2 m length 25 mm diameter sand-filled (to increase negative buoyancy) aluminum pipe connected with 30° couplings was threaded through the interior of the BCR to maintain the structural integrity of the ring shape. Two 12 m sections of the flexible PVC hose were connected with 2 (2 male, 2 female) 101.6 mm (4 inch) aluminum suction-hose quick disconnect couplings. One of the female hose couplings was tapped for two ¼-inch

NPT (National pipe thread) pipe fittings to attach both compressed air and vacuum hose fittings to each GELI. The inner membrane was constructed from 45-mil chemically welded ethylene propylene diene M-class (EPDM) rubber, cut to the inside dimensions of the BCR. The membrane was fitted with 36 equally spaced grommets around the perimeter, 100mm from the edge. Double thickness EPDM rubber was used for the perimeter of the membrane to improve the durability of the grommet connections. Nylon straps lashed around the BCR connected the membrane to the BCR by running through the grommets (Figure 5.2b). The final diameter of each GELI was 8.25m.

5.3.3 *Operation*

Buoyancy of the GELI was controlled by filling the BCR completely with compressed air to raise the GELI through the water column, or removing the air with a vacuum pump (Gast Manufacturing, Benton Harbor, MI) to induce sinking. We refer to these as the "inflation" and "evacuation" stages, respectively. Solenoid valves (Norgren Company, Littleton, CO) were used to control the stages of GELI operation by switching active connections from the air compressor (inflation) to the vacuum pump (evacuation) (Figure 5.3). During the inflation stage, a 24 volt-DC circuit was closed to open the inflation solenoid valve and allow air delivery to the BCR from an onshore air compressor. Evacuation cycles were triggered by a second circuit closure connected to the evacuation solenoid. An onshore operator controlled the GELI stages with push button closure switches wired to two 12 volt-DC acid-lead batteries in series. Inflation and evacuation stages required switch closures of 26 seconds and 18 minutes, respectively. After the evacuation stage, the operator waited 4 minutes to allow the GELI

to completely sink and come to rest on the lakebed before repeating the inflation stage, resulting in a complete cycle time near 23 minutes.

5.3.4 *Measurements*

We used a combination of instruments for observing and assessing the effects of the GELI method in July 2008. Primary measurements were taken at two locations: *in situ* (NSB), and off-site at the Noble F. Lee Municipal Airport (approximately 8.6 km away, 45°55.7'N, 89°43.9'W). Secondary measurements taken in August 2009 at nearby Crystal Lake were collected *in situ*. Downwelling longwave and shortwave radiation measurements were recorded at 10 minute intervals using an Eppley PIR radiometer and an Eppley PSP pyranometer, respectively (Eppley Laboratory, New Port, Rhode Island). Precipitation data, taken as a 10 minute sum, was also measured using a tipping bucket rain gauge. The volume required for GELI cycles was measured using a mass flow meter (Sierra Instruments Mass Trak 826, Monterey, CA) calibrated to output instantaneous air flow in slpm (standard liters per minute). This flow meter was sampled every second for a 6 hour test period to calculate average cycle air volumes. The time-series observations of 2008 in-lake environmental variables were collected by an instrumented buoy situated slightly off-center from the deepest location of the lake ("B" in Figure 5.1). A thermistor chain (Apprise Technologies, Duluth, MN) with sensors placed at the surface, 0.25m depth, and 0.5m intervals from 0.5m depth to 4.0m that sampled water temperature every 10 minutes. Wind speed and direction were recorded using a propeller-type anemometer (model 05103-L, R.M. Young, Traverse City, Michigan) at the same temporal resolution as other buoy components. Two and four point depth thermal profiles were measured for a northeast to southwest transect centered at the buoy by using HOBO temperature

loggers (V2-Pro, Onset Corporation, Bourne, MA). Two point profiles deployed near shore measured temperature at 1 and 3 m depth, while four point profiles deployed near the instrumented buoy measured temperature at 0.5, 1, 2 and 3 m depth. HOBOs logged water temperature every 10 minutes. A water quality sonde (YSI 6600V2-04, Yellow Springs, OH) was used to autonomously obtain profiles for temperature and dissolved oxygen (DO) at the buoy location by completely traversing the water column once every hour. The sonde was transported through the water column using an automated rotating cable spool with programmed 5 minute dwell periods for measurements at depths corresponding to buoy thermistors (not including surface), with an additional measurement at 0.75 m depth.

A 4 beam Acoustic Doppler Current Profiler (ADCP) (Sentinal 1200 kHz, Teledyne Technologies Inc., Thousand Oaks, CA) was used in high spatial-resolution mode 11 (see Fugate and Chant 2005) to obtain far-field velocity profiles 30 m north of the mixing disturbance during the final 2 days of the 2008 experiment ("V" in Figure 5.1). The ADCP was mounted vertically and referenced from the lakebed. Northern, eastern and vertical velocity magnitudes were collected from 5 cm cells using pulse-to-pulse coherent 1.9 Hz samples. Samples were ensemble averaged at 20-seconds. The ADCP also collected temperature measurements at 0.05 Hz. During the 2009 secondary effort, the same ADCP was deployed 35 m to the west of the GELI in Crystal Lake. A higher spatial resolution (235 vertical 2 cm cells) and 1 Hz sampling rate were used. For the 2009 measurements, we also used a burst mode where only the first 12 minutes of each hour were recorded.

5.3.5 *GELI efficiency*

The efficiency of GELI destratification was calculated according to assumptions made by Schladow (1993); which state that mechanical efficiency (η_{mech}) of water column mixing can be estimated as the ratio between changes in potential energy ($^{\Delta PE}/_{\Delta t}$) and idealized work (in this case, isentropic compression: $\dot{W}_{iso}$) during a given time period (Δt), assuming kinetic terms were negligible relative to potential terms;

$$\eta_{mech} \approx \frac{^{\Delta PE}/_{\Delta t}}{\dot{W}_{iso}}. \tag{5.1}$$

Following Zic et al. (1992), the potential energy of the water column at any point in time can be calculated if the density profile and lake bathymetry are known;

$$PE_t = g \cdot \sum_{i=1}^{\#layer} \rho_{i,t} A_i \left(z_i - z_{cv}\right) \cdot \partial z_i \,, \tag{5.2}$$

where g is the acceleration due to gravity, $\rho_{i,t}$ is the average density of layer *i* at time *t*, A_i is the cross-sectional area of layer *i*, z_i is the depth to the center of layer *i*, z_{cv} is the center of volume of the lake in the z direction, and ∂z_i is the width of layer *i* (taken as constant 0.1 m for all *i*). Isentropic work was calculated as $\dot{W}_{iso} = \dot{m} \cdot (h_{in} - h_{out})$, where $\dot{m}$ is the mass flow rate of compressed air (kg s^{-1}, converted from slpm based on instrument calibration), and h_{in} and h_{out} denote the enthalpy of inlet and outlet air in J kg^{-1}, respectively. Because changes in potential energy are also associated with directional buoyancy fluxes during heating and cooling periods (Imberger 1985), we chose to

calculate changes in potential energy as the difference between what was observed during the manipulation and what would be expected in the absence of manipulation obtained by a water temperature model.

5.3.6 *Water temperature model*

To calculate the mixing efficiency of the GELIs and estimate the thermal effects of destratification on the remainder of the ice-free season, a one-dimensional (1D) physical model was developed. The size and seasonal dynamics of the lake allowed several simplifications to this model. Wind speed (measured at the instrumented buoy) had a strong diurnal signature, with daytime speeds typically on the order of 1~2 m s^{-1}, and nighttime values mostly below instrument detection (Figure 5.4). Even at higher daytime wind speeds (> 3 m s^{-1}), the lake remained stratified to the surface, and the main source of surface layer mixing was nighttime convective cooling. Because of the wind-sheltering, high light-attenuation (1.4~2 m^{-1}), and small surface area of NSB, the seasonal evolution of the thermal structure is dominated by the molecular diffusion of heat. Therefore, we formulated our model conditions under the following assumptions: 1) The vertical flux of heat in the water column occurs at the rate of molecular diffusion during periods of positive net heat gain, 2) wind induced mixing is negligible compared to convective mixing ($w_* >> C_n u_*$, calculated as in Imberger 1985, data not shown), 3) light attenuation substances vary with depth, 4) ground water effects are negligible (Winter et al. 2003), 5) the flux of heat between the sediments and water column can be estimated by assuming a steady-state sediment temperature (Rogers et al. 1995), 6) sensible and latent heat fluxes can be estimated based on the knowledge of atmospheric conditions and water surface temperature (Monteith 1981), 7) and that all processes relevant to the

temperature dynamics of the lake can be described as 1D. For 3), we used a 6 component formulation of light attenuation (from Imberger's formulation (1985): A1 = 0.71; A2 = 0.15; A3 = 5E-5; B1 = 2.46; B2 = 1.01; B3 = $1x10^{-3}$) to characterize a notable near surface break in light extinction (data not shown), which is not captured by assuming homogeneity in the water column. For 5), we used sediment properties, steady-state temperature, and depth to steady-state from the results of Likens and Johnson (1969).

Solving for internal temperature profiles at any point in time involved first calculating changes in surface fluxes, by combining measurements and estimates for the components shown below (see Lenters et al. 2005; Ali et al. 2008 for additional details):

$$\Delta T_s = \left(\overline{\dot{A}_s} + \overline{\dot{R}_s} - \overline{E} - \overline{H}\right) \cdot \frac{\Delta t}{c_w} \quad , \qquad (5.3)$$

where the subscript *s* represents properties of the water surface, and overbars ($\overline{x}$) denote temporal averaging over the time period Δt (s). Here, ΔT_s (°C) is the change in surface water temperature, c_w is the specific heat of water (4186 J kg^{-1} $°C^{-1}$), $\dot{A}_s$ is the net advected energy (W m^{-2}), $\dot{R}_s$ is the net flux of radiant energy, E is the latent heat flux, H is the sensible heat flux; where all energy flux terms pertain only to surface fluxes. The time step chosen for the water temperature calculation was 1 hour ($\Delta t = 3600$). Remaining radiation that was not either reflected from the lake surface ($\alpha_{LW} = 0.03$, $\alpha_{SW} = 0.07$, where α is the lake surface albedo) or absorbed in the surface layer (similar to Kim 1976, we used $\dot{R}_o / \dot{R}_{s,SW} = 0.74$, where $\dot{R}_o$ is the remaining shortwave energy after penetration of the water/air interface) was partitioned into depth bins (∂z = 0.01 m) based on the light attenuation relationship from equation 3). Sediment heat contributed a directional flux based on a vertical projection of bathymetry that was

proportional to water temperature and steady-state sediment temperature. After fluxes were accounted for, layer-to-layer molecular heat transfer was driven by the temperature differential between each layer. Before progressing to the next time-step, the model checked for density instabilities in the thermal layers (usually the result of surface cooling) and propagated isothermal mixing downward until the instability was no longer present. Using this methodology, we were able to successfully reproduce the pre-manipulation thermal profiles of the bog lake. To calculate changes in potential energy in equation 2, we initialized the model with the observed water temperatures at the start of manipulation (2 July 2008 18:00) from buoy measurements.

5.4 Assessment and discussion

5.4.1 *Lake response to treatment*

The two GELIs were used to effectively mix the small bog lake during 2008 from 2 July 18:00 to 10 July 8:00 including lost repair time (see Figure 5.5). The pre-manipulation water temperature at the bottom of the lake was 6.0°C and rose to 20.1°C over the course of the manipulation, remaining unseasonably high for the rest of the summer (Figure 5.6a). The surface waters (0 to 0.5 m) cooled from 24.2°C to 20.3°C during the experiment, while modeled surface temperatures showed an expected decrease of only 1°C during the same period (Figure 5.6b). The average water column temperature increased during the experiment (Figure 5.7a), as cooler surface waters likely decreased both evaporative and outgoing longwave radiation fluxes. DO concentrations at 3.5 m depth increased from below instrument detection to 2.8 mg L^{-1} during the experiment, while the surface waters decreased from 7.0 to 3.2 mg L^{-1} (data not shown). The volumetric averaged DO (assuming horizontal homogeneity) decreased during the

treatment (Figure 5.7b); suggesting increased surface fluxes brought on by a larger concentration differential with the atmosphere were exceeded by hypolimnetic oxygen demand.

5.4.2 *GELI mixing mechanisms*

During the length of the 2008 ADCP deployment (8 July 3:10 to 10 July 9:00) high-frequency internal waves with periods ranging from 3 to 7 minutes were observed throughout the water column along the north-south directions (see Figure 5.8a), approximately 30 m from the disturbance ("V" in Figure 5.1,). Wave periods followed a function of buoyancy frequency ($N = \sqrt{-\frac{g}{\rho}\frac{\partial \rho}{\partial z}}$, where $\partial\rho/\partial z$ is calculated as the local density gradient between two adjacent buoy thermistors), as high-frequency spectral peaks in velocity appeared near *N*/8 (Figure 5.8b, dashed line). Nevertheless, the sampling interval of buoy and HOBO temperature measurements were too coarse (10 minutes) to resolve these wave signals. The variability in *N* was high during the experiment, as the mixing effort combined with natural diel buoyancy fluxes to influence wave periods at a sub-hourly scale (see Figure 5.9a and Figure 5.9b, which differ by only 2 hours). In 2009, a secondary GELI deployment on nearby Crystal Lake was conducted to capture the generation of internal waves during a period of stronger stratification. During this test, we measured extremely strong internal waves at the depth-range of the metalimnion (8-11 m; Figure 5.9c, which shows east-west velocities). These waves had a shorter period (~2 min compared to 3~7 min) than those observed during the NSB experiment, although high-frequency wave periods were once again near eight-fold the inverse of the buoyancy frequency (Figure 5.9d; 5.9e; 5.9f). We altered the cycle time of the GELI in a range of 250 to 500 seconds, and found the period of internal waves to not

depend on the cycle time of the GELI, but instead only on the ambient stratification. Observed waves were always within the range of 8 to 9 times the inverse of the buoyancy frequency, regardless of cycle time. We hypothesize that an unsteady wake formation of the GELI (similar to lab measurements of a slightly buoyant disk by Ern et al. 2007), combined with a perturbation of the thermocline during vertical movement, caused the high-frequency waves seen during both 2008 and 2009. The period of these internal waves is likely a function of both the size of disturbance and degree of stratification. A basin-scale disturbance would theoretically produce a mode-1 internal seiche, while the perturbation of a solitary water parcel would create an oscillation at the buoyancy frequency; with the physical scale of the GELI in between the two. Because internal waves can efficiently propagate a disturbance horizontally, it is postulated that the overall efficiency of the GELI was improved by increased boundary mixing (see Goudsmit et al. 1997; Boegman et al. 2005).

The unsteady operation of the GELI also appeared to induce lateral flows visible in both ADCP temperature measurements and pooled north-south velocities at the same location (2.2-2.7 m depth Figure 5.10a; 5.10b). Colder water at the depth of the ADCP seemed to originate away from the disturbance, as drops in temperature corresponded to south-bound velocities. This pattern suggests that horizontal currents were driven by the spatial heterogeneity of mixing and the periods of oscillation were influenced by the unsteady nature of the disturbance. Assuming horizontal heterogeneity in the lake could be attributed primarily to the GELI disturbance; more vertically well-mixed waters would be measured as warmer water at the bottom of the lake, while less-mixed waters would be relatively cooler at the same depth. Flows driven by this unstable case would act to draw

colder waters from away from the disturbance towards it (as the GELIs were positioned at the deepest part of the lake), replacing local bottom waters as part of an exchange flow. This pattern was observed during several periods of GELI operation, including what is shown in Figure 10. Because of the unsteady nature of the GELI operation, these patterns were also unsteady; varying in period and intensity. Contrary to the observed higher-frequency waves (see Figure 5.9), these flows did not follow patterns in ambient stratification (like internal seiche modes). While isolating the contribution of these lateral flows to the mixing efficiency of the GELIs is not possible with our instrument deployment, we postulate that shear-generated turbulence from the flows was a secondary (relative to the mixing contribution of boundary shoaling of internal waves) far-field mixing mechanism (Saggio and Imberger 2001). We assume the primary contribution of these exchange flows was to increase the spatial coverage of the GELIs by circulating denser waters into the range of the near-field mixing mechanisms.

The third mixing mechanism was the surface expulsion of higher density (colder) fluids transported from the bottom of the water column. This mixing contribution was noted by the cold water spreading at the surface after each GELI had surfaced (see Figure 5.2a, water spreading outward to the right). The membrane of the GELI during the vertical rise was bowed owing to both drag and the mass differential between the ambient fluid and what was being vertically transported by upward motion. Once the GELI reached the surface, the membrane expelled some of this water – likely a volume similar to the contribution of the deformation due to drag – but remained bowed with some of the colder water trapped at the surface. Because this was a near-field transient effect that was only noticeable at the top of each cycle, we weren't able to capture it with our

instrumentation. However, water expelled from the GELI (during the early portion of the experiment where a strong temperature differential was in place) was cold to the touch as compared to ambient surface waters. These spreading patterns were radially outward but unsteady, as each GELI would tip and spill at the surface in an unpredictable fashion. While this denser mass likely sunk to a level of neutral buoyancy, the turbulence generated during surface spreading likely increased local mixing with surface waters (visual observations approximated spreading currents to be on the order of 50 cm s^{-1}). In addition to this mechanism, we also assume that the large wake region of each GELI was a large source of turbulence to the water column. While no measurements were made to quantify this effect, the size of the GELI (8.25 m diameter) and speed of ascent (20 seconds from resting stage to surfacing for 4 m of travel during NSB ascent) would produce significant turbulence (Re > $3x10^6$, where the dimensionless Reynolds number is given by $\mathrm{Re} = U_G D_G / \nu$. U_G is the vertical velocity of the GELI, D_G is the diameter of the GELI, and ν is the kinematic viscosity of water)

5.4.3 *Efficiency/power use*

GELI cycles occurred on average every 25 minutes for the 2008 experiment, with a total air delivery volume of ~58,000 standard liters. The deviations in the potential energy of the water column for both observed and modeled cases were calculated according to Schladow (1993). Our time rate of change of potential energy for equation 5.2 was used as the difference between modeled and observed, assuming that modeled fluctuations accurately represented natural buoyancy fluxes resulting from atmospheric drivers (Figure 5.11b). Mechanical efficiency of the GELI was around 2-4% using a moving window of 6 hours. Exceptions to these values occurred during the major repair

of the evening and early morning of 6 July and 7 July 2008 (where no compressor energy was used; Figure 5.11b) and during some periods of nocturnal convection, when efficiency was negative. Negative efficiency estimates are a function of comparing the rates of change of potential energy in the unaltered (model) case to the observed case, as negative estimates arise when the unaltered water column is more rapidly losing stability (in the form of surface cooling) – due to warmer relative surface waters – than in the manipulated case . The overall efficiency of the GELI method is lower than idealized aeration (e.g., Sahoo and Luketina 2003), but represents an improvement over of actual field measurements (Szyper 1996), suggesting the GELI to be an effective alternative to existing mixing methods.

5.5 Comments and recommendations

A new mixing device, GELI, was designed, constructed, and successfully tested to create a controlled mixing event on a small lake in 2008, greatly altering the lake's thermal structure. Three mixing mechanisms for the GELIs were observed: (i) the increase of high-frequency internal waves (ii), shear and circulation resulting from lateral exchange flows, and (iii) generation of turbulence via both surface spreading and a trailing wake.

It was found that the artificial gain of dissolved oxygen to the lake due to the mixing mechanisms of the GELIs was minimal (a goal our experimental design), and was exceeded by the oxygen demand in the bog lake. While our design was specific to the experimental goals of an ecosystem manipulation, the GELIs could also aid in the study of separate physical events, by generating internal waves or by inducing artificial upwelling, adding further utility to the device.

Vertical perturbations in stratified fluids have been used to generate internal waves and mixing in lab-scale experiments (e.g., Bonneton et al. 1993; Troy and Koseff 2005; Scase and Dalziel 2006), but the same theory has yet to be extended to large-scale field experimentation. The velocity fields measured in this experimental study suggest that controlled generation of high-frequency waves is possible in natural systems. The GELI method could also be scaled down for enclosure experiments as a turbulence generation device. We noted that volumetric oxygen concentration decreased during the course of our 2008 experiment, and see this as a major difference between GELI and aeration methods when they are employed in experimental mixing, as aeration adds a bubbling-splashing region to the surface waters which greatly enhances gas exchange.

While the initial design performed well enough to accomplish the project goals, several improvements could simplify the construction and improve operation of the GELIs. Free venting solenoid valves and larger airlines allowed us to decrease the cycle time of GELI operation in 2009, adding more flexibility to future deployments. Even though these modifications represented major improvements over the initial design, the pressure at which we operated the compressor was still quite high (~400 kPa). This high enthalpy state reduced the efficiency of the GELI as calculated according to equation 1, and could be improved by reducing the pressure (this high differential was not necessary to elevate the buoyancy of the GELIs). Because of these pressure effects, the efficiency of this method only represented a 2-3 fold improvement over field measurements of aeration methods (Szyper 1996), but the air-delivery requirement was over an order of magnitude less (Schladow 1993). The GELI is a new destratification device, and as such, more research is required to improve our understanding of how to optimize the future

design of the GELI. The complexity of the flow-field generated by a GELI-like body was noted by Ern et al. (2007); an analysis that would be further complicated if stratification and mixing efficiency were considered. Both three-dimensional numerical modeling and lab study could aid in the further development of this device; where oscillation period, size, and buoyancy of the GELIs are potential design parameters. The continued study of these parameters could lead to improvements in the GELI design; creating additional utility for the method in both experimental science and lake management applications. In conclusion, the GELI mixing device offers an alternative to traditional aeration methods, while providing efficient thermal destratification.

5.6 Acknowledgements

We acknowledge funding from the National Science Foundation of the United States MCB-0702395 (Microbial Observatories) to KDM funding from the Gordon and Betty Moore Foundation, the Frasier family, and technical support for the buoy from the Global Lakes Ecological Observatory network (www.gleon.org) as well as the Northern Temperate Lakes LTER. We thank B. Dalsing, T.K. Kratz, A. Kraus, K. Milferstedt, S. Paver, M. Sas, J. Tracey, D. Welkie, L. Winslow, G. Wolf, and the staff at the University of Wisconsin Trout Lake Station for field assistance and logistical support. We would also like to acknowledge the helpful comments from two anonymous reviewers that led to the improvement of this manuscript.

5.7 References

Ali, S., N. C. Ghosh, and R. Singh. 2008. Evaluating best evaporation estimate model for water surface evaporation in semi-arid region, India. Hydrological Processes **22:** 1093-1106, doi: 10.1002/hyp.6664.

Alvarez-Cobelas, M., J. L. Velasco, M. Valladolid, A. Baltanas, and C. Rojo. 2005. Daily patterns of mixing and nutrient concentrations during early autumn circulation in

a small sheltered lake. Freshwater Biology **50:** 813-829, doi: 10.1111/j.1365-2427.2005.01364.x.

Baines, W. D., and A. M. Leitch. 1992. Destruction of stratification by bubble plume. Journal of Hydraulic Engineering-Asce **118:** 559-577.

Beisner, B. E., A. R. Ives, and S. R. Carpenter. 2003. The effects of an exotic fish invasion on the prey communities of two lakes. Journal of Animal Ecology **72:** 331-342.

Boegman, L., G. N. Ivey, and J. Imberger. 2005. The degeneration of internal waves in lakes with sloping topography. Limnology and Oceanography **50:** 1620-1637.

Bonneton, P., J. M. Chomaz, and E. J. Hopfinger. 1993. Internal waves produced by the turbulent wake of a sphere moving horizontally in a stratified fluid. Journal of Fluid Mechanics **254:** 23-40.

Carpenter, S. R., B. J. Benson, R. Biggs, J. W. Chipman, J. A. Foley, S. A. Golding, R. B. Hammer, P. C. Hanson, P. T. J. Johnson, A. M. Kamarainen, T. K. Kratz, R. C. Lathrop, K. D. Mcmahon, B. Provencher, J. A. Rusak, C. T. Solomon, E. H. Stanley, M. G. Turner, M. J. Vander Zanden, C. H. Wu, and H. L. Yuan. 2007. Understanding regional change: A comparison of two lake districts. Bioscience **57:** 323-335, doi: 10.1641/b570407.

Chipofya, V. H., and E. J. Matapa. 2003. Destratification of an impounding reservoir using compressed air - case of Mudi reservoir, Blantyre, Malawi. Physics and Chemistry of the Earth **28:** 1161-1164, doi: 10.1016/j.pce.2003.08.037.

Cole, J. J., Y. T. Prairie, N. F. Caraco, W. H. Mcdowell, L. J. Tranvik, R. G. Striegl, C. M. Duarte, P. Kortelainen, J. A. Downing, J. J. Middelburg, and J. Melack. 2007. Plumbing the global carbon cycle: Integrating inland waters into the terrestrial carbon budget. Ecosystems **10:** 171-184, doi: 10.1007/S10021-006-9013-8.

Ern, P., P. C. Fernandes, F. Risso, and J. Magnaudet. 2007. Evolution of wake structure and wake-induced loads along the path of freely rising axisymmetric bodies. Physics of Fluids **19**, doi: 10.1063/1.2794840.

Eugster, W., G. Kling, T. Jonas, J. P. Mcfadden, A. Wuest, S. Macintyre, and F. S. Chapin. 2003. CO2 exchange between air and water in an Arctic Alaskan and

midlatitude Swiss lake: Importance of convective mixing. Journal of Geophysical Research-Atmospheres **108**, doi: 10.1029/2002JD002653.

Fugate, D. C., and R. J. Chant. 2005. Near-bottom shear stresses in a small, highly stratified estuary. Journal of Geophysical Research-Oceans **110**, doi: 10.1029/2004jc002563.

Gaiser, E. E., N. D. Deyrup, R. W. Bachmann, L. E. Battoe, and H. M. Swain. 2009. Effects of climate variability on transparency and thermal structure in subtropical, monomictic Lake Annie, Florida. Fundamental and Applied Limnology **175:** 217-230, doi: 10.1127/1863-9135/2009/0175-0217.

Gerten, D., and R. Adrian. 2001. Differences in the persistency of the North Atlantic Oscillation signal among lakes. Limnology and Oceanography **46:** 448-455.

Goudsmit, G. H., F. Peeters, M. Gloor, and A. Wuest. 1997. Boundary versus internal diapycnal mixing in stratified natural waters. Journal of Geophysical Research-Oceans **102:** 27903-27914.

Hondzo, M., and T. A. Warnaars. 2008. Coupled Effects of Small-Scale Turbulence and Phytoplankton Biomass in a Small Stratified Lake. Journal of Environmental Engineering-Asce **134:** 954-960, doi: 10.1061/(asce)0733-9372(2008)134:12(954).

Imberger, J. 1985. The diurnal mixed layer. Limnology and Oceanography **30:** 737-770.

Jensen, O. P., B. J. Benson, J. J. Magnuson, V. M. Card, M. N. Futter, P. A. Soranno, and K. M. Stewart. 2007. Spatial analysis of ice phenology trends across the Laurentian Great Lakes region during a recent warming period. Limnology and Oceanography **52:** 2013-2026.

Jones, S. E., C. Y. Chiu, T. K. Kratz, J. T. Wu, A. Shade, and K. D. Mcmahon. 2008. Typhoons initiate predictable change in aquatic bacterial communities. Limnology and Oceanography **53:** 1319-1326.

Jones, S. E., T. K. Kratz, C. Y. Chiu, and K. D. Mcmahon. 2009. Influence of typhoons on annual CO2 flux from a subtropical, humic lake. Global Change Biology **15:** 243-254, doi: 10.1111/j.1365-2486.2008.01723.x.

Kim, J. W. 1976. Generalized bulk model of oceanic mixed layer. Journal of Physical Oceanography **6:** 686-695.

Kirke, B., and A. Elgezawy. 1997. Design and model tests for an efficient mechanical circulator/aerator for lakes and reservoirs. Water Research **31:** 1283-1290.

Lawson, R., and M. A. Anderson. 2007. Stratification and mixing in Lake Elsinore, California: An assessment of axial flow pumps for improving water quality in a shallow eutrophic lake. Water Research **41:** 4457-4467, doi: 10.1016/j.watres.2007.06.004.

Lemckert, C. J., and J. Imberger. 1993. Energetic bubble plumes in arbitrary stratification. Journal of Hydraulic Engineering-Asce **119:** 680-703.

Lenters, J. D., T. K. Kratz, and C. J. Bowser. 2005. Effects of climate variability on lake evaporation: Results from a long-term energy budget study of Sparkling Lake, northern Wisconsin (USA). Journal of Hydrology **308:** 168-195, doi: 10.1016/j.jhydrol.2004.10.028.

Likens, G. E., and N. M. Johnson. 1969. Measurement and analysis of annual heat budget for sediments in two Wisconsin lakes. Limnology and Oceanography **14:** 115-&.

Lydersen, E., K. J. Aanes, S. Andersen, T. Andersen, P. Brettum, T. Baekken, L. Lien, E. A. Lindstrom, J. E. Lovik, M. Mjelde, T. J. Oredalen, A. L. Solheim, R. Romstad, and R. F. Wright. 2008. Ecosystem effects of thermal manipulation of a whole lake, Lake Breisjoen, southern Norway (THERMOS project). Hydrology and Earth System Sciences **12:** 509-522.

Macintyre, S., J. P. Fram, P. J. Kushner, N. D. Bettez, W. J. O'brien, J. E. Hobbie, and G. W. Kling. 2009. Climate-related variations in mixing dynamics in an Alaskan arctic lake. Limnology and Oceanography **54:** 2401-2417.

Malm, J., and S. Zilitinkevich. 1994. Temperature distribution and current system in a convectively mixed lake. Boundary-Layer Meteorology **71:** 219-234.

Meehl, G. A., W. M. Washington, B. D. Santer, W. D. Collins, J. M. Arblaster, A. X. Hu, D. M. Lawrence, H. Y. Teng, L. E. Buja, and W. G. Strand. 2006. Climate change projections for the twenty-first century and climate change commitment in the CCSM3. Journal of Climate **19:** 2597-2616.

Meyer, J. L., M. J. Sale, P. J. Mulholland, and N. L. Poff. 1999. Impacts of climate change on aquatic ecosystem functioning and health. Journal of the American Water Resources Association **35:** 1373-1386.

Monteith, J. L. 1981. Evaporation and surface-temperature. Quarterly Journal of the Royal Meteorological Society **107:** 1-27.

Regel, R. H., J. D. Brookes, G. G. Ganf, and R. Griffiths. 2004. The influence of experimentally generated turbulence on the Mash01 unicellular Microcystis aeruginosa strain. Hydrobiologia **517:** 107-120.

Robertson, D. M., R. A. Ragotzkie, and J. J. Magnuson. 1992. Lake ice records used to detect historical and future climatic changes. Climatic Change **21:** 407-427.

Rogers, C. K., G. A. Lawrence, and P. F. Hamblin. 1995. Observations and numerical simulation of a shallow ice-covered mid-lattitude lake. Limnology and Oceanography **40:** 374-385.

Saggio, A., and J. Imberger. 2001. Mixing and turbulent fluxes in the metallimnion of a stratified lake. Limnology and Oceanography **46:** 392-409.

Sahoo, G. B., and D. Luketina. 2003. Modeling of bubble plume design and oxygen transfer for reservoir restoration. Water Research **37:** 393-401.

Scase, M. M., and S. B. Dalziel. 2006. Internal wave fields generated by a translating body in a stratified fluid: an experimental comparison. Journal of Fluid Mechanics **564:** 305-331, doi: 10.1017/s0022112006001571.

Scharf, W. 1999. Restoration of the highly eutrophic lingese reservoir. Hydrobiologia **416:** 85-96.

Schladow, S. G. 1993. Lake destratification by bubble-plume systems: Design methodology. Journal of Hydraulic Engineering-Asce **119:** 350-368.

Stephens, R., and J. Imberger. 1993. Reservoir destratification via mechanical mixers. Journal of Hydraulic Engineering-Asce **119:** 438-457.

Szyper, J. P. 1996. Comparison of three mixing devices in earthen culture ponds of four different surface areas. Aquacultural Engineering **15:** 381-396.

Trapp, R. J., N. S. Diffenbaugh, and A. Gluhovsky. 2009. Transient response of severe thunderstorm forcing to elevated greenhouse gas concentrations. Geophysical Research Letters **36**, doi: 10.1029/2008gl036203.

Trenberth, K. E. 1999. Conceptual framework for changes of extremes of the hydrological cycle with climate change. Climatic Change **42:** 327-339.

Troy, C. D., and J. R. Koseff. 2005. The generation and quantitative visualization of breaking internal waves. Experiments in Fluids **38:** 549-562, doi: 10.1007/s00348-004-0909-9.

Tsai, J. W., T. K. Kratz, P. C. Hanson, J. T. Wu, W. Y. B. Chang, P. W. Arzberger, B. S. Lin, F. P. Lin, H. M. Chou, and C. Y. Chiu. 2008. Seasonal dynamics, typhoons and the regulation of lake metabolism in a subtropical humic lake. Freshwater Biology **53:** 1929-1941, doi: 10.1111/j.1365-2427.2008.02017.x.

Visser, P. M., B. W. Ibelings, B. Vanderveer, J. Koedood, and L. R. Mur. 1996. Artificial mixing prevents nuisance blooms of the cyanobacterium Microcystis in Lake Nieuwe Meer, the Netherlands. Freshwater Biology **36:** 435-450.

Winter, T. C., D. C. Buso, D. O. Rosenberry, G. E. Likens, A. M. Sturrock, and D. P. Mau. 2003. Evaporation determined by the energy-budget method for Mirror Lake, New Hampshire. Limnology and Oceanography **48:** 995-1009.

Wuest, A., N. H. Brooks, and D. M. Imboden. 1992. Bubble plume modeling for lake restoration. Water Resources Research **28:** 3235-3250.

Wuest, A., and A. Lorke. 2003. Small-scale hydrodynamics in lakes. Annual Review of Fluid Mechanics **35:** 373-412, doi: 10.1146/annurev.fluid.35.101101.161220.

Zic, K., H. G. Stefan, and C. Ellis. 1992. Laboratory study of water destratification by a bubble plume. Journal of Hydraulic Research **30:** 7-27.

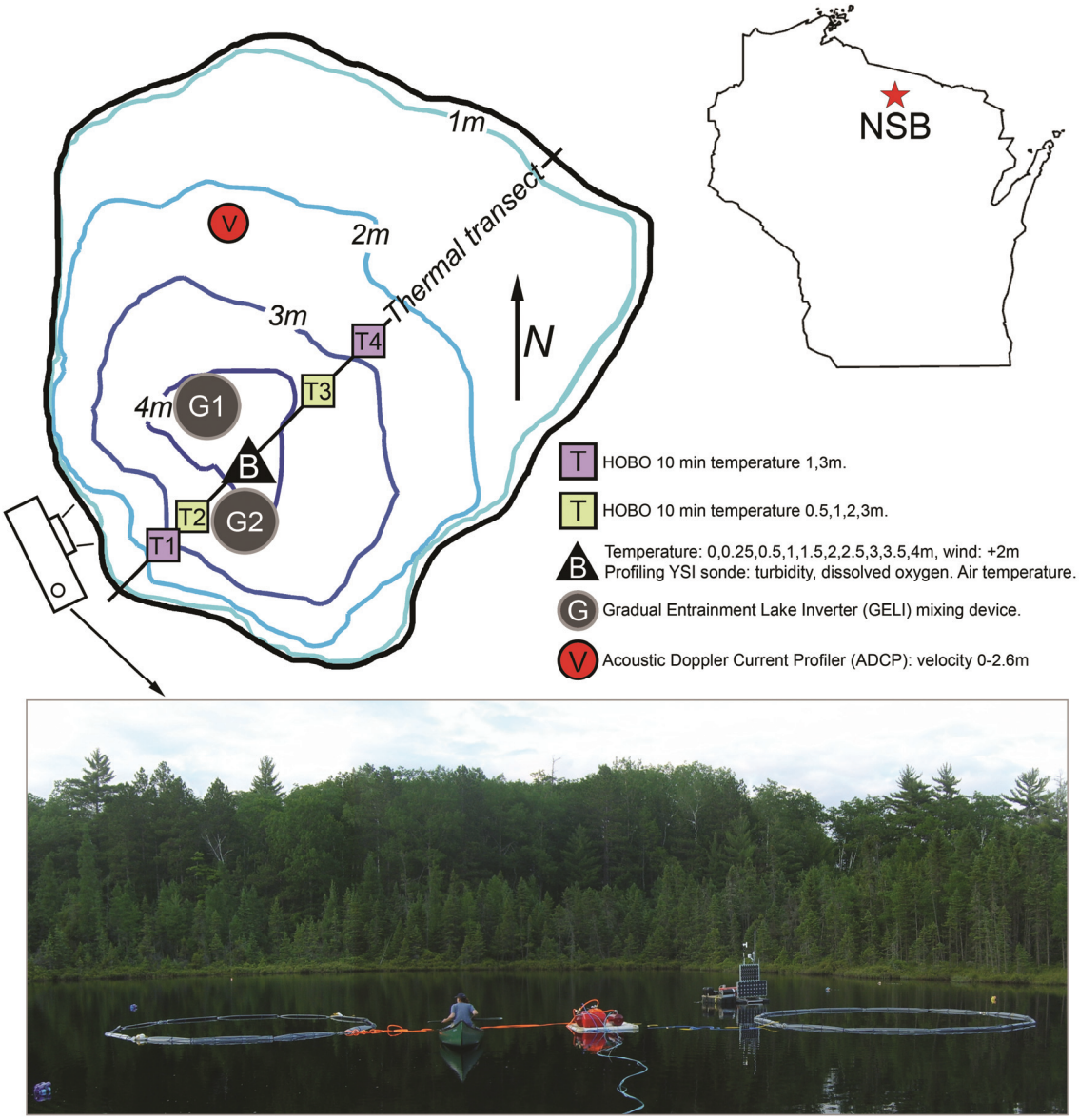

Figure 5.1: North Sparkling Bog (NSB, maximum depth 4.3m) is a strongly stratified, dimictic (spring and fall turnover), wind sheltered lake. NSB is located in the northern highlands lake district of Wisconsin. Multiple near real-time environmental sensors were deployed throughout the duration of the manipulation. T1-T4 represent local HOBO temperature profiles. B represents an instrumented buoy that measures meteorological variables as well as water temperature and dissolved oxygen. G1 and G2 represent the GELI mixing devices used to artificially mix NSB. V is an Acoustic Doppler Current Profiler (ADCP) which measured far-field velocity profiles during treatment. Camera shows perspective view of picture.

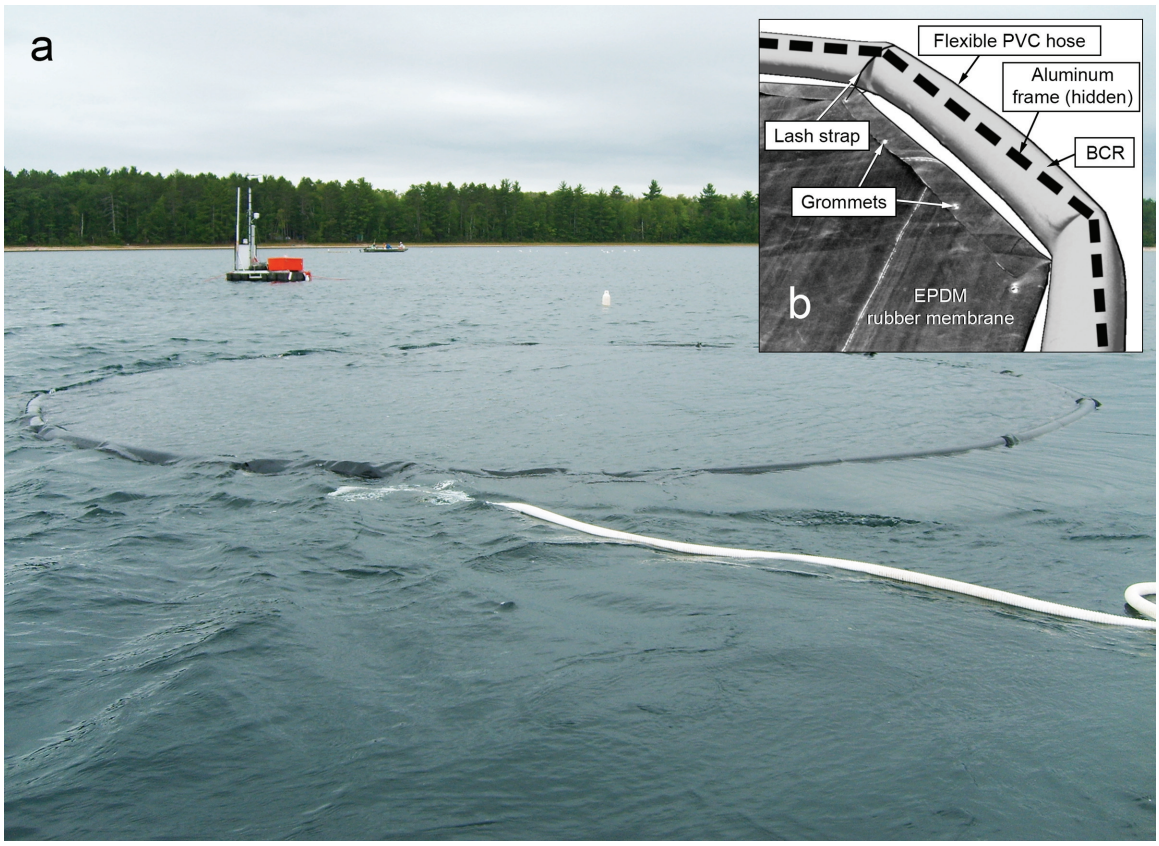

Figure 5.2: GELI components and secondary test deployment on Crystal Lake. **a**) GELI on 10 August 2009 on Crystal Lake, soon after surfacing. Lateral spreading is evident in the northwestern direction (towards the right in the image). An instrumented buoy, similar to "B" in Figure 5.1, is anchored behind the GELI. One of the major improvements to the 2008 design – a 1 inch airline – is visible in the foreground. **b**) Components and materials of the GELI mixing device. The flexible polyvinyl chloride (PVC) hose comprises the outer shell of the buoyancy controlled ring (BCR) and collapses when air is removed, but inflates to a fixed volume when air is pressurized (does not stretch). The metal frame provides structural support for the outer ring, and is internally threaded through the BCR. The ethylene propylene diene M-class (EPDM) rubber membrane is attached to the BCR via lash straps which are looped through grommet supported holes in the membrane. The flexible membrane deforms with the drag and differential density of water when moving through the water column and takes on a bowl or parachute shape when in motion.

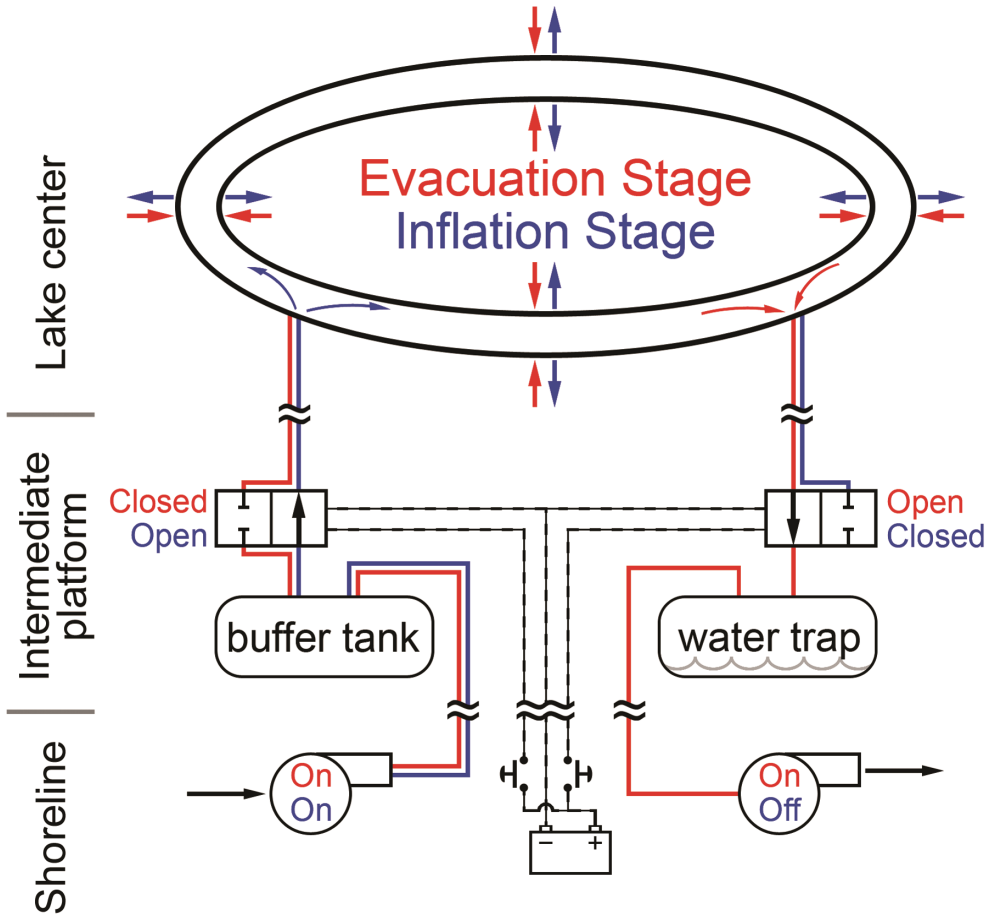

Figure 5.3: Oscillatory vertical motion of the GELI is controlled by alternating buoyancy stages of the BCR (buoyancy controlled ring) with the use of solenoid valves. During the evacuation stage (represented with red arrows), a normally closed solenoid valve is energized (right), allowing a pump to remove air from the BCR. After air is removed from the BCR, the GELI becomes negatively buoyant and sinks. During the inflation stage (represented by blue arrows), energizing a second solenoid valve (left) allows compressed air to enter the BCR from a nearby pressurized buffer tank. After the inflation stage, the buoyant GELI rises through the water column and the evacuation stage begins.

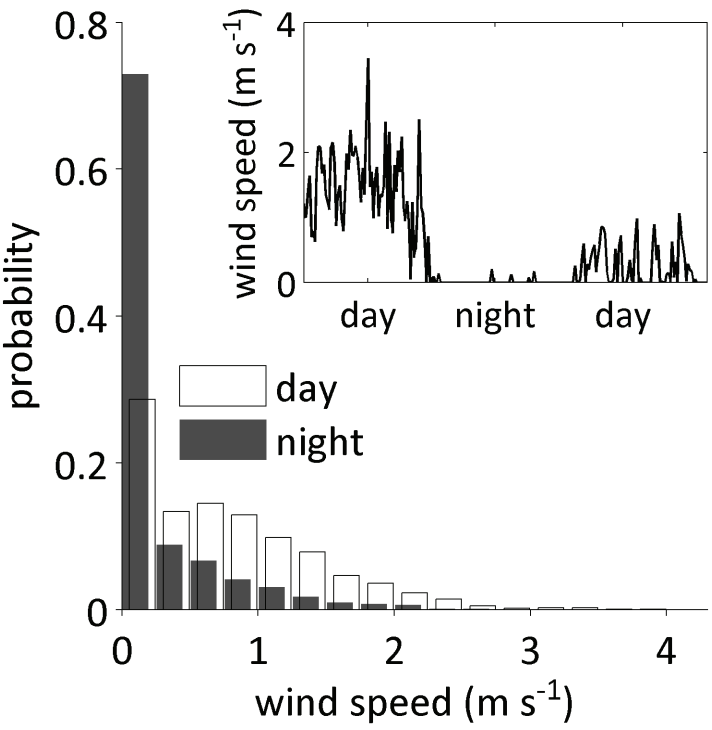

Figure 5.4: A histogram of wind speed measured at the buoy location ("B" in Figure 5.1) during the month of July 2008. Histogram bins are 0.25 m s^{-1} wide and the two time periods (night and day) are shifted by 0.05 m s^{-1} to avoid direct overlap. The upper right panel represents a typical nighttime drop in wind speed (this "night" period corresponds to the low-wind period of "a" in Figure 5.8). Propeller anemometers are inaccurate at low speeds, but we expect this basic distribution to represent day/night variability of wind speed on NSB during the study period.

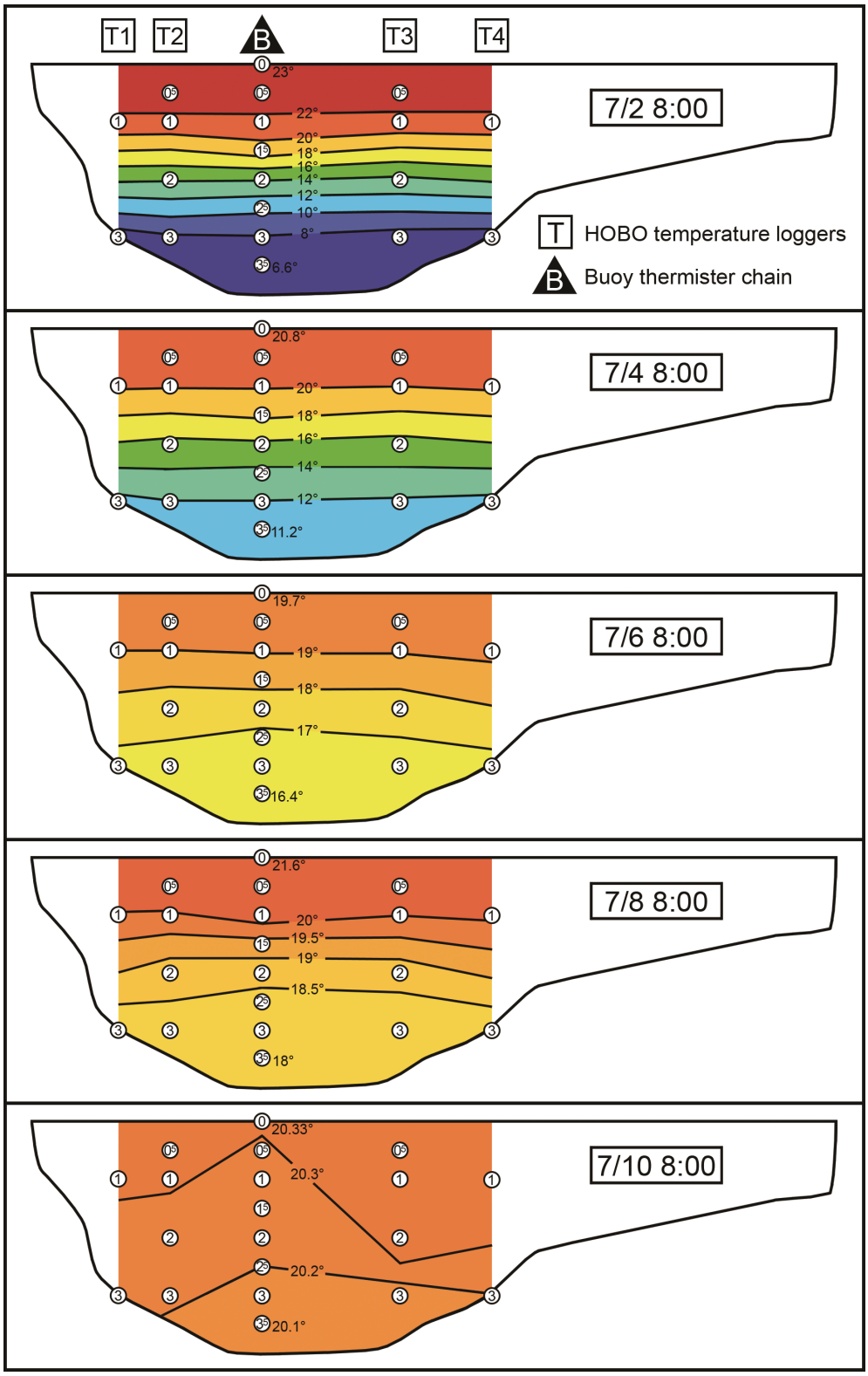

Figure 5.5: Thermal transects which show relative spatial homogeneity of NSB during mixing treatment. Transects were aggregates of high-frequency buoy data ("B" in Figure 5.1) and multiple HOBO logger chains ("T1-T4" in Figure 5.1). The lower waters were

gradually mixed with surface waters by two GELI mixing devices ("G1-G2" in Figure 5.1), resulting in a warming trend at depth. Surface waters were cooled by mixing, augmenting the surface heat flux.

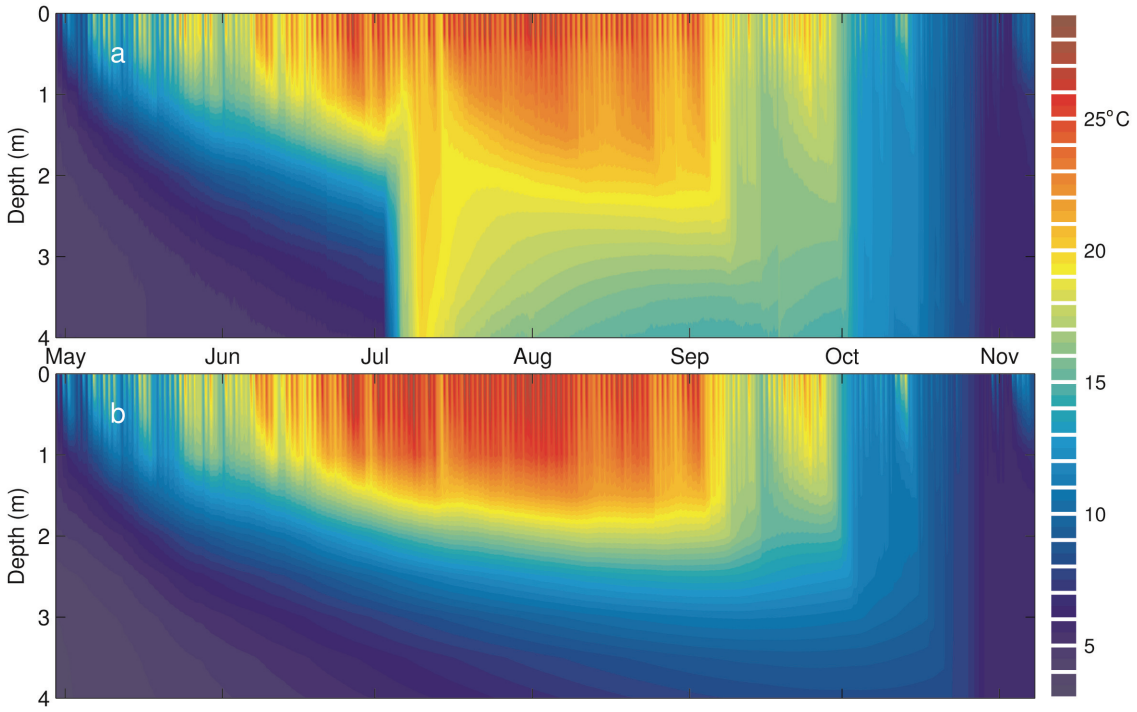

Figure 5.6: Simulated and measured temperatures during the ice-free season of 2008. **a**) Measured water temperature on North Sparkling Bog from buoy thermistors ("B" in Figure 5.1). **b**) Modeled water temperature during the same period, in the absence of an artificial mixing event (mixing experiment was 2 July to 10 July 2008).

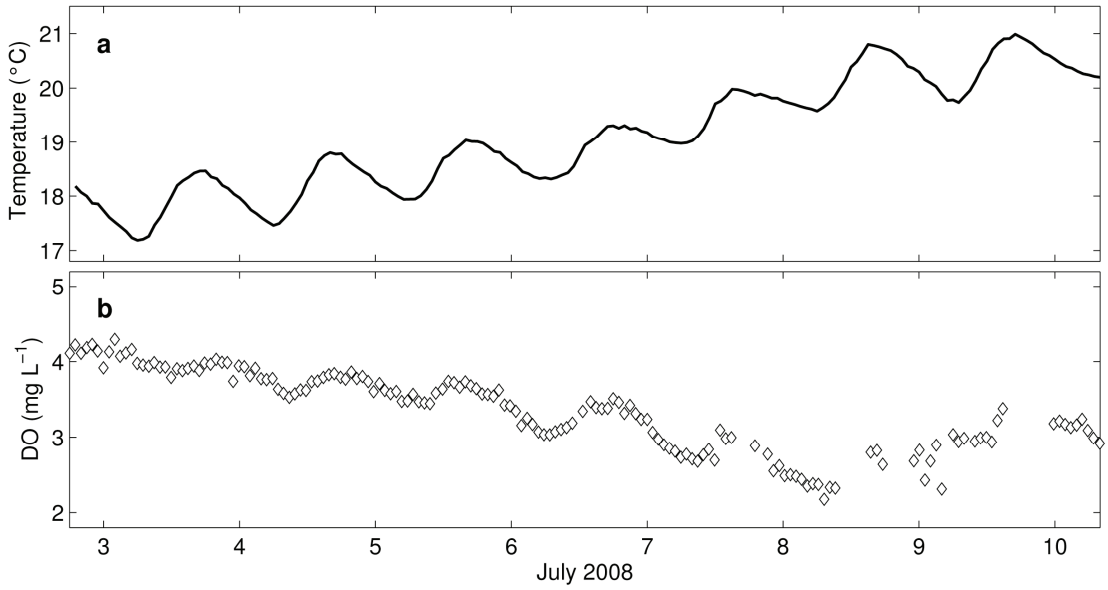

Figure 5.7: Volumetrically averaged measurements of changes in temperature and dissolved oxygen. **a**) Volumetric average temperature during the 2008 experiment, where cooler surface temperatures reduced heat loss and increase gains due to colder surface waters. **b**) Volumetric average dissolved oxygen concentration during the experiment, where changes in water column metabolism were evident as pre-manipulation oxygen levels were not conserved.

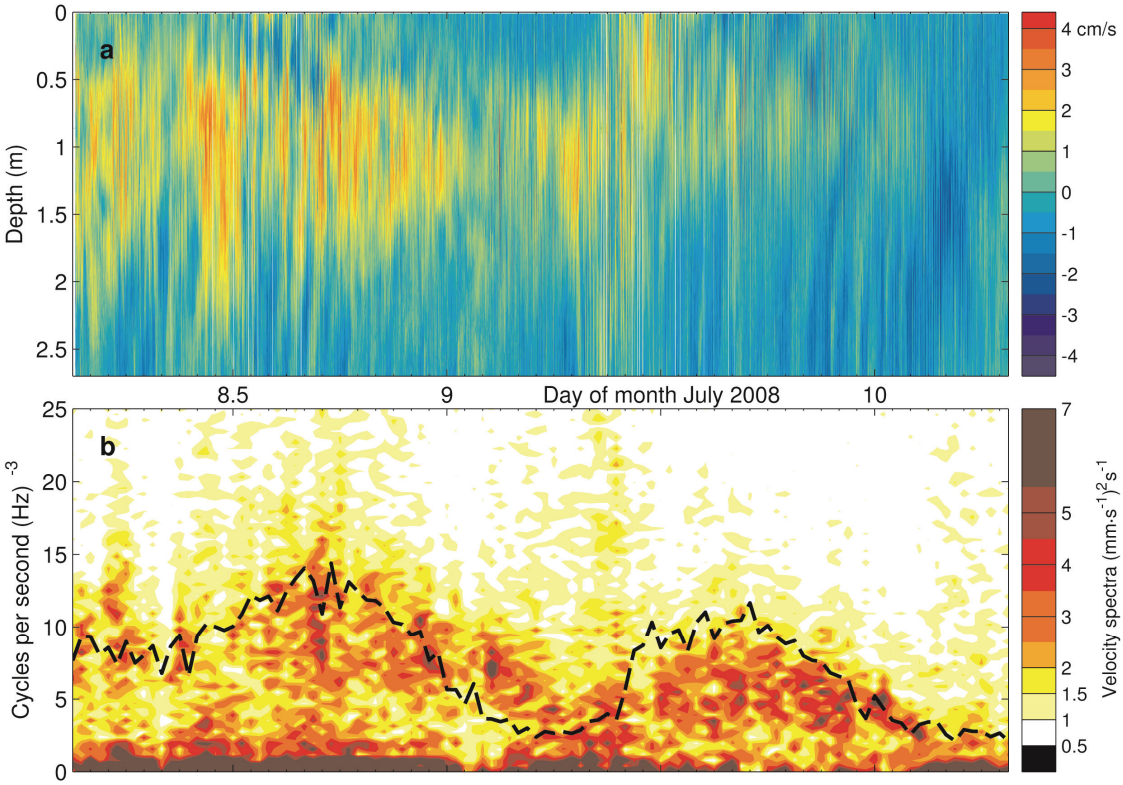

Figure 5.8: ADCP measurements taken during the 2008 experiment (30 m north of the GELIs, positive values to the north) and spectral analysis. **a**) Water column velocity measured during the length of ADCP deployment (8 July 3:00 to 10 July 9:00, 2008). High-frequency internal waves are notable throughout most of the water column, seen here as thin vertical stripes. Higher velocities were found at depths of stronger stratification (0.5 to 1.5 m), which supported the oscillations of wave motion. **b**) Spectral analysis of the 80 cm depth velocity cell. A Fast-Fourier Transform (FFT) was applied to the northern velocity data with a moving window of 30 minutes. Waveforms show spectral peaks with a strong diel signal. The buoyancy frequency (*N*) had a strong relationship with observed wave forms. *N*/8 is displayed as a dashed line, which shows good agreement with high-frequency internal wave peaks.

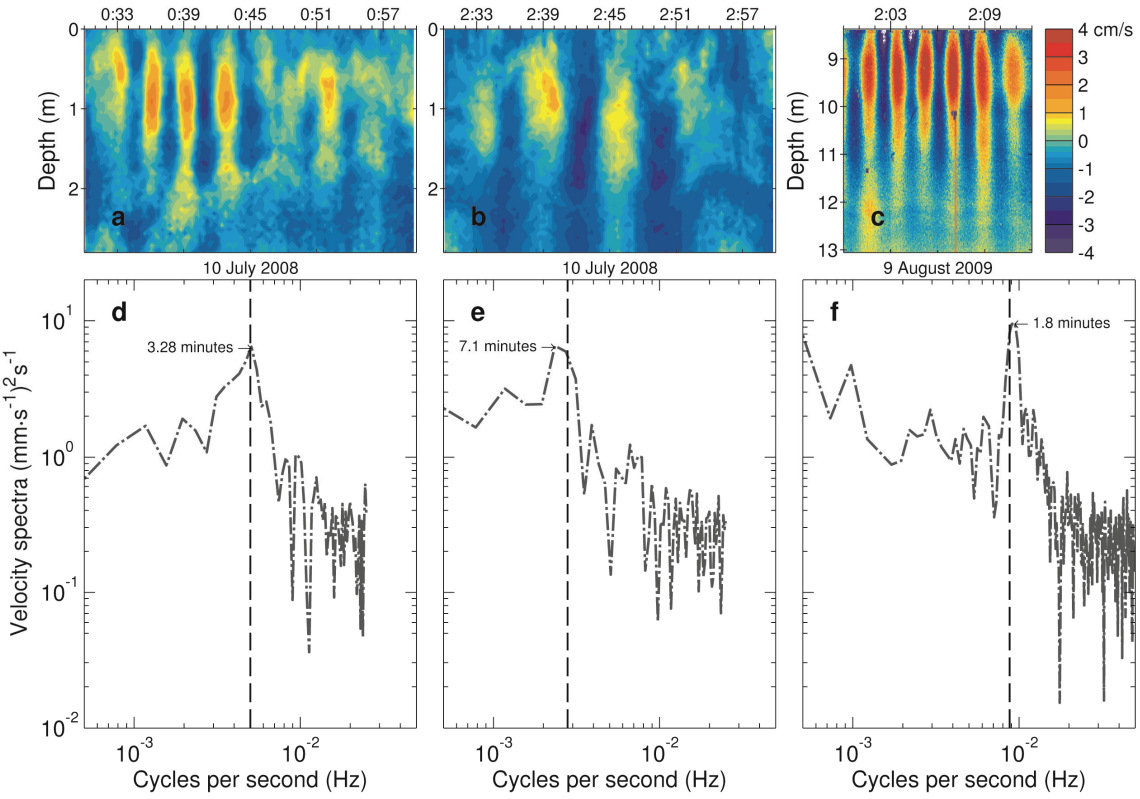

Figure 5.9: ADCP measurements for two periods in Figure 5.8a, in addition to secondary measurements taken at Crystal Lake in 2009 (35 m east of the GELI), with FFT of each time period during GELI operation. **a**) Northern velocities soon after midnight on 10 July 2008 (0:30-1:00). Waveforms were evident in the 0.5 to 1.5 m range as oscillations in the velocity signal. **b**) Northern velocities 2 hours after panel **a**, where lower frequency waveforms are present. **c**) A 12 minute period of 1 Hz eastern velocity ADCP data from the Crystal Lake test, where waveforms are located between 8 and 10 m depths. Waveforms are higher frequency and stronger than panels **a** and **b**, likely due to stronger stratification. **d**) FFT analysis of panel **a**, with spectral peak pointed out (3.28 minutes) and $N/8$ (N is 0.0401 s^{-1}) plotted as a dashed line. **e**) Same as **d** and **e**, with spectral peak of 7.1 minutes and N as 0.0224 s^{-1}. **f**) Same as **e**, with spectral peak of 1.8 minutes and N as 0.0702 s^{-1}.

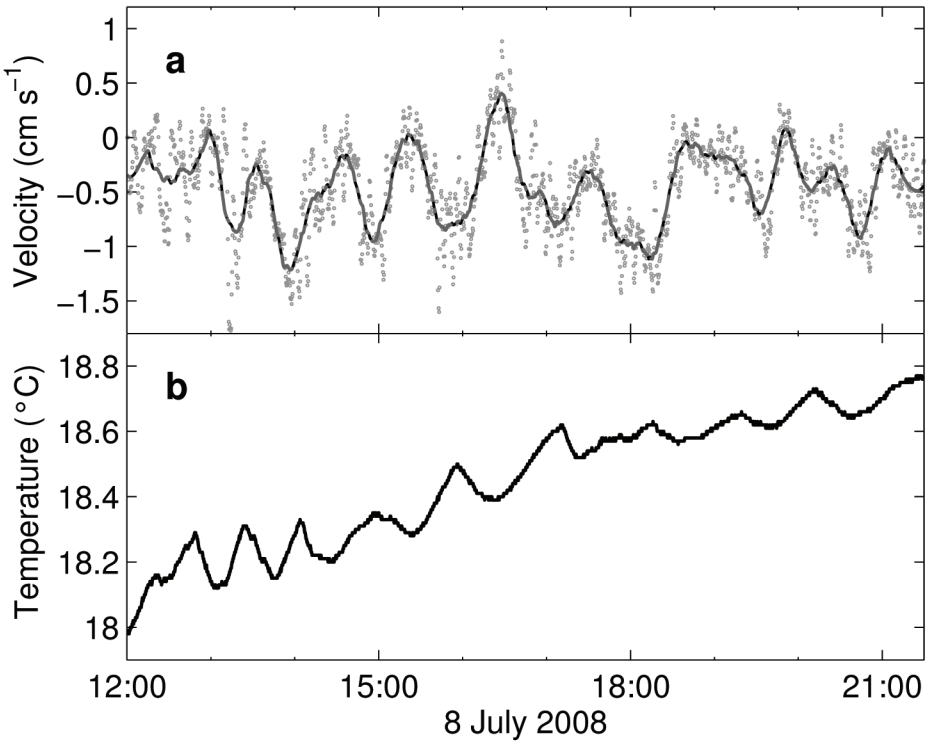

Figure 5.10: Lateral flow patterns on 8 July 2008 as observed by measurements of temperature and velocity (northern direction ADCP). **a**) Pooled mean velocities from 2.2 to 2.7 m depth, where small open circles are 20 second ensemble velocities, with the gray-black dashed line is a 3rd order Savitzky-Golay filter applied to 30 minute moving windows of the 20 second measurements. Oscillations are clear in velocity signals, where periods range from 30 to 50 minutes. During this measurement period, there was a net flow in the southern direction, potentially the result of return flows from circulation cells. **b**) Temperature measurements logged as 20 second ensemble averages from the body of the ADCP. These temperature fluctuations appeared in tandem with lagged velocity fluctuations (in **a**), potentially representing lateral exchange flows. The observed wave periods were variable and did not follow patterns related to ambient stratification.

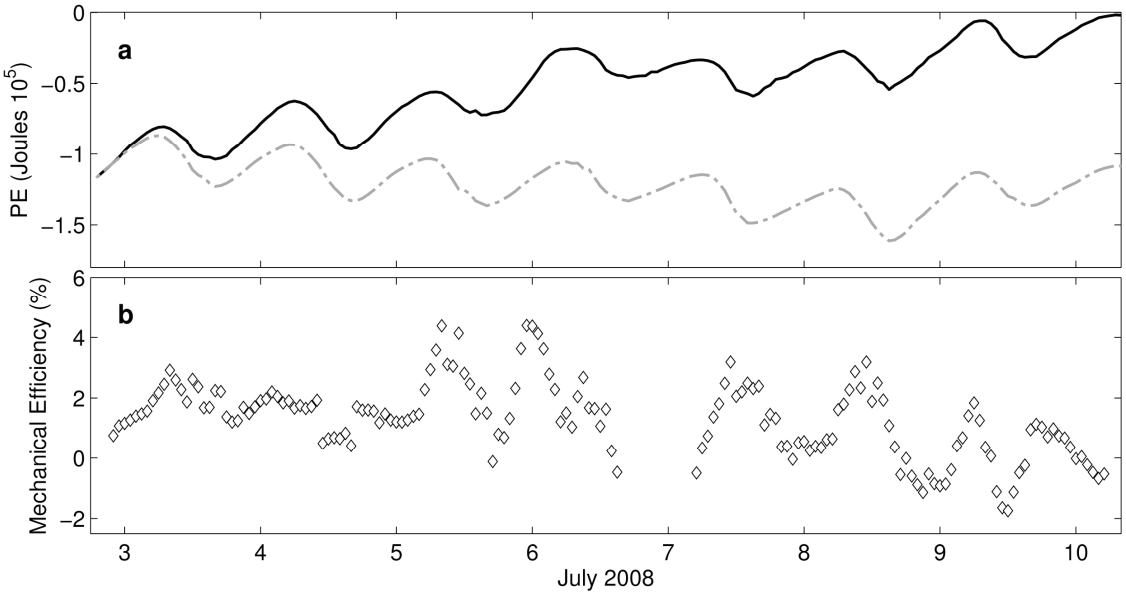

Figure 5.11: Observed and modeled changes in energy resulting from the 2008 mixing manipulation. **a**) Potential energy of the water column for both observed (black line) and modeled (gray dash-dot line). Modeled temperature (which was used to calculate changes in potential energy) is expected to represent the effects of positive and negative buoyancy fluxes in the absence of the mixing manipulation. **b**) Mechanical efficiency of the GELI method as calculated from isentropic work and changes in potential energy (except during a 12 hour break in operation 6 July to 7 July 2008). Efficiency is well above 1% for most of the experiment, but drops below 0 during nighttime convection towards the end of the experiment. We believe this trend results from modeled water column losing stability faster at night because heat is partitioned closer to the surface, so the rate of change of potential energy is greater in the unaltered case during several intervals of low stratification.

Chapter 6 - A method for estimating the diffuse attenuation coefficient (K_d) from paired thermistors

The following is in preparation for submission to Limnology & Oceanography: Methods

> Read JS, EL Kara, ML Pace, KC Rose, LA Winslow. A method for estimating the diffuse attenuation coefficient (K_d) from paired thermistors.

6.1 Abstract

A new method for estimating the diffuse attenuation coefficient (K_d) from paired thermistors was derived using a simplified representation of thermal gains from the attenuation of penetrating shortwave radiation. We show that during cases where radiative gains dominate daily temperature changes, time series measurements of water temperatures at multiple depths (z_1 and z_2) are related to one another by a scaling factor (α). K_d can then be estimated by the simple equation $K_d = \ln(\alpha)/(z_2-z_1)$. A suggested work flow was created which outlines the procedures for calculating K_d according to the paired thermistor (PT) method, and the detection of cases that violate the assumptions of the method. The PT method is best suited for lakes where radiative temperature gains are large relative to physical noise (i.e., small dark lakes), but can be employed for other lake types during certain conditions, such as low wind speeds and/or where spatially redundant measurements of temperatures are available. The optimal vertical placement of thermistors according to a priori knowledge of K_d is also described. This information can be used to inform the design of future deployments using the PT method, or for campaigns where characterizing sub-daily changes in temperatures is important. The PT method is a better physical representation of water column transparency compared to Secchi depth, and can be a useful alternative to expensive and labor intensive radiometer profiles.

6.2 Introduction

Changes in lake water transparency can be indicators of acidification (Schindler et al. 1996), increased terrestrial loading (Tanentzap et al. 2008), or algal blooms (Staehr et al. 2010). The optical measurement of the rate of decay of diffuse radiation in the water column (K_d) is inversely related to water column transparency, yielding a robust coefficient that can be used to follow changes in water clarity through time (Rose et al. 2009). K_d controls the vertical partitioning of radiative energy in the water column via attenuation of the fraction of solar radiation that penetrates below the near-surface waters (often estimated as photosynthetically active radiation, PAR; 400-700 nm). Accurate estimates of K_d require expensive instrumentation and manual sampling (e.g., Rose et al. 2009), or the use of in situ sensors that are prone to biological or chemical fouling (Staehr et al. in press). Simpler replacement metrics for water clarity (i.e., Secchi depth) are not directly related to physical measure of K_d (Kirk 1994) and these observations are often biased by user interpretation.

Transparency is directly linked to many physical properties in lakes that can be readily measured with the aid of thermistor strings, such as the rate of hypolimnetic heat gain (Chapter 4), the depth of the mixed layer (Fee et al. 1996), the duration of stratification (Persson and Jones 2008), and average water temperatures (Tanentzap et al. 2008). With sensor networks rapidly accumulating observations of water temperatures in lakes (Hanson 2007; Porter et al. 2009), these data may be used to infer other important yet difficult to measure characteristics, such as K_d. Here, we test whether high-frequency temperature data can be used to estimate K_d in a series of lakes that vary over a range in observed K_ds. We used small (< 10 ha) lakes which have relatively simple hydrodynamics to develop and test these methods. We test various simplifying physical assumptions en route to a method for estimating K_d from paired thermistors, which can

be used to follow patterns in transparency for small stably stratified lakes, and, under certain conditions, could be applicable to a broader size and transparency range of lakes.

6.3 Methods and Procedures

6.3.1 *Site description*

Details for the six small lakes included in this analysis can be found elsewhere (Chapter 4; Read et al. 2012), but in brief, all are temperate bogs or poor fens located in Vilas County (Wisconsin, USA) with no measureable surface inflows or outflows (Table 6.1). The lakes range in surface area from 0.06 ha (Timber Bog) to 3.8 ha (Mouser Bog), are surrounded by low-lying forests or wetlands, and have low wind speeds (typically < 1 m s^{-1}).

6.3.2 *Physical measurements*

Each lake had a central buoy or surface float that held a string of thermistors of varying vertical resolution within the first 2 m of the water column. The minimum spacing of thermistors across this depth range was 25 cm; with a maximum of 50 cm (Table 6.1). Thermistors were also of different brands and precision specifications (Table 6.1) and logging intervals for temperature ranged from 1 to 10 minutes. We used a single nearby station (the Noble F. Lee Airport; 45.93° N, -89.73° W) for meteorological measurements, including incoming solar radiation (Eppley PSP pyranometer) and precipitation.

Estimates of the diffuse attenuation coefficient (K_d) of PAR were made with observations of the depth-decay of PAR from one of two profiling radiometers. We used Biospherical Instruments (biospherical.com) BIC and PUV models, which sample depth and irradiance at 4 and 1 Hz, respectively. For this analysis, we make no distinction between the two Biospherical models as they were fitted with the same type of PAR photodiodes and only varied in sampling frequency. K_d was estimated according to the relationship $E_z = E_0 \exp(-K_d \cdot z)$ where E_z is PAR

irradiance at a given depth (z), and E_0 is PAR irradiance at the surface (i.e., the portion of PAR that is not reflected or absorbed in the surface layer). Observations of E_z were log-transformed and K_d was estimated as the slope of the non-linear least squares fit of the relationship given by $\log(E_z) = -K_d \cdot z + \log(E_0)$. Error estimates of K_d using this method were calculated as the 95% confidence intervals of the least squares fit to K_d in the above equation.

6.3.3 *Modeling attenuated temperature gains*

Lakes often display inter-seasonal variations in the rate of temperature gain below the mixed layer (Figure 6.1). These differences in heating rates may be the result of differences in the penetrating flux of solar radiation, rates of vertical mixing, or sediment heating (among other drivers of temperature change). In small sheltered lakes, this inter-seasonal variability in hypolimnetic temperature gains is likely a product of differences in transparency (Chapter 4). Small lakes have simplified hydrodynamics and are often better represented by one-dimensional models compared to larger lakes. Read et al. (Chapter 4) used a simple hydrodynamic model to estimate K_d by minimizing the difference between predicted and observed (via instrumented buoys) water temperatures. This method is effectively the inverse of the Jassby and Powell (1975) heat tracer method, which uses the rate of eddy diffusion as an unknown instead of K_d. Data requirements for this approach, however, are high. High-frequency observations of meteorological conditions (incoming shortwave and longwave radiation, air temperature, relative humidity, and wind speed), lake morphometry, and outward radiation, in addition to accurate estimates of the fluxes of sensible and latent heat are necessary to estimate K_d from temperature measurements using this one-dimensional hydrodynamic modeling approach. Fortunately, high-frequency meteorological and temperature data are becoming increasingly common (Porter et al. 2009).

Here, we focus on measurements of temperature where the gain of energy from the sun is much larger than other drivers that may influence water temperatures. For a simplified one-dimensional representation of a lake (see Fang and Stefan 1999), temperature change (ΔT) during an interval of time (∂t) can be parameterized by

$$\Delta T(z) = K_z/\partial z(\partial T(z)/\partial z)\cdot\partial \mathrm{t} + H(z)/(\rho C_w)\cdot\partial \mathrm{t} \qquad (6.1)$$

where K_z is the rate of eddy diffusion, z is depth (positive downward from the surface), H is a depth-specific sink or source of thermal energy, ρ is the density of water, and C_w is the specific heat of water. During daytime, at depths where significant penetrating radiation is present, H is dominated by the attenuation of penetrating radiation (K_d; approximately 400-700 nm), and $E(z) = E_0\cdot\exp(-K_d\cdot z)$. The contribution of attenuation ($H_{rad}(z)$) to $H(z)$ would then be

$$H_{rad}(\mathrm{z}) = E_0K_d\cdot\exp(-K_d\cdot z) \qquad (6.2)$$

At times and depths where H_{rad} is the dominant driver of changes in water temperatures (i.e., $H_{rad} >> K_z(\partial T(z)/\partial z)\cdot\rho C_w$; $2H_{rad} >> H$), water temperatures will display patterns that scale with E_0. Because E_0 is a portion of incoming shortwave radiation, water temperatures during these periods of H_{rad} dominance will closely resemble cumulative energy gains from solar flux (Figure 6.2).

Theoretically, measurements of E_0 in addition to measurements of water temperature during periods of H_{rad} dominance could be used to solve for K_d by combining equations 6.1 and 6.2. Instead, we note that equations 6.1 and 6.2 can be combined in a way that eliminates E_0 from

the formulation, by including a second depth measurement of water temperature. This method provides the ability to estimate a K_d that excludes the effects of a variable abledo. Temperature gains at these two depths will scale with one another relative to the average K_d across this depth range as

$$H_{rad}(z_1)/H_{rad}(z_2) = \exp(K_d \cdot z_2 - K_d \cdot z_1) \quad (6.3)$$

Applying this relationship to equation 6.1, shows that equation 6.3 is equivalent to the multiplier that best scales the time series of measurements $T(z_2)$ to $T(z_1)$. This scaling factor (α) scales temperature gains at the two relative depths, and can be explained by the linear model

$$T(z_1) = \alpha \cdot \mathrm{T}(z_2) + b, \quad (6.4)$$

where b is the offset between the two time series. Rearranging equation 6.3 and incorporating the scaling factor α,

$$K_d = \ln(\alpha)/(z_2 - z_1). \quad (6.5)$$

6.3.4 *Procedure*

We have outlined a theoretical methodology for estimating K_d from paired thermistor measurements (hereafter referred to as the PT method), but accurate estimates of K_d from this method are limited to periods when other processes which may affect temperature measurements

can be assumed to be negligible. Below, we outline a procedure for applying this simplified method to two time series of paired thermistor measurements.

The flow of the following procedure is highlighted in Figure 6.3. 1) Temperature measurements should be chosen from two depths that are shallow enough to show visible daily temperature gains, while also being below the actively mixed near-surface layer. These data should then be quality controlled to remove obviously errant values. 2) After outlier removal, these datasets should then be grouped by days, as K_d fits are most effective using a full range of daytime measurements (i.e., a greater number of datapoints). For each daytime grouping, the time of sunrise and sunset is calculated relative to the timezone of the datasets, and the daytime values are truncated to only include measurements that are not influenced by cooling (we found that the period between 3 hours after sunrise and 4 hours before sunset worked best for our lakes). 3) Both thermistor measurements should have a positive (gaining temperature) slope during the truncated period, and the shallower thermistor should display a steeper slope compared to the deeper thermistor (see equation 6.2). If either of these rules is violated, the day should be excluded from the calculation of K_d. 4) Next, the observation points of the two datasets that intersect (matching time points) are combined to solve the linear model for α (see equation 6.4). The solution for α should be positive and greater than 1, both of which are required to pass the two previous tests. If the variance of the estimate for α is too high, the day should also be excluded. 5) A daily value of K_d can be calculated according to equation 5 when truncated datasets that have met the requirements outlined above (Figure 6.4).

Various statistical tests can be utilized in the above steps, including a significance test for a positive slope and an analysis of variance. Confidence intervals for the slope parameter (α) can also be estimated. Further quality control can also then be applied to K_d estimates by propagating

uncertainty in both α and the distance between the thermistor pairs (z_2-z_1) into equation 6.5. If the paired thermistors result in multiple daily estimates of K_d, this grouping of values can also be used for statistical outlier removal if values are questionable.

6.4 Assessment and discussion

6.4.1 *Model assumptions*

The PT method described above relies on the assumption that users can selectively choose intervals during the day when the vertical attenuation of solar radiation can be assumed to be the only significant source of measured temperature change at multiple depths. Other physical processes that can influence temperatures, for example, mixing driven by wind or convection (Read et al. 2012), sediment heat gains (Likens and Johnson 1969; Fang and Stefan 1999), or inflows (Imberger and Patterson 1990) will introduce error into K_d estimates. These processes may affect variance in α if they introduce variability in heat gain or result in either under- or over-estimation of K_d if they affect one sensor but not the other. Many small lakes do not posses surface inflows, and sediment heat gains would be expected to be quite low when the optical depth of the water column is shallow (i.e., when very little light reaches the sediments). When the water column is actively increasing in stratification (a condition satisfied when surface water temperature gains are depth-dependant, with shallow waters warming more quickly; see Figure 6.4), vertical mixing rates are slow below the depth of the surface mixed layer (Macintyre et al. 2009). Small, wind-sheltered lakes have been shown to have diffusive thermal heat transfer below the actively mixed surface layer to be at or near the molecular rate ($K_z = 1.4e^{-7}$ m^2 s^{-1}; Chapter 4).

Since temperature gains (or losses) from diffusion are a function of both K_z and the vertical gradient of water temperatures (equation 6.1), we can calculate diffusive gains and

approximate their contribution to measured increases in water temperatures. For an example case, Timber Bog was extremely stratified on 27 May 2011 (Figure 6.4), and we can estimate the portion of the ~1.6 °C gain measured at 0.5m during 9:00-15:00 from the vertical diffusion of heat. Using conservative estimates of the thermal gradient between neighboring measurements (using the maximum for the day), $\partial T(z)/\partial z$ between 0.25 m and 0.5 m measurements would be 8 °C m^{-1}, and approximately 4 °C m^{-1} between 0.5 m and 0.75 m measurements. Taking into account a positive energy flux from above (energy flow from the 0.25 m towards the 0.5 m depth) and a negative loss below (positive gains to the 0.75 m at the expense of the 0.5 m depth), the net effect on water temperatures from K_z would be a gain of 0.05 °C, or approximately 3% of the measured increase in water temperature over this time period. This percentage is similar for a variety of depths above 10% light penetration and ranges of transparency (data not shown), as increased clarity results in lesser attenuation gains, but also a smaller thermal gradient to drive diffusive fluxes. While this temperature gain is not negligible, it represents a conservative thermal gradient, and as such, the actual contribution of K_z on sunny days is expected to be close to two orders of magnitude smaller than H_{rad}.

6.4.2 *Method validation*

Assuming that the proposed criteria for above method are valid, there should be reasonable agreement between this method (PT method) and other methods of estimating K_d, such as fits to the exponential decay rate of PAR. For the six lakes fitted with paired thermistors, we were able to make 25 unique estimates of K_d using the Biospherical PUV or BIC instruments that overlapped with thermistor deployments. We considered these 25 values to be ideal measurements for this method comparison, given the accuracy of this class of radiometers and the high vertical density of light measurements on a given profile (typically ~900 data points per

profile). Because transparency can vary in response to rain events or algal blooms (for example), we limited our comparisons with the paired thermistor method to be within 3 days of the optical profiles (although 16 of the 25 were taken from the same day). The PT method compared well with the 25 optical profiles (Figure 6.5), with a near 1:1 slope between the two methods. Hocking and Straskaba (1999) suggested that the 1:1 relationship between photon attenuation (measured by the radiometer) and energy attenuation (estimated by the paired thermistor method) would be expected for the darker lakes in this study, but that deviation is likely for lakes with higher transparency (as much as 20% for $K_d = 0.2$ m^{-1}).

We used two seasons (2009-2010) of data from North Sparkling Bog (Table 6.1) to highlight the utility of this method for characterizing seasonal changes in K_d. 2009 was an unusually dry year (16 cm of precipitation during June-August) and 2010 had an unusually high amount of precipitation during the summer period (45 cm of precipitation during June-August). We found a decrease in K_d during the summer months of 2009 (Figure 6.6a) while 2010 increased in K_d during the same period. During the wet year (2010) the highest measured Kd occurred in early August, while in 2009 (the dry year) the maximum Kd occurred in mid July. This difference in timing is probably due to the large difference in precipitation and hydrologic connectivity between the bog and the input of chromophoric allocthonous organic matter.

6.4.3 *Optimal thermistor placement*

In order for radiative gains to be the dominant source of temperature gains, the PT method requires adequate solar radiation, as well as thermistor placement at depths shallow enough to receive measureable changes in thermal energy through attenuation of this radiation. The signal of daytime temperature gains must be strong enough to be measured within the precision of the thermistors, and must also outweigh other sources of physical noise, such as

internal wave motions. Noise (we use the term "noise" to broadly cover sensor noise and physical processes that induce temperature fluctuations) in the daily gain signal for our study lakes varied with lake size and clarity. The smallest lake (Timber Bog; 0.06 ha) had very little noise associated with the temperature gain signal (see Figures 6.2, 6.4), and thus the PT method returned values for 80% of deployment days (50 and 75 cm depths; mean of K_d = 1.98; standard deviation of 0.38 m^{-1}). Larger lakes had noisier fits to α, and the percentage of days which satisfied the PT method procedure (Figure 6.3) decreased as lakes increased in size, likely due to increased wind speeds (Read et al. 2012). As such, the level of temperature gain required from both thermistors for proper estimates of K_d using the PT method is likely a function of lake size (where size can be used as a proxy for wind speeds). In the larger size class of lakes where we tested this method, a gain of 0.75 °C was often the minimum detectable change that could be used consistently for this method, a number which can be used to bound the placement of the bottom thermistor (z_2) for future deployments. The shallower thermistor must have significantly higher gains compared to the bottom thermistor, but should be a deep as possible so as to avoid surface layer dynamics. A 1.5 °C gain for the shallow thermistor (twice the gain of the deeper thermistor) can therefore be used to determine the appropriate depth for z_1. These theoretical constraints on temperature gains can potentially be reduced by limiting the level of measured physical noise, either by applying the method during uncharacteristically calm periods, or by spatial averaging of multiple thermistors placed at z_1 and z_2 in different locations in the lake.

A priori knowledge of Kd (either from previous measurements or an estimate from Secchi depth) can be used to inform the positioning sensors in the water column in order to best capture thermal gains during the daytime. Optimal placement of thermistors can increase the accuracy and usefulness of the PT method, while also being an important component of

thermistor chain design if accurate characterization of sub-daily heat fluxes (Jonas et al. 2003; Read et al. 2012) or delineation of the depth of the surface mixed layer (Macintyre et al. 2009; Read et al. 2011) is desired. During a six hour window centered on solar noon, a sunny day in our study region will have an average incoming solar radiation flux of close to 800 W m^{-2} during much of the stratified season (Meyers and Dale 1983). We can assume approximately 45% of this energy flux will penetrate below the near-surface layer and thus be available to be attenuated in the water column (Kirk 1994). Using this knowledge of incoming radiation and a simplified observation period (6 hours for this example), we can combine equations 6.2 and 6.1 to estimate the depth of measurements required for a given temperature gain under these conditions. Thermistor placements for these conditions are given in Table 6.2 for a range of K_d and temperature gains.

6.5 Comments and recommendations

We have outlined a novel new limnological method that uses measurements from paired thermistors to estimate the diffuse attenuation coefficient (K_d). Although this method is not well suited for situations when measureable heat gains are not dominated by attenuation (e.g., large lakes or clear lakes), most lakes are small and stained with dissolved organic carbon (Downing et al. 2006; Hanson et al. 2007; Downing 2010) and thus are good candidates for thermistor deployments that can be used to estimate K_d (Figure 6.5), or to follow seasonal patterns in transparency (Figure 6.6).

These results also suggest that thermistors chains in less transparent lakes should have finer vertical resolution compared to low K_d lakes (Table 6.2) in order to accurately characterize the vertical partitioning of light and heat. These findings can be used to inform choices for thermistor locations for resolving patterns in stratification (Macintyre et al. 2009; Read et al.

2011) or heat content (Lenters et al. 2005) in lakes of varying transparency, as well in the design of a deployment using the paired thermistor method to estimate K_d.

Small protected lakes with closely paired thermistors are the best candidates for this method, but spatial redundancy in thermistor placement may allow the method to be used on larger, clearer lakes. Increasing the sampling frequency of sensors also improves the ability to use the PT method on a given deployment (data not shown), and we found that sampling intervals between 1 and 5 minutes to yield the best results (although we did not sample at higher frequencies). In conclusion, the PT method is a new and novel way of estimating K_d when time series measurements of temperature are available – data that are becoming increasingly common in limnological campaigns (Hanson 2007; Porter et al. 2009). When applicable, the PT method is a better physical representation of water column transparency compared the commonly used metric of Secchi depth (Kirk 1994), and thus represents a promising new method for estimating K_d when field sampling is not possible or high quality radiometers are not accessible.

6.6 References

Downing, J. A. 2010. Emerging global role of small lakes and ponds: little things mean a lot. Limnetica **29:** 9-23.

Downing, J. A., Y. T. Prairie, J. J. Cole, C. M. Duarte, L. J. Tranvik, R. G. Striegl, W. H. Mcdowell, P. Kortelainen, N. F. Caraco, J. M. Melack, and J. J. Middelburg. 2006. The global abundance and size distribution of lakes, ponds, and impoundments. Limnology and Oceanography **51:** 2388-2397, doi: 10.4319/LO.2006.51.5.2388.

Fang, X., and H. G. Stefan. 1999. Projections of climate change effects on water temperature characteristics of small lakes in the contiguous US. Climatic Change **42:** 377-412, doi: 10.1023/a:1005431523281.

Fee, E. J., R. E. Hecky, S. E. M. Kasian, and D. R. Cruikshank. 1996. Effects of lake size, water clarity, and climatic variability on mixing depths in Canadian Shield lakes. Limnology and Oceanography **41:** 912-920.

Hanson, P. C. 2007. A grassroots approach to sensor and science networks. Frontiers in Ecology and the Environment **5:** 343-343.

Hanson, P. C., S. R. Carpenter, J. A. Cardille, M. T. Coe, and L. A. Winslow. 2007. Small lakes dominate a random sample of regional lake characteristics. Freshwater Biology **52:** 814-822, doi: 10.1111/j.1365-2427.2007.01730.x.

Hocking, G. C., and M. Straskraba. 1999. The effect of light extinction on thermal stratification in reservoirs and lakes. International Review of Hydrobiology **84:** 535-556.

Imberger, J., and J. C. Patterson. 1990. Physical limnology. Advances in Applied Mechanics **27:** 303-475.

Jassby, A., and T. Powell. 1975. Vertical patterns of eddy diffusion during stratification in Castle Lake, California. Limnology and Oceanography **20:** 530-543.

Jonas, T., A. Stips, W. Eugster, and A. Wuest. 2003. Observations of a quasi shear-free lacustrine convective boundary layer: Stratification and its implications on turbulence. Journal of Geophysical Research-Oceans **108:** 3328, doi: 10.1029/2002JC001440.

Kirk, J. T. O. 1994. Light and Photosynthesis in Aquatic Ecosystems, 2 ed. Cambridge University Press.

Lenters, J. D., T. K. Kratz, and C. J. Bowser. 2005. Effects of climate variability on lake evaporation: Results from a long-term energy budget study of Sparkling Lake, northern Wisconsin (USA). Journal of Hydrology **308:** 168-195, doi: 10.1016/j.jhydrol.2004.10.028.

Likens, G. E., and N. M. Johnson. 1969. Measurement and analysis of annual heat budget for sediments in two Wisconsin lakes. Limnology and Oceanography **14:** 115-&.

Macintyre, S., J. P. Fram, P. J. Kushner, N. D. Bettez, W. J. O'brien, J. E. Hobbie, and G. W. Kling. 2009. Climate-related variations in mixing dynamics in an Alaskan arctic lake. Limnology and Oceanography **54:** 2401-2417.

Meyers, T. P., and R. F. Dale. 1983. Predicting daily insolation with hourly cloud height and coverage. Journal of Climate and Applied Meteorology **22:** 537-545.

Persson, I., and I. D. Jones. 2008. The effect of water colour on lake hydrodynamics: a modelling study. Freshwater Biology **53:** 2345-2355, doi: 10.1111/J.1365-2427.2008.02049.x.

Porter, J. H., E. Nagy, T. K. Kratz, P. Hanson, S. L. Collins, and P. Arzberger. 2009. New Eyes on the World: Advanced Sensors for Ecology. Bioscience **59:** 385-397, doi: 10.1025/bio.2009.59.5.6.

Read, J. S., D. P. Hamilton, A. R. Desai, K. C. Rose, S. Macintyre, J. D. Lenters, R. L. Smyth, P. C. Hanson, J. J. Cole, P. A. Staehr, J. A. Rusak, D. C. Pierson, J. D. Brookes, A. Laas, and C. H. Wu. 2012. Lake-size dependency of wind shear and convection as controls on gas exchange. Geophysical Research Letters, doi: 10.1029/2012GL051886.

Read, J. S., D. P. Hamilton, I. D. Jones, K. Muraoka, L. A. Winslow, R. Kroiss, C. H. Wu, and E. Gaiser. 2011. Derivation of lake mixing and stratification indices from high-resolution lake buoy data. Environmental Modelling & Software **26:** 1325-1336, doi: 10.1016/j.envsoft.2011.05.006.

Rose, K. C., C. E. Williamson, S. G. Schladow, M. Winder, and J. T. Oris. 2009. Patterns of spatial and temporal variability of UV transparency in Lake Tahoe, California-Nevada. J. Geophys. Res.-Biogeosci. **114:** 9, doi: 10.1029/2008jg000816.

Schindler, D. W., S. E. Bayley, B. R. Parker, K. G. Beaty, D. R. Cruikshank, E. J. Fee, E. U. Schindler, and M. P. Stainton. 1996. The effects of climatic warming on the properties of boreal lakes and streams at the Experimental Lakes Area, northwestern Ontario. Limnology and Oceanography **41:** 1004-1017.

Staehr, P. A., K. Sand-Jensen, A. L. Raun, B. Nilsson, and J. Kidmose. 2010. Drivers of metabolism and net heterotrophy in contrasting lakes. Limnology and Oceanography **55:** 817-830, doi: 10.4319/lo.2009.55.2.0817.

Tanentzap, A. J., N. D. Yan, B. Keller, R. Girard, J. Heneberry, J. M. Gunn, D. P. Hamilton, and P. A. Taylor. 2008. Cooling lakes while the world warms: Effects of forest regrowth and increased dissolved organic matter on the thermal regime of a temperate, urban lake. Limnology and Oceanography **53:** 404-410, doi: 10.4319/LO.2008.53.1.0404.

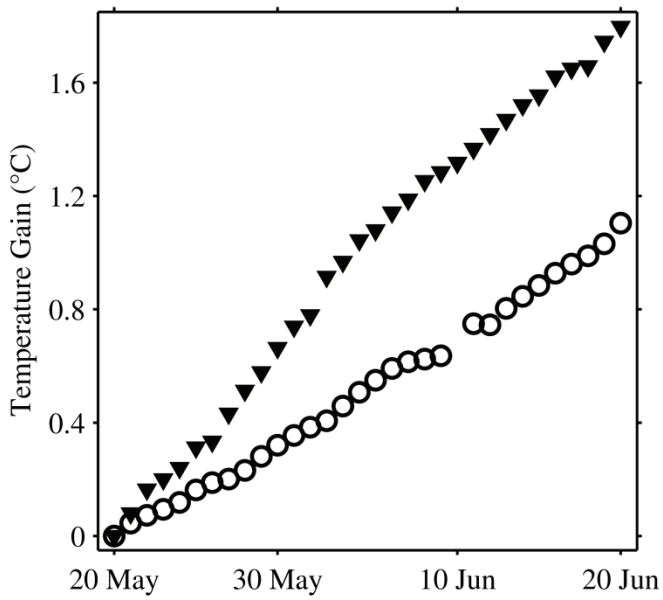

Figure 6.1: Relative temperature gains for North Sparkling Bog from 20 April to 20 June for 2009 (black triangles) and 2010 (open circles).

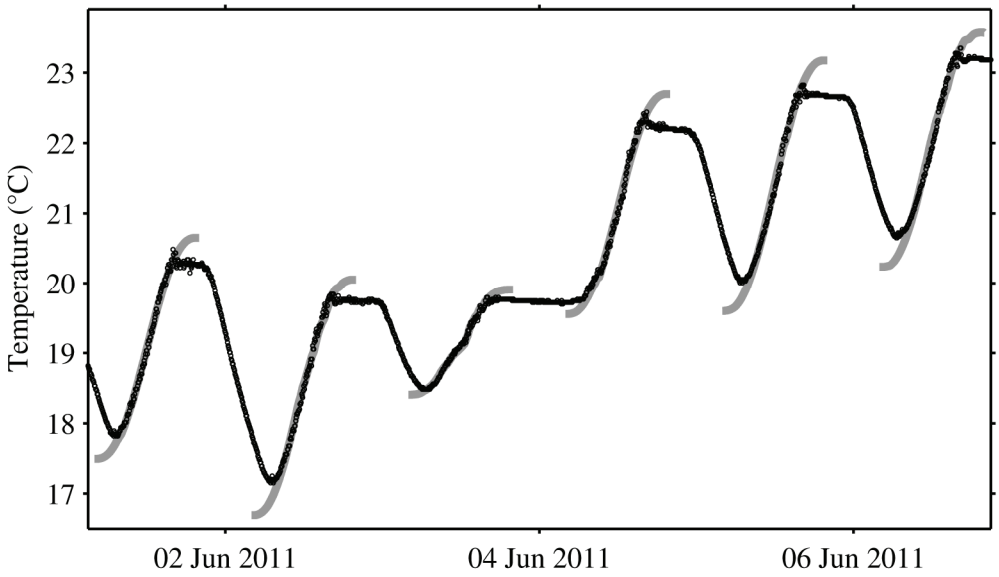

Figure 6.2: Scaled fits of daily cumulative shortwave radiation (thick grey line) to 0.5 m depth temperature measurements for Timber Bog (black dots).

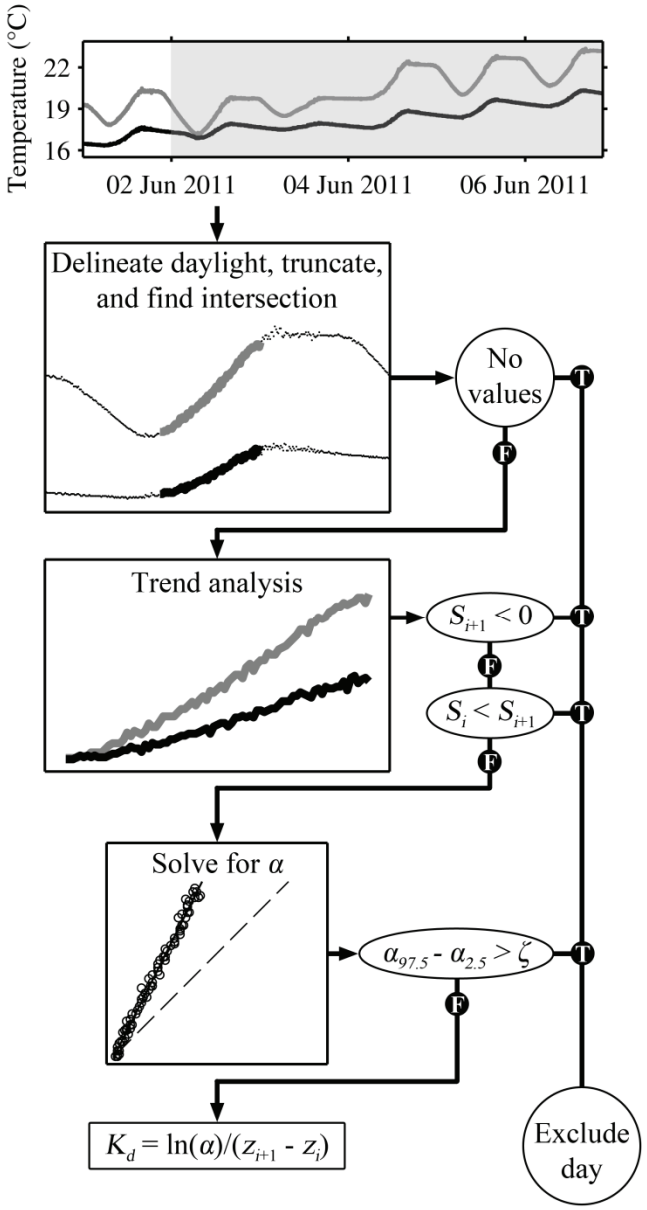

Figure 6.3: Workflow for estimating Kd from paired thermistor measurements.

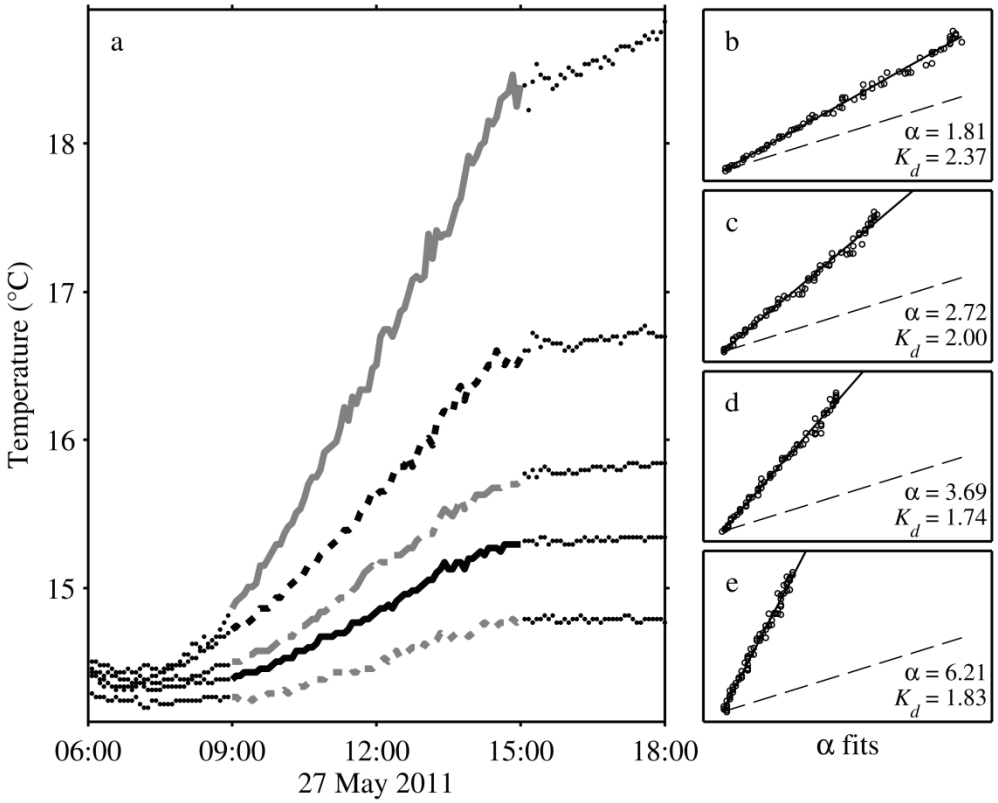

Figure 6.4: Estimates of K_d from paired thermistors on Timber Bog. **a**) Measurements of daily water temperatures were truncated (**Figure 6.3**) for K_d estimates, where dots are measurements outside the truncated range for the datasets. Temperatures from 0.25 m (grey line), 0.5 m (black dotted line), 0.75 m (grey dash-dot line), 1 m (black line) and 1.25 m (grey dotted line). **b**) α and K_d estimates from 0.25 m and 0.5 m thermistors, where black line is α, and dashed line is a 1:1 line. **c**) same as b, but for 0.25 m and 0.75 m thermistors. **d**) same as b, but for 0.25 m and 1 m thermistors. **e**) same as b, but for 0.25 m and 1.25 m thermistors.

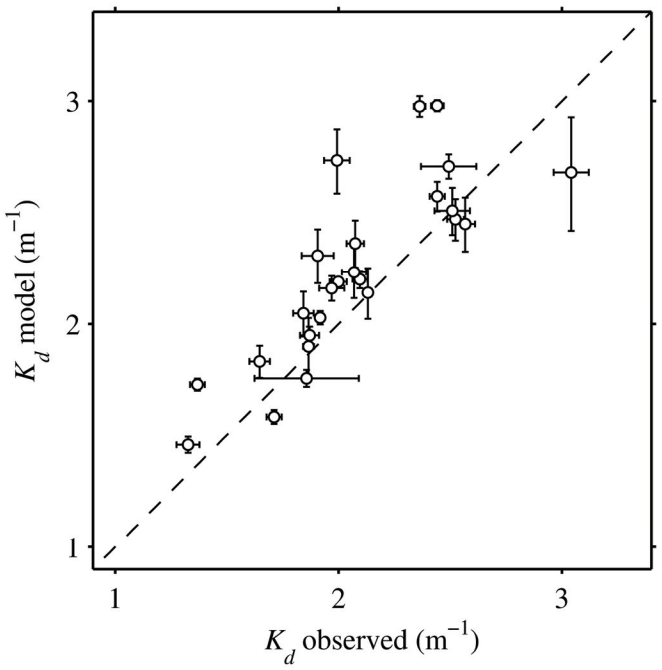

Figure 6.5: Estimated K_d (model K_d) compared to log-linear fits to the decay rate of PAR measured using Biospherical profilers (K_d observed). Error bars were calculated as 95% confidence intervals to the log-linear fit to PAR versus depth (K_d observed) and calculating model K_d using 95% confidence intervals for α.

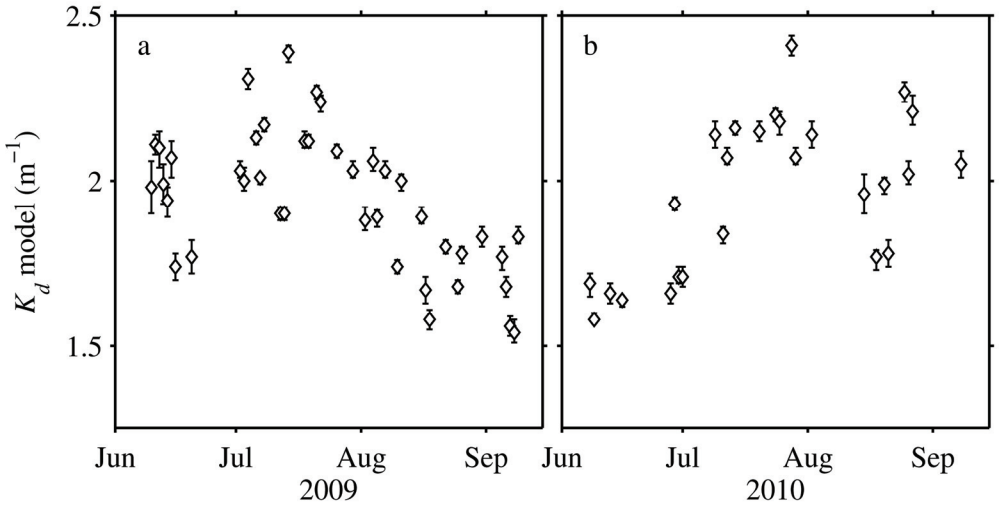

Figure 6.6: Estimates of K_d from the paired thermistor method for **a**) an unusually dry year (2009) and **b**) an unusually wet year (2010; precipitation comparisons made to the 1981-2010 record). 2009 had a decreasing trend in K_d, while 2010 increased in K_d during the summer period. Error bars were created by calculating K_d with the 95% confidence intervals to the linear fit of α.

Table 6.1: Properties for the 6 lakes used in this analysis.

Lake Name	Latitude	Longitude	Area (ha)	z_{max} (m)	Thermistor locations (m)	Precision (ºC)	Mfr.
Crystal Bog[a]	46.008	-89.606	0.55	2.5	0, 0.25, 0.5, 0.75, 1, 1.25, 1.5, 1.75, 2, 2.25	0.001	PME
Crystal Bog	46.008	-89.606	0.55	2.5	0, 0.25, 0.75, 1, 1.25, 1.75, 2, 2.25	0.01	Apprise
Jekl Bog	45.995	-89.678	0.25	3.1	0, 0.25, 0.5, 0.75, 1, 1.25, 1.5, 2, 2.5, 3	0.024	Onset
Mouser Bog	45.998	-89.722	3.78	4	0, 0.25, 0.5, 0.75, 1, 1.25, 1.5, 1.75, 2, 2.5, 3	0.024	Onset
N Sparkling Bog	46.005	-89.705	0.46	4.3	0, 0.25, 0.5, 1, 1.5, 2, 2.5, 3, 3.5, 4	0.01	Apprise
Timber Bog	46.003	-89.431	0.06	2	0, 0.25, 0.5, 0.75, 1, 1.25, 1.5, 1.75, 2	0.024	Onset
Trout Bog	46.041	-89.686	1.05	7.9	0, 0.5, 1, 1.5, 2, 2.5, 3, 4, 5, 7	0.01	Apprise

[a]2012 Crystal Bog deployment

Table 6.2: Depth (cm) placement for thermistors based on the desired temperature gain (ΔT, in °C) relative to a priori knowledge of K_d, for an average incoming solar radiation flux of 800 W m^{-2} during a six hour period.

	K_d (m^{-1})									
ΔT (°C)	0.5	0.75	1	1.25	1.5	2	2.5	3	3.5	4
0.25	262.5	229.1	200.6	178.3	160.7	134.9	116.9	103.5	93.1	84.8
0.5	123.9	136.6	131.2	122.8	114.5	100.3	89.1	80.4	73.3	67.5
0.75	42.8	82.6	90.7	90.4	87.5	80	72.9	66.9	61.7	57.3
1	-	44.2	61.9	67.4	68.3	65.6	61.4	57.3	53.5	50.1
1.25	-	14.5[a]	39.6[a]	49.5	53.4	54.5	52.5	49.8	47.1	44.6
1.5	-	-	21.4[a]	35[a]	41.3	45.3	45.2	43.7	41.9	40
2	-	-	-	11.9[a]	22.1[a]	31[a]	33.7[a]	34.2[a]	33.7[a]	32.8[a]
3	-	-	-	-	-	10.7[a]	17.5[a]	20.6[a]	22.1[a]	22.7[a]
5	-	-	-	-	-	-	-	2.6[a]	7.5[a]	9.9[a]

[a]Depths below 40 cm are likely influenced by physical surface layer processes

Chapter 7 – Conclusions

7.1 Summary

Small lakes have recently gained relevance in the study of global and regional processes like carbon and nutrient cycling (Cole et al. 2007; Downing 2010; Lewis 2011), but there is still progress to be made in estimating their global number (Seekell and Pace 2011; Mcdonald et al. 2012) and in the study of physical processes that influence lake function. This research was conducted to provide a resource for the physical limnology of small temperate lakes, and to encourage future study of these abundant – but often overlooked – lake systems. Much of this work was based on physical limnology campaigns in Vilas County (Wisconsin, USA), but the Global Lake Ecological Observatory Network (GLEON; gleon.org) provided an invaluable resource for expertise, collaboration, and data sharing (Hanson 2007).

A combination of open collaboration, information technology, and field data collection was used to address the research objectives outlined in Chapter 1. Chapter 2, Appendix A, and Appendix B provide details for the design of an open-source analytical software program (Lake Analyzer; Read et al. 2011a) which was created to facilitate comparative analysis of physical data from lakes. Chapter 3 leveraged the tools discussed in Chapter 2, as well as data collected in Vilas County from LTER lakes (lter.limnology.wisc.edu), several new study lakes, and shared data from GLEON members and other participants to perform a comparison of dominant drivers of surface mixed layer processes for a diverse group of lakes (Read et al. 2012). Chapter 3 also parameterized air-water gas exchange using high-frequency physical measurements, and these models will become part of Lake Analyzer during the next version update. Appendix C and Appendix D include details for the creation of a hydrodynamic model that was used to simulate water temperatures and vertical mixing rates in small lakes. This model was then implemented in

Chapter 4 to identify the controls on mixed layer depths and hypolimnetic temperatures in small lakes, as well as to predict water temperatures under a "no-mixing" scenario for the evaluation of the artificial destratification method described in Chapter 5 (Read et al. 2011b). Insights from Chapter 4 (the importance of water color as a driver of water temperatures in small lakes) inspired a new method for estimating water column transparency from water temperature measurements. Details for the formulation, procedure, and evaluation of this method are covered in Chapter 6. The analysis of field measurements of transparency, including a table of light attenuation coefficients for 131 unique radiometer profiles from 10 lakes can be found in Appendix E.

The goal of creating a data management and analysis platform for instrumented buoy data which is modular, adaptable, and designed for high volumes of environmental sensor data was achieved with the creation of Lake Analyzer (Read et al. 2011a). This program was the result of input and design help from the Physical Limnology GLEON working group, and includes a library of analytical scripts for the analysis of physical data from lakes. The program uses an adaptable structure that allows for future improvements and expansion, and the input data are standardized according to the gFile data standard discussed in Appendix B. The scripting and analytical effort that went into the parameterization of heat fluxes and the gas transfer velocity in Chapter 3 will be added to Lake Analyzer, further increasing the program's utility.

The physical analysis in Chapter 3 represents an important keystone of this dissertation, as the comparison of surface mixed layer drivers effectively established a defining threshold for small lakes. The remainder of this PhD research defines small lakes as convectively dominant, where convection is a greater source of mechanical mixing energy in the surface mixed layer than wind shear. This project focused on several clear patterns that were consistent across a

diverse group of lakes, including a lake-size dependency for the relative magnitudes of convection versus wind shear, and the differences in seasonal and latitudinal patterns of heat loss and wind shear on 40 lakes. This chapter also parameterized the gas transfer velocity according to instrumented buoy measurements that are becoming increasingly more common on lakes.

The publication of Chapter 5 (Read et al. 2011b) led to the development of a numerical model which could accurately simulate water temperatures, because existing models (e.g., DYRESM) were unable to predict the strong stratification and mixed layer dynamics of North Sparkling Bog (see Chapter 5). This model development was later used to simulate the effects of changing DOC loading on water temperatures and mixed layer depths in small lakes (Chapter 4).

Much of this work focused on the study of extremely stratified bog lakes, but the content of Chapter 5 contains methodology for breaking down this strong stratification. As discussed in Chapter 4, convectively dominated lakes have very little turbulence below the mixed layer, with vertical heat transfer occurring near the molecular level. The design of the Gradual Entrainment Lake Inverter (GELI; Read et al. 2011b) introduced turbulence to these otherwise quiescent waters by oscillating a gigantic (8 m diameter) disk in the water column. GELIs are controlled by alternating stages of positive and negative buoyancy using compressed air and a bladder. This method was found to be quite a bit more efficient than aerators (a much more common technique) for this destratification effort.

7.2 Conclusions

- **Wind is of decreasing importance as a driver of physical processes on small lakes**

Small lakes are fetch-limited are often wind sheltered, which leads to reduced surface wind stress (Markfort et al. 2010). For small lakes (< 10 ha), convective heat loss often outweighs the effects of wind shear as a driver of surface layer mixing (Read et al. 2012). The

gas transfer velocity (*k*), which shows significant dependence to near-surface turbulence (Mcgillis et al. 2004; Zappa et al. 2007; Tokoro et al. 2008), may show little, if any, relation to measured wind speeds (e.g., Cole and Caraco 1998) even though *k* is often parameterized solely as a function of measured winds (e.g., Crusius and Wanninkhof 2003). We developed a mechanistic formulation of *k* using instrumented buoy measurements that highlighted the role of convection as a driver of gas flux from small lakes, finding as much as 79% of *k* to be a product of convective heat loss on the smallest lake (0.06 ha). Wind shear was shown to be of increasing importance on larger lakes, where the convective influence on *k* was nearly negligible. These findings agree with the parameterization of *k* on larger lakes as a function of wind (Crusius and Wanninkhof 2003), while also predicting *k* on small, convective lakes that was similar in magnitude to a diverse group of methods for estimating k (Cole et al. 2010).

Wind speed was a lesser driver of surface layer mixing compared to convection for small lakes, but air-side convection was also an increasingly important renewal method for the fluxes of sensible and latent heat (see Appendix C). Parameterizing these fluxes according to the free and forced convection mode of Adams et al. (1990) led to improvements to the physical model CLM (Appendix C), and suggests that the importance of wind on lakes is a function of surface area for both air and water-side turbulent processes.

- **Water color is an important driver of stratification and mixed layer depths in small lakes**

Fee et al. (1996) found a relationship between epilimnetic depths and water color in many lakes in the Canadian Shield. This relationship weakened with increasing lake size, a finding that was consistent with Mazumder and Taylor (Mazumder and Taylor 1994). Snucins and Gunn

(2000) also theorized that clearer lakes may be more sensitive to climate variability. In Chapter 4, we used a mechanistic model (CLM; Appendix D) to examine the relationship between water color (transparency) and mixed layer depths, average water temperatures and climate variability. For small lakes, we found that darker waters lead to colder average water temperatures, shallower mixed layer depths, but less inter-seasonal variability in response to differences in climate. These findings suggest that transparency is very important in driving stratification and mixing patterns for small lakes (a relationship that weakens on larger lakes), and that hydrological changes that can influence water clarity may have implications for temperatures and mixed layer depths, which are two important controls on carbon processing in lakes (Hanson et al. 2011).

- **Open-source models and data sharing are important contributions to science**

The models and methods developed in Chapter 2, Chapter 3, Appendix C, Appendix D and Appendix E are important contributions to limnology, and effort was made to make these products available to interested parties, including server hosting for Lake Analyzer code (lakeanalyzer.gleon.org). Much of the foundation of this dissertation was built on the data collection of others, which allowed us to make a timely publication for limnologists that would have been impossible without collaboration and data sharing (Read et al. 2012). Many of the steps taken to make data sharing or analysis easier for others has been time consuming, but this additional effort can lead to more rapid progress in the field of limnology, and could improve the efficiency of parties willing to support an open-source mentality in their own research.

7.3 Recommendations for future research

The above dissertation research produced a number of helpful and innovative products, including shared models, publications, and seeds for future collaboration. Many of these elements can be improved by future research campaigns (or coding versions, in the case of Lake Analyzer and CLM), and there are a number of targeted objectives that would represent legitimate contributions to the field of limnology in the future.

Additional effort to explore many of the patterns from Chapter 3 with finer temporal resolution would be beneficial to the geophysical community. We compressed the results from this cross-lake comparison into lake-specific indices of mixing and gas flux, but there is a great deal of detail that exists from this work in the temporal dimension. The Geophysical Research Letters publication (Read et al. 2012) hosts hourly output files for the results data that were used to create the figures and tables in the analysis. These files would allow interested parties to explore temporal dynamics in k that were not part of the initial analysis, with limited time investment.

The gas flux estimates from Chapter 3 are encouraging, as they agree with many empirical estimates of k for various size classes of lakes, but there was insufficient validation of the final parametization of k due to the large number of lakes in the analysis and lack of overlapping gas flux estimates from other methods (i.e., eddy covariance). Including additional validation the dissipation rate of turbulent kinetic energy by more direct measures (like acoustic Doppler velocimiters or micro-structure profilers) would improve the parameterization of this model. I have taken hundreds of micro-structure profiles during the course of my dissertation which will be available at lter.limnology.wisc.edu for future work. These casts often alternated between day and night conditions (heat gain and heat loss) and targeted several extreme wind events and cold fronts. The instrumented buoy on Crystal Lake (where data are freely accessed at

lter.limnology.wisc.edu as well) can be used in tandem with microstructure profiles (and similar data from other lakes) to improve the physical model for gas flux in Chapter 3.

The design of the destratification device "GELI" (Read et al. 2011b) shows promise as an alternative to bubble aeration as means to disrupt thermal stratification. This method is currently (2012) being used on Crystal Lake (Wisconsin, USA) as part of a large-scale thermal manipulation to rid the lake of a harmful cold water invasive fish. Details for this manipulation, which include projections, can be found in Gaeta et al. (2012) or the project website (crystallakemixing.com). Improvements to this method would require substantial engineering efforts, but the cost savings opportunity compared to the use of bubble aeration for disrupting thermal stratification could be quite substantial.

Future efforts to couple CLM to a biological model would be worthwhile. Currently, it is difficult to support research from hydrodynamic models due to the closed nature of coding (e.g., DYRESM). Using an open-source model would allow greater flexibility for future research questions. This model could also be improved by adding a more streamlined function-based system to the parameterization of mixing and energy fluxes. Currently, the parameter functions (explained in Appendix D) are simple, but require at least an intermediate understanding of the scripting language MATLAB, which could be limiting. Ultimately, a hosting portal such as the product created for Lake Analyzer (lakeanalyzer.gleon.org) would improve the use of the model, resulting in additional feedback; and consequently, a model system designed by the needs of the user community.

The research in this dissertation highlights the both the importance of small lakes, and their apparent deviation from many of the physical drivers that are important on larger lakes. As global limnology expands and modeling efforts extend into all size-classes of lakes, the defining

characteristics of small lakes must be considered: 1) a significant source of mixing is derived from convective heat loss, 2) a strong dependence exists between water color and several physical properties of small lakes, and 3) the diffusion of heat (and likely dissolved gases) below the mixed layer occurs at or near molecular rates.

7.4 References

Adams, E. E., D. J. Cosler, and K. R. Helfrich. 1990. Evaporation from heated water bodies - Predicting combined forced plus free-convection. Water Resources Research **26:** 425-435.

Cole, J. J., D. L. Bade, D. Bastviken, M. L. Pace, and M. Van De Bogert. 2010. Multiple approaches to estimating air-water gas exchange in small lakes. Limnology and Oceanography-Methods **8:** 285-293, doi: 10.4319/LOM.2010.8.285.

Cole, J. J., and N. F. Caraco. 1998. Atmospheric exchange of carbon dioxide in a low-wind oligotrophic lake measured by the addition of SF6. Limnology and Oceanography **43:** 647-656, doi: 10.4319/LO.1998.43.4.0647.

Cole, J. J., Y. T. Prairie, N. F. Caraco, W. H. Mcdowell, L. J. Tranvik, R. G. Striegl, C. M. Duarte, P. Kortelainen, J. A. Downing, J. J. Middelburg, and J. Melack. 2007. Plumbing the global carbon cycle: Integrating inland waters into the terrestrial carbon budget. Ecosystems **10:** 171-184, doi: 10.1007/S10021-006-9013-8.

Crusius, J., and R. Wanninkhof. 2003. Gas transfer velocities measured at low wind speed over a lake. Limnology and Oceanography **48:** 1010-1017, doi: 10.4319/LO.2003.48.3.1010.

Downing, J. A. 2010. Emerging global role of small lakes and ponds: little things mean a lot. Limnetica **29:** 9-23.

Fee, E. J., R. E. Hecky, S. E. M. Kasian, and D. R. Cruikshank. 1996. Effects of lake size, water clarity, and climatic variability on mixing depths in Canadian Shield lakes. Limnology and Oceanography **41:** 912-920.

Gaeta, J. W., J. S. Read, J. F. Kitchell, and S. R. Carpenter. 2012. Eradication via destratification: Whole-lake mixing to selectively remove rainbow smelt, a cold-water invasive species. Ecological Applications **22:** 817-827.

Hanson, P. C. 2007. A grassroots approach to sensor and science networks. Frontiers in Ecology and the Environment **5:** 343-343.

Hanson, P. C., D. P. Hamilton, E. H. Stanley, N. Preston, O. C. Langman, and E. L. Kara. 2011. Fate of Allochthonous Dissolved Organic Carbon in Lakes: A Quantitative Approach. Plos One **6**, doi: 10.1371/journal.pone.0021884.

Lewis, W. M. 2011. Global primary production of lakes: 19th Baldi Memorial Lecture. Inland Waters **1:** 1-28, doi: 10.5268/IW-1.1.384.

Markfort, C. D., A. L. S. Perez, J. W. Thill, D. A. Jaster, F. Porte-Agel, and H. G. Stefan. 2010. Wind sheltering of a lake by a tree canopy or bluff topography. Water Resources Research **46:** W03530, doi: 10.1029/2009WR007759.

Mazumder, A., and W. D. Taylor. 1994. Thermal structure of lakes varying in size and water clarity. Limnology and Oceanography **39:** 968-976.

Mcdonald, C. P., J. A. Rover, E. G. Stets, and R. G. Striegl. 2012. The regional abundance and size distribution of lakes and reservoirs in the United States and implications for estimates of global lake extent. Limnology and Oceanography **57:** 597-606, doi: 10.4319/lo.2012.57.2.0597.

Mcgillis, W. R., J. B. Edson, C. J. Zappa, J. D. Ware, S. P. Mckenna, E. A. Terray, J. E. Hare, C. W. Fairall, W. Drennan, M. Donelan, M. D. Degrandpre, R. Wanninkhof, and R. A. Feely. 2004. Air-sea CO2 exchange in the equatorial Pacific. Journal of Geophysical Research-Oceans **109:** C08s02, doi: 10.1029/2003JC002256.

Read, J. S., D. P. Hamilton, A. R. Desai, K. C. Rose, S. Macintyre, J. D. Lenters, R. L. Smyth, P. C. Hanson, J. J. Cole, P. A. Staehr, J. A. Rusak, D. C. Pierson, J. D. Brookes, A. Laas, and C. H. Wu. 2012. Lake-size dependency of wind shear and convection as controls on gas exchange. Geophysical Research Letters, doi: 10.1029/2012GL051886.

Read, J. S., D. P. Hamilton, I. D. Jones, K. Muraoka, L. A. Winslow, R. Kroiss, C. H. Wu, and E. Gaiser. 2011a. Derivation of lake mixing and stratification indices from high-resolution lake buoy data. Environmental Modelling & Software **26:** 1325-1336, doi: 10.1016/j.envsoft.2011.05.006.

Read, J. S., A. Shade, C. H. Wu, A. Gorzalski, and K. D. Mcmahon. 2011b. "Gradual Entrainment Lake Inverter" (GELI): A novel device for experimental lake mixing. Limnology and Oceanography-Methods **9:** 14-28, doi: 10.4319/lom.2011.9.14.

Seekell, D. A., and M. L. Pace. 2011. Does the Pareto distribution adequately describe the size-distribution of lakes? Limnology and Oceanography **56:** 350-356, doi: 10.4319/lo.2011.56.1.0350.

Snucins, E., and J. Gunn. 2000. Interannual variation in the thermal structure of clear and colored lakes. Limnology and Oceanography **45:** 1639-1646.

Tokoro, T., H. Kayanne, A. Watanabe, K. Nadaoka, H. Tamura, K. Nozaki, K. Kato, and A. Negishi. 2008. High gas-transfer velocity in coastal regions with high energy-dissipation rates. Journal of Geophysical Research-Oceans **113:** 14, doi: 10.1029/2007jc004528.

Zappa, C. J., W. R. Mcgillis, P. A. Raymond, J. B. Edson, E. J. Hintsa, H. J. Zemmelink, J. W. H. Dacey, and D. T. Ho. 2007. Environmental turbulent mixing controls on air-water gas exchange in marine and aquatic systems. Geophysical Research Letters **34:** L10601, doi: 10.1029/2006GL028790.

A Appendix for the software package "Lake Analyzer"

A.1 *Additional calculations*

Variables and constants are defined in Table A.1. Details for parameter calculations can be found below.

A.1.1 *Density of water* (ρ_i)

Density of water from a given temperature (in °C), assuming negligible effects of any solutes on density, can be calculated as in Martin and McCutchen (1999) to be:

$$\rho_i = \left[1 - \frac{T_i + 288.9414}{508929.2 \cdot (T_i + 68.12963)}(T_i - 3.9863)^2\right] \cdot 1000 \qquad \text{(A.1)}$$

If solutes are non-negligible and a salinity file (.sal) is provided, density will be calculated according to the combined effects of salinity (S_i) and water temperature based on the methods of Millero and Poisson (1981):

$$\rho_i = \rho_* + A \cdot S_i + B \cdot S_i^{3/2} + C \cdot S_i \qquad \text{(A.2)}$$

where $\rho_* = 999.842594 + 6.793952 \times 10^{-2} \cdot T_i - 9.09529 \times 10^{-3} \cdot T_i^2 +$

$1.001685 \times 10^{-4} \cdot T_i^3 - 1.120083 \times 10^{-6} \cdot T_i^4 + 6.536336 \times 10^{-9} \cdot T_i^5$,

$A = 8.24493 \times 10^{-1} - 4.0899 \times 10^{-3} \cdot T_i + 7.6438 \times 10^{-5} \cdot T_i^2 -$

$8.2467 \times 10^{-7} \cdot T_i^3 + 5.3875 \times 10^{-9} \cdot T_i^4$,

$B = -5.72466 \times 10^{-3} + 1.0227 \times 10^{-4} \cdot T_i = 1.6546 \times 10^{-6} \cdot T_i^2$, and $C = 4.8314 \times 10^{-4}$.

A.1.2 *Seasonal thermocline* (*SthermD*)

Lake Analyzer defines the dominant thermocline (*thermD*) as an estimate of the depth of the greatest density change with respect to depth ($\partial\rho/\partial z$). If a secondary local maximum is found in $\partial\rho/\partial z$ at a greater depth than *thermD*, the location of *SthermD* is calculated using equation 2.1. This calculation is not performed (and *SthermD* output will be the same as *thermD*) when either the secondary local maximum is less than 20% of the absolute maximum gradient, or no secondary maximum exists. We found the 20% threshold to work best for a variety of lakes, but users can modify this parameter in the script 'FindThermoDepth.m' by changing the value of 'dRhoPerc', which represents this ratio.

A.1.3 *u-star* (u_*)

$$u_* = \sqrt{\frac{\tau_w}{\rho_e}} \tag{A.3}$$

With ρ_e as the average density (kg m^{-3}) of the epilimnion, and τ_w is the wind shear (N m^{-2}) on the water surface, given by $\tau_w = C_D \rho_{air} U^2$. ρ_{air} is the density of air (kg m^{-3}), and U is wind speed (m s^{-1}) measured at 10 m above the water surface. Wind speed measurements at any height (U_z) other than 10 m (as specified by input #4 in the .lke file) are corrected according to Amorocho and DeVries (1980):

$$U = U_z \left[1 - \frac{C_D^{0.5}}{\kappa} \ln\left(\frac{10}{z}\right) \right]^{-1} \tag{A.4}$$

Where κ is von Karman's constant (taken to be 0.4), z is the height above the water surface for the measurement of U_z. Values for C_D are given by Hicks (1972) as

$$C_D = 1 \times 10^{-3} \qquad \text{for } U < 5 \text{ (m s}^{-1}\text{)}$$

$$C_D = 1.5 \times 10^{-3} \qquad \text{for } U \geq 5 \text{ (m s}^{-1}\text{)}$$

A.1.4 *Buoyancy frequency (N^2)*

$$N^2 = \frac{g}{\rho}\frac{\partial \rho}{\partial z} \tag{A.5}$$

Where N^2 (s^{-2}) represents the local stability of the water column, based on the density gradient $\partial\rho/\partial z$.

A.1.5 *Mode 1 vertical seiche period (T_1)*

$$T_1 = \frac{2 z_D L_T}{g' z_T (z_D - z_T)} \tag{A.6}$$

Given by Monismith (1986) where L_T is the basin length at the depth of the thermocline (z_T).

A.1.6 *Error-checking of input data*

Data from both .wtr and .wnd files are error-checked before being used in any of the calculations. Outliers are removed from the dataset based on two criteria, being

greater or less than the maximum and minimum specified range values (A.2.2.7-8) or being outside 2.5 times the standard deviation of the values within a moving outlier window (A.2.2.6; .lke {7}).

A.1.7 *Down-sampling of input data*

Data from both .wtr and .wnd files are down-sampled before being used in any of the calculations according to the specified output resolution (A.2.2.1; .lke {1}). If the output resolution is less than the temporal resolution of the input data, down-sampling is not performed on these data. Down-sampled values are temporally averaged values pertaining to the output resolution, i.e. specifying an hourly output resolution (.lke {1} = 3600) for 1 minute data will result in hourly data that are each averages of the 60 values that occurred during each hourly period.

A.2 Program variables

For program variables, {*n*} represents the n^{th} line of the specific input file (i.e. .lke {4} is the 4^{th} line of the .lke file, which contains the height of the wind sensor from the lake surface). These settings specify how the program will be structured.

A.2.1 *Outputs*

Outputs (.lke {1}) are automatically created in the same directory as the .wtr and .wnd input files, called 'LakeY_results' (see Table A.2). Outputs can be entered to the .lke file in any order, but will be written to file according to a pre-determined sequence (which can be modified in the 'OutputConstructor.m' source code.

A.2.1.1 *wTemp*

If wTemp is specified as an output, water temperature (°C) with outlier removal (.lke {8} and {9}) and down-sampling (if output resolution is at least twice the input

resolution - .lke {2}) of the input water file is written to file. wTemp is the only output option that creates a separate file in addition to the 'LakeY_results' file, called 'LakeY_results_wtr'.

A.2.1.2 *wndSpd*

If selected, wind speed (m s^{-1}) is written to the results file, with outlier removal (.lke {10} and {11}), temporal wind averaging (.lke {5}) and down-sampling (where applicable) is applied.

A.2.1.3 *metaT*

If selected, the depth to the metalimnion top (m) is written to the results file, with temporal layer averaging (.lke {6}) applied. metaT is calculated according to equation 2.2 for time points where the lake is not considered mixed. When the mixed criteria is met (.lke {13}), layers are not calculated, and written to the results file as the maximum depth.

A.2.1.4 *metaB*

If selected, the depth to the metalimnion bottom (m) is written to the results file, with temporal layer averaging (.lke {6}) applied. metaB is calculated according to equation 2.2 for time points where the lake is not considered mixed. When the mixed criteria is met (.lke {13}), layers are not calculated, and written to the results file as the maximum depth.

A.2.1.5 *thermD*

If selected, the depth to the thermocline (m) is written to the results file, with temporal layer averaging (.lke {6}) applied. thermD is calculated according to equation 2.1 for time points where the lake is not considered mixed. When the mixed criteria is

met (.lke {13}), layers are not calculated, and written to the results file as the maximum depth.

A.2.1.6 *St*

If selected, Schmidt Stability (J m^{-2}) is calculated by equation 2.5, and written to the results file. Calculations are made with water temperature in the same form as wTemp, even if wTemp is not selected to be written to file.

A.2.1.7 *Ln*

If selected, Lake Number (dim) is calculated by equation 2.7, and written to the results file. Calculations of Ln are made with wTemp, metaT, metaB, uSt, St.

A.2.1.8 *W*

If selected, Wedderburn Number (dim) is calculated by equation 2.6, and written to the results file. Calculations of W are made with wTemp, wTemp, metaT, uSt.

A.2.1.9 *N2*

If selected, the Brunt-Väisälä buoyancy frequency is calculated according to equation A.5, and written to the results file.

A.2.1.10 *T1*

If selected, the mode 1 vertical seiche period is calculated according to equation A.6, and written to the results file.

A.2.1.11 *SmetaT, SmetaB, SthermD, SuSt, SLn, SW, SN2, ST1*

All as above, with effort to include the parent thermocline (deeper) for all applicable calculations (see A.1.2).

A.2.2 *Inputs*

A.2.2.1 *Output resolution*

Output resolution (.lke {2}) specifies the time-step (s) of the calculations made for A.2.1. If the temporal resolution of the input data is coarser than the entry for this input, calculations will be made according to input data resolution.

A.2.2.2 *Total depth*

Total depth (m) (.lke {3}) must be greater or equal to than the maximum depth given in the .bth file. If the total depth is not included in the .bth file, it is assumed that the area at total depth is 0 (m^2) and the depth area curve is linearly interpolated from this depth to the values in the .bth file.

A.2.2.3 *Height of wind measurement*

Height of wind measurement (m) (.lke {4}) is used for the wind speed correction factor in equation A.4.

A.2.2.4 *Wind averaging*

Wind averaging (s) (.lke {5}) is the backwards-looking smoothing window used for the calculation of uSt and SuSt. This calculation allows for the relevant wind duration to influence the calculation of wind-derived parameters.

A.2.2.5 *Thermal layer averaging*

Thermal averaging (s) (.lke {6}) is the smoothing window used for metaT, metaB, thermD, SmetaT, SmetaB, and SthermD. Temporal smoothing for thermal layers is intended to minimize the effects of internal waves on these parameters.

A.2.2.6 *Outlier window*

Outlier window (s) (.lke {7}) is the window size (seconds) for outlier removal, where measurements outside of the bounds ($\mu \pm 2.5 \cdot \sigma$) based on the standard deviation

and the mean inside the outlier window are removed. Outlier removal is performed on .wtr and .wnd files prior to down-sampling (if applicable).

A.2.2.7 *Wtr max, wtr min*

Maximum and minimum allowed water temperatures (°C) (.lke {8 and 9}), where all values of .wtr file not fitting this criteria are removed before outlier checking.

A.2.2.8 *Wnd max, wnd min*

Maximum and minimum allowed wind speeds (m s^{-1}) (.lke {10 and 11}), where all values of .wnd file not fitting this criteria are removed before outlier checking.

A.2.2.9 $\delta_{\min}$

Minimum slope for the range of the metalimnion (kg m^{-3} per meter) (.lke {12}), which is used to calculated values of metaT, metaB, SmetaT, and SmetaB according to equation 2.2.

A.2.2.10 T_{mix}

Minimum surface to bottom thermistor temperature differential (°C) (.lke {13}) before the case of 'mixed' is applied. When 'mixed' is true, all thermal layer calculations are no longer applicable, and values are given as the depth of the bottom thermistor.

A.2.2.11 *Plot figure*

Plot figure (Y/N) (.lke {14}) is used to generate and save figure outputs of all calculations selected in .lke {1}. One figure is created for each output, saved at a resolution of 150 dpi. Alterations to figure outputs (resolution and other defaults) can be modified directly in the 'OuputConstructor.m' file.

A.2.2.12 *Write results*

Write results (Y/N) (.lke {15}) is used to determine whether outputs specified in .lke {1} will be written to file. If .lke {14} and {15} are both 'N', the program will alert users that no usable output will be generated, and the program will terminate.

A.3 References

Amorocho, J., and J. J. Devries. 1980. A new evaluation of the wind stress coefficient over water surfaces. Journal of Geophysical Research-Oceans and Atmospheres **85:** 433-442, doi: 10.1029/JC085iC01p00433.

Hicks, B. B. 1972. Some evaluations of drag and bulk transfer coefficents over water bodies of different sizes. Boundary-Layer Meteorology **3:** 201-213.

Martin, J. L., and S. C. Mccutcheon. 1999. Hydrodynamics and Transport for Water Quality Modeling. Lewis Publications.

Millero, F. J., and A. Poisson. 1981. International one-atmosphere equation of state of seawater. Deep-Sea Research Part a-Oceanographic Research Papers **28:** 625-629.

Monismith, S. 1986. An experimental sudy of the upwelling response of stratified reservoirs to surface shear-stress. Journal of Fluid Mechanics **171:** 407-439.

A.4 Tables

Table A.1: Definitions of key physical parameters used in this text

Property	Units	Description
A_z	m^2	Lake area at depth z
$\Delta\rho$	kg m^{-3}	Difference in density between epilimnion and hypolimnion
$\partial\rho/\partial z$	kg m^{-3} m^{-1}	Vertical density gradient
$\partial\rho/\partial z_{i\Delta}$	kg m^{-3} m^{-1}	Vertical density gradient between measurements at i and $i+1$
g	m s^2	Acceleration due to gravity
g'	m s^2	Reduced gravity
i	-	Depth index
k	-	Total number of thermistors
κ	-	von Karman constant
L_N	-	Lake Number
L_s	m	Lake length at the water surface

L_T	m	Lake length at the depth of the thermocline
L_z	m	Lake length at depth z
N^2	s^{-2}	Local stability of the water column (buoyancy frequency)
ρ_{air}	kg m^{-3}	Density of air
ρ_e	kg m^{-3}	Average density of the epilimnion (surface mixed layer)
ρ_h	kg m^{-3}	Average density of the hypolimnion
ρ_i	kg m^{-3}	Water density at measurement 'i'
ρ_o	kg m^{-3}	Average density of the water column
S_i	-	Salinity at measurement 'i'
$\delta_{\min}$	kg m^{-3} m^{-1}	Threshold for metalimnion bounds
S_T	J m^{-2}	Schmidt stability (Idso 1973)
S_{t*}	kg m	Schmidt stability used in L_N calculation
τ_w	N m^{-2}	Surface wind shear stress
T_i	°C	Water Temperature at measurement 'i'
T_{mix}	°C	Top to bottom temperature differential for "mixed" condition
u_*	m s^{-1}	Water friction velocity
W	-	Wedderburn Number
U	m s^{-1}	Wind speed at 10 m above the water surface
U_z	m s^{-1}	Wind speed at height z above the water surface
z_e	m	Depth to the top of the metalimnion
z_h	m	Depth to the bottom of the metalimnion
z_i	m	Depth of measurement i (downward positive)
$z_{i\Delta}$	m	Mid-point depth between z_i and z_{i+1}
z_ζ	m	Depth of maximum discrete density gradient
z_T	m	Depth to maximum density gradient
z_v	m	Depth to the centre of volume of the lake
z_D	m	Depth to the bottom of the lake

Table 2: Output options and definitions

Output	**Units**	**Description**
Ln	-	Lake Number
metaB	m	Bottom of the metalimnion depth (from the surface)
metaT	m	Top of the metalimnion depth
N2	s^{-2}	Buoyancy frequency
SLn	-	Seasonal Lake Number
SmetaB	m	Bottom of the seasonal metalimnion depth
SmetaT	m	Top of the seasonal metalimnion depth
SN2	s^{-2}	Seasonal buoyancy frequency
St	J m^{-2}	Schmidt stability (Idso 1973)
ST1	s	Seasonal mode 1 vertical seiche period
SthermD	m	Seasonal thermocline depth
SuSt	m s^{-1}	Seasonal u-star
SW	-	Seasonal Wedderburn number
T1	s	Mode 1 vertical seiche period
thermD	m	Thermocline depth
uSt	m s^{-1}	u-star
W	-	Wedderburn number
wndSpd	m s^{-1}	Wind speed
wTemp	m s^{-1}	Water temperature

Appendix B – A file sharing standard for GLEON data: gFile

B.1 Background

Sharing files for environmental sensor data is often a significant hurdle to many large comparative analyses. Often, date and time formatting is region specific (i.e., mm/dd/yyyy for the United States, dd/mm/yyyy for much of Europe), which can lead to confusion and wasted time in the efforts of formatting. File types that are a proprietary compressed (and often encrypted) format save on server space, but limit the ability of outside collaborators to interpret or use these data without access to proprietary software. Throughout the course of my PhD program, I have amassed a large amount of shared environmental data, including various measurements from a total of 63 unique lakes, reservoirs, or ponds (40 of these lakes make up the global analysis described in Chapter 3). I have saved and analyzed these data in a variety of different file formats, ranging from exceedingly complex and organized (geo-referenced MATLAB structural arrays filled with timeseries objects) to incredibly simple (text files). Ultimately, I began to use a basic file type which I feel facilitates data sharing and modularity in model and software based analyses. A colleague of mine (Luke A. Winslow) and I designed this format with the purpose of standardizing data sharing in the Global Lake Ecological Observatory Network (GLEON; gleon.org), and to create a standard for GLEON data products like Lake Analyzer (see Chapter 2). We call this data type gFile, and have created a host of scripts and software that are based on this file type (such as gFileOpen.m, gFileWrite.m, gFilePivot.m, all Lake Analyzer, CLM (see Chapter 4 and Chapter 5), and functions from the surface layer analysis in Chapter 3).

B.2 gFile format

GLEON is a diverse network of aquatic scientists, and as such, it was advantageous to create file types that did not require the use of proprietary software. gFiles are tab-delimited time series text files which follow a date format standard adopted from the ISO 8601 use of descending temporal magnitude terms: yyyy-mm-dd HH:MM. This standard is recognized in basic spreadsheet programs (such as Microsoft Excel) and scripting languages (such as MATLAB). gFiles rely on external metadata to hold information relevant to time series analysis, such as time zones, sensor specifications, and any maintenance notes. These files avoid the redundancy and data flagging that is common to many environmental data standards, and instead rely on QA/QC products (e.g., error-checking in Lake Analyzer) for these purposes. gFiles are very simple streamlined text files.

The naming convention used for gFiles supports simple automation of supported tasks, such as grouping relevant measurements for analyses. Files use the convention "station name"."variable abbreviation." For example, measurements of photosynthetically active radiation (PAR) and air temperatures would be named Mendota.par and Mendota.airT, respectively. This extension-based grouping is similar to the formatting used in the DYnamic Reservoir Simulation Model (DYRESM: Patterson et al. 1984), and allows for simple decision tasks, such as "is longwave radiation available from station X? If not, model longwave radiation from the best-available combination of additional measured variables."

gFiles have 4 basic types of information condensed into text files: 1) the file extension (the replacement for ".txt") contains the variable name (i.e., ".airT" for air temperature, ".sw" for shortwave radiation), 2) a single line of headers contains depth (if a water variable) or height (if a meteorological variable) information for the variable, 3) the leftmost column of gFiles contains a series of date time stamps, and 4) values for the variable, which can contain 1 to *n* measurements

for single time point for 1 to *n* measurement depths (or heights). An example of a water temperature file (".wtr"), where temperatures are measured at depths from 0 to 2 meters is shown in Table B.1.

gFiles do not contain unit specifications for measurements, and instead rely on single standard for each supported variable. This allows transition into parent programs (such as Lake Analyzer) without the need to specify variable units. Supported file extensions and variable units are shown in Table B.2

B.3 File compression

ASCII text files are uncompressed, so gFiles can become quite large (e.g., a single year .wtr file for Lake Mendota can exceed 50 megabytes). Many of the applications and functions which use gFiles for input data support the use of zipped folders to limit the size of these files. The Lake Analyzer web portal (http://lakeanalyzer.gleon.org/) uses a single .zip file which contains a number of compressed gFiles. This application, created by Luke A. Winslow, runs Lake Analyzer on these unzipped input files and outputs downloadable results for users. The functions used in Chapter 3, which will be included in a later version update of Lake Analyzer, used .zip files from 40 lakes to calculate gas transfer velocity.

B.4 References

Patterson, J. C., P. F. Hamblin, and J. Imberger. 1984. Classification and dynamic simulation of the vertical density structure of lakes. Limnology and Oceanography **29:** 845-861.

Table B.1: Example water temperature gFile (.wtr) for measurements at 0, 0.5, 1.0, 1.5, and 2.0 m.

DateTime	wtr_0.0	wtr_0.5	wtr_1.0	wtr_1.5	wtr_2.0
yyyy-mm-dd HH:MM	12.31	11.23	11.02	10.42	9.32
yyyy-mm-dd HH:MM	12.33	11.19	11.11	10.48	9.21

Table B.2: Extensions for commonly used gFiles and corresponding unit standards.

Extension	Variable name	Units
wtr	Water temperature	°C
airT	Air temperature	°C
lw	Longwave radiation	W m^{-2}
sw	Shortwave radiation	W m^{-2}
par	Photosynthetically active radiation	µmol $s^{-1}m^{-2}$
doobs	Dissolved oxygen	mg L^{-1}
precip	Precipitation	mm
prss	Atmospheric pressure	kPa
wnd	Wind speed	m s^{-1}
rh	Relative humidity	%
lwNet	Net longwave radiation	W m^{-2}
swNet	Net shortwave radiation	W m^{-2}
vap	Vapor pressure	kPa
dosat	Percent saturation of dissolved oxygen	%
kflx	Gas transfer velocity	m day^{-1}
chla	Chlorophyll a fluorescence	RFU
wndD	Wind direction	° from N

Appendix C - Estimating sensible and latent heat fluxes

C.1 Background

Small sheltered lakes often have warmer surface water temperatures compared to larger lakes (Fee et al. 1996; Houser 2006; Caplanne and Laurion 2008). These water surface temperatures are frequently warmer than the measured overlying air temperatures. As such, the atmospheric boundary layer above small sheltered lakes is often unstable. Many water temperature modeling efforts use an assumption of atmospheric neutrality in the estimation of the fluxes of energy, latent heat flux (E), and sensible heat flux (H). While this assumption often holds for larger lakes, sensible and latent heat fluxes from small lakes may be poorly represented by a neutral boundary layer. Verburg and Antenucci (2010) found that even on a very large lake (Lake Tanganyika), the assumption of a neutral boundary layer can lead to significantly lower estimates of evaporative flux, for example. Using the 39 lakes with complete driver data (see Chapter 3), we compared the magnitude of the bulk transfer coefficient for evaporative flux using an assumption of boundary layer neutrality (C_{EN}), and a parameterization of the coefficient that includes varying conditions of stability (C_E; Verburg and Antenucci 2010). Figure C.1 highlights the comparison between these two methods of calculating the transfer coefficient, which has a significant negative relationship with lake size ($p < 0.01$). Small lakes are shown here to be more commonly unstable, and as such it is important to include these varying boundary layer conditions in the formulation of energy fluxes relevant to the prediction of water temperatures (Patterson et al. 1984).

In addition to a frequently unstable boundary layer, small lakes are also often covered partially (or sometimes completely) in a transition between the terrestrial and

lacustrine boundary layers (Markfort et al. 2010). This sheltering leads to errant on-lake wind speed measurements (see Read et al. 2012), and overestimates of fluxes when standard bulk coefficients are employed. This topic is covered in detail in Chapter 3, where we designed a sheltering model for small lakes in the global comparative analysis of drivers of surface layer mixing.

The combination of terrestrial sheltering and unstable boundary layers complicates the estimation of evaporative and sensible heat fluxes from these small lakes, which is an important component to the accurate estimate of net surface heat fluxes (Lenters et al. 2005; Macintyre and Melack 2009) and prediction of water temperatures (Patterson et al. 1984). Accurate representation of these fluxes is important, for example, because the water budget of small lakes directly influences processing rates of carbon (Hanson et al. 2011), and these fluxes are significant energy terms required for the accurate modeling of water temperatures under future scenarios (see Chapter 4).

Two complementary approaches are available to aid in the solution of this problem: 1) estimates of the sum of sensible and heat fluxes relative to incoming fluxes of energy and measurements of temperatures in the lake (the Bowen Ratio Energy Budget) and 2) predictions of these components using only meteorological observations and estimates of surface water temperatures (free and forced convection; Adams et al. 1990).

The Bowen Ratio Energy Budget (BREB) uses detailed knowledge of the changes in thermal energy stored in the lake, as well as energy fluxes into and out of the lake to estimate the sum of sensible and latent heat fluxes as a residual of the energy budget. Because small lakes have simpler hydrodynamics compared to larger lakes (a topic

covered in detail in Chapters 3 and Chapter 4), measurements of the thermal energy storage via thermistor chains has less influence from physical processes that can be dominant in larger lakes, like seiching (Spigel and Imberger 1980). In Chapter 3 we showed that the error in heat flux estimates from the thermistor method was greater in small lakes (but was also a function of the vertical resolution of thermistors). Therefore, the BREB method should provide estimates of evaporation rates with reasonable accuracy and can be used to calibrate the forced and free convection method of estimating these fluxes in model space.

C.2 Methods

C.2.1 *Bowen Ratio Energy Budget (BREB)*

Surface energy fluxes were calculated according to the Bowen ratio energy budget method (Winter et al. 2003; Lenters et al. 2005), where E and H were estimated as the residual of a whole lake energy budget (Figure C.2). This method has been shown to accurately estimate E and H assuming the measurements of other components is sufficiently accurate (Ali et al. 2008). Although the energy budget method is often superseded by eddy correlation measurements to calculate evaporation on sub-diurnal timescales (Stannard and Rosenberry 1991), much of the discrepancy between the two methods can be attributed to climatic instability and severe wind events (Assouline and Mahrer 1993). Due to the sheltered locations of our study sites, we assume that much of the wind-induced error in calculating evaporation by the BERB method is mitigated. The energy budget for a body of water inside the boundaries of the air-water and sediment-water interfaces (Figure C.2) can be written as:

$$\sum_{i=1}^{\#in} \dot{m}_i \left(h_i + \frac{v_i^2}{2} + g \cdot z_i\right) - \sum_{e=1}^{\#out} \dot{m}_e \left(h_e + \frac{v_e^2}{2} + g \cdot z_e\right) + Q - W = \frac{\partial U}{\partial t} + \frac{\partial KE}{\partial t} + \frac{\partial PE}{\partial t} \tag{C.1}$$

Where the dot ($\dot{x}$) represents a time rate, with $\dot{m}$ as the mass flow rate (kg s^{-1}) of any fluid advected into (subscript *i*) or out (subscript *e*) of the system, h being the enthalpy of the fluid, $\frac{v^2}{2}$ as kinetic energy and $g \cdot z$ as potential energy (all in J kg^{-1}). Heat transfer across the lake boundary is denoted by Q, which includes air-water and sediment-water interfaces. W is external work done on the lake boundaries, and $\frac{\partial U}{\partial t}$, $\frac{\partial KE}{\partial t}$, and $\frac{\partial PE}{\partial t}$ are the time rate of change in total internal, kinetic, and potential energies, respectively (all in units of watts). Assuming external work on the system, the rate of change of kinetic and potential energies, as well as their associated advected constituents can be neglected in the analysis of a lake system as in Lenters et al. (2005), equation C.1 can be simplified to:

$$\sum_{i=1}^{\#in} \dot{m}_i h_i - \sum_{e=1}^{\#out} \dot{m}_e h_e + Q = \frac{\partial U}{\partial t} \tag{C.2}$$

Advected terms include precipitation, ground water flow, and evaporative mass flux, and can be described by:

$$\dot{A}_{net} = \dot{m}_p h_p + \dot{m}_{Gin} h_{Gin} - \dot{m}_{Gout} h_{Gout} - \dot{m}_E h_E \tag{C.3}$$

Any advected energy associated with fluid *j* is represented as:

$$\dot{m}_j = F_j \rho_j a_j \text{ and } h_j = c_j (T_j - T_{ref}) \quad \text{(C.4)}$$

Where F_j is the flux of the fluid (m s^{-1}) across the system boundary (of area a_j), ρ_j is the density of the fluid (kg m^{-3}), c_j is the specific heat of the fluid (J kg^{-1} °C^{-1}), T_j is the temperature of the fluid (°C) and T_{ref} is an arbitrary reference temperature, assumed here to be 0°C. Density of water from a given temperature (T_w in °C), assuming negligible effects of any solutes on density, can be calculated as in Martin and McCutchen (1999) to be:

$$\rho_w = \left[1 - \frac{T_w + 288.9414}{508929.2 \cdot (T_w + 68.12963)} (T_w - 3.9863)^2\right] \cdot 1000 \quad \text{(C.5)}$$

Heat transfer (Q), includes latent and sensible energy fluxes, radiant energy exchange, and sediment conductive heat flux. These heat transfer components can be written as:

$$Q = R_{net} + Q_{sed} - (E + H) \quad \text{(C.6)}$$

For the BREB method, the sum of latent and sensible energy fluxes ($E + H$) is calculated as the residual of the whole-lake energy budget. Net radiation (R_{net}), the sum of incoming and outgoing radiative fluxes, can be written as:

$$R_{net} = [R_{SW}(1 - \alpha_{SW}) + R_{LWin}(1 - \alpha_{LW}) - R_{LWout}] \cdot A_s \quad \text{(C.7)}$$

Where α_{SW} is the short-wave albedo of the water surface (0.07), α_{LW} is the long-wave albedo of the water surface (0.03), and A_s is the area of the water surface (m^2). Outgoing long-wave radiation can be estimated from surface temperature (T_s) as:

$$R_{LWout} = \varepsilon_s \sigma T_s^4, \quad \text{(C.8)}$$

With ε_s being the emissivity of the water surface (0.97), σ the Stefan-Bolzman constant (5.6697e-8 W m^{-2} K^{-4}), and surface water measured in °C.

Total thermal energy of the lake was calculated by:

$$U_t = c_w \sum_{i=1}^{\#layer} a_i T_{i,t} \rho_{i,t} \partial z_i \quad \text{(C.9)}$$

Where a_i is the cross-sectional area of the water column (m^2), $T_{i,t}$ is the water temperature at time t, $\rho_{i,t}$ is the density of water (kg m^{-3}) at time t calculated using equation (5), ∂z_i is the thickness (m) of the i^{th} layer (used as a constant 0.01 m), with all properties determined at depth $z = z_i$ from the surface. Water temperatures were taken from buoy thermistors, which were linearly interpolated with $\partial z = 0.01$ m at time t for the calculation of U_t.

Equation (2) can then be expanded to:

$$\overline{A_{net}} + \overline{R_{net}} + \overline{Q_{sed}} + (\overline{E+H}) = \frac{\Delta U}{\Delta t} \qquad \text{(C.10)}$$

Where the overbar ($\overline{X}$) represents temporal averaging over the time period Δt . Because estimates of the sum of latent and sensible fluxes are evaluated based on the residual of equation (10), it is assumed that over the time period Δt that $\overline{E} + \overline{H} = \overline{E+H}$. Latent and sensible heat fluxes can be partitioned according to the Bowen ratio $Bw = \frac{H}{E}$, which dos Reis and Dias (1998) define as

$$\overline{Bw} = \frac{\overline{p_{air}} c_{air}}{622 \cdot \overline{L_v}} \frac{\overline{U \cdot (T_s - T_{air})}}{\overline{U \cdot (e_s - RH \cdot e_{air})}} \qquad \text{(C.11)}$$

where p_{air} is atmospheric pressure (kPa), c_{air} is the specific heat of air (assumed constant at 1011 J kg^{-1} K^{-1}), L_v is the latent heat of vaporization of water (J kg^{-1}), U is wind speed (m s^{-1}), T_s and T_{air} are water surface and air temperature, e_s and e_{air} are the saturation vapor pressures (kPa) at T_s and T_{air}, and RH is relative humidity.

Latent heat of vaporization, L_v, can be approximated from surface water temperature from Yau and Rogers (1989) as:

$$L_v = \left(-0.0000614342 \cdot T_s^3 + 0.00158927 \cdot T_s^2 - 2.36418 \cdot T_s + 2500.79\right) \cdot 1000 \qquad \text{(C.12)}$$

By solving equation (10) for $\overline{E+H}$, dividing by one plus the Bowen ratio from equation (11) yields E, and subsequently multiplying evaporation by Bowen ratio solves for sensible heat flux, H (Figure C.3).

C.2.2 *Evaporation estimates using a free and forced convection model*

Adams et al. (1990) noted an absence of field data for estimating evaporations during unstable atmospheric conditions on small lakes and ponds. These conditions are common on small lakes (see Figure C.1) and cooling ponds or geothermal waters (Adams et al. 1990). Adams et al. (1990) collected data from an experimentally heated pond during conditions that were categorized using 3 heat-loss regimes: 1) forced convection dominated by near-horizontal winds, 2) free convection arising from the density difference between the air overlying the lake and the temperature of the water surface, and 3) a combination of forced and free convection. These data were used to generate a simple model for the rate of evaporation using the additive effects of free and forced convection. Rasmussen et al. (1995) later expanded on the work of Adams et al. (1990) by adding measurements from small natural lakes. Rasmussen et al. (1995) found the simple model devised by Adams et al. (1990) to result in the best-fit between predicted and observed water temperatures compared to 6 other meteorological models for estimating evaporation using a numerical model (Hondzo and Stefan 1993). The lakes in Rasmussen et al.'s (1995) analysis were temperate and ranged in size from 7 to 1220 ha.

My original efforts to parameterize evaporation for the purpose of modeling water were completed using bulk aerodynamic formula with coefficients calibrated as part of best-fits to the observed (buoy) data. These simulations can be found in Read et al. (2011) or Chapter 5. While simulations were an accurate representation of water

temperatures during much of the year, this method was a poor fit to heat fluxes during the fall period, when the lakes would be notably warmer than the overlying air. Great improvements to these model fits were made after incorporating Adam et al.'s (1990) evaporation model, which is parameterized as

$$E = (a\Delta\theta_v^{1/3} + bU)\,(e_s - e_a) \qquad \text{(C.13)}$$

where a and b are empirically determined constants, $\Delta\theta_v$ is the difference in virtual air temperatures (°C) between the water surface and the ambient air (Brutsaert 1982), U is the measured wind speed (m s^{-1}), and e_s and e_a (both in mb) are the saturated vapor pressure and the vapor pressure of the air, respectively. The difference in virtual air (T_{va}) and water surface (T_{vs}) temperatures ($\Delta\theta_v$) is formulated as

$$T_{va} = T_a\,(1+0.61\omega_a) \qquad \text{(C.14)}$$

where T_a is the measured air temperature (°C), ω_a is the atmospheric mixing ratio for air (g kg^{-1}).

$$T_{vs} = T_s\,(1+0.61\omega_s) \qquad \text{(C.15)}$$

where ω_s is the atmospheric mixing ratio for air using the surface water temperature and assuming complete saturation (g kg^{-1}).

In order to determine the best fits to the empirical coefficients *a* and *b* in equation C.13, we estimated hourly evaporative fluxes using the BREB method (see Section C.2.1) and minimized the error between BREB estimates and the predictions for *E* from the free and forced convection formulation of Adam et al. (1990) for 8 different study lakes (see Chapter 4 for lake details). The best-fit to the BREB estimates were $a = 2.1$ and $b = 5.1$. These estimates differed from the small lake estimates of Rasmussen et al.'s (1995) analysis ($a = 2.7$ and $b = 3.1$) but our meteorological measurements were made above the lake surface (as opposed to nearby), and we did not use a wind sheltering coefficient for the measured winds. The free and forced convection estimates for *E* (using $a = 2.1$ and $b = 5.1$) versus the BREB estimates are shown in Figure C.4. This method for estimating *E* (and *H* using equation C.11) is the default parameterization of these energy fluxes in the CLM one-dimensional water temperature model (see Appendix D).

C.3 References

Adams, E. E., D. J. Cosler, and K. R. Helfrich. 1990. Evaporation from heated water bodies - Predicting combined forced plus free-convection. Water Resources Research **26:** 425-435.

Ali, S., N. C. Ghosh, and R. Singh. 2008. Evaluating best evaporation estimate model for water surface evaporation in semi-arid region, India. Hydrological Processes **22:** 1093-1106, doi: 10.1002/hyp.6664.

Assouline, S., and Y. Mahrer. 1993. Evaporation from Lake Kinneret 1: Eddy-correlation system measurements and energy budget estimates. Water Resources Research **29:** 901-910.

Brutsaert, W. 1982. Evaporation into the atmosphere: Theory, history, and applications. Kluwer.

Caplanne, S., and I. Laurion. 2008. Effect of chromophoric dissolved organic matter on epilimnetic stratification in lakes. Aquatic Sciences **70:** 123-133, doi: 10.1007/s00027-007-7006-0.

Dos Reis, R. J., and N. L. Dias. 1998. Multi-season lake evaporation: energy-budget estimates and CRLE model assessment with limited meteorological observations. Journal of Hydrology **208:** 135-147, doi: 10.1016/s0022-1694(98)00160-7.

Fee, E. J., R. E. Hecky, S. E. M. Kasian, and D. R. Cruikshank. 1996. Effects of lake size, water clarity, and climatic variability on mixing depths in Canadian Shield lakes. Limnology and Oceanography **41:** 912-920.

Hanson, P. C., D. P. Hamilton, E. H. Stanley, N. Preston, O. C. Langman, and E. L. Kara. 2011. Fate of Allochthonous Dissolved Organic Carbon in Lakes: A Quantitative Approach. Plos One **6**, doi: 10.1371/journal.pone.0021884.

Hondzo, M., and H. G. Stefan. 1993. Lake water temperature simulation model. Journal of Hydraulic Engineering-Asce **119:** 1251-1273.

Houser, J. N. 2006. Water color affects the stratification, surface temperature, heat content, and mean epilimnetic irradiance of small lakes. Canadian Journal of Fisheries and Aquatic Sciences **63:** 2447-2455, doi: 10.1139/f06-131.

Lenters, J. D., T. K. Kratz, and C. J. Bowser. 2005. Effects of climate variability on lake evaporation: Results from a long-term energy budget study of Sparkling Lake, northern Wisconsin (USA). Journal of Hydrology **308:** 168-195, doi: 10.1016/j.jhydrol.2004.10.028.

Macintyre, S., and M. Melack. 2009. Mixing dynamics in lakes across climatic zones, p. 603-612. *In* G. E. Likens [ed.], Encyclopedia of Inland Waters. Elsevier.

Markfort, C. D., A. L. S. Perez, J. W. Thill, D. A. Jaster, F. Porte-Agel, and H. G. Stefan. 2010. Wind sheltering of a lake by a tree canopy or bluff topography. Water Resources Research **46:** W03530, doi: 10.1029/2009WR007759.

Martin, J. L., and S. C. Mccutcheon. 1999. Hydrodynamics and Transport for Water Quality Modeling. Lewis Publications.

Patterson, J. C., P. F. Hamblin, and J. Imberger. 1984. Classification and dynamic simulation of the vertical density structure of lakes. Limnology and Oceanography **29:** 845-861.

Rasmussen, A. H., M. Hondzo, and H. G. Stefan. 1995. A test of several evaporation equations for water temperature simulations in lakes. Water Resources Bulletin **31:** 1023-1028.

Read, J. S., D. P. Hamilton, A. R. Desai, K. C. Rose, S. Macintyre, J. D. Lenters, R. L. Smyth, P. C. Hanson, J. J. Cole, P. A. Staehr, J. A. Rusak, D. C. Pierson, J. D. Brookes, A. Laas, and C. H. Wu. 2012. Lake-size dependency of wind shear and convection as controls on gas exchange. Geophysical Research Letters, doi: 10.1029/2012GL051886.

Read, J. S., A. Shade, C. H. Wu, A. Gorzalski, and K. D. Mcmahon. 2011. "Gradual Entrainment Lake Inverter" (GELI): A novel device for experimental lake mixing. Limnol. Oceanogr. Meth. **9:** 14-28, doi: 10.4319/lom.2011.9.14.

Spigel, R. H., and J. Imberger. 1980. The classification of mixed-layer dynamics in lakes of small to medium size. Journal of Physical Oceanography **10:** 1104-1121, doi: 10.1175/1520-0485(1980)010<1104:tcomld>2.0.co;2.

Stannard, D. I., and D. O. Rosenberry. 1991. A comparison of short-term measurements of lake evaporation using eddy-correlation and energy budget methods. Journal of Hydrology **122:** 15-22.

Verburg, P., and J. P. Antenucci. 2010. Persistent unstable atmospheric boundary layer enhances sensible and latent heat loss in a tropical great lake: Lake Tanganyika. Journal of Geophysical Research-Atmospheres **115:** D11109, doi: 10.1029/2009JD012839.

Winter, T. C., D. C. Buso, D. O. Rosenberry, G. E. Likens, A. M. Sturrock, and D. P. Mau. 2003. Evaporation determined by the energy-budget method for Mirror Lake, New Hampshire. Limnology and Oceanography **48:** 995-1009.

Yau, M. K., and R. R. Rogers. 1989. A short course in cloud physics, Third ed. Butterworth-Heinemann.

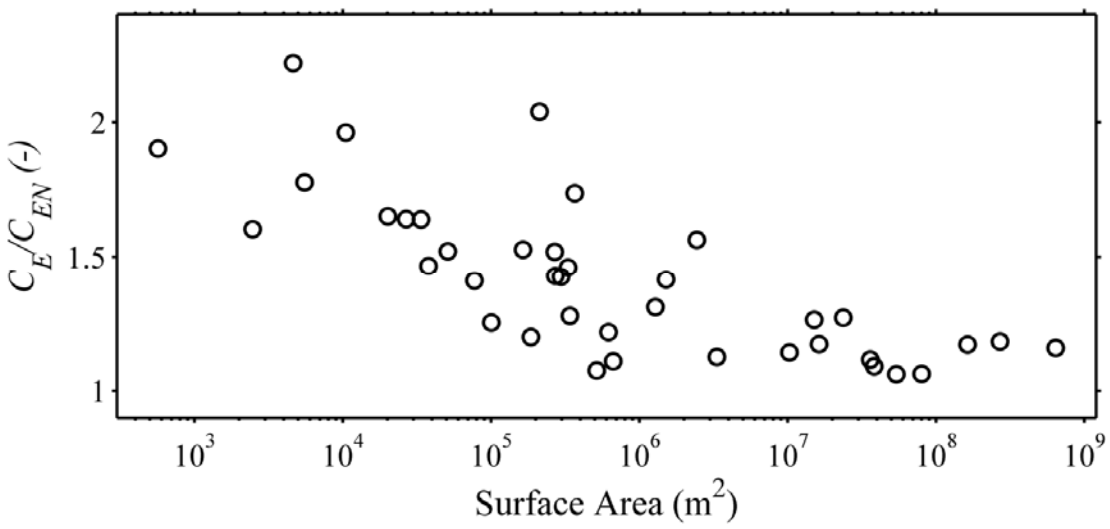

Figure C.1: The ratio of the stability sensitive latent heat transfer coefficient (C_E) to the neutral latent heat transfer coefficient (C_{EN}) for 39 temperate lakes (see Chapter 3 for details for specific lakes). Transfer coefficients were calculated according to the methods of Verburg and Antenucci (2010).

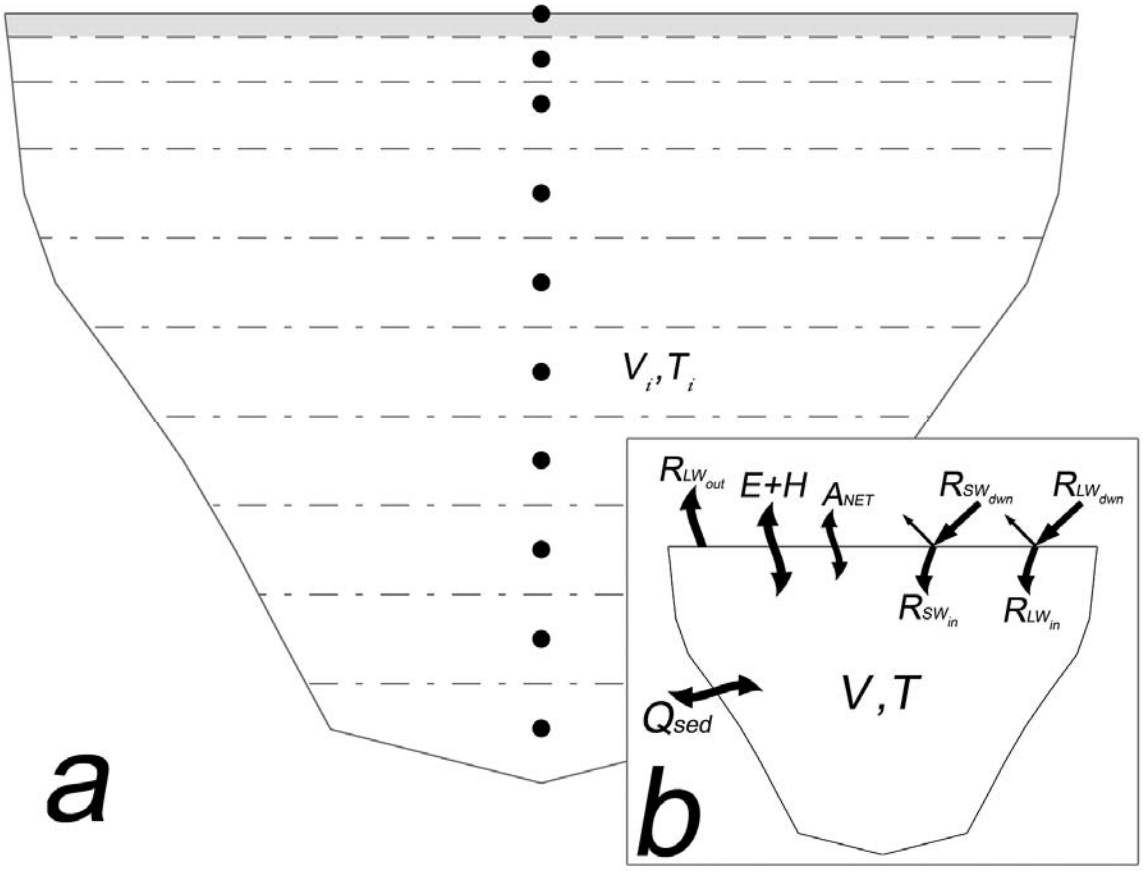

Figure C.2: Energy budget components for BREB analysis. a) The lake system with thermistors (black dots) representing horizontal slices (dashed lines). The hypsography of the lake defines the area-depth relationship. b) Flux components for the BREB analysis, including surface heat fluxes, advected energy, and sediment heat flux.

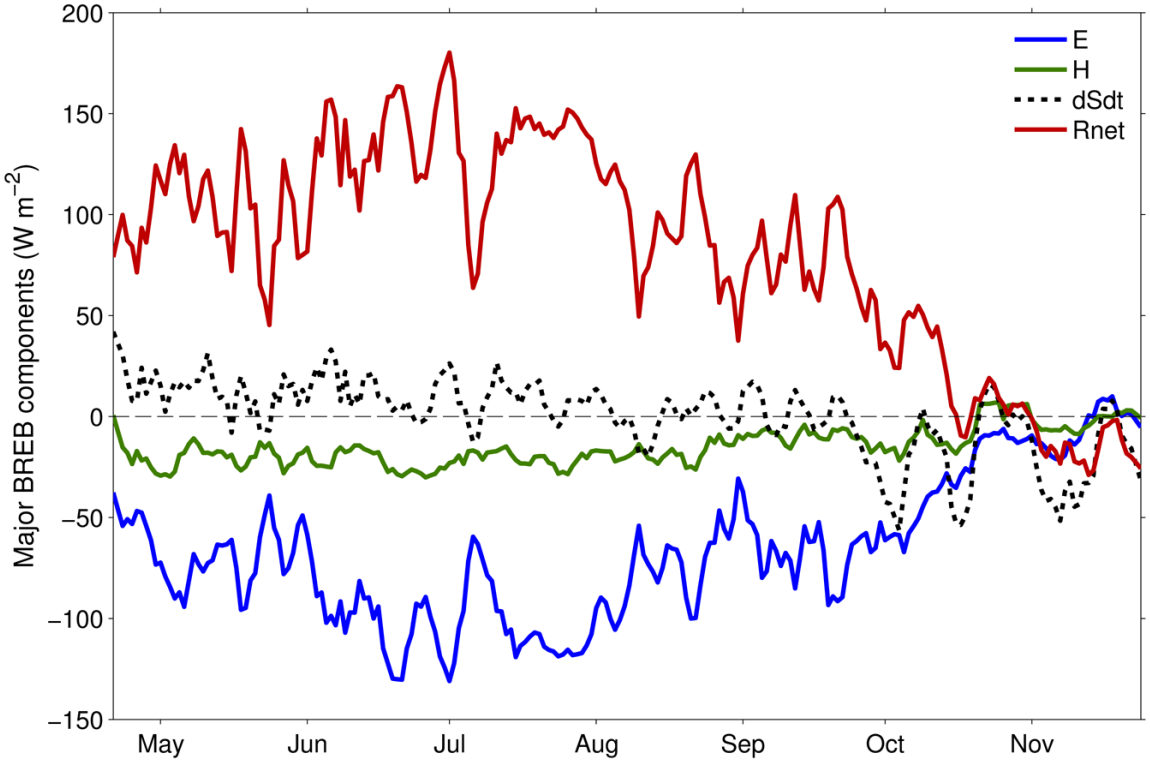

Figure C.3: An example of the dominant terms for the BREB for Trout Bog during 2009. Changes in internal energy (dSdt) reflect the balance of radiation (Rnet) and sensible (H) and latent (E) heat fluxes.

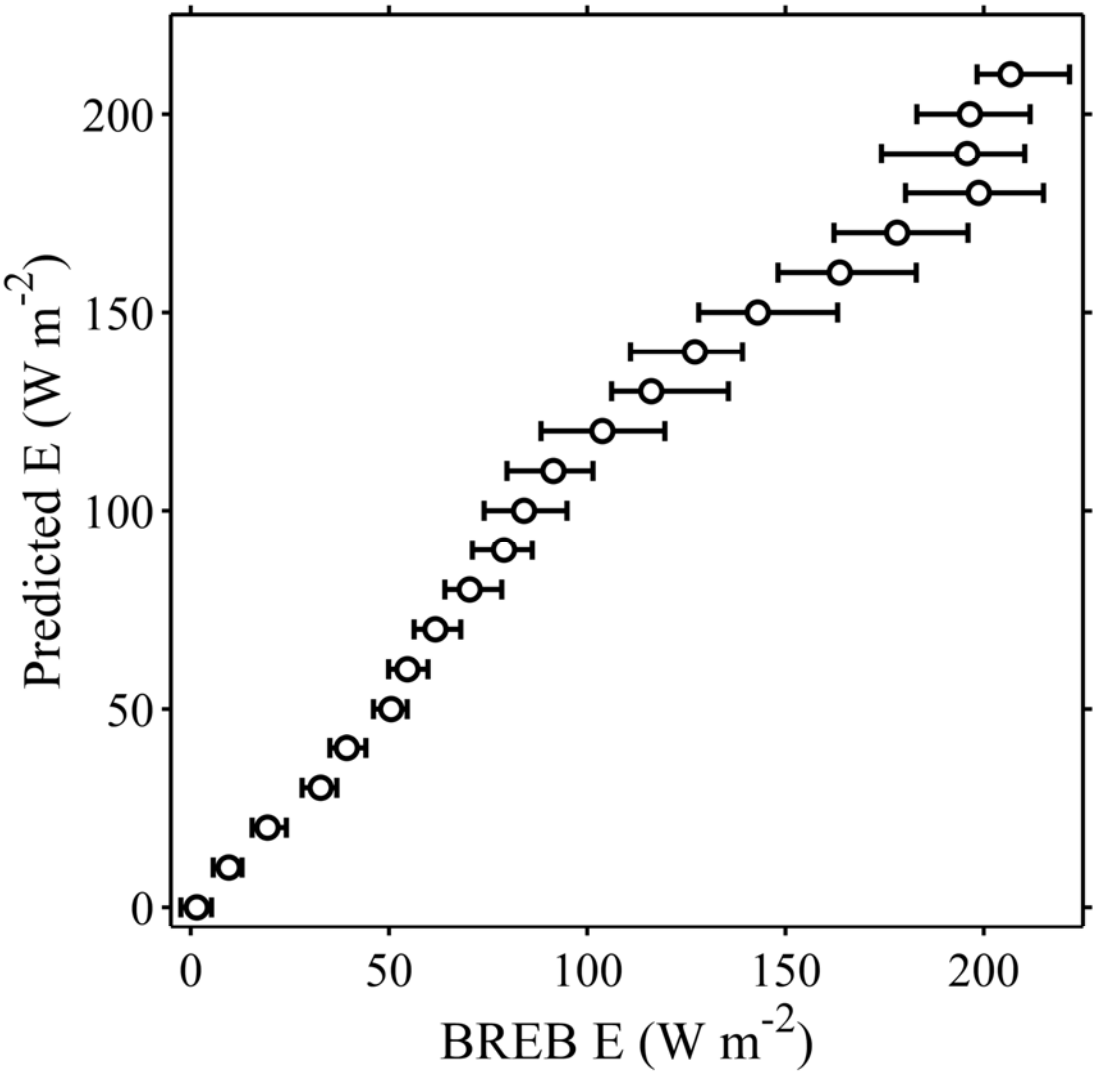

Figure C.4: Calibration of the free and forced evaporation model of Adams et al. (1990; see Section C.2.2) coefficients. Best-fits to the data (minimizing the sum of squared errors) was found with $a = 2.1$ and $b = 5.1$ (see equation C.13). Circles are the median of the estimates, and error bars represent the inter-quartile range of the data for each interval.

Appendix D – An Open-Source one-dimensional Water Temperature Model (CLM): Model description

D.1 Introduction

The Convective Lake Model (CLM) is a one-dimensional hydrodynamic model designed to simulate water temperatures and vertical mixing rates in small lakes. The model uses a vertical distribution of mixed layers and iteratively calculates the changes in energy (and corresponding changes in temperature) of the layers for each time step. Surface energy fluxes, the attenuation of shortwave energy in the water column, as well as surface mixing dynamics like wind shear and convection are included in the model, but surface water flows, groundwater fluxes, and changes in lake levels are not.

CLM is an open-source model written in the MATLAB scripting environment. Relationships defined for evaporation rates and mixing dynamics, for example, can therefore be modified with future improvements while maintaining the model foundation (similar to the modular structure of Lake Analyzer; see Appendix A). CLM is designed to evolve with the changing research needs for water quality and water temperature simulations.

D.2 Model details

D.2.1 *Surface energy fluxes*

The surface energy budget is a balance between incoming energy fluxes and heat losses from the lake. Terrestrial longwave (R_{LWin}) radiation is emitted from the atmosphere, and depends on prevailing local conditions like air temperature and cloud cover. Incoming shortwave radiation (R_{SW}) follows the diel pattern of sunlight, and is affected mainly by latitude (solar angle) and cloud cover. The lake loses heat mainly through the outward fluxes of back radiation (R_{LWout}), sensible heat fluxes (H), and evaporation (E). The balance of these components

represents the net surface energy flux (Q_0). While all other components are generally assumed to be solely surface flux components, a portion of shortwave radiation that is not reflected by the lake is absorbed in the surface layer (ζ). The remaining shortwave radiation propagates through the water column, being absorbed as heat in as it exponentially decays with depth. The net surface energy budget can be written as

$$Q_0 = R_{SW}(1- \alpha_{SW})\cdot\zeta + R_{LWin}(1- \alpha_{LW}) - R_{LWout} - E - H, \quad \text{(D.1)}$$

where α_{SW} is the shortwave albedo (the fraction of shortwave energy reflected by the lake surface) and α_{SW} is the longwave albedo. All energy components are in W m^{-2}.

When back radiation is not directly measured, R_{LWout} can be estimated from the Stefan-Boltzmann law

$$R_{LWout} = \varepsilon_s \sigma T_s^4, \quad \text{(D.2)}$$

where ε_s is the emissivity of the water surface, σ is the Stefan-Boltzmann constant (5.6697e-8 W m^{-2} K^{-4}), and T_s is the water surface temperature in degrees Kelvin. As in Lenters et al. (2005), we use a value of 0.97 for ε_s.

Latent (E) and sensible (H) heat fluxes can be estimated by a variety of methods. Most water temperature models (e.g., DYRESM) formulate the fluxes of E and H from bulk aerodynamic formulae (e.g., Henderson-Sellers 1986; Verburg and Antenucci 2010). Because of the sheltered nature of many small lakes (see Read et al. 2012), wind-based methods were often poor estimates of E and H relative to energy budget estimates. Small lakes commonly have low

wind speeds and warm surface temperatures, and therefore *E* and *H* fluxes may be better represented by models designed for heated ponds or cooling basins, where surface water temperatures are consistently warmer than air temperatures (Adams et al. 1990; Rasmussen et al. 1995). We followed the methods of Rasmussen et al. (1995) and calibrated a best-fit model for sensible and latent heat fluxes, using the additive effects of convective and wind-driven renewal of the atmospheric boundary layer (see Appendix D for additional details). The evaporative energy flux is calculated

$$E = (2.1\Delta\theta_v^{1/3} + 5.1U)\,(e_s - e_a) \qquad \text{(D.3)}$$

where $\Delta\theta_v$ is the difference in virtual air temperatures (°C) between the water surface and the ambient air (Brutsaert 1982), U is the measured wind speed (m s^{-1}), and e_s and e_a (both in mb) are the saturated vapor pressure and the vapor pressure of the air, respectively. The difference in virtual air (T_{va}) and water surface (T_{vs}) temperatures ($\Delta\theta_v$) is formulated as

$$T_{va} = T_a\,(1+0.61\omega_a) \qquad \text{(D.4)}$$

where T_a is the measured air temperature (°C), ω_a is the atmospheric mixing ratio for air (g kg^{-1}).

$$T_{vs} = T_s\,(1+0.61\omega_s) \qquad \text{(D.5)}$$

where ω_s is the atmospheric mixing ratio for air using the surface water temperature and assuming complete saturation (g kg^{-1}).

The sensible heat flux (H) is estimated relative to evaporative flux using the Bowen ratio

$$H = B \cdot E \tag{D.6}$$

where the Bowen ratio is formulated

$$B = (P_{atm} \cdot C_{pa})/(0.622 \cdot L_v)\ (T_s - T_a)/(e_s - e_a) \tag{D.7}$$

where P_{atm} is atmospheric pressure (mb), C_{pa} is the specific heat of air (J kg^{-1} $°C^{-1}$), and L_v is the latent heat of vaporization (J kg^{-1}) parameterized from Yau and Rogers (1989) as

$$L_v = (-0.0000614342 \cdot Ts^3 + 0.00158927 \cdot T_s^2 - 2.36418 \cdot T_s + 2500.79) \cdot 1000 \tag{D.8}$$

After the calculation of all flux terms in equation D.1, the total energy change over the timestep (Δt; in seconds) in Joules is calculated by multiplying Q_0 from equation D.1 by Δt. The change in water temperature of the surface layer that is predicted during the timestep is then the total energy change divided by the mass of the surface layer and divided by the specific heat of water (J kg^{-1} $°C^{-1}$). Water temperature in the surface layer is then increased or decreased relative to the magnitude of this predicted temperature change.

D.2.2 *Attenuation of penetrative shortwave energy*

The remaining portion of shortwave radiation that was not absorbed in the surface layer is attenuated either by complete absorption by sediments, or by the exponential decay of light relative to the diffuse attenuation coefficient (K_d), which is a model input parameter. Because

CLM does not model sediment-water heat exchanges, absorption of penetrating radiation by sediments is immediately applied to energy and thermal changes into the adjacent water layer. Temperature changes at depths below the surface layer are therefore a function of morphometry, penetrating shortwave energy, the value of K_d, and the model timestep. Chapter 6 is written exclusively for the purpose of modeling the attenuation of penetrative radiation, but the numerical model CLM uses discrete layers, therefore its formulation of attenuation is slightly different. The numerical code (function lyrSWgain_Attenuation.m) in CLM is as follows: The layer-by-layer function for energy attenuation from the penetrating fraction of radiation (`SWp`) is

```
kdFun = @(z1,z2) ((SWp*exp(-Kd*z1)-SWp*exp(-Kd*z2))*delTime)
```

which distributes to energy change (`delJ`; in Joules) to each layer, with the exception of the surface layer (see D.1) according to morphometric depths (`bthZ`)

```
delJ(2:numZ) = arrayfun(kdFun,bthZ(1:end-1),bthZ(2:end))
```

Next, the remainder of energy is distributed as a sediment heat flux to the bottom layer

```
delJ(numZ) = delJ(numZ)+kdFun(bthZ(end),inf)
```

This energy is then redistributed according to the shape of the lake (areal slices relative to depth layers; `bthA`) for all depth layers (excluding the surface layer)

```
for i = 1:numZ-1
      lossPcnt  = (bthA(i)-bthA(i+1))/bthA(1)
      delJ(i) = delJ(i)+sum(delJ(i+1:numZ)*lossPcnt)
      delJ(i+1:numZ) = delJ(i+1:numZ)-delJ(i+1:numZ)*lossPcnt
end
```

Changes in temperature for each layer are then calculated relative to the mass of each layer and the specific heat of water (such as in section D.1).

D.2.3 *Wind-driven mixing*

Wind-driven mixing and redistribution of thermal energy is calculated according to the wind-shear proxy for turbulence in the surface mixed layer (u_*; see Chapter 3). The model formulation for wind driven mixing (the MATLAB function LyrMix_Wind.m) first calculates u_* (`uSt`) and then the approximate turbulent kinetic energy (`TKE`) resulting from u_* as

```
TKE = rhoW*uSt^3*delTime;
```

Where `rhoW` is the density of water (kg m^{-3}). Next, the potential energy (`PE`) in the water column is calculated relative to all reference heights.

PE is given by

$$PE = g \cdot \sum_{z=1}^{Z\max} \rho_w(z) A(z) \cdot (z - z_{cv}) \cdot \partial z \,, \qquad \text{(D.9)}$$

where g is the acceleration due to gravity (m s^{-2}) and z_{cv} is the depth to the center of volume of the lake. Next, a comparison between total `TKE` and `PE` at a given depth is made to determine the depth at which `TKE` exceeds `PE`. If this is condition is true at any depth in the water column the boolean variable `mix` is declared as true.

```
for i = 1:numZ
      mass  = massPE(1:i);
      heights = depths(i)+dz - depths(1:i);      % height from point zi
      PE(i) = (sum(mass.*heights*g)-sum(mean(mass)*heights*g));
      if lt(TKE,-PE(i))
            fullMxI = i;
            mix = true;
      break
      end
end
```

If wind-driven mixing energy exceeds the potential energy relative to any depth of the simulated lake basin, mixed water temperatures are redistributed relative to these depth layers

```
if mix
```

```
        mixT = sum(wtrProfile(1:fullMxI-1))/(fullMxI-1);
        wtrMix(1:fullMxI-1) = mixT;
end
```

D.2.4 *Mixing driven by density instability*

Mixing in the water column that is driven by vertical instability (denser water overlying less dense water) is calculated according to the MATLAB function LyrMix_Instability.m. This function calculates the depth of a stability restoring overturn in the water column that would correct the inherent instability created by vertical heat fluxes from functions called earlier in the timestep. The functionality of LyrMix_Instability.m is as follows, where `rhoVar` is the density of each layer (1 to `numZ`)

```
[~,srtI] = sort(rhoVar);
differ  = reshape(srtI,1,numZ)-(1:numZ);
for ind = 1:numZ
      if gt(differ(ind),0)
            wtrProfile(ind:ind+differ(ind)) = ...
                  mean(wtrProfile(ind:ind+differ(ind)));
            rhoVar(ind:ind+differ(ind)) = ...
                  mean(rhoVar(ind:ind+differ(ind)));
      end
end
```

Profiles with stable vertical density profiles are returned following the numerically derived overturns in this function. This function has an iteration time-out of 1000 iterations, if all instabilities have not been destroyed. Unlike sections D.2.2-D.2.3, LyrMix_Instability.m includes the surface layer for numerical overturns.

D.2.5 *Vertical gradient changes driven by thermal diffusivity*

As in section D.2.2, much of the following methods are covered in detail in Chapter 6, but this section covers the numerical treatment of the vertical diffusivity of heat in the CLM formulation, which differs slightly from the text and methods in Chapter 6. The following is taken from the function LyrMix_Diffusion from the CLM program. K_z characterizes the intensity

of vertical mixing (see Jassby and Powell 1975; Macintyre et al. 2009). The total rate of heat flux between thermal layers in CLM is governed by the other mixing and energy flux terms described above, in addition to fluxes driven by the magnitude of K_z and adjacent thermal gradients (see Chapter 6). K_z is given a default value which is commonly a function of lake size (Hondzo and Stefan 1993), and was determined to be at or near the rate of the molecular diffusion of heat (1.4e-7 m^2 s^{-1}) in Chapter 4 for small, convectively dominated lakes (see Chapter 3 for definition of convectively dominated lakes). The vertical layer-to-layer flux of thermal energy is parameterized in CLM (in the function LyrMix_Diffusion.m) by first calculating the thermal gradient between adjacent layers

```
gradT(1:end-1) = (wtrProfile(1:end-1)-wtrProfile(2:end))/dz
```

followed by the mass of each layer (`massLyr`). The flux of energy between layers is then calculated (J m^{-2}) as

```
delKz = massLyr.*gradT.*Kz.*delTime*C_w/dz
```

where `C_w` is the specific heat of water. Temperature changes (`delT`) associated with K_z and the thermal gradient (`gradT`) are calculated as

```
delT = delKz./massLyr./C_w
```

Thermal gradients in CLM that are extremely sharp can result in unrealistic temperature changes if the timestep is sufficiently large. As such, CLM limits the largest temperature change between layers (`mxT`) using the LyrMix_Diffusion function to be half of the initial temperature difference between the two layers

```
mxT(1:end-1)   = (wtrProfile(1:end-1)-wtrProfile(2:end))*.5
```

When predicted changes are larger than `mxT`, `mxT` is used as the change of temperature between layers

```
ltI = lt(abs(mxT),abs(delKz./massLyr./C_w))
```

```
delT = delKz./massLyr./C_w
delT(ltI) = mxT(ltI)
```

Temperatures are incremented or decremented while satisfying conservation of energy (net flux between all layers is zero) according to

```
wtrMix(2:end) = wtrProfile(2:end)+delT(1:end-1)
wtrMix(1:end-1) = wtrMix(1:end-1)-delT(1:end-1)
wtrProfile = wtrMix
```

D.3 Model procedure

D.3.1 *Input values*

Use of CLM begins with the parent MATLAB function ConvLakeModel.m. This parent function requires the following input values (in order):

```
Kd
```

K_d (m^{-1}) is a single value representing the extinction rate of penetrating radiation in the water column, and pertains to the portion of shortwave radiation which is not absorbed as a surface flux (see D.1).

```
bthZ
```

bthZ (m) is a one-dimensional array of depths that correspond to various cross-sectional areas for the simulated lake. bthZ must contain at least two elements.

```
bthA
```

bthA (m^2) is a one-dimensional array of cross-sectional area measurements (corresponding to depths in the bthZ array) for the simulated lake. bthA must contain the same number of elements as bthZ.

```
stDate
```

stDate (MATLAB datenumber) is the start date (numerical) for the simulation. Number formatting for stDate is according to MATLAB's date format, which uses year 0, day 0 as numerical datenumber value 0 (i.e., July 7th 2012 is 735057).

`enDate`

enDate (MATLAB datenumber) is the end date (numerical) of the simulation. Number formatting for enDate is according to MATLAB's date format.

`delTime`

delTime (s) is a single value which represents the timestep of CLM calculations.

`elevation`

elevation (m) is the approximate elevation of the lake relative to sea level.

`Kz`

K_z (m^2 s^{-1}) is rate of diffusion below the mixed layer (see D.2.5)

`wtrI`

wtrI (°C) is a one-dimensional array of values representing the starting condition (corresponding to stDate) water temperatures for the simulation. These temperatures do not need to share the size or vertical location of bthZ values.

`depI`

depI (m) is a one-dimensional array of values corresponding to the depths of wtrI. depI must contain the same number of values as wtrI.

`Kz`, `wtrI` and `depI` are optional values. If no value is specified for `Kz`, the default is 1.5e-7 (m^2 s^{-1}). If no values are specified for `wtrI` or `depI`, `depI` is set to the values in `bthZ`, and all values in `wtrI` (an equal number as in `bthZ`) are set to 4 (°C).

D.3.2 *Parameter functions*

CLM's parent function, ConvLakeModel.m, uses a number of internal parameter functions, which allow easy modification into increasing or decreasing levels of complexity. Parameter functions, for example, can be used to specify a constant, give temporal dependence to a constant, or relate a constant to another variable. The following ten parameter functions are imbedded in ConvLakeModel.m.

```
StefanBoltzmann = @()(5.6697E-8)
```

The `StefanBoltzmann` function is a default constant value for the Stefan Boltzmann constant (σ, in m^{-2} K^{-4}; see equation D.2).

```
SpecificHeatWtr = @()(4186)
```

The `SpecificHeatWtr` function is a default constant value for the specific heat of water (J kg^{-1} $°C^{-1}$; `C_w` in D.2.5).

```
EmissivityWtr   = @()(0.97)
```

The `EmissivityWtr` function is a default constant value for the emissivity of the water surface (ε_s), which pertains to the rate of outward longwave radiation from the lake surface (see equation D.2).

```
SWsurfaceRat    = @()(.55)
```

The `SWsurfaceRat` function is a default constant value for the fraction of non-reflected incoming shortwave radiation that is absorbed in the surface layer (ζ in equation D.1).

```
AlbedoSW        = @()(0.07)
```

The `AlbedoSW` function is a default constant value for the albedo of incoming shortwave radiation (α_{SW} in equation D.1).

```
AlbedoLW        = @()(0.03)
```

The `AlbedoLW` function is a default constant value for the albedo of incoming longwave radiation (α_{LW} in equation D.1).

```
UwndCoef        = @(LkArea)(1.0-exp(-3e-5*LkArea))
```

The `UwndCoef` function generates a wind sheltering coefficient (see Hondzo and Stefan 1993; Markfort et al. 2010) that is applied to lakes to account for terrestrial sheltering. The value of the sheltering coefficient is dependent on the surface area of the lake (`LkArea`) which is given by the first element in the `bthA` array (i.e., `bthA(1)`).

```
DragCoef        = @()(1.3e-3)
```

The `DragCoef` function is a default constant value for the momentum transfer coefficient (embedded in `uSt` in section D.2.3).

```
AdamsA          = @()(2.1)
```

The `AdamsA` function is a default constant value for convective renewal constant (Adams et al. 1990; Rasmussen et al. 1995) in equation D.3.

```
AdamsB          = @()(5.1)
```

The `AdamsB` function is a default constant value for wind-driven renewal constant (Adams et al. 1990; Rasmussen et al. 1995) in equation D.3.

D.3.3 *CLM initialization*

CLM initializes constants that are not dependent on the temporal loop of the program (i.e., values that are not time dependent) by containing and calling non-temporal parameter functions (see D.3.2) outside the temporal loop. This step is also used to read in driver files from the specified driver data directory (a flexible file-path in the initialization section of the program). Driver files include gFiles (see Appendix B) for incoming shortwave energy (.sw files), incoming longwave energy (.lw files), ambient air temperatures (.airT files), ambient relative humidity (.rh files), and wind speeds (.wnd files). These files are opened, truncated to the simulation range (measurements between `stDate` and `enDate`; see D.3.1), and resampled to match the timestep of the program (`delTime`; see D.3.1).

CLM then initializes all temporally tracked variables that are part of the program output, including water temperatures. Water temperatures are initialized to be an m by n array, where n is the length of dates between `stDate` and `enDate` at timestep `delTime` (see D.3.1) and m is the length of the array of depth values, the minimum being 0, the maximum being `bthZ(end)`, and the vertical resolution specified by the CLM vertical layer width (`dz`) which is a default constant of 0.1 m.

D.3.4 *CLM temporal loop*

CLM calculates water temperatures iterating through time, using the previous timestep temperatures to influence the magnitude of surface energy fluxes, vertical mixing and other relevant processes. As such, CLM begins on timestep 2, where timestep 1 contains the initial temperatures specified by the user (or the default values of 4 °C) as the input (see D.3.1) of `wtrI`. The temporal loop therefore contains timestep values 2 to the length of total dates, where

```
dates = stDate:delTime/matDay:enDate
```

and `matDay` is the number of seconds in a day (86400). For each timestep, surface energy fluxes (section D.2.1) are calculated relative (when applicable) to the surface water temperatures from the previous timestep. For example, outward longwave radiation is parameterized as the energy flux relative to the surface water temperature (`Ts`) of the previous timestep (see equation D.2). After the sum of surface energy fluxes are used to increment or decrement surface water temperatures, the current timestep water temperatures are used for the remainder of calculations in the temporal loop. The initialization of the water temperatures (`wtr`) in the current timestep (`j`) based on the previous timestep (`j-1`) is as follows

```
NetJ = sum([SWs LWi -EH LWo])*delTime;
mass = densityFromTemp(Ts)*dz;
delMx= NetJ/mass/C_w
wtr(1,j) = wtr(1,j-1)+delMx;
wtr(2:end,j) = wtr(2:end,j-1);
```

where delMx is the change in temperature (°C, which can be both positive or negative) of the surface layer.

After surface energy fluxes are calculated and the current timestep (`j`) water temperatures are initialized, the CLM program then calculates the changes in temperature at depth according to the following processes, in this order: 1) attenuation of penetrative shortwave radiation (section D.2.2), 2) changes in the distribution of thermal energy according to wind-driven mixing (section D.2.3), 3) changes in the distribution of thermal energy according to convective overturns (section D.2.4), and 4) changes in the distribution of thermal energy according to the vertical diffusivity of heat. After these steps are complete, the timestep is incremented by 1, and the temporal loop described in this section begins again, until `date(j)` is equal to `date(end)`. At this point, water temperatures are given as outputs from the CLM program. Calibration and validation examples for CLM can be found in Chapter 4 and Chapter 5.

D.4 References

Adams, E. E., D. J. Cosler, and K. R. Helfrich. 1990. Evaporation from heated water bodies - Predicting combined forced plus free-convection. Water Resources Research **26:** 425-435.

Brutsaert, W. 1982. Evaporation into the atmosphere: Theory, history, and applications. Kluwer.

Henderson-Sellers, B. 1986. Calculating the surface-energy balance for lake and reservoir modeling - A review. Reviews of Geophysics **24:** 625-649.

Hondzo, M., and H. G. Stefan. 1993. Lake water temperature simulation model. Journal of Hydraulic Engineering-Asce **119:** 1251-1273.

Jassby, A., and T. Powell. 1975. Vertical patterns of eddy diffusion during stratification in Castle Lake, California. Limnology and Oceanography **20:** 530-543.

Lenters, J. D., T. K. Kratz, and C. J. Bowser. 2005. Effects of climate variability on lake evaporation: Results from a long-term energy budget study of Sparkling Lake, northern Wisconsin (USA). Journal of Hydrology **308:** 168-195, doi: 10.1016/j.jhydrol.2004.10.028.

Macintyre, S., J. P. Fram, P. J. Kushner, N. D. Bettez, W. J. O'brien, J. E. Hobbie, and G. W. Kling. 2009. Climate-related variations in mixing dynamics in an Alaskan arctic lake. Limnology and Oceanography **54:** 2401-2417.

Markfort, C. D., A. L. S. Perez, J. W. Thill, D. A. Jaster, F. Porte-Agel, and H. G. Stefan. 2010. Wind sheltering of a lake by a tree canopy or bluff topography. Water Resources Research **46:** W03530, doi: 10.1029/2009WR007759.

Rasmussen, A. H., M. Hondzo, and H. G. Stefan. 1995. A test of several evaporation equations for water temperature simulations in lakes. Water Resources Bulletin **31:** 1023-1028.

Read, J. S., D. P. Hamilton, A. R. Desai, K. C. Rose, S. Macintyre, J. D. Lenters, R. L. Smyth, P. C. Hanson, J. J. Cole, P. A. Staehr, J. A. Rusak, D. C. Pierson, J. D. Brookes, A. Laas, and C. H. Wu. 2012. Lake-size dependency of wind shear and convection as controls on gas exchange. Geophysical Research Letters, doi: 10.1029/2012GL051886.

Verburg, P., and J. P. Antenucci. 2010. Persistent unstable atmospheric boundary layer enhances sensible and latent heat loss in a tropical great lake: Lake Tanganyika. Journal of Geophysical Research-Atmospheres **115:** D11109, doi: 10.1029/2009JD012839.

Yau, M. K., and R. R. Rogers. 1989. A short course in cloud physics, Third ed. Butterworth-Heinemann.

Appendix E – Calculating the diffuse attenuation coefficient (K_d) from radiometer profiles

E.1 Introduction

The diffuse attenuation coefficient (K_d) is a metric of water column transparency that is important in determining the vertical partitioning of radiative heat gains (Chapter 4; Jassby and Powell 1975) as well as an indicator of intensity of photosynthetically active light at depth (Rose et al. 2009). Substances that attenuate incoming visible light (approximately the portion of shortwave radiation which effectively penetrates into the water column; 400-700 nm), such as algae and chromophoric dissolved organic matter (Morris et al. 1995) can vary with depth, therefore, estimates of K_d are often depth-dependent.

Outlined below is the procedure that was used to calculate the diffuse attenuation coefficient of photosynthetically active radiation (PAR) for radiometer measurements on various lakes in Vilas County and the Upper Peninsula of Michigan.

E.2 Radiometer measurements using the PUV

Field measurements of PAR were made using a Biospherical Instruments PUV profiling radiometer. This instrument measures absolute pressure (used to represent depth) and diffuse PAR (as well as specific wavelengths 305, 320, 340 and 380 nm) at 1 Hz. The PUV instrument that we used did not have a reference deck cell (a secondary duplicate sensor which is used to account for changes in incoming radiation during profiles), so we limited our measurements using the PUV to periods where clouds did not obscure the sun.

During a field profile with the PUV, computer logging of the above 1 Hz measurements commenced while the instrument was held level above the water surface for approximately 10 seconds. After this time period, the PUV was slowly lowered until the photodiode was just above the water surface. The instrument was held stationary in this position to capture an estimate of

incoming radiation in the measured wavelengths. Next, the instrument was lowered to where the photodiode was just below the water surface and held for approximately 10 seconds. This was done to allow easy calibration of the zero depth of the pressure sensor during later analysis. After the near-surface measurement period was complete, the instrument was slowly lowered from the south side of the boat, extended away from the boat edge (to minimize reflection). The profiling rate varied according to the transparency of the lake (i.e., darker lakes typically had slower profiles) but was typically < 1 cm s^{-1}. After reaching the bottom of the lake (although some cases had abbreviated profiles, or profile depths that were limited by the length of the cable, which was 20 m), data collection was stopped and user notes (e.g., lake name, cloud cover, other observations that may have influenced the profile) were stored in memory. Measurements were limited to between the hours of 10:00 and 16:00, with a few exceptions.

Profiles from the PUV were stored in Microsoft database files (.mdb files), which we converted to text files named according to the lake and the starting time of the profile (e.g., a Crystal Lake profile on May 8th of 2011 starting at 13:21 would be named CR_2011_05_08_1321.txt). Each file contained a row of notes (see above), followed by a header row describing the data columns, and the observations taken each second from the beginning to the end of the profile. These data include time (yyyy-mm-dd HH:MM:SS), ground signal, instrument depth (not corrected), 305 nm radiation, 320 nm radiation, 340 nm radiation, 380 nm radiation, quantum flux of PAR, sensor temperature, water temperature (taken from a thermistor outside the body of the PUV), and measurement frame number. An example PAR profile from the PUV is shown in Figure E.1 (relative to % surface PAR) for North Sparkling Bog.

E.3 Calculating K_d from PUV profiles

Raw data files (the text files described above) were processed in two ways: 1) depth measurements were modified by including the proper offset relative to the water surface, and 2) errant values were manually removed. For 1), a log-linear plot of PAR versus depth was created, and the depth of the step change between PAR measurements (when the sensor moved from being slightly above the water surface to slightly below the water surface) was stored as the depth offset. Errant values were removed by manual selection of points in MATLAB from a log-linear plot of PAR versus depth. Only obviously errant data points were removed (e.g., the passage of a cloud that temporarily obscured the sun). The processed data were re-written into processed text files using the format described above, which were depth-corrected and did not include rows with errant measurements.

Assuming K_d does not vary with depth, K_d can be estimated according to the relationship $E_z = E_0\exp(-K_d \cdot z)$ where E_z is PAR irradiance at a given depth (z), and E_0 is PAR irradiance at the surface (i.e., the portion of PAR that is not reflected or absorbed in the surface layer). K_d did vary with depth for many of the field profiles, so K_d was estimated across depth ranges instead of including the entire profile. The exponential decay rate is best estimated by an exponential function, but residuals to the fit are non-linear, due to the depth-dependent exponential decrease in signal as well as measurement noise. As such, we followed the methods of others (e.g., Fee et al. 1996; Rose et al. 2009) and estimated K_d by first log-transforming PAR observations. The K_d calculation methods can be found in the script solveLogDecay.m, which calculates K_d for a user-specified depth range for a given input text file, which is separated into `depth` (depth-corrected PUV depth measurements and `vals` (in this case, PAR observations). Inputs are transformed into uniform vectors:

```
varL = length(depth);
x = reshape(vals,varL,1);
```

```
x = log(x);
y = reshape(depth,varL,1);
```

and a linear model (`s`) is created in MATLAB which uses a Non-linear least squares approach to the function solution.

```
s = fitoptions('Method','NonlinearLeastSquares',...
      'Lower',[-inf,-inf],...
      'Upper',[inf,inf],...
      'Startpoint',[1 1],...
      'MaxFunEvals',1000,...
      'MaxIter',1000);
```

Because the equation which represents the depth-decay of PAR was log-transformed, the function is defined as

```
funcT = '-Kd*y+A';
```

Where `A` is equivalent to $\log(E_0)$. The solution to the function is then determined with the MATLAB fit function

```
f = fittype(funcT,'coefficients',{'A','Kd'},'options',s,...
      'independent','y','dependent','x');
[coef,gofit] = fit(y,x,f);
```

Where `coef` is a MATLAB structure which contains the non-linear least squares estimate for K_d and $\log(E_0)$, as well as 95% confidence intervals for both coefficients. The MATLAB structure `gofit` contains goodness of fit metrics (such as R^2) for the model fit.

Fits to K_d from PUV profiles are displayed in Table E.1 for several lakes in Vilas County (WI) and the Upper Peninsula of Michigan. Because these lakes varied in transparency, K_d fits were calculated over the range of PAR (relative to E_0) between approximately 50% and 1%.

E.4 Acknowledgements

I would like to thank the Williamson lab, including Craig Williamson, Kevin Rose, and Erin Overholt for allowing us to use the PUV from 2010-2012, as well as intellectual contributions to this work and frequent logistical support. Eric Brown, Mike Caballero, Colin

Smith, and Kevin Hayek also helped out with this field work. Kevin Rose was an appreciated collaborator and resource for my research on the influence of the optical properties of water on lake physics. These data were included in four of the five analytical chapters in this dissertation.

E.5 References

Fee, E. J., R. E. Hecky, S. E. M. Kasian, and D. R. Cruikshank. 1996. Effects of lake size, water clarity, and climatic variability on mixing depths in Canadian Shield lakes. Limnology and Oceanography **41:** 912-920.

Jassby, A., and T. Powell. 1975. Vertical patterns of eddy diffusion during stratification in Castle Lake, California. Limnology and Oceanography **20:** 530-543.

Morris, D. P., H. Zagarese, C. E. Williamson, E. G. Balseiro, B. R. Hargreaves, B. Modenutti, R. Moeller, and C. Queimalinos. 1995. The attentuation of solar UV radiation in lakes and the role of dissolved organic carbon. Limnology and Oceanography **40:** 1381-1391.

Rose, K. C., C. E. Williamson, S. G. Schladow, M. Winder, and J. T. Oris. 2009. Patterns of spatial and temporal variability of UV transparency in Lake Tahoe, California-Nevada. J. Geophys. Res.-Biogeosci. **114:** 9, doi: 10.1029/2008jg000816.

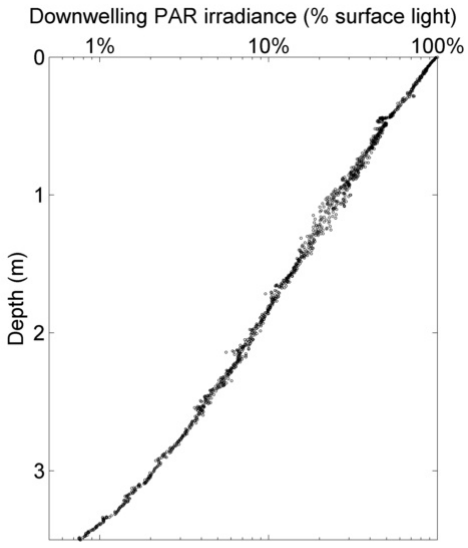

Figure E.1: An example PUV profile from North Sparkling Bog. PAR irradiance values have been normalized according to the irradiance at the water surface.

Table E.1: K_d fits and 95% confidence interval range for 131 PUV profiles from 10 lakes. z_1 and z_2 are the top and bottom depths (respectively) for K_d fits, and represent approximately 50% and 1% of E_0. In cases where the bottom depth measurement was 1% of E_0, the maximum depth of the profile was used for z_2.

Lake Name	Date	Latitude	Longitude	z_1	z_2	K_d
Crystal Bog	2010-07-16	46.0076	-89.6064	0.298	2.01	2.29 ±0.018
Crystal Bog	2010-07-28	46.0076	-89.6064	0.269	1.79	2.58 ±0.011
Crystal Bog	2010-07-29	46.0076	-89.6064	0.295	1.96	2.35 ±0.012
Crystal Bog	2010-08-03	46.0076	-89.6064	0.265	1.76	2.61 ±0.011
Crystal Bog	2012-04-12	46.0076	-89.6064	0.225	0.786	3.13 ±0.038
Crystal Bog	2012-04-29	46.0076	-89.6064	0.268	1.81	2.55 ±0.017
Crystal Lake	2010-06-22	46.0017	-89.6124	2.54	16.9	0.272 ±0.003
Crystal Lake	2010-07-02	46.0017	-89.6124	2.44	16.2	0.284 ±0.002
Crystal Lake	2010-07-15	46.0017	-89.6124	2.43	16.1	0.285 ±0.002
Crystal Lake	2010-07-25	46.0017	-89.6124	2.85	18.4	0.244 ±0.003
Crystal Lake	2010-08-06	46.0017	-89.6124	2.88	18.5	0.24 ±0.003
Crystal Lake	2010-08-12	46.0017	-89.6124	2.71	18	0.255 ±0.002
Crystal Lake	2010-08-19	46.0017	-89.6124	2.66	17.7	0.261 ±0.001
Crystal Lake	2010-08-28	46.0017	-89.6124	2.59	17.2	0.268 ±0.002
Crystal Lake	2010-09-13	46.0017	-89.6124	2.1	14	0.328 ±0.002
Crystal Lake	2010-09-29	46.0017	-89.6124	2.13	14.2	0.325 ±0.001
Crystal Lake	2010-11-01	46.0017	-89.6124	1.82	12.2	0.378 ±0.002
Crystal Lake	2011-04-29	46.0017	-89.6124	2.45	16.3	0.283 ±0.001
Crystal Lake	2011-05-04	46.0017	-89.6124	2.16	14.4	0.321 ±0.001
Crystal Lake	2011-05-04	46.0017	-89.6124	2.19	14.6	0.316 ±0.001
Crystal Lake	2011-05-12	46.0017	-89.6124	1.81	12.2	0.377 ±0.002
Crystal Lake	2011-05-16	46.0017	-89.6124	1.88	12.5	0.368 ±0.001
Crystal Lake	2011-05-16	46.0017	-89.6124	1.86	12.5	0.368 ±0.001
Crystal Lake	2011-05-26	46.0017	-89.6124	1.93	10.4	0.358 ±0.001
Crystal Lake	2011-05-26	46.0017	-89.6124	1.94	10.5	0.36 ±0.001
Crystal Lake	2011-05-28	46.0017	-89.6124	1.94	12.8	0.358 ±0.001
Crystal Lake	2011-06-02	46.0017	-89.6124	1.87	12.4	0.373 ±0.002
Crystal Lake	2011-06-02	46.0017	-89.6124	1.88	12.4	0.371 ±0.002
Crystal Lake	2011-06-02	46.0017	-89.6124	1.85	12.3	0.373 ±0.002
Crystal Lake	2011-06-05	46.0017	-89.6124	1.85	12.2	0.378 ±0.002
Crystal Lake	2011-06-05	46.0017	-89.6124	1.86	12.4	0.371 ±0.002
Crystal Lake	2011-06-08	46.0017	-89.6124	1.88	12.3	0.375 ±0.001
Crystal Lake	2011-06-08	46.0017	-89.6124	1.86	12.4	0.372 ±0.001
Crystal Lake	2011-06-08	46.0017	-89.6124	1.86	12.5	0.369 ±0.001

Crystal Lake	2011-06-12	46.0017	-89.6124	1.8	11.9	0.385 ±0.002
Crystal Lake	2011-06-12	46.0017	-89.6124	1.89	12.6	0.366 ±0.001
Crystal Lake	2011-06-12	46.0017	-89.6124	1.9	12.5	0.368 ±0.001
Crystal Lake	2011-06-12	46.0017	-89.6124	1.91	12.6	0.365 ±0.001
Crystal Lake	2011-06-13	46.0017	-89.6124	1.83	12	0.385 ±0.001
Crystal Lake	2011-06-13	46.0017	-89.6124	1.77	11.8	0.391 ±0.001
Crystal Lake	2011-06-17	46.0017	-89.6124	1.86	12.1	0.379 ±0.003
Crystal Lake	2011-06-17	46.0017	-89.6124	1.85	12.1	0.379 ±0.002
Crystal Lake	2011-06-24	46.0017	-89.6124	1.76	11.7	0.395 ±0.004
Crystal Lake	2011-06-29	46.0017	-89.6124	1.89	12.4	0.37 ±0.004
Crystal Lake	2011-06-29	46.0017	-89.6124	1.88	12.4	0.372 ±0.005
Crystal Lake	2011-06-29	46.0017	-89.6124	1.82	12.3	0.375 ±0.003
Crystal Lake	2011-06-29	46.0017	-89.6124	1.91	12.5	0.369 ±0.003
Crystal Lake	2011-06-29	46.0017	-89.6124	1.87	12.4	0.371 ±0.003
Crystal Lake	2011-07-04	46.0017	-89.6124	1.92	12.8	0.361 ±0.002
Crystal Lake	2011-07-04	46.0017	-89.6124	1.89	12.6	0.367 ±0.002
Crystal Lake	2011-07-06	46.0017	-89.6124	1.86	12.4	0.373 ±0.003
Crystal Lake	2011-07-06	46.0017	-89.6124	1.88	12.5	0.369 ±0.003
Crystal Lake	2011-07-06	46.0017	-89.6124	1.85	12.2	0.375 ±0.002
Crystal Lake	2011-07-08	46.0017	-89.6124	1.88	12.4	0.37 ±0.003
Crystal Lake	2011-07-08	46.0017	-89.6124	1.87	12.5	0.369 ±0.003
Crystal Lake	2011-07-08	46.0017	-89.6124	1.9	12.5	0.368 ±0.002
Crystal Lake	2011-07-10	46.0017	-89.6124	1.89	12.6	0.366 ±0.003
Crystal Lake	2011-07-10	46.0017	-89.6124	1.92	12.7	0.361 ±0.003
Crystal Lake	2011-07-10	46.0017	-89.6124	1.9	12.7	0.363 ±0.003
Crystal Lake	2011-07-11	46.0017	-89.6124	1.9	12.6	0.364 ±0.002
Crystal Lake	2011-07-20	46.0017	-89.6124	1.94	12.9	0.358 ±0.003
Crystal Lake	2011-07-20	46.0017	-89.6124	1.99	13.2	0.35 ±0.003
Crystal Lake	2011-07-25	46.0017	-89.6124	2.06	13.8	0.335 ±0.004
Crystal Lake	2011-07-25	46.0017	-89.6124	2.08	13.9	0.331 ±0.004
Crystal Lake	2011-07-26	46.0017	-89.6124	2.17	14.4	0.32 ±0.004
Crystal Lake	2011-07-26	46.0017	-89.6124	2.18	14.4	0.319 ±0.003
Crystal Lake	2011-07-29	46.0017	-89.6124	2.06	13.8	0.334 ±0.004
Crystal Lake	2011-07-29	46.0017	-89.6124	2.02	13.4	0.344 ±0.004
Crystal Lake	2011-08-03	46.0017	-89.6124	2.11	14	0.328 ±0.004
Crystal Lake	2011-08-11	46.0017	-89.6124	2.17	14.4	0.319 ±0.004
Crystal Lake	2011-08-11	46.0017	-89.6124	2.17	14.5	0.317 ±0.004
Crystal Lake	2011-08-16	46.0017	-89.6124	2.28	15	0.307 ±0.002
Crystal Lake	2011-08-16	46.0017	-89.6124	2.22	14.7	0.312 ±0.003
Crystal Lake	2011-08-22	46.0017	-89.6124	2.31	15.4	0.299 ±0.003

Crystal Lake	2011-08-22	46.0017	-89.6124	2.36	15.7	0.294 ±0.003
Crystal Lake	2011-08-24	46.0017	-89.6124	2.45	16.2	0.285 ±0.003
Crystal Lake	2011-08-24	46.0017	-89.6124	2.49	16.6	0.278 ±0.004
Crystal Lake	2011-09-10	46.0017	-89.6124	2.61	17.3	0.265 ±0.003
Crystal Lake	2011-09-10	46.0017	-89.6124	2.62	17.3	0.266 ±0.003
Crystal Lake	2011-10-03	46.0017	-89.6124	2.68	16.5	0.261 ±0.007
Crystal Lake	2011-11-07	46.0017	-89.6124	2.14	14.3	0.322 ±0.002
Crystal Lake	2012-03-25	46.0017	-89.6124	2.34	15.6	0.295 ±0.001
Crystal Lake	2012-03-25	46.0017	-89.6124	2.41	16.1	0.287 ±0.001
Crystal Lake	2012-04-04	46.0017	-89.6124	2.06	13.7	0.337 ±0.002
Crystal Lake	2012-04-05	46.0017	-89.6124	2.01	13.4	0.345 ±0.000
Crystal Lake	2012-04-12	46.0017	-89.6124	1.91	12.7	0.363 ±0.001
Crystal Lake	2012-04-12	46.0017	-89.6124	2.06	13.7	0.337 ±0.001
Crystal Lake	2012-04-12	46.0017	-89.6124	1.94	12.9	0.355 ±0.001
Crystal Lake	2012-04-17	46.0017	-89.6124	1.97	13.1	0.352 ±0.001
Crystal Lake	2012-04-23	46.0017	-89.6124	1.82	12.1	0.381 ±0.001
Crystal Lake	2012-04-23	46.0017	-89.6124	1.85	12.3	0.375 ±0.001
Crystal Lake	2012-04-29	46.0017	-89.6124	1.85	12.4	0.372 ±0.002
Jekl Bog	2011-06-05	45.9946	-89.6775	0.356	2.41	1.9 ±0.018
Mouser Bog	2011-06-05	45.9977	-89.7215	0.356	2.39	1.93 ±0.018
N Sparkling Bog	2010-06-22	46.0048	-89.7052	0.492	3.27	1.41 ±0.006
N Sparkling Bog	2010-07-02	46.0048	-89.7052	0.475	3.16	1.46 ±0.005
N Sparkling Bog	2010-07-16	46.0048	-89.7052	0.442	2.94	1.57 ±0.004
N Sparkling Bog	2010-07-23	46.0048	-89.7052	0.405	2.7	1.7 ±0.008
N Sparkling Bog	2010-07-25	46.0048	-89.7052	0.419	2.8	1.65 ±0.006
N Sparkling Bog	2010-07-28	46.0048	-89.7052	0.409	2.71	1.7 ±0.006
N Sparkling Bog	2010-08-03	46.0048	-89.7052	0.368	2.45	1.88 ±0.008
N Sparkling Bog	2010-08-09	46.0048	-89.7052	0.396	2.64	1.74 ±0.007
N Sparkling Bog	2010-08-12	46.0048	-89.7052	0.339	2.25	2.05 ±0.006
N Sparkling Bog	2010-08-23	46.0048	-89.7052	0.374	2.5	1.84 ±0.006
N Sparkling Bog	2010-08-27	46.0048	-89.7052	0.368	2.44	1.89 ±0.004
N Sparkling Bog	2010-11-02	46.0048	-89.7052	0.229	1.52	3.02 ±0.012
Sparkling Lake	2011-05-03	46.0082	-89.7004	1.64	10.9	0.422 ±0.001
Sparkling Lake	2011-08-17	46.0082	-89.7004	2.96	17	0.234 ±0.002
Sparkling Lake	2011-08-17	46.0082	-89.7004	3.05	16.9	0.227 ±0.003
S Sparkling Bog	2010-07-25	46.0034	-89.7053	0.344	2.28	2.02 ±0.009
S Sparkling Bog	2010-07-28	46.0034	-89.7053	0.355	2.36	1.95 ±0.010
S Sparkling Bog	2010-08-03	46.0034	-89.7053	0.312	2.08	2.22 ±0.008
S Sparkling Bog	2010-08-09	46.0034	-89.7053	0.277	1.84	2.51 ±0.013
S Sparkling Bog	2010-08-23	46.0034	-89.7053	0.274	1.83	2.52 ±0.013

Trout Bog	2010-07-02	46.0411	-89.6861	0.33	2.13	2.17 ±0.016
Trout Bog	2010-07-15	46.0411	-89.6861	0.323	2.14	2.15 ±0.015
Trout Bog	2010-07-16	46.0411	-89.6861	0.345	2.31	2 ±0.015
Trout Bog	2010-07-21	46.0411	-89.6861	0.329	2.17	2.11 ±0.031
Trout Bog	2010-07-21	46.0411	-89.6861	0.339	2.24	2.04 ±0.019
Trout Bog	2010-07-28	46.0411	-89.6861	0.309	2.06	2.24 ±0.017
Trout Bog	2010-08-04	46.0411	-89.6861	0.324	2.15	2.15 ±0.013
Trout Bog	2010-08-27	46.0411	-89.6861	0.333	2.21	2.09 ±0.007
Trout Bog	2011-07-08	46.0411	-89.6861	0.219	1.45	3.18 ±0.014
Trout Bog	2012-04-12	46.0411	-89.6861	0.173	0.726	3.94 ±0.040
Trout Bog	2012-04-12	46.0411	-89.6861	0.169	0.451	3.96 ±0.061
Trout Lake	2011-08-11	46.0293	-89.6720	2.2	14.7	0.314 ±0.001
Trout Lake	2011-08-11	46.0293	-89.6720	2.19	14.7	0.314 ±0.002
Ward	2012-04-21	46.2548	-89.5172	0.46	3.04	1.52 ±0.009
Ward	2012-04-21	46.2548	-89.5172	0.437	2.98	1.54 ±0.006
Ward	2012-04-24	46.2548	-89.5172	0.322	2.18	2.11 ±0.023
Ward	2012-04-24	46.2548	-89.5172	0.355	2.34	1.96 ±0.019